# Output ที่ได้จากโครงการ

จำนวนบัณฑิตที่จบการศึกษา

1.1 บัณฑิตปริญญาเอก 3 คน ได้แก่

1. นายศุภกร อัจฉริยวุฒิ ภาควิชาวิศวกรรมเคมี มจธ. ทำวิทยานิพนธ์ เรื่อง Mass transfer study and mathematical modeling of gas-liquid membrane contacting process for $CO_2$ absorption.
2. นายสาครินทร์ ไขศรี ภาควิชาวิศวกรรมเคมี มจธ. ทำวิทยานิพนธ์ เรื่อง Absorption and desorption processes for $CO_2$ capture by using membrane contactor.
3. นายวุฒิกร สายแก้ว ภาควิชาวิศวกรรมเคมี ม.อุบลราชธานี ทำวิทยานิพนธ์ เรื่อง Fouling of nanofiltration membrane by natural organic matter and heavy metals.

1.2 บัณฑิตปริญญาโท 9 คน ได้แก่

1. นายสาธิต วราวุฒิ ภาควิชาวิศวกรรมเคมี มจธ. ทำวิทยานิพนธ์ เรื่อง การลดปริมาณแอลกอฮอล์ในไวน์ด้วยกระบวนการกลั่นแบบออสโมติก
2. นายสหเวช บำเพิง ภาควิชาวิศวกรรมเคมี มจธ. ทำวิทยานิพนธ์ เรื่อง การถ่ายเทมวลในการใช้โอโซนเพื่อบำบัดน้ำล้างสีย้อมในกระบวนการเมมเบรนคอนแทคเตอร์
3. นายวิชิตพันธ์ รองวงศ์ ภาควิชาวิศวกรรมเคมี มจธ. ทำวิทยานิพนธ์ เรื่อง ผลของสารละลายดูดกลืนและการเติมเกลือต่อสมรรถนะของกระบวนการเมมเบรนคอนแทคเตอร์
4. นายธรากร สุวรรณชาติ ภาควิชาวิศวกรรมเคมี มจธ. ทำวิทยานิพนธ์ เรื่อง การใช้โอโซนเพื่อบำบัดน้ำล้างสีย้อมด้วยกระบวนการเมมเบรนคอนแทคเตอร์ : ผลของตัวแปรในการดำเนินการและสารช่วยย้อม
5. นางสาวกมลชนก แสงสว่าง ภาควิชาวิศวกรรมเคมี สจล. ทำวิทยานิพนธ์ เรื่อง การลดปริมาณฟอร์มัลดีไฮด์ในน้ำทิ้งอุตสาหกรรมด้วยกระบวนการ membrane bioreactor
6. นางสาวปิ่นนภา หาญณรงค์ ภาควิชาวิศวกรรมเคมี มจธ. ทำวิทยานิพนธ์ เรื่อง การปรับปรุงคุณสมบัติชอบน้ำของเยื่อแผ่นอัลตราฟิลเตรชัน PES ด้วย $Al_2O_3$ เพื่อลดการเกิดฟาวลิง
7. นายไพบูลย์ เย็นพันธุ์ ภาควิชาวิศวกรรมเคมี มจธ. ทำวิทยานิพนธ์ เรื่อง การศึกษาการแยก Pb2+ ในกระบวนการ Micellar-enhanced ultrafiltration (MEUF) ด้วยสารลดแรงตึงผิวผสม
8. นายกิตติคุณ เมฆทรัพย์ ภาควิชาวิศวกรรมเคมี มจธ. ทำวิทยานิพนธ์ เรื่อง การเคลือบผิวเยื่อแผ่น PVDF ด้วยไคโตซานเพื่อป้องกันการเปียกในกระบวนการกลั่นแบบออสโมติก
9. นายพัฒนุตน์ คัมภีรภาพสุนทร ภาควิชาวิศวกรรมเคมี มจธ. ทำวิทยานิพนธ์ เรื่อง การผลิตและการหาคุณลักษณะของเยื่อแผ่นอัลตราฟิลเตรชันโพลิเมอร์ผสม Polysulfone/Cellulose acetate

# ผลงานตีพิมพ์ในวารสารวิชาการนานาชาติ

1. **S. Atchariyawut, R. Jiraratananon***, R. Wang. Separation of $CO_2$ from $CH_4$ by using gas–liquid membrane contacting process, J. Membrane Science, 304 (2007), 163-172.
2. **C. Jarusutthirak*, S. Mattaraj, R. Jiraratananon**. Factors affecting nanofiltration performances in natural organic matter rejection and flux decline, Separation and Purification Technology, 58 (2007), 68–75.
3. **S. Atchariyawut, R. Jiraratananon***, R. Wang. Mass transfer study and modeling of gas–liquid membrane contacting process by multistage cascade model for CO2 absorption, Separation and Purification Technology, 63 (2008), 15–22.
4. **S. Mattaraj*, C. Jarusutthirak, R. Jiraratananon**. A combined osmotic pressure and cake filtration model for crossflow nanofiltration of natural organic matter, J. Membrane Science, 322 (2008), 475-483.
5. S. **Khaisri**, D. deMontigny, P*. Tontiwachwuthikul, **R. Jiraratananon**. Comparing membrane resistance and absorption performance of three different membranes in a gas absorption membrane contactor, Separation and Purification Technology, 65 (2009), 290–297.
6. S. **Atchariyawut**, J. Phattaranawik, T. Leiknes, **R. Jiraratananon***. Application of ozonation membrane contacting system for dye wastewater treatment, Separation and Purification Technology, 66 (2009), 153-158
7. **S. Varavuth, R. Jiraratananon*, S. Atchariyawut**. Experimental study on dealcoholization of wine by osmotic distillation process, Separation and Purification Technology, 66 (2009), 313–321.
8. **S. Boributh, A. Chanachai, R. Jiraratananon***. Modification of PVDF membrane by chitosan solution for reducing protein fouling, J. Membrane Science, 342 (2009), 97-104.
9. **W. Rongwong, R. Jiraratananon*, S. Atchariyawut**. Experimental study on membrane wetting in gas–liquid membrane contacting process for $CO_2$ absorption by single and mixed absorbents, Separation and Purification Technology, 69 (2009), 118-125.
10. S. **Khaisri**, D. deMontigny, P*. Tontiwachwuthikul, **R. Jiraratananon**. A mathematical model for gas absorption membrane contactors that studies the effect of partially wetted membranes, J. Membrane Science, 347 (2010), 228-239.

11. P. **Yenphan, A. Chanachai, R. Jiraratananon***. Experimental study on micellar-enhanced ultrafiltration (ME UF) of aqueous solution and wastewater containing lead ion with mixed surfactants, Desalination, 253 (2010), 30-37.
12. S. Mattaraj*, W, Phimpha, P. Hongthong, **R. Jiraratananon.** Effect of operating conditions and solution chemistry on model parameters in crossflow reverse osmosis of natural organic matter, Desalination, 253 (2010), 38-45.
13. S. **Bamperng, T. Suwannachart, S. Atchariyawut, R. Jiraratananon***, Ozonation of dye wastewater by membrane contactor using PVDF and PTFE membranes, (2010) Separation and Purification Technology. **72(2010)186-193.**
14. S. **Mattaraj,* W. Saikaew, R. Jiraratananon**. Nanofiltration Performance of Lead Solution: Effects of concentration, solution pH and ionic strength, Water Science and Technology: water supply. **10.2(2010)193-200.**
15. K. **Meksarp, A. Chanachai, R. Jiraratananon***, Coating of hollow fibre PVDF membrane with chitosan for protection against wetting and flavor loss in osmotic distillation, (2010) Separation and Purification Technology. **72(2010)217-224.**

Available online at www.sciencedirect.com
ScienceDirect
ELSEVIER
Journal of Membrane Science 304 (2007) 163–172
journal of MEMBRANE SCIENCE
www.elsevier.com/locate/memsci

# Separation of $CO_2$ from $CH_4$ by using gas–liquid membrane contacting process

Supakorn Atchariyawut[a], Ratana Jiraratananon[a,*], Rong Wang[b]

[a] Department of Chemical Engineering, King Mongkut's University of Technology Thonburi, Bangkok 10140, Thailand
[b] Institute of Environmental Science & Engineering, Nanyang Technological University, Innovation Center (NTU), Block 2, Unit 237, 18 Nanyang Drive, Singapore 637723, Singapore

Received 26 April 2007; received in revised form 18 July 2007; accepted 20 July 2007
Available online 26 July 2007

## Abstract

The separation of carbon dioxide ($CO_2$) from methane ($CH_4$) by using a gas–liquid membrane contactor was studied in order to confirm the potential of the process. The experiments were performed in a membrane contactor constructed with 0.2 μm pore size microporous PVDF hollow fibers. Pure water, aqueous sodium hydroxide (NaOH) solution and aqueous monoethanolamine (MEA) solution were employed as the absorbents. Sodium chloride (NaCl) was also used as an additive in the NaOH aqueous solution. The effects of operating parameters such as the gas and liquid velocity, concentration of NaOH solution, absorbent temperature, and NaCl concentration on the $CO_2$ flux were investigated along with the mass transfer analysis of the process. In addition, the impacts of the flow pattern and the membrane module packing density as well as the long-term performance were also investigated, aiming to obtain a full picture and a deep insight on the system.

It was found that the $CO_2$ flux was enhanced by the increase of NaOH solution concentration, NaOH solution temperature and the $CO_2$ volume fraction in the feed stream, but the increase of water temperature resulted in decreasing the $CO_2$ flux. The retentate selectivity obtained in this work was not satisfactory due to the laboratory scale of the membrane module used. However, the percentage of $CH_4$ recovery was very high, suggesting that no significant $CH_4$ loss took place during the operation. Counter-current flow mode took the advantage of higher mass transfer over co-current one, and the $CO_2$ flux increased with increasing membrane module packing density. Long-term performance tests showed that the NaOH solution was more suitable than other absorbents to be applied to the PVDF microporous hollow fiber contactors, as the NaOH aqueous solution can provide a higher separation performance and the $CO_2$ flux was kept almost unchanged over a long period of operation. Furthermore, the PVDF membrane gave the membrane resistance around 22% of the total resistance for pure $CO_2$ absorption in water.

*Keywords:* $CO_2/CH_4$ separation; Membrane contactors; Gas absorption; Operating conditions; Packing density

## 1. Introduction

The separation of $CO_2$ from $CH_4$ is one of the important processes in many industrial areas such as natural gas processing, biogas purification, enhanced oil recovery and flue gas treatment [1,2]. $CO_2$ in natural gas must be removed because it causes pipe corrosion, reduces the heating value, takes up volume in the pipeline and is able to solidify in cryogenic process. Besides, being a greenhouse gas, the emission of $CO_2$ from the combustion of fossil fuel is a serious concern associated with global climate change.

Conventional absorption processes are generally operated in the contactor devices, e.g., packed and plate columns, which require huge space and high investment cost. In addition, they also suffer from several operational limitations including flooding, entrainment and foaming [3]. Membrane gas permeation process is an alternative separation process for capturing $CO_2$, but low gas flux and $CH_4$ loss are the two main problems in gas permeation process [4]. Thus, it is imperative to develop more efficient processes for upgrading low quality gases than presently available ones. The hollow fiber membrane gas–liquid contacting process, which integrates the advantage of traditional absorption and membrane processes, can potentially overcome those operational limitations and is considered as a competitively alternative technology. Membranes that are used in membrane contacting process act as barrier to separate liquid and gas phases

---

[*] Corresponding author. Tel.: +66 2470 9222; fax: +66 2428 3534.
*E-mail address:* ratana.jir@kmutt.ac.th (R. Jiraratananon).

0376-7388/$ – see front matter © 2007 Elsevier B.V. All rights reserved.
doi:10.1016/j.memsci.2007.07.030

and provide interfacial areas for the two phases. Therefore, the separation performance depends on the interaction between interested gas solute and liquid absorbent. The use of membrane contactor offers a number of advantages over conventional dispersed processes such as high surface area per unit contact volume, individual gas and liquid flow channels, compactness of structure and easiness to scale up [3,5,6].

Qi and Cussler [7,8] were the pioneers who employed microporous polypropylene (PP) hollow fiber membrane for $CO_2$ removal using NaOH solution as an absorbent. Following their original work, there were many works focusing on gas–liquid membrane contactors for gas separation processes such as removal of $CO_2$, $H_2S$, $SO_2$ from flue gases and natural gas, eliminating VOC from $N_2$/air by using mineral oils, and separating olefin/paraffin with silver nitrate as an absorbent [7–11].

The majority of study on the gas–liquid membrane contacting process applications is for $CO_2/N_2$ separation (flue gas treatment) [12–18]. There were limited reports on $CO_2/CH_4$ separation using membrane contactors. Teplykov et al. [19] carried out the theoretical simulation to study biogas (40% $CO_2$ and 60% $CH_4$) purification by using polyvinyltrimethylsilane (PVTMS) nonporous membrane contactor operated in a recirculation mode. The simulation results seemed to be useful to be applied in biogas separation. The Henry's constants for water with $CO_2$ and $CH_4$ at 25 °C are $3.36 \times 10^{-7}$ and $1.38 \times 10^{-8}\ \mathrm{mol\,dm^{-3}\,Pa^{-1}}$, respectively [20]. Due to the large difference, the gas–liquid membrane contacting process can be potentially applied for $CO_2/CH_4$ separation.

In the present work, the separation of $CO_2$ from $CO_2/CH_4$ mixture using the gas–liquid membrane contacting process was performed. Three types of absorbents, pure water, NaOH and monoethanolamine (MEA) aqueous solutions were used in the experiments. NaCl was also employed as an additive in the NaOH aqueous solution. The operating conditions that affected the system performance such as the gas and liquid velocities, the concentration of NaOH solution, absorbent temperature and NaCl concentration were investigated thoroughly in combination with mass transfer analyses. The long-term performances of the systems using pure water, NaOH and MEA as the absorbents were also monitored and compared with each other. In addition, the quantitative analysis of the membrane resistance was also performed in order to gain a better understanding of the effect of membrane mass-transfer resistance on the system performance.

## 2. Theory

### 2.1. Mass transfer in gas–liquid membrane contacting process

Fig. 1 shows the transport of the interested gas in the gas–liquid membrane contactor from the gas phase through the porous membrane into the liquid phase which can be described by the resistance-in-series model, expressed by Eq. (1) [21].

$$\frac{1}{K_{ol}} = \frac{1}{k_l} + \frac{Hd_o}{k_m d_{ln}} + \frac{Hd_o}{k_g d_i} \tag{1}$$

where $K_{ol}$ is the overall mass transfer coefficient based on liquid-phase (m/s), $k_l$, $k_m$, $k_g$ are the individual mass transfer coefficients of the liquid phase, membrane and gas phase, respectively. $H$ represents Henry's constant. $d_i$, $d_o$, $d_{ln}$ are the inner, outer and logarithmic mean diameters of the fibers, respectively. From the above equation, the overall mass transfer resistance is the summation of individual mass transfer resistance (also see Fig. 1).

In the gas–liquid membrane contacting process operation, either the gas phase or liquid phase can be fed through the shell side or tube side of the hollow fiber membrane module. However, flow of liquid in the tube side takes more advantage than that in the shell side [17]. For the liquid flow in tube side, the well-known Graetz-Lévêque mass transfer correlation was widely used to predict accurately the tube side mass-transfer

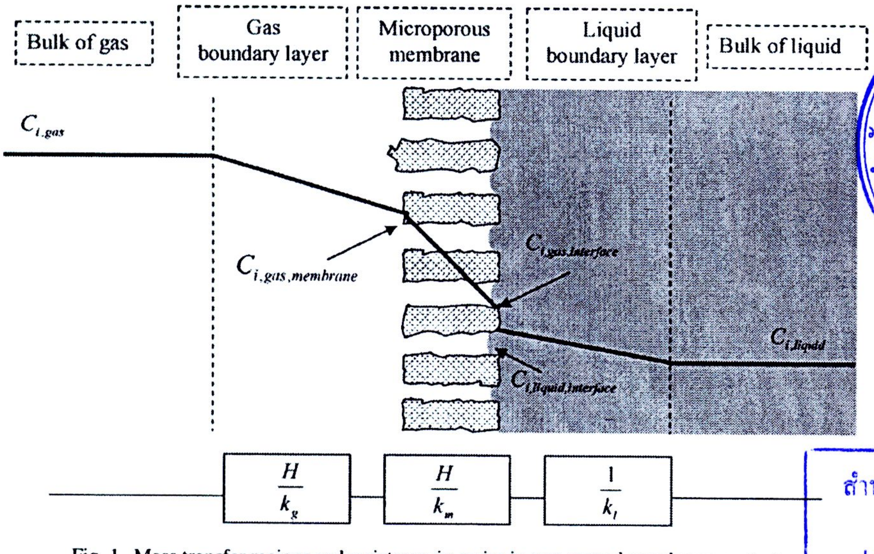

Fig. 1. Mass transfer regions and resistance-in-series in non-wetted membrane contactor.

coefficient [3,22]:

$$Sh = \frac{k_l d_i}{D} = 1.62\left(\frac{d_i^2 V}{LD}\right)^{1/3} \quad (2)$$

where $Sh$ is Sherwood number, $D$ the diffusion coefficient, $L$ is the tube length and $V$ is the fluid velocity.

### 2.2. Gas solubility in salt solutions

When salt concentration in a liquid phase increases, the gas solubility in the liquid is normally found to decrease. This phenomenon is referred as "salting-out" effect. The effect of salt concentration on the $CO_2$ and $CH_4$ solubility can be explained by the Sechenov relation [23]:

$$\log\left(\frac{c_{G,0}}{c_G}\right) = Kc_s \quad (3)$$

where $c_{G,0}$ and $c_G$ denote the gas solubility in pure water and in a salt solution, respectively, and $c_s$ is the molar concentration of the salt. The parameter $K$ ("Sechenov constant") is specific to the gas as well as the salt used. In this work, NaCl was added into the NaOH aqueous absorbent in order to improve the product gas quality and to increase $CH_4$ recovery.

### 2.3. Penetration pressure

In the gas–liquid membrane contacting process, the operation in dry mode (gas-filled membrane pore) is more advantageous than that in the wet mode (liquid-filled membrane pore) because of the higher diffusivity of the gas. The liquid will not wet the membrane when pressure difference between liquid stream and the gas phase in membrane pores is lower than the penetration pressure [3] defined as the following:

$$\Delta P = \frac{-2\sigma \cos\theta}{r_p} \quad (4)$$

where $\Delta P$ is the penetration pressure or wetting pressure, $\sigma$ is the surface tension of the liquid, $\theta$ is the contact angle formed between fluid and the membrane pore and $r_p$ is the membrane pore radius.

Table 1
Specifications of the hollow fiber membrane module used

| | |
|---|---|
| Fiber o.d. (μm) | 1000 |
| Fiber i.d. (μm) | 650 |
| Module i.d. (mm) | 10 |
| Membrane pore size (μm) | 0.2 |
| Membrane porosity | 0.75 |
| Number of fibers | 50[a], 35, 20[a] |
| Effective module length (mm) | 270 |
| Effective contact area ($m^2$) | 0.019 |

[a] The modules were only used to study the effect of module packing density.

For water at 25 °C, $\sigma$ is 72.8 mN/m [24] and the contact angle between water and PVDF membrane used in this work is 100° (measured by FACE, Contact angle meter, model CA-A, Kyowa Interface Science Co., Ltd.). Therefore, the wetting pressure of 0.2 μm pore size of PVDF membrane is 0.126 MPa. In order to maintain a dry mode in the membrane pores, the pressure difference between gas and liquid streams in all experiments was kept lower than 0.1 MPa.

## 3. Experimental

Hydrophobic porous polyvinylidenefluoride (PVDF) hollow fiber membranes used in the experiment were kindly provided by Memcor Australia (South Windsor, New South Wales, Australia). The characteristics of the membrane are shown in Table 1. A 99% grade NaOH purchased from THASCO Chemical Co., Ltd., Thailand and a 99% grade MEA obtained from Carlo Erba Reagenti were mixed with RO water, respectively, to prepare aqueous absorbents with desired concentrations. Potassium hydrogen phthalate (KHP) were purchased from Merck Ltd., Thailand. Methane (99.9%) and Carbon dioxide (99.8%) were obtained from Thai Industrial Gases PLC, Thailand.

The experimental setup is schematically shown in Fig. 2. Pure $CO_2$ or $CO_2/CH_4$ mixture with a volume ratio of 50:50 or 20:80, which is in the composition range of biogas or natu-

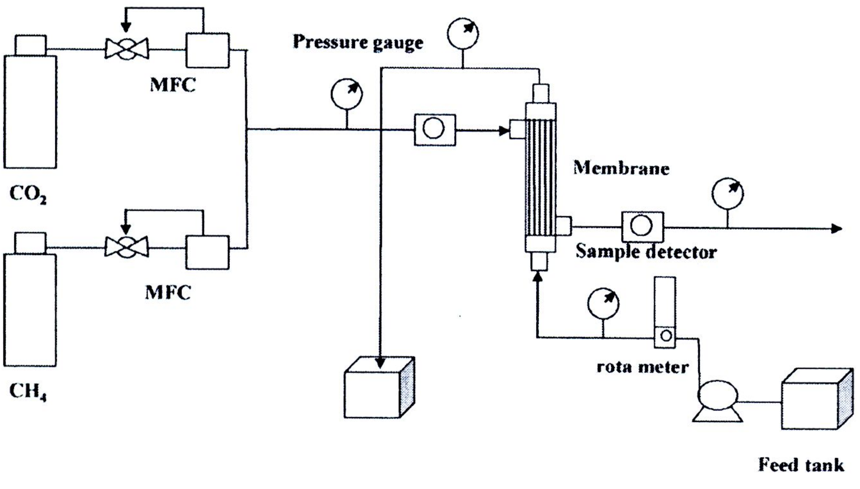

Fig. 2. Schematic diagrams of a gas–liquid membrane contactor unit.

ral gas, was used as the feed gas while pure water, NaOH, and MEA aqueous solutions were employed as absorbents. In the experiment, the flow rate of the feed gas supplied from compressed gas cylinders was adjusted and controlled by Aalborg (GFC model) mass flow controllers, and then it was fed through the shell side of the membrane module. The inlet and outlet gas volume flow rates were measured by a digital bubble meter. The liquid absorbent was pumped by a peristaltic pump (L/S® Easy-load® II, Masterflex model 77201-62) from the feed tank through a rotameter into the tube side of the hollow fibers. The pressure gauges were used to indicate the inlet and outlet pressures of the gas and liquid. When $CO_2/CH_4$ mixture was used as the feed gas, Gas Chromatograph (6890 Hewlett Packard, TCD) was used to analyze the inlet and outlet gases compositions. Potassium hydrogen phthalate (KHP), which is a primary standard solution for titration, was used for the confirmation of the absorbent concentration. All of the data were collected after the experiment had been operated for 30 min to ensure the system to reach the steady state. The results of each run were averaged from five times of sampling.

The system and operating parameters, which influenced the process performance, i.e., $CO_2$ concentration in the feed, NaOH and MEA concentrations, the gas flow rate, the absorbent flow rate, the absorbent's temperature and NaCl concentration, were varied based on the experimental design. In order to improve the product gas quality, a 1 M NaOH aqueous solution with the presence of 1, 3, 5 M NaCl in the absorbent were studied. Either pure $CO_2$ or mixed gas flow rate were varied from 200 to 400 ml/min to investigate the effect of gas flow rate. The effect of liquid absorbent temperatures was also studied by altering the absorbent temperature from 30 to 50 °C. All of the experiments were performed at the room temperature, therefore, the gas phase temperature in this work was approximately 30 °C.

## 4. Results and discussion

### 4.1. Separation of $CO_2$ from $CH_4$

The separation factor has been widely used to indicate the efficiency of membrane gas separation processes [25,26]. Generally, in the gas–liquid membrane contacting system, the retentate stream was the desired product since the $CO_2$ in the feed gas diffused through the membrane pores and was absorbed in the aqueous absorbent. Therefore, the retentate selectivity was selected to describe the process efficiency, which can be calculated by the following equation:

$$\alpha_{R,CH_4/CO_2} = \left(\frac{C_{CH_4,R}/C_{CO_2,R}}{C_{CH_4,F}/C_{CO_2,F}}\right) \tag{5}$$

where $\alpha_{R,CO_2/CH_4}$ represents the retentate selectivity. $C_{CO_2,R}$, $C_{CO_2,F}$, $C_{CH_4,R}$ and $C_{CH_4,F}$ are the concentrations of $CO_2$ in the retentate, $CO_2$ in the feed, $CH_4$ in retentate and $CH_4$ in the feed, respectively.

In this work, the retentate selectivity was approximately 1.20 and 1.72 for using water and 1 M NaOH as absorbents, respectively. These values were achieved under the following experimental conditions: 2.3 and 0.07 m/s liquid and gas velocity, respectively, and 30 °C of the operating temperature. It was found that the values of selectivity were quite low. From the above equation, it can be found that the retentate selectivity depends on the difference between the inlet and outlet gas concentrations which are influenced by the membrane area, and also by other variables for example gas and liquid velocities, the type of the absorbent used, and gas concentration. Since the experiments were carried out in the lab-scale apparatus, the membrane area was fairly low; consequently, the retentate selectivity was also low. Recently, Teplyakov et al. reported that the recycle membrane contactor system (RMCs) could offer high retentate selectivity for $CO_2/CH_4$ separation [19]. It may be a feasible approach to be used in practical applications.

The percentage recovery ($S$) is another performance indicator of gas separation processes. In the case of the retentate stream being the product, the $CH_4$ recovery can be calculated as follows:

$$S = \frac{Q_{CH_4,R}}{Q_{CH_4,F}} \times 100 \tag{6}$$

where $Q_{CH_4,R}$ and $Q_{CH_4,F}$ are the $CH_4$ flow rates in the retentate and feed, respectively.

The concentration of $CH_4$ and $CO_2$ were measured by the Gas Chromatography. The $CO_2/CH_4$ mixture with a volume ratio of 20/80 at 200 ml/min total gas flow rate was used as feed gas. The $CH_4$ and $CO_2$ concentrations in the retentate stream were 83.2% and 16.8%, respectively, at 193.1 ml/min total gas flow rate of retentate stream, for using water as the absorbent at 30 °C. The liquid velocity was 2.57 m/s while the gas velocity used was 0.07 m/s (200 ml/min). The $CH_4$ recovery of every experiment in this study was approximately 100%, which suggested that no significant $CH_4$ loss took place during the process operation. However, the membrane modules used were relatively small and the system may have undetected loss of $CH_4$. Nevertheless, this is one attractive benefit of using the gas–liquid membrane contacting process for $CO_2$ removal from $CO_2/CH_4$ gas mixture. Due to the high recovery of $CH_4$, the effects of operating conditions on $CH_4$ flux cannot be presented. Therefore, the efficiency of system was evaluated in terms of $CO_2$ flux.

### 4.2. Effects of operating conditions on the $CO_2$ flux ($CO_2/CH_4$ mixture as the feed gas)

In this study, the $CO_2$ flux which was used to indicate the process efficiency can be estimated by the following equation [27]:

$$J_{CO_2} = \frac{(Q_F \times C_{CO_2,F} - Q_R \times C_{CO_2,R}) \times 273.15 \times 1000}{22.4 \times T_g \times A_T} \tag{7}$$

where $J_{CO_2}$ is the $CO_2$ flux. $C_{CO_2,F}$ and $C_{CO_2,R}$ are the $CO_2$ concentrations in the feed and retentate streams, respectively. $Q_F$ and $Q_R$ are the gas flow rates at the inlet and outlet of the membrane module, respectively. $T_g$ is the gas temperature. $A_T$ is the mass transfer area.

Fig. 3 depicts the relationship between the $CO_2$ flux and the liquid velocity for pure water and NaOH with different concen-

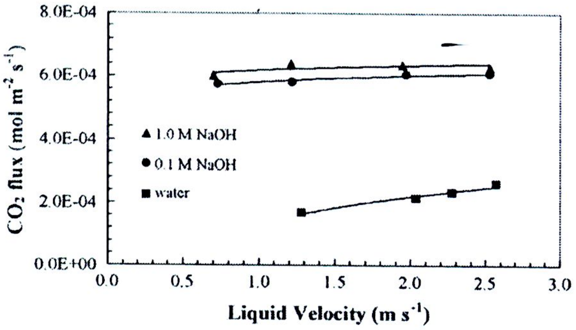

Fig. 3. Effects of liquid velocity and NaOH concentration on $CO_2$ flux (absorbent temperature: 30 °C, gas flow rate: 200 ml/min, feed gas: 20/80 $CO_2/CH_4$).

trations as the absorbents. The amount of $CO_2$ absorbed into the liquid phase was increased since the mass transfer coefficient ($k_l$) increased with the liquid velocity (see Eq. (2)). There are many literatures that reported the same trend of the experimental results [6,15,27]. It can also be seen that the use of a chemical absorbent improved the separation efficiency significantly as $CO_2$ chemically reacted with $OH^-$, leading to the increase of mass transfer coefficient in the liquid phase ($CO_2$ concentration difference between the gas and liquid phases increased). The higher the NaOH concentration used, the higher the $CO_2$ flux obtained. The $CO_2$ flux in the case of 1 M NaOH as the absorbent was about six times higher than that using water as the absorbent. Similar observations on the effect of absorbent concentration on the mass transfer rate were reported in literatures [14,27]. Additionally, the figure also shows that the change in NaOH absorbent velocity slightly influenced the $CO_2$ flux, thus, the system performance using NaOH as absorbent was controlled by the gas phase or the membrane. On the other hand, when water was used as absorbent, the system exhibited a liquid phase control mass transfer because the increase in water velocity significantly affected the $CO_2$ flux.

Fig. 4 shows the effect of absorbent temperature on the $CO_2$ flux, where NaOH aqueous solutions and water were still used as the absorbent. Increasing the temperature of the NaOH absorbent resulted in an increase of the $CO_2$ flux because of the increase of chemical reaction rate between NaOH and $CO_2$. These results can be confirmed with the literature. Kucka et al. [28] studied the reaction kinetics between $CO_2$ and hydroxide ion in the temperature range from 20 to 50 °C. It was found that the reaction rate constant increased with increasing temperature. Moreover, the liquid absorbent viscosity decreased and the diffusion increased with increasing liquid temperature, thus the mass transfer rate was enhanced. Vazquez et al. [29] measured the viscosity of NaOH aqueous solutions over the temperature range of 25–40 °C by employing a Shott-Geräte AVS 350 automatic Ubbelohde viscometer. They found that the viscosity of 1 M NaOH at 25 °C was 0.9281 mPa s and was 0.6817 mPa s at 40 °C. In contrast, when water was used as the absorbent, the $CO_2$ flux decreased with increasing temperature due to the decrease of the gas solubility. Versteeg and van Swaaji observed that the solubility of $CO_2$ in water decreased with increasing temperature, for instance, the solubility of $CO_2$ in water was 0.815 mol/mol at 25 °C and was 0.648 mol/mol at 35 °C [30]. The increase in liquid absorbent temperature also decreased $CH_4$ solubility. Therefore, the system operated by using NaOH with a high temperature as the absorbent will take an advantage of increasing $CO_2$ flux and reducing the $CH_4$ loss.

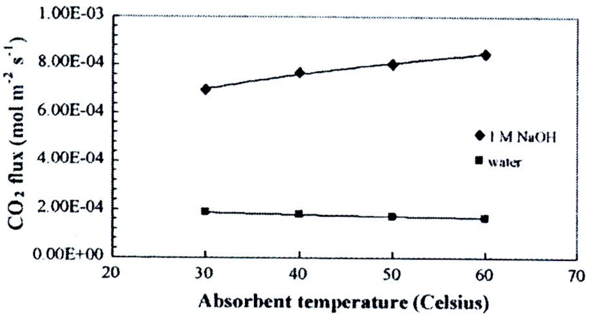

Fig. 4. Effects of liquid velocity and absorbent temperature on $CO_2$ flux (liquid velocity: 1.31 m/s, gas flow rate: 200 ml/min, feed gas: 20/80 $CO_2/CH_4$).

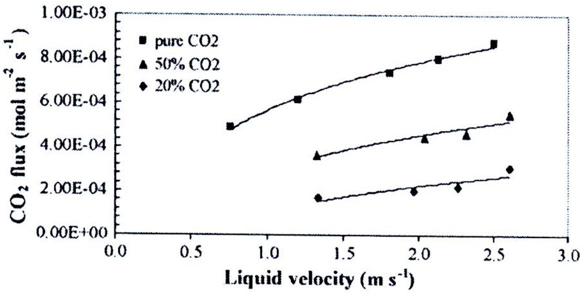

Fig. 5. Effect of gas concentration on $CO_2$ flux (absorbent: water, absorbent temperature: 30 °C, gas flow rate: 200 ml/min).

In practice, $CO_2$ is present over a wide range of concentration in the gas stream mixed with $CH_4$. $CO_2$ content is 5–30% for crude natural gas, and is around 40–50% for biogas [21,31]. In order to confirm the versatility of the membrane contactor, the effect of $CO_2$ concentration in the feed gas on the $CO_2$ flux was also studied using pure water as absorbent and the result is shown in Fig. 5. The increase in gas concentration resulted in an increase of the $CO_2$ flux, as the increase in $CO_2$ concentration led to the enhancement of the driving force of the system. In addition, the increase of $CO_2$ concentration in the feed stream also influenced the removal efficiency and the results are shown in Fig. 6. It can be seen that the $CO_2$ removal efficiency increased with increasing $CO_2$ concentration also because of the increase of the driving force. The $CO_2$ removal efficiency was determined by the following equation:

$$\eta = \left( \frac{Q_F \times C_{CO_2,F} - Q_R \times C_{CO_2,R}}{Q_F \times C_{CO_2,F}} \right) \times 100 \qquad (8)$$

where $\eta$ represents the removal efficiency, $C_{CO_2,F}$ and $C_{CO_2,R}$ are the $CO_2$ concentrations in the feed and retentate streams, respectively. $Q_F$ and $Q_R$ are the gas flow rates at the inlet and outlet of membrane module, respectively.

Fig. 7 illustrates the variation of the $CO_2$ flux as a function of the liquid velocity at different gas flow rates for pure $CO_2$ and $CO_2/CH_4$ mixture. For water–pure $CO_2$ system, change in

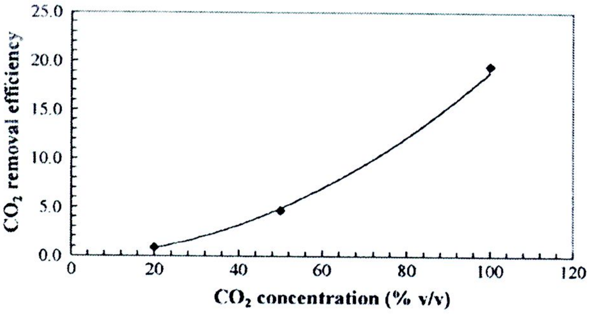

Fig. 6. Effect of $CO_2$ concentration in the feed stream on separating efficiency (absorbent: water, absorbent temperature: 30 °C, liquid velocity: 2.5 m/s, gas flow rate: 200 ml/min).

$CO_2$ flux was negligible as the gas velocity was increased. The main mass transfer resistance of pure $CO_2$–water system was in the liquid phase. Thus, the increase in gas velocity did not affect the $CO_2$ flux much. This agreed with the results presented by Wang et al. [15]. For water–$CO_2$/$CH_4$ mixture system, the $CO_2$ flux decreased as the gas flow rate increased because of the decrease in contact time between the gas and liquid phases. Yan et al. [27] reported the effect of gas flow rate on the $CO_2$ flux using potassium glycinate (PG) and monoethanolamine (MEA) as absorbents. They found that increase of gas velocity led to enhancement of the $CO_2$ mass transfer. This result contrasts with our finding because reactive absorbents (chemical absorption) were used in their work. Conversely, when the water (physical absorption) was used as absorbent, the $CO_2$ mass transfer was limited by the gas solubility in the liquid.

### 4.3. *Effect of NaCl addition into the NaOH absorbent*

The gas–liquid membrane contacting processes were normally operated by passing the absorbent solution and the feed gas on the opposite sides of the microporous membrane. Therefore, water vapors in the liquid phase were able to diffuse through the membrane pores due to the vapor pressure difference. To improve the quality of product gas and to increase $CH_4$ recovery, the addition of NaCl salt into the absorbent was studied. The influence of NaCl presence on a 1 M NaOH aqueous solution on the $CO_2$ flux and the percentage of relative humidity of the outlet gas are shown in Fig. 8. It can be seen that the increase in NaCl concentration resulted in the reduction of the gas humidity, as NaCl addition led to a decrease of water activity. Chenlo et al. [32] reported the value of water activity for pure water at 25 °C was 1.000 and it became 0.807 for a 5 M NaCl solution. In present work, the percentage of the gas humidity decreased around 3% when 5 M NaCl salt was added into the absorbent solution.

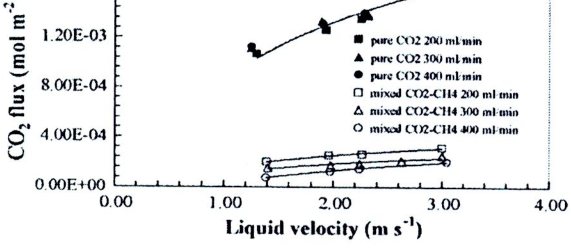

Fig. 7. Effect of gas flow rate on $CO_2$ flux at different liquid velocities (water temperature: 30 °C, feed gas: 20/80 $CO_2$/$CH_4$ and pure $CO_2$).

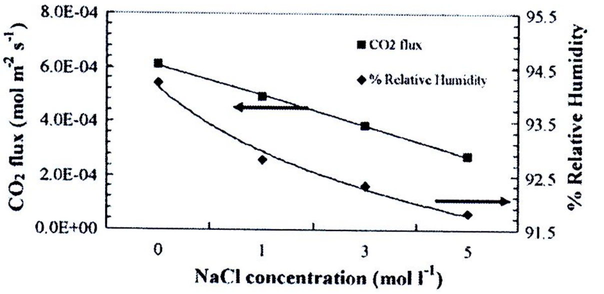

Fig. 8. Effects of NaCl addition on 1 M NaOH absorbent on $CO_2$ flux and outlet gas humidity (absorbent temperature: 40 °C, gas flow rate: 200 ml/min, feed gas: 20/80 $CO_2$/$CH_4$).

However, the presence of the salt in the solution also decreased the $CO_2$ flux as a result of salting out effect. From the calculation based on Eq. (3) (see also [23] and Appendix A), the Henry's constant for water with $CO_2$ decreased from $3.36 \times 10^{-7}$ mol dm$^{-3}$ Pa$^{-1}$ (no NaCl) to $6.36 \times 10^{-8}$ mol dm$^{-3}$ Pa$^{-1}$ (with 5 M NaCl). For water with $CH_4$, the Henry's constant decreased from $1.38 \times 10^{-8}$ mol dm$^{-3}$ Pa$^{-1}$ (no NaCl) to $1.53 \times 10^{-9}$ mol dm$^{-3}$ Pa$^{-1}$ (with 5 M NaCl). Obviously, the $CH_4$ recovery was also improved though $CO_2$ flux was decreased. Additionally, it was expected that as the NaCl salt concentration was increased, the solution viscosity would increase. The increase of absorbent solution viscosity directly influenced the decrease of gas diffusivity in the liquid. Therefore, the liquid phase mass transfer coefficient and molar flux of $CO_2$ and $CH_4$ decreased with increasing salt concentration due to the decrease of diffusivity (see also Eq. (2)). This is another reason to support that the $CH_4$ recovery would increase as the NaCl concentration increased.

It seems there existed a compromise to reduce the gas humidity, increase $CH_4$ recovery and to achieve a high $CO_2$ absorption flux by adding NaCl into the absorbent. Thus, in the case of fairly high operating temperature under which $CH_4$ loss was negligible, the use of NaCl to decrease gas humidity and increase $CH_4$ recovery may not be effective because of the sizeable reduction of $CO_2$ flux. Conversely, if the process was applied at a low temperature, the $CH_4$ loss may become a considerable problem. The addition of NaCl into the absorbent may be one option to be considered.

### 4.4. *Effects of flowing pattern and module packing density on $CO_2$ absorption performance*

Fig. 9 shows the $CO_2$ flux under different flowing patterns, i.e., the gas and liquid flowed co-currently and counter-currently. It was found that a higher $CO_2$ flux was achieved in the counter-

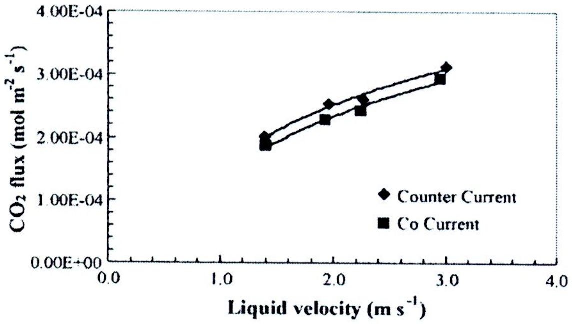

Fig. 9. Comparison of the $CO_2$ flux at different flow patterns of operation (water temperature: 30 °C, gas flow rate: 200 ml/min, feed gas: 20/80 $CO_2/CH_4$).

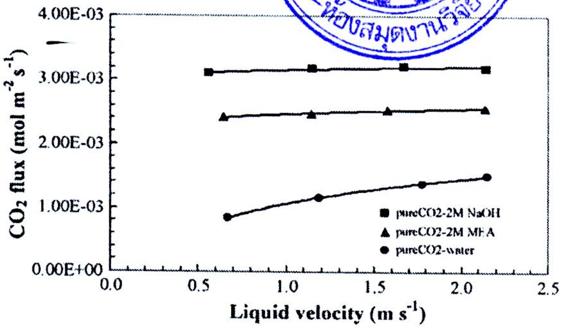

Fig. 11. $CO_2$ flux using 2 M MEA, 2 M NaOH and water as the absorbents (absorbent temperature: 30 °C, gas flow rate: 200 ml/min).

current mode than that in the co-current mode of operation. This was because the counter-current flow provided a higher log mean concentration difference (driving force). Similar results were reported in the literature [17].

The membrane module packing density ($\phi$) is defined as:

$$\phi = n_{\text{fibers}} \times \left(\frac{d_o}{D_i}\right)^2 \tag{9}$$

where $n_{\text{fibers}}$ is number of fibers, $d_o$ and $D_i$ are the outside diameter of fiber and inner diameter of module, respectively.

The effect of the module packing density on the $CO_2$ flux is shown in Fig. 10. The experiments were carried out using pure $CO_2$ as the feed gas and pure water as the absorbent to avoid any error arising from the analysis of the gas and chemical absorbent concentrations. It was found that the $CO_2$ flux increased with an increasing in packing density. This may be due to the fact that the increase in the module packing density led to the fiber turning into more ordered and the effect of preferential flow becoming less. Similar experimental results were also reported in the literature [33]. This result would possibly be useful for the design of large-scale hollow fiber membrane modules for similar applications.

### *4.5. Long-term performance of PVDF membrane contactors using different absorbents*

Fig. 11 shows the $CO_2$ flux using pure water, 2 M NaOH or 2 M MEA aqueous solutions as the liquid absorbents. Pure $CO_2$ was used as the feed gas. It is well understood that the physical absorption (water as the absorbent) suffers the lower separation efficiency than chemical absorption (reactive absorbents of NaOH and MEA). In the case of chemical absorptions, a higher $CO_2$ flux was achieved using NaOH than MEA with the same concentration. This result can be explained by the fact that the reaction rate constant of $CO_2$ and $OH^-$ was higher than that of $CO_2$ and MEA, as reported by many researchers. For example, Kucka et al. [28] reported that the reaction rate constant between $CO_2$ and hydroxide ions ($OH^-$) at 30 °C was 11,000 $m^3\,kmol^{-1}\,s^{-1}$, while the reaction rate constant of $CO_2$ and MEA at 30 °C was approximately 7740 $m^3\,kmol^{-1}\,s^{-1}$ as reported by Seda et al. [34]. Moreover, based on Gong et al.'s calculation [35], the reaction rate constant for the pair of $CO_2$ and $OH^-$ was 12,037.73 $m^3\,kmol^{-1}\,s^{-1}$ and was 8983 $m^3\,kmol^{-1}\,s^{-1}$ for $CO_2$ and MEA at 30 °C.

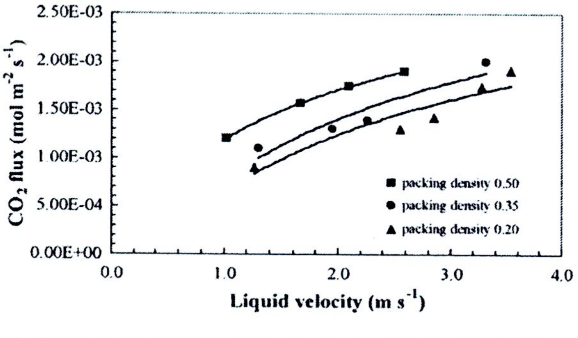

Fig. 10. Effect of membrane packing density on $CO_2$ flux (pure $CO_2$–water system, water temperature: 30 °C, gas flow rate: 200 ml/min).

The comparison of $CO_2$ flux in the long-term test by using pure water, NaOH and MEA as the absorbents were also carried out. The experimental results are shown in Fig. 12. The $CO_2$ flux seemed to maintain constant through 15 days of testing when pure water was used as the absorbent. Similar result was reported by the pervious work [36]. The $CO_2$ flux of 2 M NaOH used as absorbent reduced approximately 15% in the initial 3 days of operation and then the flux almost did not change. It can also be found that, when using 2 M MEA as the absorbent, the $CO_2$ flux continuously decreased about 43% of the initial flux

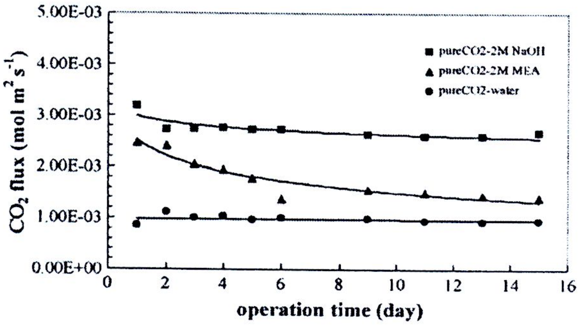

Fig. 12. Long-term performance of the membrane contactor using water, 2 M MEA and 2 M NaOH solutions as the absorbents (absorbent temperature: 30 °C, absorbent velocity: 1.15 m/s, gas flow rate: 200 ml/min).

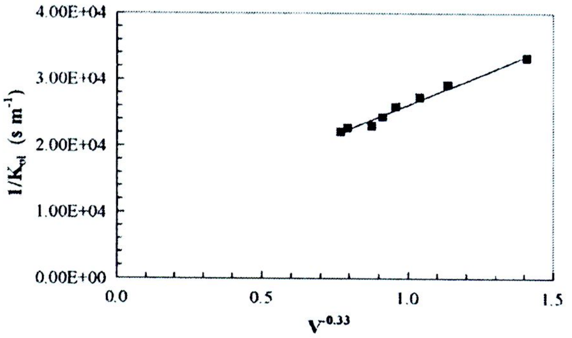

Fig. 13. Wilson plot of PVDF hollow fiber membrane (pure $CO_2$–water system, water temperature: 30 °C, gas flow rate: 200 ml/min).

during 15 days of operation. The decrease in the $CO_2$ flux came from the increase of the total mass transfer resistance. Since the system was operated at the same conditions, obviously, the membrane contributed to the increased portion according to the resistance-in-series model. This result revealed that the PVDF microporous membrane was wetted by the 2 M MEA aqueous solution. A little wetting of the membrane occurred in the initial short time of operation using the 2 M NaOH solution as the absorbent.

Moreover, according to Eq. (4), the contact angle ($\theta$) and surface tension ($\sigma$) can also be used to assess the possibility of membrane wetting. The contact angles between PVDF membrane and water, 2 M NaOH, 2 M MEA were 100°, 90°, 82°, respectively (measured by FACE, Contact angle meter, model CA-A, Kyowa Interface Science Co., Ltd.). The surface tension at 28.5 °C of water, 2 M NaOH, 2 M MEA were 71.3, 62.1, 67.3 mN m$^{-1}$, respectively (measured by ring C mode, Digital tensiometer K9, KRUSS). Referring to the above data and Eq. (4), the penetration pressure of PVDF membrane with water, NaOH solution, and MEA solution were 0.124, 0, and −0.094 MPa, respectively. It can be seen that the possibility of MEA wetting the PVDF membrane was higher than using NaOH and water as the absorbents. It was thus not surprising to see that the PVDF membrane was wetted by 2 M MEA aqueous solutions in present study.

It suggested that NaOH was more suitable as an absorbent to the PVDF microprous hollow fiber contactor as it yielded a high and constant flux throughout the long period of operation.

### 4.6. *Membrane mass-transfer resistance*

The important downside of operating the gas–liquid membrane contactor when compared with the conventional processes is the addition of an extra mass-transfer resistance caused by the membrane. Therefore, the quantitative analysis of the membrane resistance was performed in order to gain a better understanding of the effect of membrane mass-transfer resistance on the system performance. In this work, Wilson plot method was used to determine the value of membrane mass-transfer resistance and the details of the method were explained in the previous work [36]. Fig. 13 depicts the Wilson plot of $1/K_{ol}$ versus $V^{-0.33}$ for the water–pure $CO_2$ system. The power of liquid velocity, 0.33, was achieved from the Lévêque's correlation as water was fed into the tube side of the fibers for providing a best straight line of the Wilson plot:

$$\frac{1}{K_{ol}} = 18087V^{-0.33} + 8082, \quad R^2 = 0.9798 \tag{10}$$

Based on the above equation, the membrane mass-transfer coefficient can be obtained via the interception of the equation. The membrane resistance of the PVDF membrane was around 22% of the total resistances at the 0.25 m/s liquid velocity. This result of the membrane resistance was in line comparing with the previous work [36].

## 5. Conclusions

The potential of the gas–liquid membrane contacting process for $CO_2/CH_4$ separation was evaluated via a series of experimental study in combination with mass transfer analysis. It was found that the $CH_4$ recovery from the $CO_2/CH_4$ mixture was approximately 100% in the membrane contactor though the retentate selectivity obtained in this work was not satisfactory because of the small membrane module used. The $CO_2$ flux was almost maintained the same with increasing NaOH velocity and was significantly enhanced when water velocity was increased. The $CO_2$ flux was six times higher using a 1 M NaOH aqueous solution than using pure water as the absorbent. The increase in NaOH temperature resulted in an increase of the $CO_2$ flux because the mass transfer coefficient in the liquid phase was enhanced. Conversely, when water was used as absorbent, the $CO_2$ flux decreased with increasing the temperature due to the decrease of $CO_2$ solubility. The addition of NaCl into the 1 M NaOH solution reduced the outlet gas humidity and increased $CH_4$ recovery, but the $CO_2$ flux was reduced. The increase in $CO_2$ concentration in the feed gas stream enhanced the $CO_2$ flux as the driving force of the system was increased. The $CO_2$ removal efficiency also increased with increasing $CO_2$ concentration in the feed stream.

In this work, the feed gas stream was fed into the shell side of membrane module. Counter-current flow mode of operation can take the advantage of higher mass transfer over co-current flow mode and the $CO_2$ flux increased with increasing membrane module packing density. Long-term performance tests using pure water, 2 M NaOH and 2 M MEA solutions as the absorbents show that the NaOH solution was more suitable than other absorbents to be applied to the PVDF microporous hollow fiber contactors because the NaOH aqueous solution can provide a higher separation performance and the $CO_2$ flux was kept almost unchanged over 15 days of operation.

## Acknowledgements

The authors wish to thank the Thailand Research Fund (TRF) for the financial support through the Royal Golden Jubilee Ph.D. Program and the TRF senior research scholar grant.

## Appendix A. Calculation example of gas solubility in the salt solution [23]

In order to calculate the $CO_2$ solubility at 25 °C for the solution including 1 M NaOH and 5 M NaCl, the following equations were applied:

$$h_G = h_{G,0} + h_T(T - 298.15\,K) \tag{A.1}$$

where $h_G$, $h_{G,0}$ and $h_T$ are gas specific parameter, gas specific parameter at 298.15 K, and gas specific parameter for the temperature effect, respectively. $T$ is the temperature.

For $CO_2$, $h_{G,0}$ is $-0.0172\,m^3\,kmol^{-1}$ and $h_T$ is $-0.338 \times 10^{-3}\,m^3\,kmol^{-1}\,K^{-1}$, therefore,

$$h_G = -0.0172 - 0.338 \times 10^{-3}(298.15 - 298.15) = -0.0172$$

The gas solubility in salt solution can be calculated as follows

$$\log\left(\frac{c_{G,0}}{c_G}\right) = \sum(h_i + h_G)c_i \tag{A.2}$$

where $c_{G,0}$ and $c_G$ denote the gas solubility in pure water and in a salt solution, respectively, and $c_i$ is the molar concentration of the salt. $h_i$ is ion-specific parameter.

For NaOH and NaCl aqueous solution, $h_i$ are 0.1143, 0.0839, and 0.0318 for $Na^+$, $OH^-$, and $Cl^-$, respectively.

$$\begin{aligned}\log\left(\frac{c_{G,0}}{c_G}\right) &= 6(0.1143 - 0.0172) \quad (Na^+)\\ &+ 1(0.0839 - 0.0172) \quad (OH^-)\\ &+ 5(0.0318 - 0.0172) \quad (Cl^-)\\ &= 0.7723\end{aligned}$$

As the $CO_2$ solubility in pure water is $3.36 \times 10^{-7}\,mol\,dm^{-3}\,Pa^{-1}$, the $CO_2$ solubility with the presence of salt is $6.36 \times 10^{-8}\,mol\,dm^{-3}\,Pa^{-1}$.

## Nomenclature

| | |
|---|---|
| $A_T$ | mass-transfer area based on inside surface area of gas–liquid contact ($m^2$) |
| $c_G$ | gas solubility in salt solution ($mol\,mol^{-1}$) |
| $c_{G,0}$ | gas solubility in pure water ($mol\,mol^{-1}$) |
| $c_i$ | concentration of ion ($kmol\,m^{-3}$) |
| $c_s$ | concentration of the salt ($mol\,dm^{-3}$) |
| $C_{CO_2,F}$ | concentration of carbon dioxide in feed stream ($mol\,mol^{-1}$) |
| $C_{CO_2,R}$ | concentration of carbon dioxide in retentate stream ($mol\,mol^{-1}$) |
| $C_{CH_4,F}$ | concentration of methane in feed stream ($mol\,mol^{-1}$) |
| $C_{CH_4,R}$ | concentration of methane in retentate stream ($mol\,mol^{-1}$) |
| $d_i$ | inside diameter of membrane (m) |
| $d_{ln}$ | logarithmic mean diameter of membrane (m) |
| $d_o$ | outside diameter of membrane (m) |
| $D$ | diffusion coefficient of carbon dioxide in the liquid phase ($m^2\,s^{-1}$) |
| $D_i$ | inner diameter of module (m) |
| $h_i$ | ion-specific parameter ($m^3\,kmol^{-1}$) |
| $h_G$ | gas specific parameter ($m^3\,kmol^{-1}$) |
| $h_{G,0}$ | gas specific parameter at 298.15 K ($m^3\,kmol^{-1}$) |
| $h_T$ | gas specific parameter for the temperature effect ($m^3\,kmol^{-1}\,K^{-1}$) |
| $H$ | Henry's constant |
| $J_{CO_2}$ | $CO_2$ flux ($mol\,m^{-2}\,s^{-1}$) |
| $k_l$ | individual mass transfer coefficient of liquid phase ($m\,s^{-1}$) |
| $k_m$ | individual mass transfer coefficient of membrane ($m\,s^{-1}$) |
| $k_g$ | individual mass transfer coefficient of gas phase ($m\,s^{-1}$) |
| $K$ | Sechenov constant |
| $K_{ol}$ | overall mass transfer coefficient ($m\,s^{-1}$) |
| $L$ | effective length of the membrane module (m) |
| $n_{fibers}$ | number of fibers |
| $\Delta P$ | penetration pressure (Pa) |
| $Q_{CH_4,F}$ | methane flow rate in feed stream ($m^3\,s^{-1}$) |
| $Q_{CH_4,R}$ | methane flow rate in retentate stream ($m^3\,s^{-1}$) |
| $Q_F$ | total gas flow rate in feed stream ($m^3\,s^{-1}$) |
| $Q_R$ | total gas flow rate in retentate stream ($m^3\,s^{-1}$) |
| $r_p$ | membrane pore radius (m) |
| $S$ | percentage recovery |
| $Sh$ | Sherwood number |
| $T_g$ | gas temperature (K) |
| $V$ | velocity ($m\,s^{-1}$) |

*Greek letters*

| | |
|---|---|
| $\alpha_{R,CH_4/CO_2}$ | retentate selectivity |
| $\phi$ | membrane module packing density |
| $\eta$ | removal efficiency |
| $\theta$ | contact angle (°) |
| $\sigma$ | surface tension ($mN\,m^{-1}$) |

## References

[1] T.S. Chung, J. Ren, R. Wang, D. Li, Y. Liu, K.P. Pramoda, W.W. Loh, Development of asymmetric 6FDA-2,6DAT hollow fiber membranes for $CO_2/CH_4$ separation Part 2. Suppression of plasticization, J. Membr. Sci. 214 (2003) 57–69.

[2] C. Cao, T.S. Chung, Y. Lui, R. Wang, K.P. Pramoda, Chemical cross-linking modification of 6FDA-2,6-DAT hollow fiber membranes for natural gas separation, J. Membr. Sci. 216 (2003) 257–268.

[3] A. Gabelman, S.T. Hwang, Hollow fiber membrane contactors, J. Membr. Sci. 159 (1999) 61–106.

[4] B.D. Bhide, A. Voskericyan, S.A. Stern, Hybrid processes for the removal of acid gases from natural gas, J. Membr. Sci. 140 (1998) 27–49.

[5] S. Karoor, K.K. Sirkar, Gas absorption studies in microporous hollow fiber membrane modules, Ind. Eng. Chem. Res. 32 (1993) 674–684.

[6] J.L. Li, B.H. Chen, Review of $CO_2$ absorption using chemical solvent in hollow fiber membrane contactors, Sep. Purif. Technol. 41 (2005) 109–122.

[7] Z. Qi, E.L. Cussler, Microporous hollow fibers for gas absorption. I: mass transfer in the liquid, J. Membr. Sci. 23 (1985) 321–332.

[8] Z. Qi, E.L. Cussler, Microporous hollow fibers for gas absorption. II. Mass transfer across the membrane, J. Membr. Sci. 23 (1985) 333–345.

[9] D.C. Nymeijer, T. Visser, R. Assen, M. Wessling, Composite hollow fiber gas–liquid membrane contactors for olefin/paraffin separation, Sep. Purif. Technol. 37 (2004) 209–220.

[10] K. Nymeijer, T. Visser, R. Assen, M. Wessling, Super selective membranes in gas–liquid membrane contactors for olefin/paraffin separation, J. Membr. Sci. 232 (2004) 107–114.

[11] T.K. Poddar, S. Majumdar, K.K. Sirkar, Membrane-based absorption of VOCs from a gas stream, AIChE J. 42 (11) (1996) 3267–3282.

[12] P.H.M. Feron, A.E. Jansen, $CO_2$ separation with polyolefin membrane contactors and dedicated absorption liquids: performances and prospects, Sep. Purif. Technol. 27 (2002) 231–242.

[13] H.A. Rangwala, Absorption of carbon dioxide into aqueous solutions using hollow fiber membrane contactors, J. Membr. Sci. 112 (1996) 229–240.

[14] R. Wang, D.F. Li, D.T. Liang, Modeling of $CO_2$ capture by three typical amine solutions in hollow fiber membane contactors, Chem. Eng. Process. 43 (2004) 849–856.

[15] R. Wang, H.Y. Zhang, P.H.M. Feron, D.T. Liang, Influence of membrane wetting on $CO_2$ capture in microporous hollow fiber membrane contactors, Sep. Purif. Technol. 46 (2005) 33–40.

[16] M. Mavroudi, S.P. Kaldis, G.P. Sakellaropoulos, A study of mass transfer resistance in membrane gas–liquid contacting processes, J. Membr. Sci. 272 (2006) 103–115.

[17] D. deMontigny, P. Tontiwachwuthikul, A. Chakma, Using polypropylene and polytetrafluoroethylene membranes in a membrane contactor for $CO_2$ absorption, J. Membr. Sci. 277 (2006) 99–107.

[18] H.Y. Zhang, R. Wang, D.T. Liang, J.H. Tay, Modeling and experimental study of $CO_2$ absorption in a hollow fiber membrane contactor, J. Membr. Sci. 279 (2006) 301–310.

[19] V.V. Teplyakov, A.Y. Okunev, N.I. Laguntsov, Computer design of recycle membrane contactor systems for gas separation, Sep. Purif. Technol. (2006), doi:10.1016/j.seppur.2006.06.002, in press.

[20] R. Sander, Compilation of Henry's Law constant for inorganic and organic species of potential importance in environmental chemistry, 1999, available at: http://www.mpch-mainz.mpg.de/~sander/res/henry.html.

[21] K.K. Sirkar, Other new membrane processes, in: W.S.W. Ho, K.K. Sirkar (Eds.), Membrane Handbook, Chapman & Hall, New York, 1992, pp. 885–899.

[22] M.C. Yang, E.L. Cussler, Designing hollow-fiber contactors, AIChE J. 32 (11) (1986) 1910–1916.

[23] S. Weisenberger, A. Schumpe, Estimation of gas solubilities in salt solution at temperatures from 273 K to 363 K, AIChE J. 42 (1) (1996) 298–3~~00.~~

[24] B.E. Poling, J.M. Prausnitz, J.P. O'Connell, Surface Tension, The Properties of Gases and Liquids, McGraw-Hill Book, New York, 2001.

[25] S.A. Stern, Polymers for gas separations: the next decade, J. Membr. Sci. 94 (1994) 1–65.

[26] M. Mulder, Basic Principles of Membrane Technology, Kluwer Academic Publishers, Netherlands, 1996.

[27] S.P. Yan, M.X. Fang, W.F. Zhang, S.Y. Wang, Z.K. Xu, Z.Y. Luo, K.F. Cen, Experimental study on the separation of $CO_2$ from flue gas using hollow fiber membrane contactors without wetting, Fuel Process. Technol. 88 (2007) 501–511.

[28] L. Kucka, E.Y. Kenig, A. Gorak, Kinetics of gas–liquid reaction between carbon dioxide and hydroxide ions, Ind. Eng. Chem. Res. 41 (2002) 5952–5957.

[29] G. Vazquez, E. Alvarez, R. Varela, A. Cancela, J.M. Navaza, Density and viscosity of aqueous solution of sodium dithionite, sodium hydroxide, sodium dithionite + sucrose and sodium dithionite + sodium hydroxide + sucrose from 25 °C to 40 °C, J. Chem. Eng. Data 41 (1996) 244–248.

[30] G.F. Versteeg, W.P.M.v. Swaaij, Solubility and diffusivity of acid gases ($CO_2$, $N_2O$) in aqueous alkanolamine solutions, J. Chem. Eng. Data 33 (1988) 29–34.

[31] E. Favre, Carbon dioxide recovery from post-combustion processes: can gas permeation membranes compete with absorption? J. Membr. Sci. 294 (2007) 50–59.

[32] F. Chelo, R. Moreira, G. Pereira, B. Bello, Kinematic viscosity and water activity of aqueous solutions of glycerol and sodium chloride, Eur. Food Res Technol. 219 (2004) 403–408.

[33] J. Wu, V. Chen, Shell-side mass transfer performance of randomly packed hollow fiber modules, J. Membr. Sci. 172 (2000) 59–74.

[34] E. Sada, H. Kumazawa, Z.Q. Han, H. Matsuyama, Chemical kinetics of the reaction of carbon dioxide with ethanolamines in nonaqueous solvents, AIChE J. 31 (8) (1985) 1297–1303.

[35] Y. Gong, Z. Wang, S. Wang, Experiments and simulation of $CO_2$ removal by mixed amines in a hollow fiber membrane module, Chem. Eng. Process. 45 (2006) 652–660.

[36] S. Atchariyawut, C. Feng, R. Wang, R. Jiraratananon, D.T. Liang, Effect of membrane structure on mass-transfer in the membrane gas–liquid contacting process using microporous PVDF hollow fibers, J. Membr. Sci. 285 (2006) 272–281.

Available online at www.sciencedirect.com

ScienceDirect

Separation and Purification Technology 58 (2007) 68–75

Separation and Purification Technology

www.elsevier.com/locate/seppur

# Factors affecting nanofiltration performances in natural organic matter rejection and flux decline

Chalor Jarusutthirak[a,*], Supatpong Mattaraj[b], Ratana Jiraratananon[c]

[a] *Faculty of Science, King Mongkut's Institute of Technology Ladkrabang, Bangkok 10520, Thailand*
[b] *Department of Chemical Engineering, Faculty of Engineering, Ubon Rachathani University, Thailand*
[c] *Faculty of Engineering, King Mongkut's University of Technology Thonburi, Bangkok 10140, Thailand*

## Abstract

A crossflow bench-scale test cell was used to investigate factors (i.e. NOM concentration, ionic strength, and solution pH) affecting natural organic matter (NOM) rejection and flux decline during nanofiltration (NF). Experimental results revealed that increased NOM concentration increased permeate flux decline, salt rejection, and NOM rejection, enhancing NOM accumulation on membrane surface. At high concentration of NOM, permeate flux curve corresponded to cake formation model. Increased ionic strength from 0.004 M to 0.1 M illustrated higher flux decline, possibly as a result of increasing osmotic pressure from higher concentration of salt. Solutions possessing high ionic strength (0.05 M) showed greater flux decline and NOM rejection than those having low ionic strength (0.01 M). Increased solution pH from 4 to 10 exhibited greater flux decline, caused by increasing salt rejection and enhancing salt concentration on membrane surface.

*Keywords:* Flux decline; Fouling; Nanofiltration; Natural organic matter; Permeate flux

## 1. Introduction

Natural organic matter (NOM) is naturally occurring and widely distributed throughout all aquatic environments containing in surface water [1]. NOM components consist of a heterogeneous mixture of complex organic materials, including humic substances (humic and fulvic acids), low molecular weight (hydrophilic) acids, proteins, carbohydrates, carboxylic acids, amino acids, and hydrocarbons [2]. Aquatic humic substances are colored, polyelectrolytic, organic acids isolated from water on XAD resins, nonvolatile and range in molecular weight from 500 to 5000 [1]. They play an important role as a precursor of disinfection by-products (DBPs) during chlorination process of water treatment [3]. The DBPs, e.g. trihalomethanes (THMs) and haloacetic acids (HAAs), possibly deteriorate human health due to their carcinogenic characters. Thus, a minimization of NOM as DBP-precursor is an alternative method to reduce potential adverse effects of the DBPs. Of particular interest is the use of nanofiltration (NF) membranes to control the formation of disinfection by-products (DBPs) by removing precursors, including dissolved natural organic matter (NOM). It has been reported that NF membrane is found to be effective in removal of NOM from surface water [4–7]. Typically, NF membrane has a molecular weight cutoff between 300 and 1000, while NF membrane operates at low pressure in the range of 344.6–1034 kPa (50–150 psi). Crossflow nanofiltration was investigated to reduce NOM fouling on membrane surface. Typical crossflow velocities in spiral-wound elements with mesh spacers range from 0.05 m s$^{-1}$ to 1.5 m s$^{-1}$ [8], similar to full-scale membrane operation. Membrane fouling can decrease permeate flux due to adsorption/deposition of solute on the membrane, accumulation of solute near the membrane surface, and gradual non-recoverable changes in cake formation. The main mechanisms of NOM fouling by NF membrane are described by size exclusion and electrostatic effects. However, the rejected NOM accumulation on membrane surface and/or in the membrane pores, causes membrane fouling, thus enhancing high operation and maintenance cost associated with membrane cleaning and replacement. Several investigators explained influencing factors causing membrane fouling, e.g. NOM concentration, feed water characteristics, inorganic scalants, and membrane properties [5–7,9].

The objectives of this study are to investigate factors (i.e. different NOM concentrations, ionic strength, and solution pH) affecting crossflow nanofiltration performances in natural

---

[*] Corresponding author. Tel.: +66 2326 4111x6245; fax: +66 2326 4415.
*E-mail addresses:* kjchalor@kmitl.ac.th (C. Jarusutthirak), mattaraj@ubu.ac.th (S. Mattaraj), ratana.jir@kmutt.ac.th (R. Jiraratananon).

1383-5866/$ – see front matter © 2007 Elsevier B.V. All rights reserved.
doi:10.1016/j.seppur.2007.07.010

**Nomenclature**

| | |
|---|---|
| $A_m$ | membrane area ($m^2$) |
| $C_{bulk}$ | bulk concentration ($mg\,L^{-1}$) |
| $J_v$ | permeate flux ($L\,m^{-2}\,h^{-1}$ or LMH) |
| $J_0$ | initial permeate flux ($L\,m^{-2}\,h^{-1}$ or LMH) |
| $J^*$ | permeate flux associated with the back-transport mass transfer ($L\,m^{-2}\,h^{-1}$ or LMH) |
| $k$ | rate constant or fouling coefficient |
| $k_A$ | kinetic rate constant for the pore blockage model ($h^{-1}$) |
| $k_B$ | kinetic rate constant for the pore constriction model ($m^{-0.5}\,h^{-0.5}$) |
| $k_C$ | kinetic rate constant for the intermediate blocking model ($m^{-1}$) |
| $k_D$ | kinetic rate constant for the cake formation model ($h\,m^{-2}$) |
| $n$ | dimensionless filtration constant |
| $n_0$ | initial number of pores |
| $P_f$ | operating pressure in feed (kPa) |
| $P_p$ | operating pressure in permeate (kPa) |
| $P_r$ | operating pressure in retentate (kPa) |
| $R_c$ | the resistance of the polarization and cake ($m^{-1}$) |
| $R_{f,NOM}$ | feed rejection of NOM |
| $R_{f,s}$ | feed rejection of salt |
| $R_m$ | resistance due to membrane |
| $R_{r,NOM}$ | retentate rejection of NOM |
| $R_{r,s}$ | retentate rejection of salt |
| $r_0$ | initial pore radius of membrane (m) |
| $t$ | operating period (min) |

*Greek letters*

| | |
|---|---|
| $\alpha_{block}$ | pore blockage efficiency |
| $\alpha_{cake}$ | specific resistance of cake layer ($m\,mg^{-1}$) |
| $\alpha_{pore}$ | standard pore block efficiency |
| $\delta_c$ | depth of the particle cake (m) |
| $\delta_m$ | membrane thickness (m) |
| $\Delta\pi$ | osmotic pressure ($=\pi_m - \pi_p$) (kPa) |
| $\sigma$ | osmotic reflection coefficient |

organic matter rejection and flux decline. A field reverse osmosis was used to separate organic matter from natural water source and further set up as a feed solution for NF experiments. A crossflow bench-scale test cell was used to determine NF performances during filtration experiments. Mathematical models were used to interpret membrane performances of NF membrane. Finally, an integrated understanding of NOM rejection and membrane fouling during NF membrane leads to efficient operations of NF processes.

## 2. Theoretical basis

Mathematical models have been illustrated to explain permeate flux decline in the dead-end operation during filtration [10–12]. The mathematical models can be shown as follows

$$\frac{dJ_v}{dt} = -kJ_v(J_v)^{2-n} \qquad (1)$$

where $k$ is a rate constant or fouling coefficient and $n$ is the dimensionless filtration constant: (1) cake formation model corresponds to $n = 0$, (2) intermediate blocking model corresponds to $n = 1$, (3) pore constriction or standard blocking model corresponds to $n = 1.5$, and (4) complete pore blocking corresponds to $n = 2.0$.

For a crossflow membrane system, the additional term ($J^*$) is included in the mathematical fouling models expressed by Field et al. [12]. The mathematical models can be illustrated in the following equations [6]:

- Type I. Pore blocking model (or complete pore blocking model):

  The rate of change in the number of open pores is assumed to be proportional to the rate of particle convection to the membrane surface:

$$\frac{dJ_v}{dt} = -\frac{\alpha_{block} A_m C_{bulk} J_0}{n_0}(J_v - J^*) = -k_A(J_v - J^*) \qquad (2)$$

  where $\alpha_{block}$ is the pore blockage efficiency, $A_m$ the membrane area ($m^2$), $C_{bulk}$ the bulk concentration ($mg\,L^{-1}$), $J_v$ the permeate flux ($L\,m^{-2}\,h^{-1}$), $J_0$ the initial permeate flux ($L\,m^{-2}\,h^{-1}$), $J^*$ the permeate flux associated with the back-transport mass transfer ($L\,m^{-2}\,h^{-1}$), $t$ the operating period (min), $n_0$ the initial number of pores, and $k_A$ is the kinetic rate constant for the pore blockage model ($min^{-1}$).
- Type II. Pore constriction model (or standard blocking model):

  The rate of change in the pore volume is assumed to relate to the rate of particle convection to the membrane surface:

$$\frac{dJ_v}{dt} = -\frac{(2\alpha_{pore} A_m C_{bulk} J_0)^{0.5}}{\pi r_0^2 \delta_m} J_v^{0.5}(J_v - J^*) = -k_B J_v^{0.5}(J_v - J^*) \qquad (3)$$

  where $\alpha_{pore}$ is the standard pore block efficiency, $\delta_m$ the membrane thickness (m), $r_0$ the initial pore radius of membrane (m), and $k_B$ is the kinetic rate constant for the pore constriction model ($LMH^{-0.5}\,min^{-1}$ or $m^{-0.5}\,min^{-0.5}$).
- Type III. Intermediate blocking model:

  The rate of change in the cake thickness (limit on the membrane surface) is assumed to relate with the rate of particle convection to the membrane surface:

$$\frac{dJ_v}{dt} = -\frac{\alpha_{cake} R_c}{(R_m + R_c)\delta_c} A_m C_{bulk} J_v (J_v - J^*) = -k_C J_v (J_v - J^*) \qquad (4)$$

  where $\delta_c$ is the depth of the particle cake (m), $\alpha_{cake}$ the specific resistance of cake layer ($m\,mg^{-1}$), $R_m$ is the resistance due to membrane, $R_c$ the resistance of the polarization and cake ($m^{-1}$), and $k_C$ is the kinetic rate constant for the intermediate blocking model ($LMH^{-1}\,min^{-1}$ or $m^{-1}$).

- Type IV. Cake formation model:

  The hydraulic resistance caused by the particle cake is assumed to be proportional to the cake mass, $m_{\text{cake}}$:

$$\frac{\mathrm{d}J_{\text{v}}}{\mathrm{d}t} = -\frac{\alpha_{\text{cake}}C_{\text{bulk}}}{R_{\text{m}}J_0}J_{\text{v}}^2(J_{\text{v}} - J^*) = -k_{\text{D}}J_{\text{v}}^2(J_{\text{v}} - J^*) \qquad (5)$$

where $\alpha_{\text{cake}}$ is the specific resistance of cake layer (m mg$^{-1}$) and $k_{\text{D}}$ is the kinetic rate constant for the cake formation model (LMH$^{-2}$ min$^{-1}$ or min m$^{-2}$).

## 3. Experimental

### 3.1. Natural water

Natural water was taken from water reservoir at Ubon Ratchathani's University (UBU), Thailand, which served as water supply in UBU community. Natural water consists of total organic carbon (TOC) and UV$_{254\,\text{nm}}$ at about 4.54 mg L$^{-1}$ and 0.185 cm$^{-1}$, respectively. Specific ultraviolet absorbance (SUVA), determined by the ratio between UV$_{254\,\text{nm}}$ and TOC, was approximately 4.07 L mg$^{-1}$ m$^{-1}$. The natural water used was softwater as its low conductivity and hardness (31.9 µS cm$^{-1}$ (at 25 °C) and 15.4 mg L$^{-1}$ as CaCO$_3$, respectively).

### 3.2. Natural organic matter

Natural organic matter (NOM) was isolated using a field reverse osmosis (RO) system. The procedure was recently studied by Kilduff et al. [13]. This RO was a polyamide thin-film composite (TFC) RO membrane (model AG4040F-spiral-wound crossflow, GE Osmonics Inc., USA), which provides high performance for concentrating NOM. Field RO system consists of pretreatment (i.e. sand filtration, 5-µm polypropylene (PP) and 1-µm PP cartridge prefilter in series with a sodium-form cation exchange softener) to remove multivalent cations (Ca$^{2+}$ and Mg$^{2+}$), and followed by 1-µm and 0.45 µm PP cartridge filters. The pretreated water was subsequently transferred to a 150-L stainless steel drum as a sample reservoir. The pretreated water was then pumped by a transfer pump (model PL-95 M, Bomba-Elias, Bacelona, Spain) through the RO system while a high-pressure stainless steel multi-stage vertical centrifugal pump (Model CRN3-25, GRUNDFOS), was used to isolate NOM from the pretreated water. A back pressure valve was used to adjust the operating pressures ranging from 554.9 kPa to 1413 kPa (80.5–205 psi). The pretreated water was used about 1000 L while the concentrated water was collected with a concentration of factor about 28–30. The final concentrated NOM solution in the sample reservoir was collected after system cleaning and kept in a refrigerator (4 °C) to minimize microbial activity.

### 3.3. Nanofiltration membrane

Thin-film polysulfone nanofiltration membrane, obtained from GE Osmonics, Inc., was used to investigate NF performance on membrane surface. This membrane model is the HL 2540F1072 (series 7933937). According to the manufacturer's information, the membrane has a molecular weight cutoff (MWCO) of 150–300 Da, determined with glucose and sucrose compounds. The operating pH was in the range of 3.0–9.0 while the cleaning pH was in the range of 1.0–10.0. Low chlorine resistance was about 0.1 ppm. The maximum operating temperature was about 50 °C. The nanofiltration sheets were stored in 1% Na$_2$S$_2$O$_5$ and kept in 4 °C to minimize bacterial activity.

### 3.4. Crossflow nanofiltration experiment using crossflow bench-scale test cell

Fig. 1 shows the schematic diagram of bench-scale crossflow nanofiltration experimental set-up with recycle loop. The system consists of a stainless steel test cell (SEPA, Osmonics) that houses a single membrane sheet of 0.014 m$^2$ with a maximum operating pressure of 1000 psi. A high-pressure stainless steel piston feed pump (30 mL min$^{-1}$ @ 3000 psi, Eldex, Model CC-100-S-4, Napa, CA, USA) was used for membrane operating pressures while a high capacity booster recycle pump (Gear pump, Model 75211-35, Cole-Parmer Instrument, Co., Vernon Hills, IL, USA) was used to adjust a high crossflow velocity in the recycle loop. Hydraulic hand pump was used to hold the system pressure at the top of bench-scale test

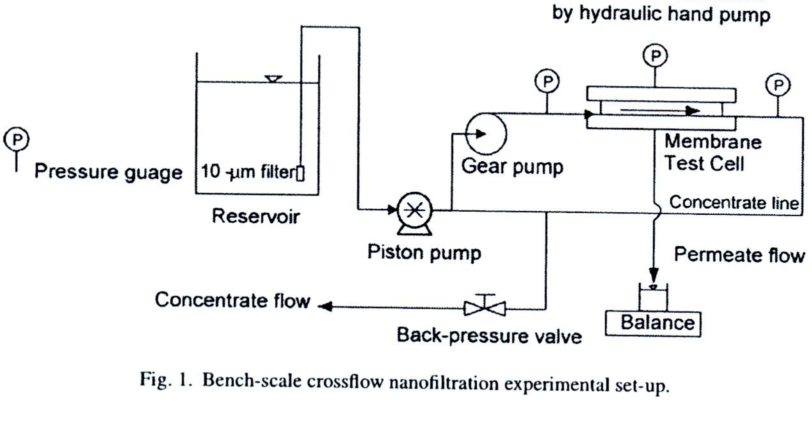

Fig. 1. Bench-scale crossflow nanofiltration experimental set-up.

cell. Mesh feed spacer was used to create hydrodynamic flow conditions similar to that employed in full-scale spiral-wound elements. Inlet temperature was approximately 25 °C and kept constant throughout filtration experiments. Recovery was operated at 85% during filtration experiments, and crossflow velocity of 0.1 m $s^{-1}$ (similar to that of full-scale membrane) corresponding to a flowrate of 530 mL $min^{-1}$ in the recycle loop [8].

### 3.5. Filtration experiments

Filtration procedure was basically followed with Jarusutthirak et al. [6]. Membrane NF sheets were rinsed with cleaned DI water and then transferred to the bench-scale test cell. The membrane sheets were then cleaned with citric acid solution of pH 3–4, and followed with sodium hydroxide solution of pH 10 for 30 min each. Cleaned water flux was determined with a function of transmembrane pressure. Cleaned DI water was subsequently tested for 30-min membrane compaction with an initial water flux of 45 LMH (L $m^{-2}$ $h^{-1}$). Cleaned water flux was subsequently determined with increased operating pressure before NOM solution was used with the system. Feed NOM solutions were prepared for each tested condition. Prior to NOM filtration, a 200–300 mL NOM solution was initially used to flush the bench-scale system. NOM solution was then filtered through the NF membrane. The piston feed pump was subsequently adjusted in order to achieve an initial permeate flux of 45 LMH with 85% recovery. The transmembrane pressure was recorded and kept constant during filtration experiment. Permeate and retentate flow was periodically measured using analytical balance (Model BL-2200H, Shimadzu, Japan) in order to calculate permeate flux and recovery throughout filtration experiments. Permeate and retentate samples were conducted to determine NOM and conductivity rejection. After filtration was terminated, two steps of cleaning, i.e. hydrodynamic cleaning followed by chemical cleaning, were performed; First, for hydrodynamic cleaning, DI water was recirculated in the recycle loop for 30 min with a crossflow velocity of 0.25 m $s^{-1}$, which was higher than that during operation. For chemical cleaning, alkaline solution (using NaOH) with pH of 10, was first used to recirculate in the system, and followed with acidic solution (using HCl) with pH of 3 at a crossflow velocity of 0.25 m $s^{-1}$ for 30 min each. After each cleaning, water fluxes at different operating pressures were measured to determine water flux recovery.

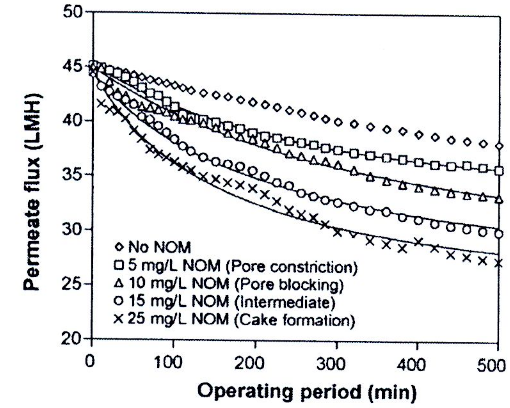

Fig. 2. Influence of NOM concentrations on permeate flux.

## 4. Results and discussion

### 4.1. Influence of NOM concentration on NOM rejection and flux decline

Fig. 2 shows the influence of NOM concentration on permeate flux. NOM concentrations were varied from 0 mg $L^{-1}$ to 25 mg $L^{-1}$ with constant solution pH of 7 and ionic strength of 0.01 M NaCl (1170 μS $cm^{-1}$ at 25 °C). Dot points were the experimental data while solid lines were fitted well with fouling mathematical models. Table 1 shows the model parameters obtained from mathematical models on different NOM concentrations.

It was observed that as NOM concentrations increased from 0 mg $L^{-1}$ to 25 mg $L^{-1}$, permeate flux decline became more significant. Normalized permeate flux ($t = 8$ h) decreased from 0.85 to 0.61 as NOM concentration increased from 0 mg $L^{-1}$ to 25 mg $L^{-1}$. In the absence of NOM, permeate flux decreased during filtration experiment as a result of increased osmotic pressure from salt concentration (i.e. ionic strength of 0.01 M NaCl). This can be explained by the following equation:

$$J_v = L_p(\Delta P - \sigma \Delta \pi) = \frac{Q_p}{A_m} \tag{6}$$

where $\Delta P$ is the average transmembrane pressure $((P_f + P_r)/2 - P_p)$ (kPa), $L_p$ the membrane permeability (L $m^{-2}$ $h^{-1}$ $kPa^{-1}$ or LMH $kPa^{-1}$), $\sigma$ the osmotic reflection coefficient $(=(1 - C_p)/C_m)$, $\Delta\pi$ the osmotic pressure $(=\pi_m - \pi_p)$ (kPa), and $A_m$ is the effective membrane area ($m^2$).

Table 1
Model parameters from mathematical models on different NOM concentrations

| Concentration (mg $L^{-1}$) | Model parameter | | | | | | | | | | | |
|---|---|---|---|---|---|---|---|---|---|---|---|---|
| | Pore blocking | | | Pore constriction | | | Intermediate | | | Cake formation | | |
| | $k_A$ ($h^{-1}$) | $J^*$ (LMH) | SSE | $k_B$ ($m^{-0.5}$ $h^{-0.5}$) | $J^*$ (LMH) | SSE | $k_C$ ($m^{-1}$) | $J^*$ (LMH) | SSE | $k_D$ (h $m^{-2}$) | $J^*$ (LMH) | SSE |
| 5 | 0.294 | 35.4 | 2.803 | 1.205 | 34.3 | 2.359 | 6 | 34.3 | 2.615 | 114 | 32.7 | 2.785 |
| 10 | 0.246 | 32.3 | 5.31 | 0.968 | 30.2 | 5.756 | 4.5 | 29.5 | 5.41 | 108 | 29 | 5.474 |
| 15 | 0.309 | 29.7 | 1.816 | 1.275 | 27.8 | 1.761 | 5.88 | 26.8 | 1.635 | 167.4 | 27.4 | 5.356 |
| 25 | 0.397 | 28.1 | 17.707 | 1.729 | 26.6 | 18.426 | 8.7 | 26.3 | 16.355 | 221.4 | 25.6 | 15.186 |

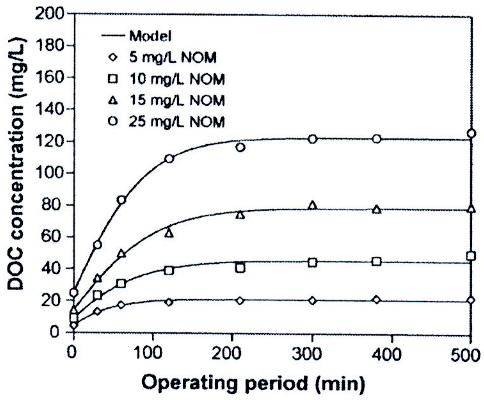

Fig. 3. NOM concentration in retentate during NF operation at different initial concentrations of NOM.

From Eq. (6), at a constant operating pressure, the increase of osmotic pressure by NaCl could decrease permeate flux. In addition, it was reported that the flux decline of solutions having NaCl alone was caused by an increased osmotic effect, while increasing flux decline of feed solution containing both salt and NOM resulted from a combination of resistance from an NOM deposition and an increasing osmotic effect [5]. The increase of NOM concentration caused higher flux decline. At NOM concentration of 25 mg $L^{-1}$, permeate flux showed the greatest flux reduction. According to membrane fouling model, increased NOM concentrations from 5 mg $L^{-1}$ to 25 mg $L^{-1}$ changed fouling mechanisms from pore blocking/pore constriction model (at low NOM concentration) to cake formation model (at high NOM concentration). Model parameters, permeate flux associated with the back-transport mass transfer ($J^*$) and kinetic rate constants, were obtained from minimizing sum squared error (SSE) between experimental data and mathematical models. The overall model parameters were tabulated in Table 1. Solutions having high NOM concentration decreased permeate flux during filtration. This was caused by increased NOM accumulation, suggesting increased cake formation on the membrane surface.

Fig. 3 exhibits the increasing NOM concentration introduced to membrane during the filtration processes while the process performances of NF membrane, in terms of NOM rejection, at different NOM concentrations were tabulated in Table 2. The equation was used to calculate steady-state retentate concentration for NOM ($C_{ss,NOM}$) and salt ($C_{ss,s}$) based on overall mass balance reported by Kilduff et al. [5]. At 25-mg $L^{-1}$ NOM, the feed rejection ($R_{f,NOM}$) and retentate rejection of NOM ($R_{r,NOM}$) exhibited the highest value about 88.4% and 97.6%, respectively. It was evident that increased NOM concentration increased feed rejection of NOM from 75.3% to 88.4% while NOM rejections based on retentate were relatively high from 94.9% to 97.6%. At 25-mg $L^{-1}$ NOM concentration, the average feed rejection shows the highest NOM rejection, indicating an increased NOM accumulation on the membrane surface. In addition, permeate flux curve corresponded with cake formation model, suggesting increased NOM mass deposited on the membrane surface. The steady-state NOM concentration of 25-mg $L^{-1}$ NOM concentration was approximately 122.1 mg $L^{-1}$. With increased NOM concentration from 0 mg $L^{-1}$ to 25 mg $L^{-1}$, the rejections of salt in the feed and retentate line increased in the range of 3.51–5.7% and 21.4–28.2%, respectively. This indicated a relatively low rejection of salt concentration when compared with an aromatic polyamide thin-film composite membrane (NF-70, Dow-FilmTec, Minneapolis, MN) at the same condition studied by Kilduff et al. [5]. They reported that the feed salt rejection ranged from 46.3% to 72.7% with an increased NOM concentration from 0 mg $L^{-1}$ to 25 mg $L^{-1}$. They also indicated an increased with osmotic effect due to the presence of NOM, thus increased salt rejection by the result of electrostatic repulsion between $Cl^-$ ions and charged functional groups on the NOM molecules. However, in the absence of NOM, the salt rejection can be caused by electrostatic repulsion between $Cl^-$ ions and negatively charged NF membrane. This may affect NF membrane pores while the results were confirmed by pore blocking model. These experimental results fitted relatively well with the pore blocking model in the absence of NOM concentration.

Table 2
Process performance of NF membrane caused by NOM concentration

| Parameters | NOM concentration (mg $L^{-1}$) | | | | |
|---|---|---|---|---|---|
| | 0 | 5 | 10 | 15 | 25 |
| $C_{p,NOM}$ (mg $L^{-1}$) | – | 1.08 | 1.93 | 3.2 | 2.9 |
| $C_{ss,NOM}$ (mg $L^{-1}$) | – | 21.2 | 45.5 | 79.06 | 122.1 |
| $C_{p,s}$ (mol $L^{-1}$) | 0.011 | 0.0105 | 0.0104 | 0.0103 | 0.0102 |
| $C_{ss,s}$ (mol $L^{-1}$) | 0.014 | 0.01426 | 0.01392 | 0.0138 | 0.0142 |
| $R_{f,NOM}$ (%) | – | 75.3 | 78.5 | 77.7 | 88.4 |
| $R_{r,NOM}$ (%) | – | 94.9 | 95.8 | 95.9 | 97.6 |
| $R_{f,s}$ (%) (salt) | 3.51 | 4.3 | 5.4 | 4.6 | 5.7 |
| $R_{r,s}$ (%) (salt) | 21.4 | 26.3 | 25.3 | 25.4 | 28.2 |

### 4.2. *Influence of ionic strength on permeate flux*

Fig. 4 presents the influence of ionic strength on permeate flux. Solutions contained no NOM and pH of 7, while ionic strength concentrations were varied from 0.004 M to 0.1 M NaCl. Experimental results showed that increased ionic strength from 0.004 M to 0.1 M NaCl decreased permeate flux curve, These indicated an increased salt concentration on membrane

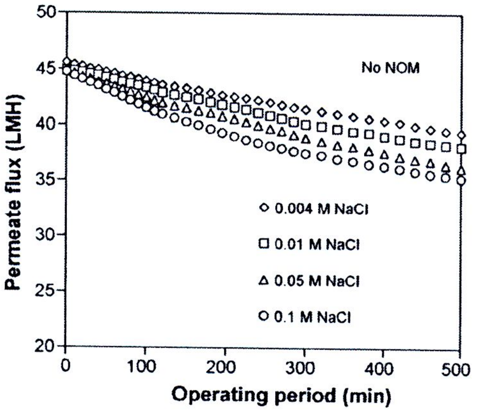

Fig. 4. Influence of ionic strength in the absence of NOM on permeate flux.

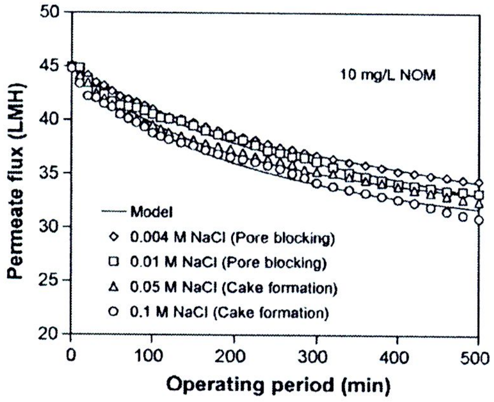

Fig. 5. Influence of ionic strength in the presence of NOM on permeate flux.

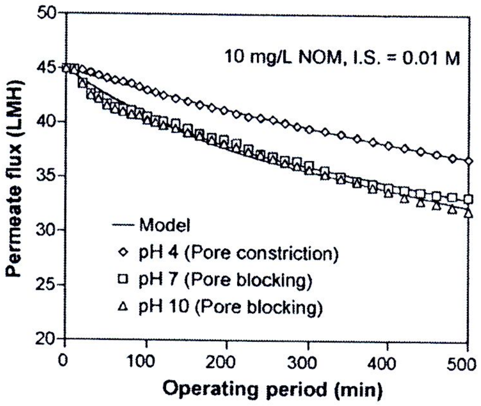

Fig. 6. Influence of pH on permeate flux for ionic strength of 0.01 M NaCl.

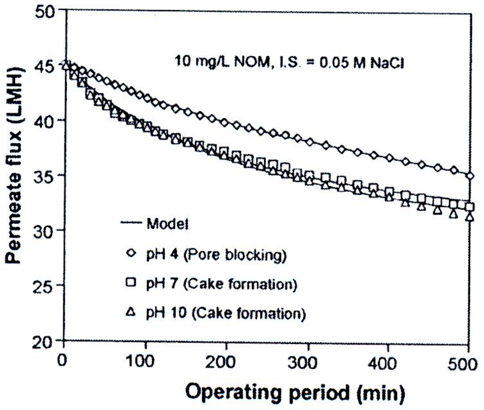

Fig. 7. Influence of pH on permeate flux for ionic strength of 0.05 M NaCl.

surface, which can decrease permeate volume passing through the NF membrane surface. Increased ionic strength can reduce charge repulsion caused by charge interaction between positively charged $Na^+$ and negatively charged NF membrane, thus enhancing a reduction of permeates flux and salt rejection. These phenomena can also be explained by the effect of increasing osmotic pressure in the system with higher concentration of NaCl salt. Braghetta et al. [14] found that membrane fouling increased by decreasing pH and increasing ionic strength.

In the presence of 10-mg $L^{-1}$ NOM, permeate flux curves were investigated by varying ionic strengths from 0.004 M to 0.1 M NaCl. Fig. 5 shows the effect of ionic strength in the presence of NOM on permeate flux. Table 3 presents the model parameters on ionic strength in the presence of NOM. It was observed that increased ionic strength slightly increased permeate flux decline. At low ionic strength (0.004 M and 0.01 M NaCl), the permeate flux curves were fitted with pore blocking model based on minimized sum squared error. This suggests that charge interaction between positively charged $Na^+$ and negatively charged NF membrane dominates permeate flux decline. However, the permeate flux curves with high ionic strength (0.05 M and 0.1 M NaCl) were fitted relatively well with cake formation model. This indicates the charge interaction between positively charged $Na^+$ and negatively charged NOM functional groups, causing NOM accumulation on the membrane surface. Braghetta et al. [15] indicated that NOM accumulation increased with high ionic strength, suggesting a reduction of charge repulsion and increased potential build-up on the membrane surface.

From Table 3, the kinetic rate constants for pore blocking ($k_A$) of 0.004 M and 0.01 M NaCl were approximately 0.263 $h^{-1}$ and 0.246 $h^{-1}$, while the minimum SSEs were about 0.516 and 5.31, respectively. The kinetic rate constants for cake formation model ($k_D$) of 0.05 M and 0.1 M NaCl were about 156 h $m^{-2}$ and 150 h $m^{-2}$, while the minimum SSEs were 3.693 and 7.06, respectively.

### 4.3. Influence of pH on permeate flux

Solution pH can influence permeate flux and rejection. Figs. 6 and 7 show the influence of pH on permeate flux for ionic strength of 0.01 M and 0.05 M NaCl, respectively. Dot points were the experimental data while solid lines were followed with mathematical models. Table 4 presents model parameters affected by solution pH. At low ionic strength of

Table 3
Model parameters on ionic strength in the presence of NOM

| Concentration | Model parameter | | | | | | | | | | | |
|---|---|---|---|---|---|---|---|---|---|---|---|---|
| | Pore blocking | | | Pore constriction | | | Intermediate | | | Cake formation | | |
| | $k_A$ ($h^{-1}$) | $J^*$ (LMH) | SSE | $k_B$ ($m^{-0.5}$ $h^{-0.5}$) | $J^*$ (LMH) | SSE | $k_C$ ($m^{-1}$) | $J^*$ (LMH) | SSE | $k_D$ (h $m^{-2}$) | $J^*$ (LMH) | SSE |
| 0.004 M NaCl | 0.263 | 33.7 | 0.516 | 1.055 | 32.1 | 0.659 | 5.52 | 32.4 | 0.951 | 120 | 31.4 | 0.977 |
| 0.01 M NaCl | 0.246 | 32.3 | 5.31 | 0.968 | 30.2 | 5.756 | 4.5 | 29.5 | 5.41 | 108 | 29 | 5.474 |
| 0.05 M NaCl | 0.355 | 33.1 | 3.895 | 1.5 | 32 | 5.683 | 7.08 | 31.6 | 4.906 | 156 | 30.6 | 3.693 |
| 0.1 M NaCl | 0.325 | 31.5 | 7.327 | 1.35 | 30 | 9.466 | 6.54 | 29.6 | 8.443 | 150 | 28.6 | 7.06 |

Table 4
Model parameters affected by solution pH

| Ionic strength | Model parameter | | | | | | | | | | | |
|---|---|---|---|---|---|---|---|---|---|---|---|---|
| | Pore blocking | | | Pore constriction | | | Intermediate | | | Cake formation | | |
| | $k_A$ ($h^{-1}$) | $J^*$ (LMH) | SSE | $k_B$ ($m^{-0.5} h^{-0.5}$) | $J^*$ (LMH) | SSE | $k_C$ ($m^{-1}$) | $J^*$ (LMH) | SSE | $k_D$ ($h\,m^{-2}$) | $J^*$ (LMH) | SSE |
| I.S. = 0.01 M | | | | | | | | | | | | |
| pH 4 | 0.069 | 26.8 | 0.726 | 0.238 | 20.2 | 0.678 | 1.5 | 24.9 | 1.085 | 31.2 | 22.4 | 1.613 |
| pH 7 | 0.246 | 32.3 | 5.31 | 0.968 | 30.2 | 5.756 | 4.5 | 29.5 | 5.41 | 108 | 29 | 5.474 |
| pH 10 | 0.232 | 31.2 | 6.456 | 0.892 | 28.7 | 7.992 | 4.02 | 27.5 | 7.437 | 79.2 | 24.3 | 6.615 |
| I.S. = 0.05 M | | | | | | | | | | | | |
| pH 4 | 0.171 | 33.3 | 0.263 | 0.637 | 30.7 | 0.489 | 2.76 | 29.3 | 0.455 | 50.7 | 25.6 | 0.412 |
| pH 7 | 0.355 | 33.1 | 3.895 | 1.5 | 32 | 5.683 | 7.08 | 31.6 | 4.906 | 156 | 30.6 | 3.693 |
| pH 10 | 0.317 | 32 | 3.41 | 1.308 | 30.5 | 5.135 | 6.12 | 29.9 | 4.406 | 132 | 28.42 | 3.317 |

0.01 M, increased solution pH from 4 to 7 increased permeate flux decline. The retentate rejections of salt were determined in the range of 16.0%, 25.5%, and 37.3% with increased solution pH of 4, 7, and 10, respectively. Solutions having high solution pH of 7 and 10 showed greater salt rejection than those having low solution pH. This indicated that increased salt rejection increased permeate flux decline, suggesting increased charge repulsion between negatively charged NF membrane and functional groups in the NOM molecules for high solution pH. Kilduff et al. [5] reported that the effect of pH on solution rejection was an important factor on permeate flux decline compared with the effect of membrane permeability.

Solutions having solution pH of 4 exhibited relatively low rejection. This can be affected by charge interaction between positively charged $H^+$ and negatively charged NF membrane, allowing salt passage through the NF membrane surface, and decreasing salt rejection. Based on fitting mathematical models, permeate flux curves were correlated with pore constriction and pore blocking model. It was observed that the retentate rejections of NOM were approximately 91.6–94.9%, indicating relatively low rejections compared with those of high ionic strength of 0.05 M. From Table 4, the kinetic rate constants of fouling mechanisms for solution pH 4, 7, and 10 were about 0.238 $(m\,h)^{-1/2}$ ($k_B$, pore constriction), 0.246 $h^{-1}$ ($k_A$, pore blocking), and 0.232 $h^{-1}$($k_A$, pore blocking), respectively.

At high ionic strength of 0.05 M NaCl, increased solution pH from 4 to 10 showed similar trend for permeate flux curve of low ionic strength of 0.01 M NaCl. The permeate flux curve of pH 7 and 10 exhibited the greatest permeate flux reduction. However, permeate flux curves of pH 7 and 10 show no significant difference. The retentate rejections of salt were 17.9%, 15.9%, and 26.1% with increasing solution pH of 4, 7, and 10, respectively. At low solution pH of 4, permeate flux curves were related to pore blocking model, while permeate flux curves were related to cake formation model at solution pH of 7 and 10. The retentate rejections of NOM were approximately 95.3–96.4% with increasing solution pH from 4 to 10. This suggests that high ionic strengths (0.05 M NaCl) can dominate permeate flux curve compared with the effect of solution pH on salt rejection. Permeate flux decline can be caused by reduced charge repulsion between positively charged $Na^+$ and functional groups in the NOM molecules, thus increased NOM accumulation on the membrane surface. This was confirmed by permeate flux curves, which correspond to cake formation model for solution pH of 7 and 10. From Table 4, the kinetic rate constants of fouling mechanisms for solution pH 4, 7, and 10 were about 0.171 $h^{-1}$ ($k_A$, pore blocking), 156 $h\,m^{-2}$ ($k_D$, cake formation), and 132 $h\,m^{-2}$ ($k_D$, cake formation), respectively.

Salt rejection can affect permeate flux curve. Solutions having high solution pH of 7 and 10 showed greater salt rejection than those having low solution pH. Solution pH of 4 exhibited less permeate flux decline than solution pH of 7 and 10. These were observed for both low and high ionic strengths. Solutions having low solution pH of 4 and high ionic strength can affect membrane surface, reducing charge repulsion between positively charged $Na^+$ and $H^+$ and negatively charged NF membrane. This allows an increased salt passage through the NF membrane surface, thus decreased salt rejection and permeate flux decline.

## 5. Conclusions

Performances of nanofiltration membrane in terms of NOM rejection and permeate flux decline were influenced by NOM concentration, ionic strength, and solution pH. Mathematical fouling models were used to evaluate fouling mechanisms on the membrane surface. The increase of NOM concentration from 0 $mg\,L^{-1}$ to 25 $mg\,L^{-1}$ caused higher NOM rejection, membrane fouling, and greater flux decline, as a result of NOM accumulation on membrane surface. From low to high NOM concentration, fouling mechanisms exhibited a change of fouling patterns from pore blocking and pore constriction model (low NOM concentration) to cake formation model (high NOM concentration). In the absence of NOM, increased ionic strength from 0.004 M to 0.1 M decreased permeate flux, caused by osmotic effect of feed solutions. In the presence of NOM, feed solutions possessing high ionic strength of 0.05 M NaCl showed greater flux decline than those with low ionic strength of 0.01 M NaCl, possibly indicated by a combination of resistance from NOM accumulation and osmotic effects. The experimental results were corresponded with cake formation model. The increase of solution pH from 4 to 10 showed greater flux decline, affected by increased salt concentrations on membrane surface and/or pores. These results were related with pore blocking and pore constriction model.

## Acknowledgements

The authors would like to thank the Thailand Research Fund (TRF) and the Commission on Higher Education, Thailand, for financial support. We also would like to thank the Department of Chemical Engineering, Faculty of Engineering, Ubon Rachathani University, Thailand, for all equipments applied in this research.

## References

[1] E.M. Thurman, Organic GeoChemistry of Natural Waters, Martinus Nijhoff/Dr. W. Junk Publishers, Dordrecht, 1985.
[2] E. Tipping, Cation binding by humic substances, Cambridge Environmental Chemistry Series, 1948, ISBN 0 521 62146 1.
[3] S.W. Krasner, M.J. McGuire, J.G. Jacangelo, N.L. Patania, K.M. Reagan, E.M. Aieta, The occurrence of disinfection by-products in US drinking water, J. AWWA 81 (8) (1989) 41–53.
[4] P. Fu, H. Ruiz, K. Thompson, C. Spangenberg, Selecting membranes for removing NOM and DBP precursors, J. AWWA 86 (12) (1994) 55–72.
[5] J.E. Kilduff, S. Mattaraj, G. Belfort, Flux decline during nanofiltration of naturally-occurring dissolved organic matter: effects of osmotic pressure, membrane permeability, and cake formation, J. Membr. Sci. 239 (1) (2004) 39–53.
[6] C. Jarusutthirak, S. Mattaraj, R. Jiraratananon, Influence of inorganic scalants and natural organic matter on nanofiltration membrane fouling, J. Membr. Sci. 287 (2007) 138–145.
[7] S. Hong, M. Elimelech, Chemical and physical aspects of natural organic matter (NOM) fouling of nanofiltration membranes, J. Membr. Sci. 132 (1997) 159–181.
[8] S.C. Allgeier, R.S. Summers, Evaluating NF for DBP control with the RBSMT, J. AWWA 87 (3) (1995) 87–99.
[9] M. Mattari, L. Puro, J. Nuortila-Jokinen, M. Nystrom, Fouling effects of polysaccharides and humic acid in nanofiltration, J. Membr. Sci. 165 (2000) 1–17.
[10] J. Hermia, Constant pressure blocking filtration laws: application to power-law non-newtonian fluids, Trans. Inst. Chem. Eng. 60 (1982) 183–187.
[11] C.-C. Ho, A.L. Zydney, A combined pore blockage and cake filtration model for protein fouling during microfiltration, J. Membr. Sci. 232 (2000) 389–399.
[12] R.W. Field, D. Wu, J.A. Howell, B.B. Gupta, Critical flux concept for microfiltration fouling, J. Membr. Sci. 100 (1995) 259–272.
[13] J.E. Kilduff, S. Mattaraj, A. Wigton, M. Kitis, T. Karanfil, Effects of reverse osmosis isolation on reactivity of naturally occurring dissolved organic matter in physicochemical processes, Water Res. 38 (4) (2004) 1026–1036.
[14] A. Braghetta, F.A. DiGiano, W.P. Ball, Nanofiltration of natural organic matter: pH and ionic strength effects, J. Environ. Eng. 123 (7) (1997) 628–641.
[15] A. Braghetta, F.A. DiGiano, W.P. Ball, NOM accumulation at NF membrane surface: impact of chemistry and shear, J. Environ. Eng. 124 (11) (1998) 1087–1098.

Separation and Purification Technology 63 (2008) 15–22

Contents lists available at ScienceDirect

Separation and Purification Technology

journal homepage: www.elsevier.com/locate/seppur

# Mass transfer study and modeling of gas–liquid membrane contacting process by multistage cascade model for $CO_2$ absorption

Supakorn Atchariyawut[a], Ratana Jiraratananon[a,*], Rong Wang[b]

[a] *Department of Chemical Engineering, King Mongkut's University of Technology Thonburi, Bangkok 10140, Thailand*
[b] *Institute of Environmental Science & Engineering, Nanyang Technological University, Innovation Center (NTU), Block 2, Unit 237, 18 Nanyang Drive, Singapore 637723, Singapore*

ARTICLE INFO

*Article history:*
Received 31 January 2008
Received in revised form 3 March 2008
Accepted 4 March 2008

*Keywords:*
$CO_2$ separation
Membrane contactors
Gas absorption
Mass transfer resistance analysis
Mathematical modeling

ABSTRACT

The objective of this work was to characterize the main mass transfer resistance for $CO_2$ capture in the gas–liquid membrane contacting process by both physical and chemical absorption conditions. The characterization was performed based on the resistance-in-series model as well as the Wilson-plot method. In addition, a multistage cascade model, which is able to predict the time for the system to reach a steady-state condition, was developed to describe $CO_2$ absorption in the membrane contacting process. The cascade model was numerically solved by using the MATLAB program.

It was found that the main mass transfer resistance of the physical absorption (using pure water as an absorbent) and the chemical absorption (using 2 M NaOH as an absorbent) was in the liquid phase and in the membrane, respectively. The membrane mass transfer resistance in the case of physical absorption presented approximately 36% of the total resistances at a liquid velocity of 2.13 m/s. For the chemical absorption condition applied, the membrane mass transfer resistance occupied around 99% of the total resistance. The results of simulation by the cascade model agreed well with the experimental results when the overall mass transfer coefficient obtained form the experiment was employed. The model can potentially be used with various operating conditions including the liquid velocity, gas concentration, and reactive absorbent used.

## 1. Introduction

$CO_2$ has been regarded as the main contributor to global climate change which directly results in serious environmental problems. Half of the anthropogenic $CO_2$ emission sources are emitted from the combustion of fossil fuels in industries and power plants worldwide [1]. This is because the majority of the world's electricity generation is based on the use of approximately 80% fossil fuels. Nowadays, the environmental concern and energy conservation are increasingly gaining attention; therefore, the low energy consumption and efficient technologies for $CO_2$ capture and removal from the gas mixtures released from industrial sources need to be developed. These technologies are also applicable for $CO_2/CH_4$ separation from natural gas and biogas.

Membrane contacting process is a hybrid of gas absorption and membrane separation processes. The hollow fiber membranes used only act as a barrier between the liquid and gas phases. The use of membrane contactors can potentially overcome the operational limitations of conventional dispersion processes such as flooding, entraining, channeling and foaming, and offers a number of advantages including high surface area per unit contact volume, individual gas and liquid flow channels, compactness of structure, easiness to scale up and known gas and liquid interfacial area.

Due to these advantages, the hollow fiber gas–liquid membrane contacting process has been paid attention by a number of researchers to employ for gas separation. Qi and Cussler [2] originally utilized the polypropylene (PP) hollow fiber membrane for $CO_2$ capture by using NaOH as an absorbent. Recently, the gas–liquid membrane contactors have been broadly studied. Feron and Jansen [3] reported the effect of operating conditions such as $CO_2$ partial pressure, liquid loading and temperature on the $CO_2$ removal by using PP hollow fiber membranes and CORAL as an absorbent. deMontigny et al. [4] used the polytetrafluoroethylene (PTFE) and PP hollow fiber membranes with monoethanolamine and 2-amino-2-methyl-1-propanol as absorbents for $CO_2$ separation. They found that the PTFE membrane was more suitable than the PP membrane because the system performance can be maintained for a longer operation time by using the PTFE membrane. A pilot-scale plant of membrane contactor for $CO_2$ removal was studied by Yeon et al. [5]. The $CO_2$ absorption rate per unit volume

---

* Corresponding author. Tel.: +66 2470 9222; fax: +66 2428 3534.
*E-mail address:* ratana.jir@kmutt.ac.th (R. Jiraratananon).

1383-5866/$ – see front matter © 2008 Elsevier B.V. All rights reserved.
doi:10.1016/j.seppur.2008.03.005

**Nomenclature**

| | |
|---|---|
| $A_T$ | mass transfer area based on inside surface area of gas–liquid contact ($m^2$) |
| $C_g$ | concentration of carbon dioxide in the gas phase ($mol\,m^{-3}$) |
| $C_l$ | concentration of carbon dioxide in the liquid phase ($mol\,m^{-3}$) |
| $C_{CO_2,F}$ | concentration of carbon dioxide in feed stream ($mol\,mol^{-1}$) |
| $C_{CO_2,R}$ | concentration of carbon dioxide in retentate stream ($mol\,mol^{-1}$) |
| $\Delta C_{l,av}$ | logarithmic mean concentration difference of carbon dioxide in the liquid phase ($mol\,m^{-3}$) |
| $d_i$ | inside diameter of membrane (m) |
| $d_{ln}$ | logarithmic mean diameter of membrane (m) |
| $d_o$ | outside diameter of membrane (m) |
| $D$ | diffusion coefficient of carbon dioxide in the liquid phase ($m^2\,s^{-1}$) |
| $G$ | gas flow rate ($m^3\,h^{-1}$) |
| $H$ | Henry's constant |
| $J_{CO_2}$ | $CO_2$ flux ($mol\,m^{-2}\,s^{-1}$) |
| $k_g$ | individual mass transfer coefficient of gas phase ($m\,s^{-1}$) |
| $k_l$ | individual mass transfer coefficient of liquid phase ($m\,s^{-1}$) |
| $k_m$ | individual mass transfer coefficient of membrane ($m\,s^{-1}$) |
| $K_{ol}$ | overall mass transfer coefficient ($m\,s^{-1}$) |
| $K_{ol,cor}$ | overall mass transfer coefficient based on calculation from correlation ($m\,s^{-1}$) |
| $K_{ol,exp}$ | overall mass transfer coefficient based on the experimental result ($m\,s^{-1}$) |
| $l_m$ | thickness of the hollow fiber (m) |
| $L$ | liquid flow rate ($m^3\,h^{-1}$) |
| $Q_l$ | liquid volumetric flow rate ($m^3\,s^{-1}$) |
| $Q_n$ | $CO_2$ transfer rate ($mol\,h^{-1}$) |
| $Q_F$ | total gas flow rate in feed stream ($m^3\,s^{-1}$) |
| $Q_R$ | total gas flow rate in retentate stream ($m^3\,s^{-1}$) |
| $Re$ | Reynold number |
| $Sc$ | Schmidt number |
| $Sh$ | Sherwood number |
| $t$ | time (h) |
| $T_g$ | gas temperature (K) |
| $v$ | velocity ($m\,s^{-1}$) |
| $V_G$ | gas phase volume ($m^3$) |
| $V_L$ | liquid phase volume ($m^3$) |
| $X$ | $CO_2$ concentration in liquid phase ($mol\,m^{-3}$) |
| $Y$ | $CO_2$ concentration in gas phase ($mol\,m^{-3}$) |

*Greek letters*

| | |
|---|---|
| $\varepsilon_m$ | porosity of the membrane |
| $\tau_m$ | tortuosity of the membrane |

achieved from the membrane contactor was 2.7 times higher than that from a packed column. The use of Potassium glycinate (PG) as an absorbent with the PP membrane in the membrane contacting process almost did not wet the membrane for a long period of operation performed by Yan et al. [6]. Based on these literatures, it can be confirmed that the gas–liquid membrane contacting process is practical and efficient to apply for $CO_2$ separation.

Process simulation can lead to a better insight on the process characteristics. The mathematical modeling of the membrane contactor has been performed by many researchers. For instance, Karoor and Sirkar [7] investigated both experimentally and theoretically the gas absorption of $CO_2$, $SO_2$, $CO_2$–$N_2$ mixtures and $SO_2$–air mixtures in PP hollow fiber membrane contactors. Lee et al. [8] conducted the mathematical simulation of $CO_2$ absorption and desorption in a hollow fiber membrane contactor by using potassium carbonate solutions as an absorbent. The model was inserted with the non-linear reversible term of $CO_2$ reacted with the absorbent. The effect of membrane wetting on the PP hollow fiber membrane by DEA solutions was theoretically studied by Wang et al. [9]. They found that 5% of the membrane pores wetted may result in 20% reduction of overall mass transfer coefficient. More recent studies include Keshavarz et al. [10], Bottino et al. [11], and Al-Marzouqi et al. [12]. The mathematical model developed by Keshavarz et al. [10] has analyzed the effect of partially wetted membrane on the absorption performance. The small fraction of membrane wetting can significantly decrease the absorption flux. In addition, the effect of chemical reaction inside the wetted membrane pores on predicting membrane wetting fraction was also considered. Bottino et al. [11] developed the mathematical model for predicting the gas removal efficiency of $CO_2$ separation from $N_2$ in gas–liquid membrane contactors. The simulations were in good agreement with the experimental results. The two-dimensional mathematical model was proposed to simulate the $CO_2/CH_4$ separation performance in a membrane contactor by Al-Marzouqi et al. [12]. This model was developed based on the non-wetted mode of operation, laminar parabolic velocity profile of gas flow in the tube side and Happel's free surface model for characterizing the liquid flow in the shell side. Good agreement between the simulated and experimental results was found.

The present work aims to characterize the main mass transfer resistance to $CO_2$ transfer in the gas–liquid membrane contacting process both by physical and chemical absorption. The characterization was performed based on the resistance-in-series model and Wilson-plot method. In addition, a multistage cascade model was developed with the intention of predicting the $CO_2$ flux under various operating conditions. This model is a dynamic one which is able to predict the time for the system to reach a steady-state condition. The simulation was conducted by using the overall mass transfer coefficient achieved from the experiments.

## 2. Theory

### 2.1. Basic principle of mass transfer in a membrane contactor

For the gas–liquid membrane contacting process, the resistance-in-series model has been used to describe the mass transfer mechanism. Fig. 1 depicts the mass transport of the interested gas for non-wetted mode of operation of membrane contactors, i.e., diffusion from the bulk gas through the membrane pores and dissolution in the liquid absorbent. The resistance-in-series model can be expressed as

$$\frac{1}{K_{ol}} = \frac{1}{k_l} + \frac{Hd_o}{k_m d_{ln}} + \frac{Hd_o}{k_g d_i} \tag{1}$$

where $K_{ol}$ is the overall mass transfer coefficient based liquid-phase (m/s), $k_l$, $k_m$, and $k_g$ are the individual mass transfer coefficients of the liquid phase, membrane and gas phase, respectively. $H$ represents Henry's constant. $d_i$, $d_o$, and $d_{ln}$ are the inner, outer and logarithmic mean diameters of the fibers, respectively. The overall mass transfer resistance is the summation of mass transfer resistance in each phase.

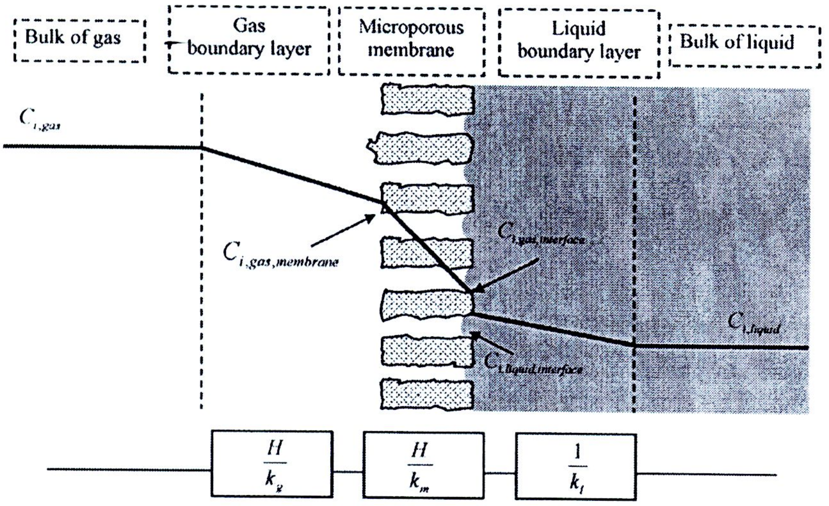

**Fig. 1.** Mass transfer regions and resistance-in-series in non-wetted membrane contactor [18].

The overall mass transfer coefficient, $K_{\mathrm{ol}}$, can be calculated based on experiments by the following equation [9]:

$$K_{\mathrm{ol}} = \frac{Q_{\mathrm{l}}(C_{\mathrm{l,out}} - C_{\mathrm{l,in}})}{A_{\mathrm{T}}\Delta C_{\mathrm{l,av}}} \tag{2}$$

The logarithmic mean concentration, $\Delta C_{\mathrm{l,av}}$, is expressed as

$$\Delta C_{\mathrm{l,av}} = \frac{(HC_{\mathrm{g,in}} - C_{\mathrm{l,out}}) - (HC_{\mathrm{g,out}} - C_{\mathrm{l,in}})}{\ln(HC_{\mathrm{g,in}} - C_{\mathrm{l,out}}/HC_{\mathrm{g,out}} - C_{\mathrm{l,in}})} \tag{3}$$

where $A_{\mathrm{T}}$ is the gas–liquid contact area, $C_{\mathrm{l,in}}$, $C_{\mathrm{l,out}}$ are the liquid phase inlet and outlet concentrations, $C_{\mathrm{g,in}}$, $C_{\mathrm{g,out}}$ are the gas phase inlet and outlet concentrations, and $Q_{\mathrm{l}}$ is the liquid volumetric flow rate.

In the operation of a membrane contactor, either the gas phase or liquid phase can be fed through the shell side or tube side of the hollow fiber membrane module. However, flow of liquid in the tube side takes more advantage than that in the shell side [4] which also depends on the packing density of the membrane module used. In addition, when asymmetric membranes used, the location of the skin layer has to be considered in order to decide the flow configuration. For the tube side, the well-known Graetz-Lévêque mass transfer correlation was widely used to predict the tube side mass transfer coefficient [13,14]

$$Sh = \frac{k_{\mathrm{l}}d_{\mathrm{i}}}{D} = 1.62\left(\frac{d_{\mathrm{i}}^2 V}{LD}\right)^{1/3} \tag{4}$$

where $Sh$ is Sherwood number, $D$ is the diffusion coefficient, $L$ is the tube length and $V$ is the fluid velocity.

Many correlations have been proposed to determine the shell side mass transfer coefficient [14–16]. However, each of them is applicable to a certain limited range of operation. In general, it can be expressed in the following form:

$$Sh = aRe^{\alpha}Sc^{\beta} \tag{5}$$

where $Re$ and $Sc$ are Reynolds and Schmidt numbers, respectively.

The membrane mass transfer coefficient in a completely non-wetted case can be calculated using the following equation [17]:

$$k_{\mathrm{m}} = \frac{D_{\mathrm{g,eff}}\varepsilon_{\mathrm{m}}}{\tau_{\mathrm{m}} l_{\mathrm{m}}} \tag{6}$$

where $D_{\mathrm{g,eff}}$ is the effective diffusion coefficient of pure gas filled in the pores. It is calculated from the summation between the molecular self-diffusion coefficient and the diffusion coefficient which is the interaction of gas molecules and membrane wall [17]. $\varepsilon_{\mathrm{m}}$, $l_{\mathrm{m}}$ are the porosity, thickness of the membrane provided by the manufacturer, respectively. $\tau_{\mathrm{m}}$ is the tortuosity achieving from the correlation [18]. In order to estimate the overall mass transfer coefficient based on Eq. (1), Eqs. (4) and (6) were used to determine the liquid phase and membrane mass transfer coefficients.

### 2.2. Wilson plot

The Wilson plot is the technique to experimentally determine the membrane mass transfer resistance in the gas–liquid membrane contacting process based on the resistance-in-series model. A plot of $1/K_{\mathrm{ol}}$ versus $1/V^{\alpha}$ gives a straight line. The value of the empirical, $\alpha$, is chosen for achieving the best straight line. In the gas–liquid membrane contacting process, if the resistance in the gas phase is much smaller than the total resistance, the term $H/k_{\mathrm{g}}$ in Eq. (1) becomes negligible. Thus, the interception of the Wilson plot represents the value of membrane mass transfer resistance.

### 2.3. Mathematical modeling

A multistage countercurrent extraction cascade model [19] was applied to describe the $CO_2$ absorption flux operating in a membrane contactor. In this study, the liquid absorbents which were pure water or NaOH solution were fed through the lumen of the membrane while the gas phase flowed in the shell side. The membrane module was divided into $N$ countercurrent stages, as indicated in Fig. 2. A material balance at stage n was performed in order to develop the main equations for the mathematical model.

For any given stage $n$, the material balance can be written as

(Rate of accumulation of mass of $CO_2$ in the system)

= (Mass flow of the $CO_2$ into the system)

− (Mass flow of the $CO_2$ out of the system)

+ (Rate of mass transfer of $CO_2$ into the system)

Thus, the material balance of $CO_2$ in the liquid can be expressed as

$$V_{\mathrm{L}}\frac{\mathrm{d}X_n}{\mathrm{d}t} = L(X_{n-1} - X_n) + Q_n \tag{7}$$

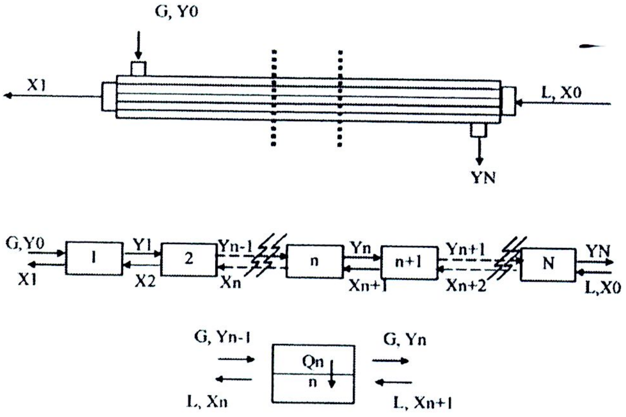

Fig. 2. Multistage cascade model of hollow fiber membrane contactor.

The $CO_2$ balance in the gas phase is as follows

$$V_G\frac{dY_n}{dt} = G(Y_{n+1} - Y_n) - Q_n \tag{8}$$

where

$$Q_n = K_{ol}(HY_n - X_n) \tag{9}$$

$V_L$, $V_G$, $L$ and $G$ are the phase volumes of the liquid phase and gas phase, liquid flow rate, and gas flow rate, respectively. $X$ and $Y$ are $CO_2$ molar concentrations in the liquid phase and the gas phase, respectively. $Q_n$ is the $CO_2$ rate transferred from the gas to liquid phase.

The Eqs. (7)–(9) were solved by using a built-in ordinary differential equation (ODE) solver, i.e., ODE23 in the MATLAB program. This solver is the numerical technique which comes from Runge–Kutta method. Therefore, the mass balance error should be estimated in order to confirm the accuracy of the numerical solution. The initial values which have to be previously input for solving the model are the gas and liquid flow rates, the phase volume of gas and liquid, $CO_2$ concentrations in the inlet gas and liquid phases, the number of divided stages, and the overall mass transfer coefficient.

The overall mass transfer coefficient ($K_{ol}$) can be obtained from the resistance-in-series model (Eqs. (1), (4)–(6)) or from the experiments (Eq. (2)). This is a dynamic system since the term of time exists in the main mass transfer model. However, the effect of operating condition on $CO_2$ absorption flux can be also obtained at steady-state condition by collecting the data which do not change with time for each condition.

**Table 1**
Specifications of the hollow fiber membrane module used

| | |
|---|---|
| Fiber o.d. (μm) | 1000 |
| Fiber i.d. (μm) | 650 |
| Module i.d. (mm) | 10 |
| Membrane pore size (μm) | 0.2 |
| Membrane porosity | 0.75 |
| Number of fibers | 35 |
| Effective module length (mm) | 270 |
| Effective contact area (m$^2$) | 0.019 |

## 3. Experimental

Hydrophobic porous polyvinylidenefluoride (PVDF) hollow fiber membranes used in this work were kindly supplied by Memcor Australia (South Windsor, New South Wales, Australia). Table 1 shows the characteristics of the membranes used. A 99% grade NaOH purchased from THASCO Chemical Co., Ltd., Thailand was mixed with RO water to prepare an aqueous absorbent with desired concentrations. Potassium hydrogen phthalate (KHP) were purchased from Merck Ltd., Thailand. Methane (99.9%) and Carbon dioxide (99.8%) were obtained from Thai Industrial Gases PLC, Thailand.

Fig. 3 shows the schematic diagram of the experimental setup. Pure $CO_2$ or $CO_2/CH_4$ mixture with a volume ratio of 50:50 or 20:80, which is in the composition range of biogas and natural gas, was used as the feed gas while the RO water or 2 M NaOH was employed as the absorbent. In the experiment, the flow rate of the feed gas supplied from compressed gas cylinders was adjusted and controlled by Aalborg (GFC model) mass flow controllers, and then it was fed through the shell side of the membrane module. The inlet and outlet gas volume flow rates were measured by a digital bubble meter. The liquid absorbent was pumped by a peristaltic pump (L/S® Easy-load® II, Masterflex model 77201-62) from the feed tank through a rotameter into the tube side of the hollow fibers. The pressure gauges were used to indicate the inlet and outlet pressures of the gas and liquid. When $CO_2/CH_4$ mixture was used as the feed gas, Gas Chromatograph (6890 Hewlett Packard, TCD) was used to analyze the inlet and outlet gas compositions. Potassium hydrogen phthalate, which is a primary standard solution for titration, was used for the confirmation of the absorbent concentration. All of the

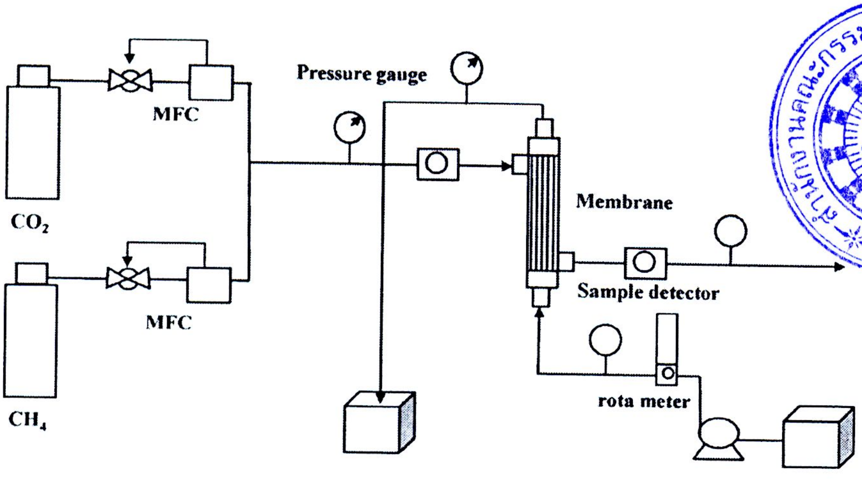

Fig. 3. Schematic diagrams of a gas–liquid membrane contactor unit.

data were collected after the experiment had been operated for 30 min to ensure that the system reached steady state. The results of each run were averaged from five times of sampling. The operating parameters, which influenced the process performance, i.e., $CO_2$ concentration in the feed, the gas flow rate, and the absorbent flow rate were varied. The effect of liquid absorbent and gas phase velocities were studied to characterize the mass transfer resistance of the system in each phase for both using pure water and 2 M NaOH solution as absorbents. All of the experiments were performed at the room temperature; therefore, the gas phase temperature in this work was approximately 30 °C. In this work, the $CO_2$ flux which was used to indicate the process efficiency was estimated by the following equation [6]:

$$J_{CO_2} = \frac{(Q_F \times C_{CO_2,F} - Q_R \times C_{CO_2,R}) \times 273.15 \times 1000}{22.4 \times T_g \times A_T} \quad (10)$$

where $J_{CO_2}$ is the $CO_2$ flux. $C_{CO_2,F}$ and $C_{CO_2,R}$ are the $CO_2$ concentrations in the feed and retentate streams, respectively. $Q_F$ and $Q_R$ are the gas flow rates at the inlet and outlet of the membrane module, respectively. $T_g$ is the gas temperature. $A_T$ is the mass transfer area.

## 4. Results and discussion

### 4.1. Mass transfer analysis in physical and chemical absorption process

In conventional absorption processes, the solute gas has to encounter with two mass transfer resistances, i.e., the gas phase and liquid phase boundary layers. For the gas–liquid membrane contacting process, there is an additional mass transfer resistance caused by the membranes. With the purpose of obtaining the better understanding of membrane role in the process, the membrane mass transfer resistance was quantitatively and qualitatively characterized in this section.

Fig. 4 shows the effect of liquid absorbent velocity on the $CO_2$ flux, where pure water and a 2 M NaOH solution were used as the absorbents. The use of a chemical absorbent enhanced the $CO_2$ flux due to the reaction between $CO_2$ and $OH^-$. The increase of $CO_2$ flux with the liquid velocity was the result of the increase of the liquid phase mass transfer coefficient ($k_l$ in Eq. (4)). It can be seen that increase of pure water velocity significantly resulted in $CO_2$ flux increase. On the other hand, using a 2 M NaOH solution as an absorbent, the $CO_2$ flux was slightly affected with increasing the velocity of the NaOH solution because the main mass transfer resistance was not in the liquid phase. This result corresponds with the previous studies [9,20]. The effect of gas phase velocity on $CO_2$ flux was also studied and the results for both pure water and a 2 M NaOH solution used as absorbents are shown in Fig. 5. In the case of using pure water as an absorbent, the $CO_2$ flux seemed to be constant when the gas velocity was increased. Due to the low solubility of $CO_2$ in pure water, the increase of gas velocity had negligible effect of $CO_2$ flux. Wang et al. [9] reported the same trend of results. Using 2 M NaOH as an absorbent, it was found that the $CO_2$ flux was reduced at high gas velocity which was expected since the contact time of the phases was decreased. Therefore, less amount of gas was available for the reaction, and this obviously affected the $CO_2$ flux.

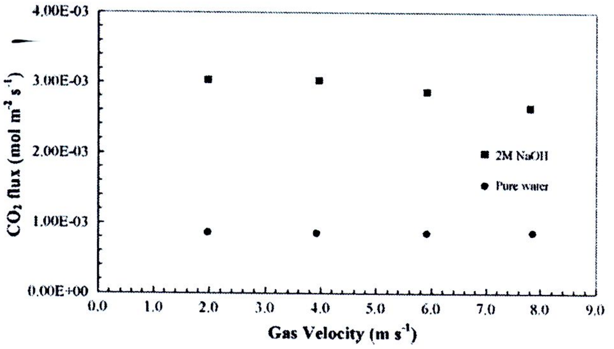

**Fig. 5.** Effect of gas phase ($CO_2$) velocity on $CO_2$ flux (absorbent temperature: 30 °C, liquid velocity: 0.68 m/s, feed gas: pure $CO_2$).

Based on the above results of the effects of the liquid and gas velocities on the $CO_2$ flux, it can be concluded that, for physical absorption, the main mass transfer resistance was in the liquid phase. For chemical absorption (NaOH solutions used as an absorbent), the mass transfer was dominated by the membrane. This is because the change of both gas and liquid phase velocity hardly affected the mass transfer rate.

To quantitatively investigate the membrane mass transfer resistance in the gas–liquid membrane contacting process, the Wilson-plot method which employs the resistance-in-series model was applied. Fig. 6 shows the Wilson plot of $1/K_{ol}$ versus $V^{-0.33}$ for pure water and pure $CO_2$ system using the experimental data from Fig. 4. The equation which correlated the overall mass transfer resistance with individual mass transfer resistances is as follows

$$\frac{1}{K_{ol}} = 18087V^{-0.33} + 8082, \quad R^2 = 0.9798 \quad (11)$$

where $K_{ol}$ is the overall mass transfer coefficient based on liquid phase and $V$ is the liquid velocity.

According to the above equation, the membrane mass transfer resistance ($Hd_o/k_m d_{ln}$) of the PVDF membranes used in this work can be obtained from the intercept value, i.e., 8082 s/m.

For physical absorption, it can be observed that the membrane mass transfer resistance presented approximately 36% of the total

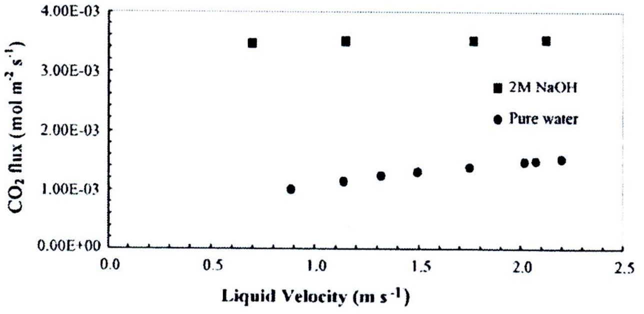

**Fig. 4.** Effect of pure water and 2 M NaOH absorbent velocity on $CO_2$ flux (absorbent temperature: 30 °C, gas flow rate: 200 ml/min, feed gas: pure $CO_2$).

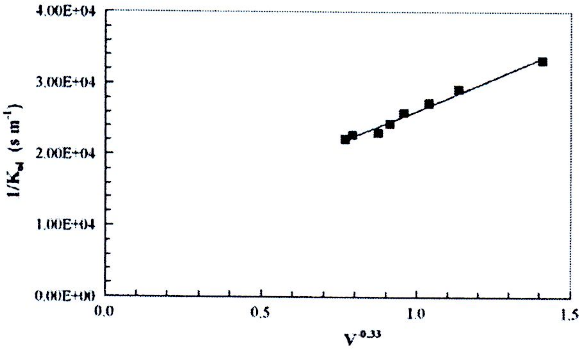

**Fig. 6.** Wilson plot of PVDF hollow fiber membrane (pure $CO_2$–water system, water temperature: 30 °C, gas flow rate: 200 ml/min).

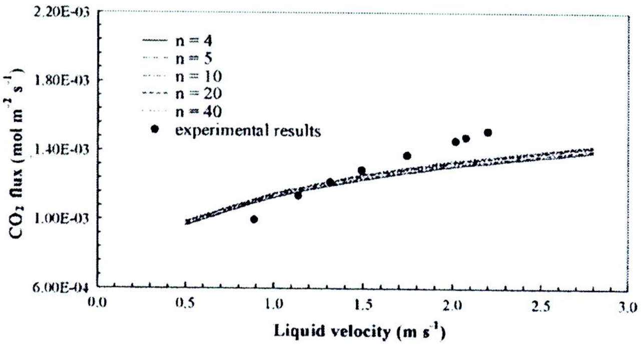

**Fig. 7.** Comparison of the experimental results with the simulated results at various divided stages (absorbent temperature: 30 °C, gas flow rate: 200 ml/min, feed gas: pure $CO_2$, absorbent: pure water).

resistance ($(Hd_o/k_m d_{ln})/(1/K_{ol})$) at a liquid velocity of 2.13 m/s. Due to the pure $CO_2$ used as feed gas in the physical absorption experiment, the gas phase mass transfer resistance can be neglected, therefore, the liquid phase mass transfer resistance of this system was 64% of the total resistance. If the liquid velocity increases, the ratio of membrane mass transfer resistance to total mass transfer resistance will increase. Since the liquid phase mass transfer resistance decreases with increasing liquid velocity (mass transfer coefficient in liquid phase increases).

For chemical absorption, the overall mass transfer resistance ($1/K_{ol}$) achieving from the experiments for pure $CO_2$ gas phase and 2 M NaOH as an absorbent was 8128.7 s/m at 2.13 m/s liquid velocity. The membrane mass transfer resistance for chemical absorption experiments can also be obtained from Eq. (11) because the same membrane was used for both cases ($Hd_o/k_m d_{ln} = 8082$ s/m at 2.13 m/s liquid velocity). Therefore, the ratio of membrane mass transfer resistance to total mass transfer resistance ($(Hd_o/k_m d_{ln})/(1/K_{ol})$) exhibited around 99% for chemical absorption.

### 4.2. Study on mathematical modeling

#### 4.2.1. Model validation

In the present study, the multistage countercurrent extraction cascade model was used to simulate the $CO_2$ absorption flux in the gas–liquid membrane contacting process. Due to the numerical solving method used, the estimated error of mass balance had to be performed aiming to confirm the reliability of the model. For pure water/pure $CO_2$ system studied, the average error of mass balance was around 3% which can be acceptable for the numerical solving method.

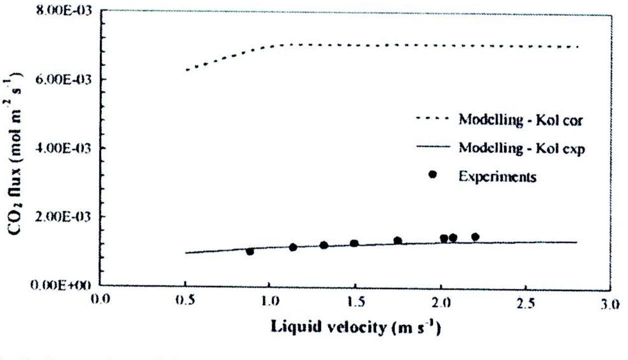

**Fig. 8.** Comparison of the experimental results with the predicted flux by overall mass transfer coefficient achieved from the experiments and from the correlations (absorbent temperature: 30 °C, gas flow rate: 200 ml/min, feed gas: pure $CO_2$, absorbent: pure water).

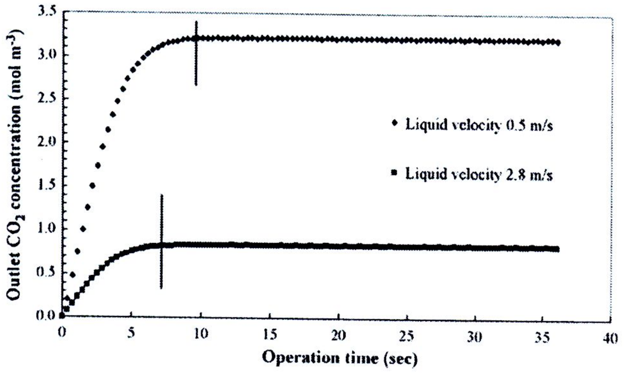

**Fig. 9.** Outlet $CO_2$ concentration with the operation time for various liquid velocity (absorbent temperature: 30 °C, gas flow rate: 200 ml/min, feed gas: pure $CO_2$).

In order to estimate the $CO_2$ flux by using the multistage cascade model, the membrane module was divided into small stages. The effect of the number of divided stages on estimated $CO_2$ flux was shown in Fig. 7. The $CO_2$ flux achieved from 40 divided stages was around 2% higher than that from 4 divided stages. Therefore, the number of divided stages hardly influenced the predicted $CO_2$ flux. In this work, the simulated $CO_2$ flux was performed by dividing the membrane module into five stages.

Fig. 8 depicts the $CO_2$ flux simulated by the multistage countercurrent extraction cascade model using the overall mass transfer coefficients obtained from the experiments based on Eq. (11) ($K_{ol,exp}$) and from the correlations ($K_{ol,cor}$). $K_{ol,cor}$ was calculated from the individual mass transfer correlation (Eqs. (4)–(6)) as well as based on the resistance-in-series model in Eq. (1). It can be seen that the predicted flux based on $K_{ol,exp}$ agreed well with the experimental result. From the simulated result, the cascade model can potentially be applied for predicting the $CO_2$ absorption flux in the membrane contactor. It can also be suggested that this model will be useful for scaling up the gas–liquid membrane contacting system when the $K_{ol}$ in each system is obtained from the experiment.

The simulated $CO_2$ fluxes obtaining from $K_{ol,cor}$ was six times higher than those from $K_{ol,exp}$. Referring to the previous work [21], this may be explained that the membranes were partially wetted by the absorbent. Therefore, the simulation results were higher than the experimental results because Eq. (6) was used to estimate the membrane mass transfer coefficient in the case of completely gas-filled membrane pore [17].

#### 4.2.2. Simulation for time to reach a steady state

Generally, the absorption performance of a gas–liquid membrane contacting process is evaluated at the steady-state condition. At a steady state, each process parameter such as $CO_2$ concentrations in the gas and liquid outlets are independent of time. All values of simulated $CO_2$ flux presented in this study were achieved at steady state. Fig. 9 shows the $CO_2$ concentrations in the liquid absorbent outlet at various liquid velocities. The system reached the steady state at 6.84 and 10.80 s at 2.8 and 0.5 m/s liquid velocity, respectively. It can be seen that as the liquid velocity increased, the system rapidly reached the steady-state condition due to the decrease of the retention time in the membrane module. This is one of the advantages of using this dynamic model which is able to predict the time to reach the process steady state. In addition, it can also be found that the $CO_2$ concentration in the liquid phase outlet decreased with increasing the liquid velocity since the gas to liquid ratio in the membrane module was decreased. Similar experimental results were reported in the literature [10].

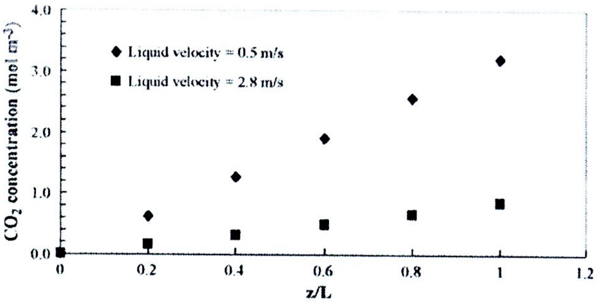

**Fig. 10.** $CO_2$ concentration in the liquid phase along the membrane module for various liquid velocities (absorbent temperature: 30 °C, gas flow rate: 200 ml/min, feed gas: pure $CO_2$, absorbent: pure water).

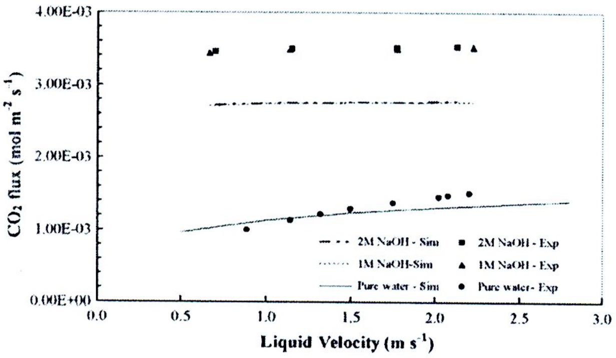

**Fig. 11.** Effect of physical and chemical absorption on $CO_2$ flux (absorbent temperature: 30 °C, gas flow rate: 200 ml/min, feed gas: pure $CO_2$).

### 4.2.3. $CO_2$ concentration profile

Based on the cascade model used in this work, the membrane module was divided into five small stages to simulate the $CO_2$ flux of pure water–pure $CO_2$ system. Therefore, the change of $CO_2$ concentration along the length of the membrane module can be estimated from the outlet concentration of $CO_2$ in each small stage. Fig. 10 depicts the $CO_2$ concentration in the liquid phase as a function of membrane module length by varying liquid phase velocity. The $CO_2$ concentration increased along the length of membrane module. The change of $CO_2$ concentration along the membrane module length at a liquid flow rate of 2.8 m/s was less than that at 0.5 m/s liquid flow rate due to the gas/liquid ratio in membrane module which directly affected the contact time between two phases.

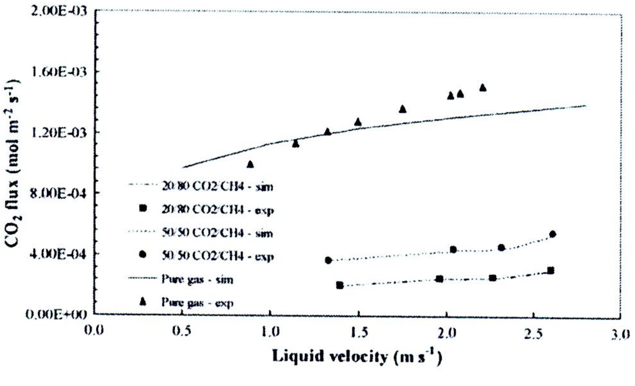

**Fig. 12.** Effect of gas concentrations on $CO_2$ flux (absorbent temperature: 30 °C, gas flow rate: 200 ml/min, liquid absorbent: water).

### 4.2.4. Effects of operating parameters on $CO_2$ flux

The effect of liquid velocity on the $CO_2$ flux is shown in Fig. 11. For physical absorption the predicted flux agreed well with the experimental data with the maximum difference of 6%. It was observed that the $CO_2$ flux in the case of using 2 M NaOH as an absorbent was around three times higher than that of using pure water as an absorbent in the system of pure $CO_2$ as feed gas (see Section 4.1). In chemical absorption, the difference of $CO_2$ flux between experimental and simulation results were around 20%. This appears to be the limitation of this model when applied with the higher overall mass transfer coefficient ($K_{ol}$) in the case of chemical absorption.

Fig. 12 shows the effect of gas concentration on $CO_2$ flux. The pure $CO_2$, 50/50 and 20/80 of $CO_2/CH_4$ mixture gas were used as the feed gases while pure water was used as the absorbent. It was found that the $CO_2$ flux increased with increasing $CO_2$ concentration as a result of the increase of the driving force of the system. Additionally, it can be found that the simulated $CO_2$ fluxes were in good agreement with the experimental observations for various $CO_2$ concentrations in the feed gas.

In the process simulation, the overall mass transfer coefficient for the system has to be achieved. For the pure $CO_2$ used as feed gas, the overall mass transfer coefficient can be calculated based on Eq. (11) which is the averaged overall mass transfer coefficient. For the gas mixture (50/50 and 20/80 $CO_2/CH_4$), the overall mass transfer coefficient was obtained from Eq. (2) at each experimental condition. Therefore, the perfect fit was obtained. It was found that the simulated results were in good agreement with the experimental results for the physical absorption scheme. Therefore, the multistage cascade model can potentially be employed to design the large-scale gas–liquid membrane contacting process when the overall mass transfer coefficient of the system is known.

## 5. Conclusions

The main mass transfer resistance in the gas–liquid membrane contacting process was analyzed by a set of the experimental results for both physical and chemical absorption conditions. It was found that, for physical absorption, the system was controlled by the liquid phase. In the case of chemical absorption, the mass transfer was dominated by the membrane. The membrane mass transfer resistance was quantitatively determined by the Wilson-plot method and the resistance-in-series model. It was observed that membrane mass transfer resistance was around 36% and 99% of the total mass transfer resistances for physical and chemical absorption conditions, respectively.

In addition, a multistage cascade model was developed to estimate the $CO_2$ flux. The simulated $CO_2$ fluxes based on the experimental overall mass transfer coefficient agreed well with the experimental results. Therefore, the multistage cascade model can potentially be used to design the larger scale system based on the overall mass transfer coefficient obtained form the laboratory scale in each system. Changing the $CO_2$ concentrations in the feed gas and the use of NaOH as an absorbent, the simulated results were still in good agreement with the experimental results. By using this model, the time for the process to reach steady state can also be estimated. As the liquid velocity increased, the system reached steady state more rapidly. Additionally, the concentration profile along with the membrane module was able to be simulated.

## Acknowledgements

The authors gratefully acknowledge the financial support from the Thailand Research Fund (TRF) and from the Commission on

Higher Education, Thailand through the Royal Golden Jubilee Ph.D. Program and the TRF senior research scholar grant.

## References

[1] U. Desideri, A. Paolucci, Performance modeling of a carbon dioxide removal system for power plants, Energy Convers. Manage. 40 (1999) 1899–1915.

[2] Z. Qi, E.L. Cussler, Microporous hollow fibers for gas absorption. I. Mass transfer in the liquid, J. Membr. Sci. 23 (1985) 321–332.

[3] P.H.M. Feron, A.E. Jansen, $CO_2$ separation with polyolefin membrane contactors and dedicated absorption liquids: performances and prospects, Sep. Purif. Technol. 27 (2002) 231–242.

[4] D. deMontigny, P. Tontiwachwuthikul, A. Chakma, Using polypropylene and polytetrafluoroethylene membranes in a membrane contactor for $CO_2$ absorption, J. Membr. Sci. 277 (2006) 99–107.

[5] S.H. Yeon, K.S. Lee, B. Sea, Y.I. Park, K.H. Lee, Application of pilot-scale membrane contactor hybrid system for removal of carbon dioxide from flue gas, J. Membr. Sci. 257 (2005) 156–160.

[6] S.P. Yan, M.X. Fang, W.F. Zhang, S.Y. Wang, Z.K. Xu, Z.Y. Luo, K.F. Cen, Experimental study on the separation of $CO_2$ from flue gas using hollow fiber membrane contactors without wetting, Fuel Process. Technol. 88 (2007) 501–511.

[7] S. Karoor, K.K. Sirkar, Gas absorption studies in microporous hollow fiber membrane modules, Ind. Eng. Chem. Res. 32 (1993) 674–684.

[8] Y. Lee, R.D. Noble, B.Y. Yeom, Y.I. Park, K.H. Lee, Analysis of $CO_2$ removal by hollow fiber membrane contactors, J. Membr. Sci. 194 (2001) 57–67.

[9] R. Wang, H.Y. Zhang, P.H.M. Feron, D.T. Liang, Influence of membrane wetting on $CO_2$ capture in microporous hollow fiber membrane contactors, Sep. Purif. Technol. 46 (2005) 33–40.

[10] P. Keshavarz, J. Fathikalajahi, S. Ayatollahi, Analysis of $CO_2$ separation and simulation of a partially wetted hollow fiber membrane contactor, J. Hazard. Mater. 152 (2008) 1237–1247.

[11] A. Bottino, G. Capannelli, A. Comite, R.D. Felice, R. Firpo, $CO_2$ removal from a gas stream by membrane contactor, Sep. Purif. Technol. 59 (2008) 85–90.

[12] M.H. Al-Marzouqi, M.H. El-Naas, S.A.M. Marzouk, M.A. Al-Zarooni, N. Abdullatif, R. Faiz, Modeling of $CO_2$ absorption in membrane contactors, Sep. Purif. Technol. 59 (2008) 286–293.

[13] A. Gabelman, S.T. Hwang, Hollow fiber membrane contactors, J. Membr. Sci. 159 (1999) 61–106.

[14] M.C. Yang, E.L. Cussler, Designing hollow-fiber contactors, AIChE. J. 32 (11) (1986) 1910–1916.

[15] R. Prasad, K.K. Sirkar, Dispersion-free solvent extraction with microporous hollow-fiber modules, AIChE J. 34 (1988) 177–188.

[16] S.R. Wickramasinghe, M.J. Semmens, E.L. Cussler, Mass transfer in various hollow fiber geometries, J. Membr. Sci. 69 (1992) 235–250.

[17] M. Mavroudi, S.P. Kaldis, G.P. Sakellaropoulos, A study of mass transfer resistance in membrane gas–liquid contacting processes, J. Membr. Sci. 272 (2006) 103–115.

[18] S.B. Iversen, V.K. Bhatia, K. Dam-Johansen, G. Jonsson, Characterization of microporous membranes for use in membrane contactors, J. Membr. Sci. 130 (1997) 205–217.

[19] J. Ingham, I.J. Dunn, E. Heinzle, J.E. Prenosil, Chemical engineering dynamics: an introduction to modeling and computer simulation, 2nd ed., Wiley-VCH, 2000.

[20] S. Atchariyawut, R. Jiraratananon, R. Wang, Separation of $CO_2$ from $CH_4$ by using gas–liquid membrane contacting process, J. Membr. Sci. 304 (2007) 163–172.

[21] S. Atchariyawut, C. Feng, R. Wang, R. Jiraratananon, D.T. Liang, Effect of membrane structure on mass-transfer in the membrane gas–liquid contacting process using microporous PVDF hollow fibers, J. Membr. Sci. 285 (2006) 272–281.

Journal of Membrane Science 322 (2008) 475–483

Contents lists available at ScienceDirect

Journal of Membrane Science

journal homepage: www.elsevier.com/locate/memsci

# A combined osmotic pressure and cake filtration model for crossflow nanofiltration of natural organic matter

Supatpong Mattaraj[a,*], Chalor Jarusutthirak[b], Ratana Jiraratananon[c]

[a] *Department of Chemical Engineering, Faculty of Engineering, Ubon Ratchathani University, Ubon Ratchathani 34190, Thailand*
[b] *Department of Chemistry, Faculty of Science, King Mongkut's Institute of Technology Ladkrabang, Bangkok 10520, Thailand*
[c] *Department of Chemical Engineering, Faculty of Engineering, King Mongkut's University of Technology Thonburi, Bangkok 10140, Thailand*

ARTICLE INFO

*Article history:*
Received 11 April 2008
Received in revised form 21 May 2008
Accepted 26 May 2008
Available online 7 July 2008

*Keywords:*
Cake filtration
Nanofiltration
Natural organic matter
Osmotic pressure

ABSTRACT

A combined osmotic pressure and cake filtration model for crossflow nanofiltration of natural organic matter (NOM) was developed and successfully used to determine model parameters (i.e. permeability reduction factor ($\eta$) and specific cake resistance ($\alpha_{cake}$)) for salt concentrations, NOM concentrations, and ionic strength of salt species ($Na^+$ and $Ca^{++}$). In the absence of NOM, with increasing salt concentration from 0.004 to 0.1 M, permeability reduction factor ($\eta$)) decreased from 0.99 to 0.72 and 0.94 to 0.44 for monovalent cation ($Na^+$) and divalent cation ($Ca^{++}$), respectively. This reduced membrane permeability was due to salt concentrations and salt species. In the presence of NOM, specific cake resistance tended to increase with increasing NOM concentration and ionic strength in the range of $0.85 \times 10^{15}$–$3.66 \times 10^{15}$ m kg$^{-1}$. Solutions containing divalent cation exhibited higher normalized flux decline ($J_v/J_{vo}$ = 0.685–0.632) and specific cake resistance ($\alpha_{cake}$ = $2.89 \times 10^{15}$–$6.24 \times 10^{15}$ m kg$^{-1}$) than those containing monovalent cation, indicating a highly compacted NOM accumulation, thus increased permeate flow resistance during NF filtration experiments. After membrane cleaning, divalent cation exhibited lower water flux recovery than monovalent cation, suggesting higher non-recoverable ($R_{non\text{-}rec}$) resistance than monovalent cation.

## 1. Introduction

Nanofiltration (NF) is widely increasing in the application of drinking water treatment due to high removal efficiency in natural organic matter (NOM), the disinfection by-product (DBP) precursors during chlorination process, and in water softening for removing divalent cations from natural waters [1]. Nanofiltration membranes have molecular weight cut-offs (MWCO) ranging between 300 and 1000 Da [2], while the performances of NF membranes lie between reverse osmosis (RO) membranes (high operating pressure from 1400 to 6800 kPa) and ultrafiltration (UF) membranes (low operating pressure from <70 to 500 kPa) [3]. The separation mechanism of NF membranes is described in terms of charge and sieving effect [4]. Sieving effect is related to solute size responsible for the rejection of uncharged solutes by NF membranes, while charge effect is influenced by the electrostatic interactions between the ion species/valence types and membrane charges, as explained by the Donnan exclusion phenomena [5].

Natural organic matter is considered as a major cause of membrane fouling during NF [6]. NOM components consist of a heterogeneous mixture of complex organic materials, including humic substances, low molecular weight (hydrophilic) acids, proteins, carbohydrates, carboxylic acids, amino acids, and hydrocarbons [7]. Humic substances, the predominant compounds of NOM in surface waters, are amorphous, acidic, yellow-to-brown in color, hydrophilic, and chemically complex polyelectrolytes with the molecular weights ranging from a few hundreds to tens of thousands [8]. They comprise a large fraction of the dissolved organic matter (DOM), typically 30–80% of dissolved organic carbon (DOC) [9]. Molecular weight ranges of aquatic humic substances are from 500 to 5000 [10]. The major functional groups include carboxylic acids, phenolic hydroxyl, carbonyl, and hydroxyl groups [9].

Solution chemistry (i.e. ionic strength, mono- and divalent cations) can influence membrane performance (i.e. solution flux decline and rejection [11]). Increased ionic strength can increase solution flux decline, while divalent cation has a greater flux decline than monovalent cation in membrane fouling [12]. Concentration of salt solutions by NF membranes can result in enhanced rejections depending on ion species [13]. Divalent cations have significant effects on membrane surface charge [14], thus affecting membrane performance. The rejections of divalent cation (calcium) and

---

* Corresponding author. Tel.: +66 45 353 344; fax: +66 45 353 333.
*E-mail addresses:* mattas@ubu.ac.th, supatpong.m@hotmail.com (S. Mattaraj), kjchalor@kmitl.ac.th (C. Jarusutthirak), ratana.jir@kmutt.ac.th (R. Jiraratananon).

0376-7388/$ – see front matter © 2008 Elsevier B.V. All rights reserved.
doi:10.1016/j.memsci.2008.05.049

monovalent cation (sodium) were reported to range approximately 13–96% and 10–87%, respectively [15].

In our previous work [16], we investigated different factors affecting crossflow nanofiltration performances in natural organic matter rejection and flux decline. Four mathematical models (i.e. pore blocking, pore constriction, intermediate, and cake formation) were used to interpret membrane performances of NF membrane. However, we could not apply those mathematical models for solutions having salt alone. This was possibly affected by osmotic pressure caused by high salt concentration at the membrane surface. In addition, solutions having NOM were significantly affected by cake formation, especially at high NOM concentration and ionic strength, while model parameters were not characterized for specific cake resistance. Therefore, this paper integrates mathematical models for osmotic pressure caused by salt solution and cake filtration model obtained from NOM solution during crossflow nanofiltration. The objective of this study was to determine model parameters, i.e. permeability reduction factor ($\eta$) based on osmotic pressure effect and specific cake resistance ($\alpha_{cake}$) using a combined osmotic pressure and cake filtration model. The results of this work could provide an evidence for changes in the model parameters as a function of salt concentrations, NOM concentrations, and ionic strength of salt species (sodium and calcium). The model parameters corresponded to the combination effects of osmotic pressure by salts/ion species that changed membrane permeability and cake formation caused by NOM accumulation at the membrane surface. The model parameters could give an insight interpretation of flux decline and rejection characteristics during crossflow NF of NOM with the presence of salts. The effects of ion species/valence types were investigated to compare solution flux curves with different solution chemistry.

## 2. Theory

### 2.1. Mass balance

The overall system mass balance model can be determined based on the bench-scale crossflow NF test cell with a recycle loop [16]. It is described as a completely stirred tank reactor (CSTR). The mass balance can be written as follows:

$$V_{sys}\frac{dC_{reten}}{dt} = Q_{feed}C_{feed} - Q_{reten}C_{reten} - Q_{perm}C_{perm} - k_a(C_{ss} - C_{reten}) \times V_{sys} \qquad (1)$$

where $V_{sys}$ is the system volume (about 72 mL); $Q$ and $C$ are the subscriptions for flow and concentration in the feed line (feed), in the retentate line (reten), and in the permeate line (perm); $C_{ss}$ is the steady-state concentration in the retentate line; $k_a$ is the overall mass transfer coefficient (min$^{-1}$) (= $k_1a_s$); $k_1$ is the mass transfer coefficient (m s$^{-1}$) equaling to the ratio between salt diffusion coefficient ($D$) and boundary layer thickness ($\delta$); $a_s$ is the volumetric specific surface area (m$^2$ m$^{-3}$) that equals to the ratio between the effective membrane surface area and the system volume; $t$ is the operating time (min). The units of flow and concentration are mL min$^{-1}$ and mg L$^{-1}$ or mol L$^{-1}$, respectively, depending on solution types. Using a fourth-order Runge–Kutta routine, the overall mass transfer coefficient and the steady-state concentration were varied to minimize the sum of squared error (SSE) for each feed solution.

### 2.2. Solution flux

Solution flux can be determined as a function of membrane permeability, $L_p$ (LMH kPa$^{-1}$), and the net transmembrane pressure gradient ($\Delta P - \sigma\Delta\pi$) (kPa), while the non-recoverable fouling occurs in many instances during filtration, imparting an additional resistance to solution flux [3]:

$$J_v = L_p(\Delta P - \sigma\Delta\pi) = \frac{(\Delta P - \sigma\Delta\pi)}{\mu(R_m + R_{non\text{-}rec})} \qquad (2)$$

where $J_v$ is the solution flux (L m$^{-2}$ h$^{-1}$, LMH); $\Delta P$ is the averaged transmembrane pressure (kPa); $\sigma$ is the osmotic reflection coefficient (estimated by the intrinsic membrane rejection, $R_{mem} = 1 - C_{perm}/C_{mem}$); $C_{mem}$ is the concentration at the membrane surface; $\Delta\pi$ is the difference in osmotic pressure of the solution at the membrane and in permeate line, $\Delta\pi = \pi_{mem} - \pi_{perm}$ (kPa); $R_m$ is the membrane hydraulic resistance (m$^{-1}$); and $R_{non\text{-}rec}$ is the non-recoverable resistance occurring during filtration (m$^{-1}$); and $\mu$ is the dynamic viscosity (kg m$^{-1}$ s$^{-1}$).

Under constant-pressure operation, and assuming constant membrane permeability and in the absence of NOM cake on membrane surface, the change in solution flux is related to the change in osmotic pressure as a result of solute accumulation at the membrane surface:

$$\frac{dJ_v}{dt} = -\frac{\sigma}{\mu(R_m + R_{non\text{-}rec})}\frac{d\Delta\pi}{dt} \qquad (3)$$

The osmotic pressure is directly related to salt concentration, with $\pi$ (kPa) = $\alpha C$ (mol L$^{-1}$), where $\alpha$ = 4814.5 (NaCl) [3] and $\alpha$ = 7418.8 ($CaCl_2$) at 25 °C (calculated using Van't Hoff equation). The permeate concentration is correlated to the concentration at the membrane surface by the rejection, $C_{perm} = (1 - R_{mem})C_{mem}$. Making these substitutions,

$$\begin{aligned}\frac{dJ_v}{dt} &= -\frac{\sigma\alpha}{\mu(R_m + R_{non\text{-}rec})}\left(\frac{dC_{mem}}{dt} - \frac{dC_{perm}}{dt}\right)\\ &= -\frac{\sigma\alpha R_{mem}}{\mu(R_m + R_{non\text{-}rec})}\left(\frac{dC_{mem}}{dt}\right)\end{aligned} \qquad (4)$$

The interface concentration ($C_{mem}$) is calculated from $\sigma\Delta\pi = \sigma(\pi_{mem} - \pi_{perm})$ under steady-state condition. The value of $\sigma$ is assumed to be equal to the intrinsic rejection for each salt concentration. From the experiments, the ratio $\beta = C_{mem}/C_{reten}$ (salt concentration polarization) is related to salt concentration. Taking this parameter in the above equation and having an additional term of permeability reduction factor due to the effect of salt ($\eta$), the change in solution flux with time can be rewritten as follows:

$$\frac{dJ_v}{dt} = -\eta\frac{\sigma\alpha R_{mem}\beta}{\mu(R_m + R_{non\text{-}rec})}\left(\frac{dC_{reten}}{dt}\right) \qquad (5)$$

where $\eta(1/\mu(R_m + R_{non\text{-}rec})) = \eta L_p = L_{p,s} = (1/\mu(R_{m,s} + R_{non\text{-}rec}))$ ($L_{p,s}$ is the membrane permeability in the presence of salt solution). The membrane resistance in the presence of salt ($R_{m,s}$) including the permeability reduction factor can be determined as follows:

$$R_{m,s} = \frac{R_m + (1 - \eta)R_{non\text{-}rec}}{\eta} \qquad (6)$$

In Eq. (5), the change in the retentate concentration with time can be calculated from the mass balance as described in Eq. (1).

### 2.3. Combined osmotic pressure and cake filtration model

A combined osmotic pressure and cake filtration model can be developed to describe the nanofiltration performance of a solution containing both salt and NOM. From the previous work, the fouling of nanofiltration membranes can be described by cake filtration model [17,18]. The model has also been used to describe flux in ultrafiltration and microfiltration [19,20]. The cake filtration model incorporates an additional term of cake resistance ($R_c$) as follows:

$$J_v = \frac{(\Delta P - \sigma \Delta \pi)}{\mu(R_{m,s} + R_{non\text{-}rec} + R_c)} \qquad (7)$$

In our work, we describe the combination effects of osmotic pressure and cake with the change in solution flux as a function of time. The change in solution flux is related to the change in osmotic pressure as a result of salt concentration polarization, and the change in the hydraulic resistance of the NOM cake formed on the membrane surface:

$$\frac{dJ_v}{dt} = -\frac{\sigma_s \alpha_s R_{mem,s} \beta_s}{\mu(R_{m,s} + R_{non\text{-}rec} + R_c)}\left(\frac{dC_{reten,s}}{dt}\right) - \frac{J_v}{(R_{m,s} + R_{non\text{-}rec} + R_c)}\left(\frac{dR_c}{dt}\right) \qquad (8)$$

Therefore, Eq. (8) is the combined osmotic pressure and cake filtration model for crossflow nanofiltration. The subscript s refers to salt species (i.e. NaCl or $CaCl_2$). In the results, normalized solution flux ($J_v/J_{vo}$) is determined by the ratio between solution flux ($J_v$) and an initial solution flux ($J_{vo}$). In the cake filtration with constant specific cake resistance ($\alpha_{cake}$), the change in cake resistance is related to the rate of change in cake mass, $m_{cake}$ (kg), which equals to the net rate of mass transport towards the membrane surface, i.e., the convective flux, $J_v$, minus the effective flux, $J^*$ (LMH), associated with back-transport resulting from crossflow. Therefore,

$$\frac{dR_c}{dt} = \alpha_{cake}\frac{dm_{cake}}{A_m dt} = \alpha_{cake} C_{reten,NOM}(t)(J_v - J^*) \qquad (9)$$

where $\alpha_{cake}$ is the specific cake resistance (m $kg^{-1}$), $C_{reten,NOM}$ is the NOM concentration in the retentate line (kg $m^{-3}$) and $A_m$ is the membrane area ($m^2$). The specific cake resistance, as predicted by the Carman–Kozeny equation, can be determined as a function of cake porosity ($\varepsilon_{cake}$) (–), density ($\rho$) (kg $m^{-3}$), particle diameter ($d_p$) (m) as follows [21]:

$$\alpha_{cake} = \left(\frac{180(1-\varepsilon_{cake})^2}{\rho d_p^2 \varepsilon_{cake}^3}\right) \qquad (10)$$

Eqs. (8) and (9) can be determined using the fitting parameters (i.e. specific cake resistance and the effective back-transport flux) in a fourth-order Runge–Kutta routine in order to minimize the sum squared errors between the experimental data and estimated data from cake filtration model. In this work, the combined osmotic pressure and cake filtration model (Eq. (8)) was applied with the experimental results in order to determine model parameters with different solution conditions.

## 3. Experimental

### 3.1. Natural organic matter (NOM) and Isolation

Natural organic matter, obtained from the surface water reservoir at Ubon Ratchathani's University (UBU), Thailand, was isolated by using a polyamide thin-film composite (TFC) reverse osmosis membrane (model: AG4040F-spiral wound crossflow, GE osmonics, USA). The isolation procedure was previously described by Jarusutthirak et al. [16] and by Kilduff et al. [22]. Natural water characteristics were previously shown by Jarusutthirak et al. [16]. The feed solutions for NF experiments were prepared by mixing NOM isolates and/or salts with deionized water to obtain the required concentrations.

### 3.2. Crossflow nanofiltration experiments

Crossflow nanofiltration experiments were carried out by using a bench-scale crossflow nanofiltration test cell with a recycle loop [12,16]. The system volume ($V_{sys}$) was approximately 72 mL. This was obtained by a tracer study characterized with the dispersion and tanks-in-series model as described by Levenspiel [23]. Thin-film nanofiltration membrane, obtained from GE Osmonics, Inc., USA, was used to investigate flux decline and rejection characteristics during NF experiments. The membrane information and filtration procedure was previously reported by Jarusutthirak et al. [16]. Membrane sheets were cleaned and pre-compacted with initial water flux of 45 LMH. After membrane compaction, average membrane permeability ($L_p$) was approximately $4.152 \times 10^{-8} \pm 0.062 \times 10^{-8}$ m $s^{-1}$ $kPa^{-1}$(0.149 LMH $kPa^{-1}$, number of samples are 16 samples) (95% confidence interval) at 25 °C. The membrane hydraulic resistance ($R_m = 1/\mu L_p$) was also determined to be $2.694 \times 10^{13}$ $m^{-1}$ (at 25 °C). The nanofiltration sheets were stored in 1% $Na_2S_2O_5$ and kept in a refrigerator (4 °C) to minimize bacterial activity.

### 3.3. Analytical methods

NOM concentrations were measured as dissolved organic matter using total organic carbon analyzer (Shimadzu corporation, TOC-VCPH model, Japan). Standard solutions were prepared using potassium hydrogen phthalate in deionized water, which was used as a blank. UV absorbance was measured using a UV–vis spectrophotometer (Shimadzu corporation, model UV mini 1240, Japan). Conductivity and solution pH were measured using conductivity meter (model: inoLab cond Level 2, Germany) and pH meter (model: inoLab pH level 1, Wissenschaftlich-Technische Werkstatten, GMBH, Germany), respectively. Ionic strength of samples was calculated using a correlation between conductivity and ionic strength; for NaCl standards, I.S. (mol $L^{-1}$) = $0.5\Sigma C_i Z_i^2 = 9.5 \times 10^{-6}$ (μS $cm^{-1}$) and for $CaCl_2$ standard, I.S. (mol $L^{-1}$) = $1.429 \times 10^{-5}$ (μS $cm^{-1}$).

### 3.4. Membrane cleaning

After filtration was terminated, two steps of cleaning, i.e. hydrodynamic cleaning followed by chemical cleaning, were performed: first, for hydrodynamic cleaning, DI water was recirculated in the recycle loop for 30 min with a crossflow velocity of 0.25 m/s, which was higher than that during filtration operation. For chemical cleaning, alkaline solution (using NaOH) with pH of 10 was first used to recirculate in the system, and followed with acidic solution (using HCl) with pH of 3 at a crossflow velocity of 0.25 m/s for 30 min each. After each cleaning, water fluxes with different operating pressures were measured to determine water flux recovery.

## 4. Results and discussion

### 4.1. Effect of NaCl concentration on normalized solution flux and model parameter

Fig. 1 illustrates the effect of NaCl concentration on normalized solution flux. Dot points were the experimental data, while the solid lines were the values obtained from the mathematical model (Eq. (5)). Normalized solution flux curve decreased with increasing NaCl concentration. The reason for a flux decline was an increase of the osmotic pressure of the retentate as its concentration was increased due to a continuous removal of the

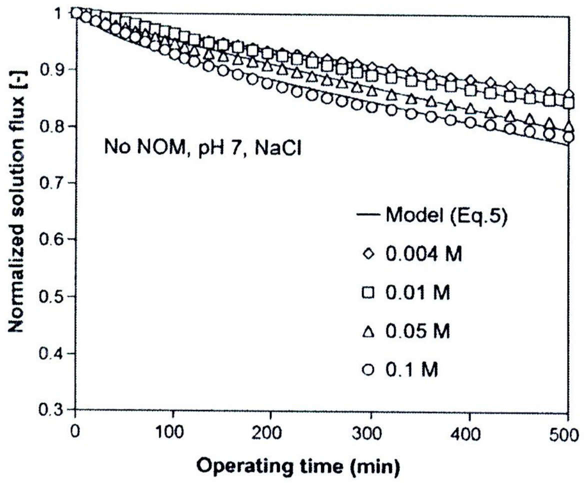

Fig. 1. Effect of NaCl concentration on normalized solution flux.

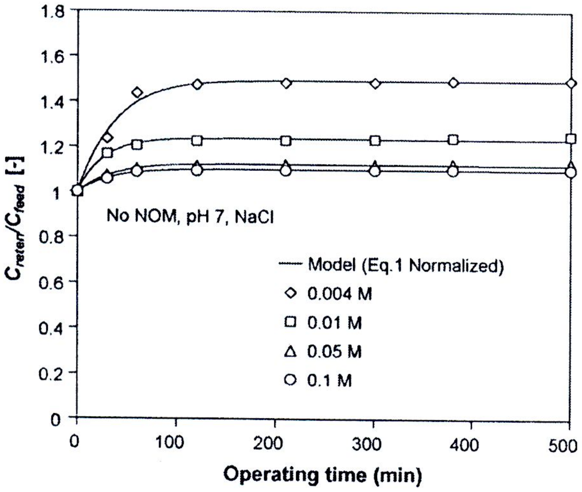

Fig. 2. Normalized retentate salt concentrations during NF operation.

permeate. Permeability reduction factor ($\eta$) was the model parameter fitted to the experimental data (based on Eq. (5)). Table 1 shows model parameters and nanofiltration performance at different initial salt concentrations. In the absence of NOM and pH of 7, increased NaCl concentrations from 0.004 to 0.1 M reduced normalized flux and permeability reduction factor from 0.864 to 0.788 and 0.99 to 0.72, respectively. This was possibly caused by the increased osmotic pressure as mentioned earlier. Fig. 2 exhibits normalized retentate salt concentrations in a recycle loop with different initial salt concentrations. The solid lines shown in the figure were determined using the mass balance (Eq. (1)). The lines were the ratio between retentate salt concentrations and feed salt concentrations. It was observed that normalized retentate salt concentrations decreased with increasing feed salt concentrations, possibly caused by the effect of salt rejection. Increased salt concentrations from 0.004 to 0.1 M tended to decrease the retentate salt rejections from 35.8% to 10% along with filtration period (see Table 1). The results suggested that the effect of ions at the membrane–solution interface enhanced a reduction of electrical double layer thickness, thus allowing salt passage through the membrane surface. Negatively charged chloride ion was possibly repelled from the negatively charged membrane, while positively charged sodium ion was attracted to the membrane surface, indicating increased ion concentration in the membrane matrix and increased screening of charge moieties [24]. This can enhance the changes in the membrane pore size due to polymer matrix compaction. This corresponded to reduced permeability reduction factor (decreased membrane permeability). With increasing salt concentration from 0.004 to 0.1 M, the intrinsic membrane rejection decreased from 44.2% to 18%, while the salt concentration polarization ($\beta$) decreased from 1.149 to 1.097. Similar trends were observed with the results from Fig. 2. The ratios of $J_v/k_1$ were relatively constant about 0.318–0.3. The permeability reduction factors ($\eta$) decreased from 0.99 to 0.72, indicating higher values than those of tight polyamide NF-70 membrane, previously studied by Kilduff et al. [3]. They reported that the permeability reduction factors ($\eta$) decreased from 0.96 to 0.52 with increasing salt concentration from 0.004 to 0.1 M NaCl. In addition, the averaged mass transfer coefficient of $3.39 \times 10^{-5}$ m s$^{-1}$ showed a higher value than that of the tight polyamide NF-70 membrane ($1.6 \times 10^{-5}$ m s$^{-1}$) determined using the same mass balance (Eq. (1)). This indicated less boundary layer thickness ($\delta$) of salt solution for the loose NF membrane than that for the tight NF membrane. For the tight NF membrane, the intrinsic membrane rejection showed higher values than those of the loose NF membrane. The rejections decreased from 90% to 72.5% with increasing salt concentration from 0.004 to 0.1 M NaCl.

**Table 1**

Model parameters and nanofiltration performance at different salt concentrations

| Parameters | NaCl concentration (M) | | | |
|---|---|---|---|---|
| | 0.004 | 0.01 | 0.05 | 0.1 |
| $J_v/J_{vo}$ (–) | 0.864 | 0.848 | 0.808 | 0.788 |
| $J_v \times 10^6$ (m s$^{-1}$) | 10.8 | 10.6 | 10.1 | 9.85 |
| $C_{mem}$ (M) | 0.0077 | 0.0162 | 0.0653 | 0.1216 |
| $C_{reten}$ (M) | 0.0067 | 0.0143 | 0.0589 | 0.1108 |
| $C_{perm}$ (M) | 0.0043 | 0.0112 | 0.0513 | 0.0997 |
| $\beta$ ($C_{mem}/C_{reten}$) | 1.149 | 1.133 | 1.109 | 1.097 |
| $R_{feed}$ (%) | 5.6–18.0 (6.9) | 2.2–5.8 (3.5) | 1.4–5.9 (3.7) | 0.1–3.0 (1.6) |
| $R_{reten}$ (%) | 33.6–38.0 (35.8) | 19.3–22.0 (21.4) | 12.3–14.4 (12.9) | 8.1–10.6 (10.0) |
| $R_{mem}$ (%) | 44.2 | 30.9 | 21.4 | 18.0 |
| $\eta$ | 0.99 | 0.94 | 0.78 | 0.72 |
| $\eta L_p$ (m s$^{-1}$ kPa$^{-1}$) × $10^8$ | 4.11 | 3.92 | 3.24 | 2.98 |
| $k_1$ (m s$^{-1}$) × $10^5$ | 3.60 | 3.36 | 3.32 | 3.28 |
| $J_v/k_1$ | 0.318 | 0.315 | 0.304 | 0.30 |
| Average $k_1$ (m s$^{-1}$) | $3.39 \times 10^{-5}$ | | | |

Operating conditions: initial flux = $1.25 \times 10^{-5}$ m s$^{-1}$, crossflow velocity = 0.1 m s$^{-1}$, recovery = 0.85, temperature = 25 °C. Average membrane permeability ($L_p$) was $4.152 \times 10^{-8} \pm 0.062 \times 10^{-8}$ m s$^{-1}$ kPa$^{-1}$ (0.149 LMH kPa$^{-1}$). The values in the parenthesis are the averaged rejections.

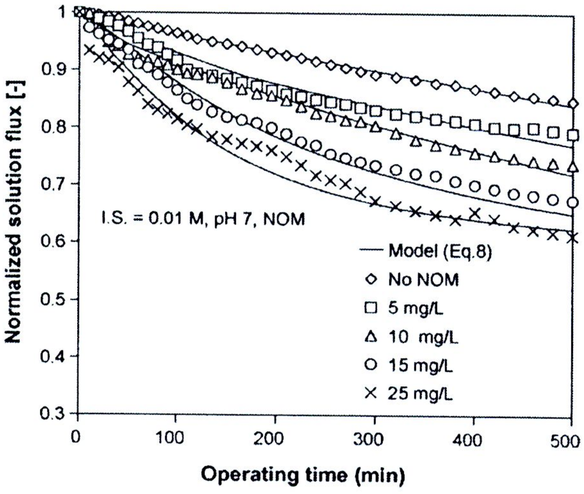

**Fig. 3.** Effect of NOM concentration on normalized solution flux.

### 4.2. *Effect of NOM concentration on normalized solution flux and model parameter*

Fig. 3 shows the effect of NOM concentration on normalized solution flux. Dot points were the experimental data, while the solid lines were followed with the combined osmotic pressure and cake filtration model (Eq. (8)). NOM concentration ranged from 0 to 25 mg $L^{-1}$ with ionic strength of 0.01 M NaCl and solution pH of 7. Model parameters and nanofiltration performance on the influence of NOM concentration are tabulated in Table 2. In the absence of NOM, normalized solution flux decreased based on the effect of osmotic pressure caused by increased salt concentration at the membrane surface. At the ionic strength of 0.01 M and pH of 7, normalized solution flux and retentate salt rejection were approximately 0.848 and 21.4%, respectively. In the presence of NOM, normalized solution flux tended to decrease from 0.793 to 0.614 with increasing NOM concentration from 5 to 25 mg $L^{-1}$, while the retentate salt rejection slightly increased from 25.3% to 28.2%. In the similar trend, increased NOM concentration from 5 to 25 mg $L^{-1}$ increased the feed and retentate NOM rejections from 75.3% to 88.4% and 94.3% to 97.1%, respectively. Solutions having high NOM concentration of 25 mg $L^{-1}$ resulted in the highest rejection of salt and NOM rejection in the feed and retentate line, possibly due to combination effects of osmotic pressure by salt concentration and cake formation by NOM accumulation. The experimental results suggest the reduction of charge repulsion due to charge interaction between negatively charged NOM and positively charged sodium ion, causing NOM cake formation at the membrane surface. In addition, the negatively charged NOM molecules can be repelled from the membrane surface, indicating an increase in the averaged feed and retentate rejections of NOM. With the constant membrane resistance in the presence of salt ($R_{m,s}$), the fitted parameters (i.e. the specific cake resistance, $\alpha_{cake}$ and the effective flux, $J^*$), can be obtained using the combined osmotic pressure and cake filtration model (Eq. (8)). From the table, increased NOM concentration ranging from 5 to 25 mg $L^{-1}$ increased specific cake resistance from $0.89 \times 10^{15}$ to $3.66 \times 10^{15}$ m $kg^{-1}$ (increased by 75.7%), while the effective flux tended to decrease with increasing NOM concentration as shown in Fig. 4. The increase in specific cake resistance can be explained by a decrease in cake porosity with increasing NOM concentration, causing more compacted NOM accumulation at the membrane surface. This could be explained using Eq. (10). The specific cake resistance can be sensitive to changes in solution properties. The membrane used in this study resulted in lower specific cake resistance and flux decline than that of the tight polyamide NF-70 membrane [3]. This suggests that membrane properties have significant effects on changes in solution flux due to the combination effects of osmotic pressure by salt concentration and NOM cake formation at the membrane surface.

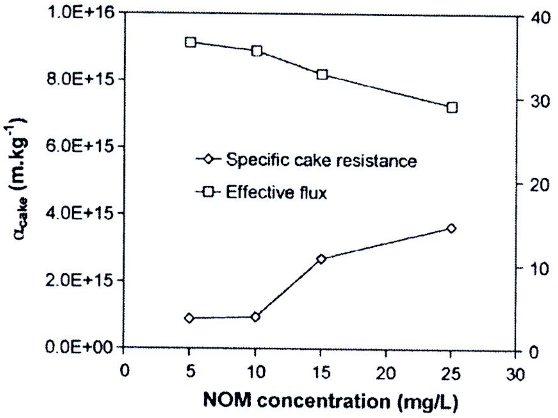

**Fig. 4.** Effect of NOM concentration on specific cake resistance and effective flux.

### 4.3. *Effect of ionic strength on normalized solution flux in the presence of NOM*

Solutions having constant 10 mg $L^{-1}$ NOM and pH of 7 were investigated at different ionic strengths. Fig. 5 shows the effect of ionic strength on normalized solution flux. Dot points were the experimental data while the solid lines were fitted well with the combined osmotic pressure and cake filtration model (Eq. (8)). Model parameters and nanofiltration performance on the effect of ionic strength are tabulated in Table 3. With increasing ionic strength from 0.004 to 0.1 M NaCl, normalized solution flux decreased from 0.763 to 0.69. The increase in ionic strength

**Table 2**
Model parameters and nanofiltration performance: effect of NOM concentration

| Parameters | NOM concentration (mg $L^{-1}$) | | | |
|---|---|---|---|---|
| | 5 | 10 | 15 | 25 |
| $J_v/J_{vo}$ (–) | 0.793 | 0.739 | 0.676 | 0.614 |
| $J_v \times 10^6$ (m $s^{-1}$) | 9.9 | 9.2 | 8.5 | 7.7 |
| $R_{feed,s}$ (%) | 3.6–5.2 (4.3) | 4.2–9.1 (5.4) | 2.7–12.2 (4.6) | 4.2–11.6 (5.7) |
| $R_{reten,s}$ (%) | 24.6–27.0 (26.3) | 24.3–26.5 (25.3) | 22.9–27.6 (25.4) | 23.5–30.5 (28.2) |
| $R_{feed,NOM}$ (%) | 74.4–77.3 (75.3) | 76.4–81.0 (78.5) | 75.1–83.9 (77.7) | 87.0–91.1 (88.4) |
| $R_{reten,NOM}$ (%) | 92.5–94.9 (94.3) | 92.7–95.8 (94.9) | 93.3–95.9 (95.0) | 96.0–97.6 (97.1) |
| $\alpha_{cake}$ (m $kg^{-1}$) $\times 10^{-15}$ | 0.89 | 0.95 | 2.70 | 3.66 |
| $J^* \times 10^6$ (m $s^{-1}$) | 10.1 | 9.9 | 9.1 | 8.1 |

The values in the parenthesis are the averaged rejections.

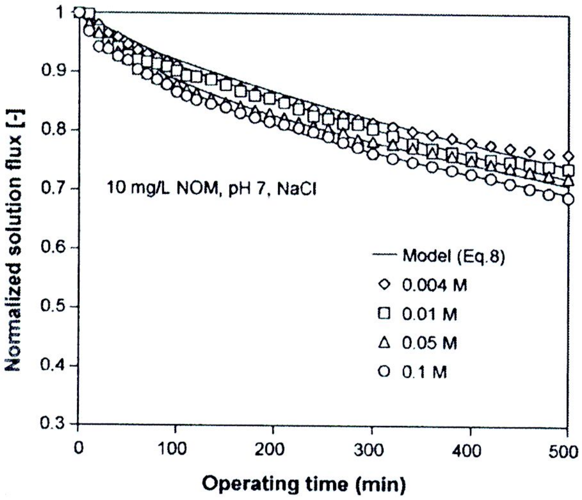

**Fig. 5.** Effect of ionic strength on normalized solution flux.

decreased the salt rejection, indicating charge screening at the membrane surface, thus increased salt passage through the membrane. The feed and retentate salt rejections decreased from 9.6% to 1.7% and from 28.4% to 11.2%, respectively. Braghetta et al. [24] explained that increased ionic strength would normalize charge at the membrane surface (sulfonated polysulfone NF membrane) and compressed a double layer thickness (i.e. membrane compaction occurred). Solutions having NOM showed higher salt rejection than those having no NOM, especially at high ionic strength. This was caused by reduced charge repulsion between positively charged $Na^+$ and negatively charged NOM. The NOM rejections in the feed ($R_{\mathrm{feed,NOM}}$) and retentate line ($R_{\mathrm{reten,NOM}}$) reduced from 78.5% to 64.7% and 95.3% to 91.3% with increasing ionic strengths. This suggests the changes in NOM configuration due to reduced charge repulsion between ionized functional groups on NOM molecules. Previous study suggested that NOM molecules are configured more as rigid, compact, and spherocolloidal macromolecules (small hydrodynamic radius) at low pH and high ionic strength or high NOM concentration [25]. This can enhance the passage of the spherocolloidal NOM molecules through the membrane surface, thus decreased NOM rejection. Based on the combined osmotic pressure and cake filtration model, the specific cake resistance increased from $0.85 \times 10^{15}$ to $2.73 \times 10^{15}\,\mathrm{m\,kg^{-1}}$ (increased by about 69%) with increasing ionic strengths from 0.004 to 0.1 M NaCl. The experimental results were possibly explained by reduced charge repulsion between NOM molecules, resulting in more densely compacted NOM layer, thus decreased cake porosity at the membrane surface.

### *4.4. Effect of divalent cations on normalized solution flux in the presence of NOM*

Divalent cation (i.e. $Ca^{++}$) can significantly influence membrane fouling on NF membrane [1,11]. Fig. 6 shows the effect of divalent cation on normalized solution flux. Solid lines are model fitted to the experimental data, represented as dot points. Model parameters and nanofiltration performance due to the effect of divalent cation are tabulated in Table 4. Solutions containing $10\,\mathrm{mg\,L^{-1}}$ NOM and pH of 7 were tested with different ionic strengths using calcium chloride. It was observed that increased ionic strengths from 0.004 to 0.1 M $CaCl_2$ decreased normalized solution flux from 0.685 to 0.632 (at 8-h operation). The salt rejections increased with increasing ionic strengths using calcium chloride. The averaged salt rejections in the feed and retentate line were about 4.7–11.3% and 24.2–37.9%, respectively. These showed higher salt rejections than those of NaCl solution, indicating calcium-NOM accumulation on the membrane surface. The permeability reduc-

**Table 3**
Model parameters and nanofiltration performance: effect of ionic strength

| Parameters | Ionic strength (M) | | | |
|---|---|---|---|---|
| | 0.004 | 0.01 | 0.05 | 0.1 |
| $J_v/J_{vo}$ (–) | 0.763 | 0.739 | 0.723 | 0.69 |
| $J_v \times 10^6$ ($\mathrm{m\,s^{-1}}$) | 9.5 | 9.2 | 9.0 | 8.6 |
| $R_{\mathrm{feed,s}}$ (%) | 7.1–19.2 (9.6) | 4.2–9.1 (5.4) | 0.6–8.7 (2.7) | 0.1–10.0 (1.7) |
| $R_{\mathrm{reten,s}}$ (%) | 27.0–31.9 (28.4) | 24.3–26.5 (25.3) | 12.1–15.9 (13.7) | 10.2–15.9 (11.2) |
| $R_{\mathrm{feed,NOM}}$ (%) | 75.9–82.1 (78.0) | 76.4–81.0 (78.5) | 76.3–81.3 (77.9) | 61.6–72.5 (64.7) |
| $R_{\mathrm{reten,NOM}}$ (%) | 93.4–96.0 (95.2) | 92.7–95.8 (94.9) | 92.3–96.4 (95.3) | 89.5–92.2 (91.3) |
| $\alpha_{\mathrm{cake}}$ ($\mathrm{m\,kg^{-1}}$) $\times 10^{-15}$ | 0.85 | 0.95 | 1.53 | 2.73 |
| $J^* \times 10^6$ ($\mathrm{m\,s^{-1}}$) | 9.93 | 9.9 | 9.4 | 8.99 |

The values in the parenthesis are the averaged rejections.

**Table 4**
Model parameters and nanofiltration performance: effect of divalent cation

| Parameter | $CaCl_2$ concentration (M) | | | |
|---|---|---|---|---|
| | 0.004 | 0.01 | 0.05 | 0.1 |
| $J_v/J_{vo}$ (–) | 0.685 | 0.664 | 0.648 | 0.632 |
| $J_v \times 10^6$ ($\mathrm{m\,s^{-1}}$) | 8.56 | 8.30 | 8.10 | 7.90 |
| $R_{\mathrm{feed,s}}$ (%) | 1.5–13.8 (5.2) | 2.3–9.2 (4.7) | 7.3–20.6 (11.3) | 7.9–22.0 (9.9) |
| $R_{\mathrm{reten,s}}$ (%) | 21.4–31.8 (30.9) | 23.2–26.2 (24.2) | 37.9–38.5 (37.9) | 35.3–39.6 (37.8) |
| $\beta$ ($C_{\mathrm{mem}}/C_{\mathrm{reten}}$) | 1.272 | 1.217 | 1.049 | 1.036 |
| $R_{\mathrm{feed,NOM}}$ (%) | 66.4–78.3 (69.9) | 79.5–84.7 (82.3) | 80.9–84.0 (82.0) | 75.7–79.9 (77.3) |
| $R_{\mathrm{reten,NOM}}$ (%) | 91.1–96.2 (94.4) | 95.1–97.7 (97.0) | 93.4–96.6 (95.7) | 90.6–96.1 (94.4) |
| $\eta$ | 0.94 | 0.76 | 0.61 | 0.44 |
| $\eta L_p$ ($\mathrm{m\,s^{-1}\,kPa^{-1}}$) $\times 10^8$ | 3.90 | 3.16 | 2.53 | 1.83 |
| $\alpha_{\mathrm{cake}}$ ($\mathrm{m\,kg^{-1}}$) $\times 10^{-15}$ | 2.89 | 3.52 | 5.14 | 6.24 |
| $J^* \times 10^6$ ($\mathrm{m\,s^{-1}}$) | 9.12 | 9.02 | 8.86 | 8.57 |

The values in the parenthesis are the averaged rejections.

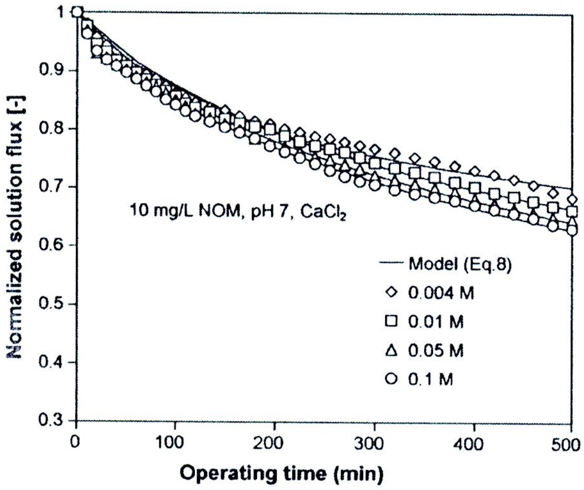

**Fig. 6.** Effect of divalent cation on normalized solution flux.

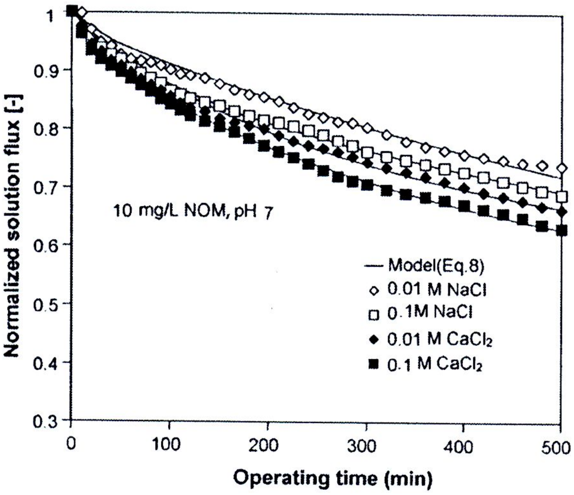

**Fig. 7.** Effect of mono- and divalent cations on normalized solution flux.

tion factor ($\eta$) decreased from 0.94 to 0.44 with increasing ionic strengths. This was possibly caused by reduced charge repulsion between positively charged $Ca^{++}$ ion and negatively charged NF membrane, thus compressing a double layer thickness at the membrane surface. Previous study found that divalent cation caused a marked effect on membrane surface charge [14]. With increasing ionic strengths, averaged NOM rejections in the feed and retentate increased from 69.9% to 82.3% and 94.4% to 97%, respectively. This showed the opposite trend with increasing ionic strengths using monovalent ($Na^+$) ion, where a change in NOM configuration could dominate the rejection results. The rejections obtained from the divalent cation illustrated relatively high rejections compared with monovalent ($Na^+$) ion. This resulted in the opposite effect from monovalent ($Na^+$) ion. This was possibly caused by the dominant effect from a compacted NOM cake formation by decreased charge repulsion between positively charged $Ca^{++}$ ion and negatively charged NOM molecules, thus enhancing NOM accumulation. This corresponds to high specific cake resistance ($\alpha_{cake}$) about $2.89 \times 10^{15}$–$6.24 \times 10^{15}$ m kg$^{-1}$, respectively (increased by 53.7%). The increase in specific cake resistance could decrease cake porosity, suggesting a densely packed NOM cake layer at the membrane surface. Schafer et al. [1] confirmed that higher calcium concentration caused severe NF fouling and increased non-recoverable fouling. Previous study explained that calcium act with humic carboxyl functional group, suggesting a reduction of NOM charge and electrostatic repulsion between humic macromolecules [11].

Mono- and divalent cations can influence nanofiltration performance (i.e. solution flux and rejection). The model parameters (i.e. permeability reduction factor and specific cake resistance) can be evaluated with the combined osmotic pressure and cake filtration model (Eq. (8)). This describes the effect of osmotic pressure caused by increased salt concentration polarization, while the effects of cake formation model are based on NOM cake formation at the membrane surface. Fig. 7 exhibits the effect of mono- and divalent cations on normalized solution flux. With similar ionic strengths, solutions having divalent $Ca^{++}$ cation showed greater solution flux decline than those having monovalent $Na^+$ cation. This suggested that divalent cation had greater effects on charge combination between membrane surface charge and NOM macromolecules than monovalent cation. This could cause higher salt and NOM rejections (previously described). In addition, model parameters could be changed with different ion species. Fig. 8 exhibits the effect of mono- and divalent cations on permeability reduction factor (filled symbols) and specific cake resistance (open symbols). Increased ionic strengths from 0.004 to 0.1 M using mono- and divalent cations tended to decrease the permeability reduction factor and to increase the specific cake resistance. Divalent $Ca^{++}$ cation showed greater values of permeability reduction factor and specific cake resistance than monovalent $Na^+$ cation. The decreases in permeability reduction factors of mono- and divalent cations were determined to be 0.99–0.72 and 0.94–0.44, respectively. The increases in specific cake resistance of mono- and divalent cations were about $0.85 \times 10^{15}$–$2.73 \times 10^{15}$ and $2.89 \times 10^{15}$–$6.24 \times 10^{15}$ m kg$^{-1}$, respectively. The experimental results indicated that divalent cation has a marked effect on reduced charge repulsion between positively charged divalent cation ($Ca^{++}$) and negatively charged NF membrane, causing a reduced double layer thickness at the membrane surface. This corresponds to lower permeability reduction factor with increasing ionic strengths. Divalent cation influenced an increase in cake formation on the membrane surface. This was caused by a reduction of charge repulsion between NOM molecules by increasing positive calcium ion concentrations. This resulted in an increase in specific cake resistance with increasing ionic strengths.

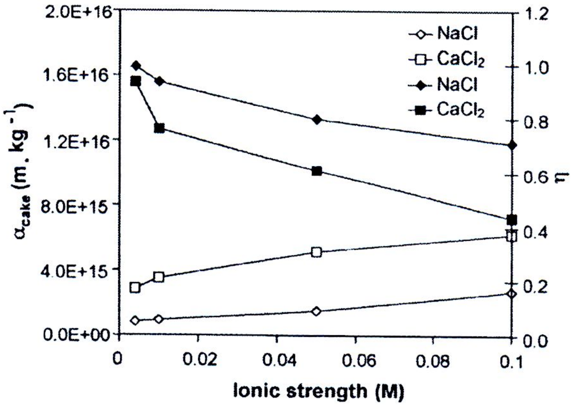

**Fig. 8.** Effect of mono- and divalent cations on $\eta$ (filled symbols) and $\alpha_{cake}$ (open symbols).

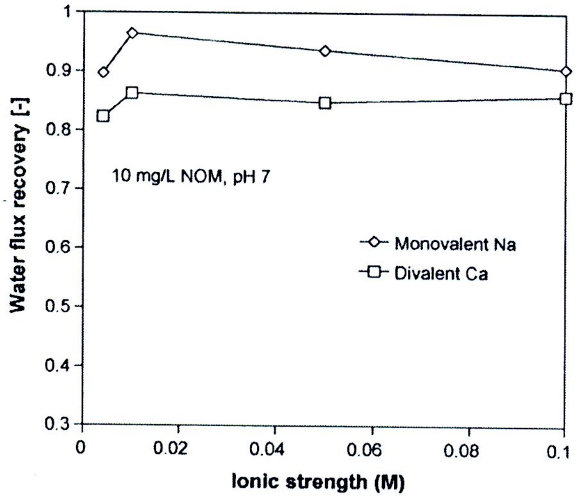

**Fig. 9.** Water flux recovery after chemical cleaning for mono- and divalent cations.

### 4.5. Water flux recovery

Fig. 9 describes water flux recovery after chemical cleaning for mono- and divalent cations. The experimental results were taken after hydrodynamic and chemical cleaning of NOM solution. It was observed that water flux recovery was less than 1 for different salt species ($Na^+$ and $Ca^{++}$). This suggested different interactions between NOM–salt species and the membrane, causing non-recoverable resistance ($R_{\text{non-rec}}$) on the membrane surface. With increasing ionic strength from 0.004 to 0.1 M, non-recoverable resistances for monovalent $Na^+$ cation were approximately $2.91 \times 10^{12}$, $1.06 \times 10^{12}$, $1.85 \times 10^{12}$, and $2.58 \times 10^{12}$, respectively. For divalent $Ca^{++}$ cation, non-recoverable resistances were about $6.1 \times 10^{12}$, $4.52 \times 10^{12}$, $4.99 \times 10^{12}$, and $4.62 \times 10^{12}$, respectively. Divalent $Ca^{++}$ cation resulted in lower water flux recovery (higher $R_{\text{non-rec}}$) than movalent $Na^+$ cation. This indicated a more compacted Ca–NOM cake layer (lower cake porosity), and thus increased permeate flow resistance during filtration experiments. The experimental results agreed with the results from Wang et al. [26]. They indicated that divalent cations seemed to be more readily adsorbed on the membrane surface than monovalent ions because divalent cations could act as a bridge between the membrane surface and the negatively charged humic acid molecules and also between the negatively charged function groups of humic acid that were not in contact with the membrane, resulting a highly compacted fouling layer at the membrane surface [26].

## 5. Conclusions

A combined osmotic pressure and cake filtration model for crossflow nanofiltration of NOM solution can be used successfully to characterize model parameters (i.e. permeability reduction factor and specific cake resistance) for salt concentrations, NOM concentrations, ionic strength of salt species ($Na^+$ and $Ca^{++}$). This model can be explained in terms of salt and NOM combination, while the mathematical models from the previous work [16] could not be applied to interpret model parameters due to the effect of salt alone and combined salt and NOM solution. Based on the combined osmotic pressure and cake filtration model, permeability reduction factor was used to describe the change in membrane permeability in the presence of salt concentrations and ion species, while specific cake resistance was used to interpret NOM accumulation at the membrane surface. In the absence of NOM, increased NaCl salt concentrations ranging from 0.004 to 0.1 M decreased normalized solution flux, while permeability reduction factor decreased from 0.99 to 0.72. With increasing ionic strengths, divalent cation ($Ca^{++}$) exhibited greater flux decline than monovalent cation ($Na^+$), thus corresponding a relatively low permeability reduction factor. This indicated a reduction of charge repulsion between positively charged salt and negatively charged NF membrane, thus decreased double layer thickness at the membrane surface. The results suggested significant effects of charge screening at the membrane surface due to divalent cation. In the presence of NOM, solutions having high NOM concentrations caused a reduction of normalized solution flux, thus resulting in increased specific cake resistances. Solutions having divalent cation presented higher salt rejection and specific cake resistances than those having monovalent cation. This resulted in a reduction of charge repulsion between calcium and NOM functional groups, thus increasing a highly compacted NOM accumulation at the membrane surface (lower cake porosity), thus increased permeate flow resistance during filtration experiments. After membrane cleaning, divalent cation exhibited lower water flux recovery than monovalent cation, suggesting higher non-recoverable ($R_{\text{non-rec}}$) resistance than monovalent cation.

## Acknowledgements

The authors would like to thank the Thailand Research Fund (TRF) for TRF senior research scholar grant (no. RTA5080014) and the Commission on Higher Education, Thailand, for financial support. We also would like to thank the Department of Chemical Engineering, Faculty of Engineering, Ubon Rachathani University, Thailand, for all equipments applied in this research.

**Nomenclature**

| | |
|---|---|
| $a_s$ | volumetric specific surface area ($m^2\,m^{-3}$) |
| $A_m$ | membrane area ($m^2$) |
| $C_{\text{feed}}$ | concentration in the feed line ($mg\,L^{-1}$ or $mol\,L^{-1}$) |
| $C_{\text{mem}}$ | concentration at the membrane surface ($mg\,L^{-1}$ or $mol\,L^{-1}$) |
| $C_{\text{perm}}$ | concentration in the permeate line ($mg\,L^{-1}$ or $mol\,L^{-1}$) |
| $C_{\text{reten}}$ | concentration in the retentate line ($mg\,L^{-1}$ or $mol\,L^{-1}$) |
| $C_{\text{reten,NOM}}$ | NOM concentration in the retentate line ($kg\,m^{-3}$) |
| $C_{\text{reten,s}}$ | concentration in the retentate line in the presence of salt ($mol\,L^{-1}$) |
| $C_{ss}$ | steady-state concentration in the retentate line ($mg\,L^{-1}$ or $mol\,L^{-1}$) |
| $d_p$ | particle diameter (m) |
| $D$ | salt diffusion coefficient ($m^2\,s^{-1}$) |
| $J^*$ | effective flux associated with back-transport resulting from crossflow (LMH) |
| $J_v$ | solution flux ($L\,m^{-2}\,h^{-1}$, LMH) |
| $J_{vo}$ | initial solution flux ($L\,m^{-2}\,h^{-1}$, LMH) |
| $k_a$ | overall mass transfer coefficient ($min^{-1}$) ($=k_1 a_s$) |
| $k_1$ | mass transfer coefficient ($m\,s^{-1}$) |
| $L_p$ | membrane permeability ($LMH\,kPa^{-1}$) |
| $L_{p,s}$ | membrane permeability in the presence of salt ($LMH\,kPa^{-1}$) |
| $m_{\text{cake}}$ | cake mass (kg) |
| $P$ | transmembrane pressure (kPa) |
| $Q_{\text{perm}}$ | flow in the permeate line ($mL\,min^{-1}$) |

| | |
|---|---|
| $\overline{Q}_{\text{reten}}$ | flow in the retentate line (mL min$^{-1}$) |
| $R_c$ | cake resistance (m$^{-1}$) |
| $R_{\text{feed}}$ | rejection in the feed stream (–) |
| $R_m$ | membrane hydraulic resistance (m$^{-1}$) |
| $R_{m,s}$ | membrane resistance in the presence of salt (m$^{-1}$) |
| $R_{\text{mem}}$ | intrinsic membrane rejection (–) |
| $R_{\text{mem,s}}$ | intrinsic membrane rejection in the presence of salt (–) |
| $R_{\text{non-rec}}$ | non-recoverable resistance (m$^{-1}$) |
| $R_{\text{reten}}$ | rejection in the retentate stream (–) |
| $t$ | operating time (min) |
| $V_{\text{sys}}$ | system volume (mL) |
| *Greek letters* | |
| $\alpha$ | correlation between osmotic pressure and salt concentration (kPa L mol$^{-1}$) |
| $\alpha_{\text{cake}}$ | specific cake resistance (m kg$^{-1}$) |
| $\beta$ | salt concentration polarization (–) |
| $\delta$ | boundary layer thickness (m) |
| $\varepsilon_{\text{cake}}$ | cake porosity (–) |
| $\eta$ | permeability reduction factor (–) |
| $\mu$ | dynamic viscosity (kg m$^{-1}$ s$^{-1}$) |
| $\pi$ | osmotic pressure (kPa) |
| $\pi_{\text{mem}}$ | osmotic pressure at the membrane surface (kPa) |
| $\pi_{\text{perm}}$ | osmotic pressure in the permeate line (kPa) |
| $\rho$ | density (kg m$^{-3}$) |
| $\sigma$ | osmotic reflection coefficient (–) |

## References

[1] A.I. Schafer, A.G. Fane, T.D. Waite, Nanofiltration of natural organic matter: removal, fouling and the influence of multivalent ions, Desalination 118 (1998) 109–122.

[2] P. Eriksson, Nanofiltration extends the range of membrane filtration, Environ. Prog. 7 (1) (1998) 58–62.

[3] J.E. Kilduff, S. Mattaraj, G. Belfort, Flux decline during nanofiltration of naturally- occurring dissolved organic matter: effects of osmotic pressure, membrane permeability, and cake formation, J. Membr. Sci. 239 (1) (2004) 39–53.

[4] J. Schaep, B. Van der Bruggen, C. Vandecasteele, D. Wilms, Influence of ion size and charge in nanofiltration, Sep. Pur. Technol. 14 (1998) 155–162.

[5] A. Yaroshchuk, E. Staude, Charged membranes for low pressure reverse osmosis properties and applications, Desalination 86 (1992) 115–134.

[6] A. Seidel, M. Elimelech, Coupling between chemical and physical interaction in natural organic matters (NOM) fouling of nanofiltration membranes: implications for fouling control, J. Membr. Sci. 203 (2002) 245–255.

[7] E. Tipping, Cation binding by humic substances, Cambridge Environmental Chemistry Series, 1948, ISBN 0-521-62146-1.

[8] M. Schnitzer, S.U. Khan, Humic Substances in the Environment, Mercel Decker, New York, 1972.

[9] S.W. Krasner, J.-P. Croue, J. Buffle, E.M. Perdue, Three approaches for characterizing NOM, J. AWWA 88 (6) (1996) 66–79.

[10] E.M. Thurman, Organic Geochemistry of Natural Waters, Martinus Nijhoff/Dr. W. Junk Publishers, Dordrecht, 1985.

[11] S. Hong, M. Elimelech, Chemical and physical aspects of natural organic matter (NOM) fouling of nanofiltration membranes, J. Membr. Sci. 132 (1997) 159–181.

[12] C. Jarusutthirak, S. Mattaraj, R. Jiraratananon, Influence of inorganic scalants and natural organic matter on nanofiltration membrane fouling, J. Membr. Sci. 287 (2007) 138–145.

[13] A. Seidel, J.J. Waypa, M. Elimelech, Role of charge (Donnan) exclusion in removal of Arsenic from water by a negatively charged porous nanofiltration membrane, Environ. Eng. Sci. 18 (2) (2001) 105–113.

[14] A.E. Childress, M. Elimelech, Effect of solution chemistry on the surface charge of polymeric reverse osmosis and nanofiltration membranes, J. Membr. Sci. 119 (1996) 253–268.

[15] A.I. Schafer, A.G. Fane, T.D. Waite, Fouling effects on rejection in the membrane filtration of natural waters, Desalination 131 (2000) 215–224.

[16] C. Jarusutthirak, S. Mattaraj, R. Jiraratananon, Factors affecting nanofiltration performances in natural organic matter rejection and flux decline, Sep. Pur. Technol. 58 (2007) 68–75.

[17] J. Cho, G.L. Amy, J. Pellegrino, Membrane filtration of natural organic matter: initial comparison of rejection and flux decline characteristics with ultrafiltration and nanofiltration membranes, Water Res. 33 (1999) 2517–2526.

[18] J.E. Kilduff, S. Mattaraj, J. Sensibaugh, J.P. Pieracci, Y. Yuan, G. Belfort, Modeling flux decline during nanofiltration of NOM with poly (arylsulfone) nanofiltration membranes modified using UV-assisted graft polymerization, Environ. Eng. Sci. 19 (6) (2002) 477–496.

[19] R.W. Field, D. Wu, J.A. Howell, B.B. Gupta, Critical flux concept for microfiltration fouling, J. Membr. Sci. 100 (1995) 259–272.

[20] L.J. Zeman, A.L. Zydney, Microfiltration and Ultrafiltration: Principles and Applications, M. Dekker, New York, 1996.

[21] M.R. Wiesner, P. Aptel, Mass transport and permeate flux and fouling in pressure-driven processes, in: Water Treatment Membrane Processes, J. Mallevialle, P.E. Odendaal, M.R. Wiesner (Eds.), McGraw-Hill, New York, ISBN 0-07-0019-7-00151996.

[22] J.E. Kilduff, S. Mattaraj, A. Wigton, M. Kitis, T. Karanfil, Effects of reverse osmosis isolation on reactivity of naturally occurring dissolved organic matter in physicochemical processes, Water Res. 38 (4) (2004) 1026–1036.

[23] O. Levenspiel, Chemical Reaction Engineering, third ed., John Wiley & Sons, Inc., 1999.

[24] A. Braghetta, F.A. DiGiano, W.P. Ball, Nanofiltration of natural organic matter: pH and ionic strength effects, J. Environ. Eng., ASCE 123 (7) (1997) 628–641.

[25] K. Ghosh, M. Schnitzer, Macromolecular structures of humic substances, Soil Sci. 129 (5) (1980) 266–276.

[26] Z. Wang, Y. Zhao, J. Wang, S. Wang, Studies on nanofiltration membrane fouling in the treatment of water solutions containing humic acids, Desalination 178 (2005) 171–178.

Separation and Purification Technology 65 (2009) 290–297

Contents lists available at ScienceDirect

Separation and Purification Technology

journal homepage: www.elsevier.com/locate/seppur

# Comparing membrane resistance and absorption performance of three different membranes in a gas absorption membrane contactor

Sakarin Khaisri[a], David deMontigny[b,*], Paitoon Tontiwachwuthikul[b], Ratana Jiraratananon[a]

[a] Department of Chemical Engineering, King Mongkut's University of Technology Thonburi, Bangkok 10140, Thailand
[b] International Test Centre for $CO_2$ Capture, University of Regina, Regina, SK, Canada S4S 0A2

ARTICLE INFO

*Article history:*
Received 19 August 2008
Received in revised form 27 October 2008
Accepted 28 October 2008

*Keywords:*
Polytetrafluoroethylene
Polypropylene
Polyvinylidene fluoride
Carbon dioxide capture
Membrane contactors

ABSTRACT

Hollow fiber membrane contactors have been studied extensively in the last decade. Gas absorption membrane (GAM) contactors are a developing technology that overcome the disadvantage of conventional equipment. Three different membranes, including polytetrafluoroethylene (PTFE), polypropylene (PP), and polyvinylidene fluoride (PVDF), were used to test the performance of a GAM system in both physical and chemical absorption studies. In the physical absorption experiments, pure $CO_2$ and de-ionized water were used in the GAM system. A Wilson plot was used to determine the membrane resistance in this work. From the results, the PVDF membrane had a higher $CO_2$ flux than PP membranes and the highest membrane resistance. In the chemical absorption experiments, a simulated flue gas stream (15% $CO_2$ and 85% air) was treated with monoethanolamine (MEA) solutions. Experimental results showed that the $CO_2$ absorption performance can be ranked as PTFE > PVDF > PP. While the PTFE membrane had the best performance in the GAM system, the PVDF membrane is an alternative membrane that could be used. The stability of PTFE and PVDF membranes was tested continuously over 60 h of operation. The PTFE membranes maintained their absorption performance, while the PVDF membranes did not maintain their absorption performance over the operating time.

## 1. Introduction

Most of the energy in the world comes from fossil fuels, such as coal, oil and gas. However, the combustion of fossil fuels inevitably results in the emission of air pollutants and a huge release of carbon dioxide ($CO_2$). Since $CO_2$ is a major greenhouse gas, it should be removed from industrial flue gas streams. Many methods exist to remove $CO_2$ by absorption into aqueous solutions using conventional equipment including packed columns, bubble columns, and spray columns. The conventional equipment has operational problems including flooding, channeling, entrainment, and foaming [1]. Gas absorption membrane (GAM) systems are an alternative technology for capturing $CO_2$. In general, a microporous membrane is used in the GAM system to separate the gas and liquid-phases as shown in Fig. 1. Mass transfer occurs when $CO_2$ diffuses across the membrane and absorbs into the absorbent. This configuration offers many advantages including independent gas and liquid flow, high surface area, and linear scale-up as reviewed by Li and Chen [2].

GAM systems were first developed by Qi and Cussler for this application [3,4]. In their work, they studied GAM systems in terms of a mass transfer coefficient because the GAM system has an interfacial area per unit volume that is higher than conventional equipment. However, they found that the membrane itself increases the overall mass transfer resistance significantly if the membranes are wetted. This is because the membrane morphology was changed, as reported by Wang et al. [5]. The non-wetted mode of operation has been confirmed to offer the best performance in GAM systems by several authors [5–8]. deMontigny et al. [9] compared the overall mass transfer coefficient between GAM systems and packed columns. Polytetrafluoroethylene (PTFE) and polypropylene (PP) were used in the GAM system and were compared with Sulzer DX structured packing in a packed column. Experiments were carried out by absorbing $CO_2$ into aqueous monoethanolamine (MEA) and 2-amino-2-methyl-1-propanol (AMP) solutions. The overall mass transfer coefficient in their GAM system was higher than the packed column by roughly three times. Nishikawa et al. [10] investigated the performance of GAM systems and packed beds to compare both systems. It was found that the PTFE membrane had an overall mass transfer coefficient that was more than five times higher than the packed bed column. They found that the PTFE membranes had stability for more than 6600 h. Recently, PTFE, and PP membranes have been used in GAM systems

---

* Corresponding author. Tel.: +1 306 337 2277; fax: +1 306 585 4855.
*E-mail address:* david.demontigny@uregina.ca (D. deMontigny).

1383-5866/$ – see front matter © 2008 Elsevier B.V. All rights reserved.
doi:10.1016/j.seppur.2008.10.035

Separation and Purification Technology 65 (2009) 290–297

Contents lists available at ScienceDirect

Separation and Purification Technology

journal homepage: www.elsevier.com/locate/seppur

# Comparing membrane resistance and absorption performance of three different membranes in a gas absorption membrane contactor

Sakarin Khaisri[a], David deMontigny[b,*], Paitoon Tontiwachwuthikul[b], Ratana Jiraratananon[a]

[a] *Department of Chemical Engineering, King Mongkut's University of Technology Thonburi, Bangkok 10140, Thailand*
[b] *International Test Centre for CO₂ Capture, University of Regina, Regina, SK, Canada S4S 0A2*

ARTICLE INFO

*Article history:*
Received 19 August 2008
Received in revised form 27 October 2008
Accepted 28 October 2008

*Keywords:*
Polytetrafluoroethylene
Polypropylene
Polyvinylidene fluoride
Carbon dioxide capture
Membrane contactors

ABSTRACT

Hollow fiber membrane contactors have been studied extensively in the last decade. Gas absorption membrane (GAM) contactors are a developing technology that overcome the disadvantage of conventional equipment. Three different membranes, including polytetrafluoroethylene (PTFE), polypropylene (PP), and polyvinylidene fluoride (PVDF), were used to test the performance of a GAM system in both physical and chemical absorption studies. In the physical absorption experiments, pure $CO_2$ and de-ionized water were used in the GAM system. A Wilson plot was used to determine the membrane resistance in this work. From the results, the PVDF membrane had a higher $CO_2$ flux than PP membranes and the highest membrane resistance. In the chemical absorption experiments, a simulated flue gas stream (15% $CO_2$ and 85% air) was treated with monoethanolamine (MEA) solutions. Experimental results showed that the $CO_2$ absorption performance can be ranked as PTFE > PVDF > PP. While the PTFE membrane had the best performance in the GAM system, the PVDF membrane is an alternative membrane that could be used. The stability of PTFE and PVDF membranes was tested continuously over 60 h of operation. The PTFE membranes maintained their absorption performance, while the PVDF membranes did not maintain their absorption performance over the operating time.

## 1. Introduction

Most of the energy in the world comes from fossil fuels, such as coal, oil and gas. However, the combustion of fossil fuels inevitably results in the emission of air pollutants and a huge release of carbon dioxide ($CO_2$). Since $CO_2$ is a major greenhouse gas, it should be removed from industrial flue gas streams. Many methods exist to remove $CO_2$ by absorption into aqueous solutions using conventional equipment including packed columns, bubble columns, and spray columns. The conventional equipment has operational problems including flooding, channeling, entrainment, and foaming [1]. Gas absorption membrane (GAM) systems are an alternative technology for capturing $CO_2$. In general, a microporous membrane is used in the GAM system to separate the gas and liquid-phases as shown in Fig. 1. Mass transfer occurs when $CO_2$ diffuses across the membrane and absorbs into the absorbent. This configuration offers many advantages including independent gas and liquid flow, high surface area, and linear scale-up as reviewed by Li and Chen [2].

GAM systems were first developed by Qi and Cussler for this application [3,4]. In their work, they studied GAM systems in terms of a mass transfer coefficient because the GAM system has an interfacial area per unit volume that is higher than conventional equipment. However, they found that the membrane itself increases the overall mass transfer resistance significantly if the membranes are wetted. This is because the membrane morphology was changed, as reported by Wang et al. [5]. The non-wetted mode of operation has been confirmed to offer the best performance in GAM systems by several authors [5–8]. deMontigny et al. [9] compared the overall mass transfer coefficient between GAM systems and packed columns. Polytetrafluoroethylene (PTFE) and polypropylene (PP) were used in the GAM system and were compared with Sulzer DX structured packing in a packed column. Experiments were carried out by absorbing $CO_2$ into aqueous monoethanolamine (MEA) and 2-amino-2-methyl-1-propanol (AMP) solutions. The overall mass transfer coefficient in their GAM system was higher than the packed column by roughly three times. Nishikawa et al. [10] investigated the performance of GAM systems and packed beds to compare both systems. It was found that the PTFE membrane had an overall mass transfer coefficient that was more than five times higher than the packed bed column. They found that the PTFE membranes had stability for more than 6600 h. Recently, PTFE, and PP membranes have been used in GAM systems

---

* Corresponding author. Tel.: +1 306 337 2277; fax: +1 306 585 4855.
*E-mail address:* david.demontigny@uregina.ca (D. deMontigny).

1383-5866/$ – see front matter © 2008 Elsevier B.V. All rights reserved.
doi:10.1016/j.seppur.2008.10.035

**Nomenclature**

| | |
|---|---|
| $A_T$ | mass transfer area based on outside surface area of gas–liquid contact (m$^2$) |
| $a_v$ | specific surface area (m$^2$/m$^3$) |
| $C_g$ | concentration of carbon dioxide in gas-phase (mol/m$^3$) |
| $C_l$ | concentration of carbon dioxide in liquid-phase (mol/m$^3$) |
| $\Delta C_{l,av}$ | logarithmic mean concentration difference of carbon dioxide in liquid-phase (mol/m$^3$) |
| $d_i$ | inside diameter of membrane (m) |
| $d_{\ln}$ | logarithmic mean diameter of membrane (m) |
| $d_o$ | outside diameter of membrane (m) |
| $D_{g,eff}$ | effective diffusion coefficient of gas in the gas-filled membrane pores (m$^2$/s) |
| $G_I$ | inert gas flow rate (kmol/m$^2$ h) |
| $H$ | Henry's constant |
| $J$ | absorption flux (mol/m$^2$ s) |
| $k_g$ | gas-phase mass transfer coefficient (m/s) |
| $k_l$ | liquid-phase mass transfer coefficient (m/s) |
| $k_m$ | membrane mass transfer coefficient (m/s) |
| $K_g$ | overall gas-phase mass transfer coefficient (kmol/m$^2$ h kPa) |
| $K_{ol}$ | overall liquid-phase mass transfer coefficient (m/s) |
| $l_m$ | membrane thickness (m) |
| $Q_l$ | liquid volumetric flow rate (m$^3$/s) |
| $P$ | total system pressure (kPa) |
| $v$ | liquid velocity (m/s) |
| $y$ | CO$_2$ mole fraction in the bulk gas-phase |
| $y^*$ | CO$_2$ mole fraction in equilibrium with $C_l$ |
| $Y$ | mole ratio |
| $Z$ | membrane length (m) |

*Greek letters*

| | |
|---|---|
| $\alpha$ | constant |
| $\varepsilon_m$ | membrane porosity |
| $\tau_m$ | membrane tortuosity |

[5,10–12]. For example, Rangwala [12] studied PP membranes in GAM systems using sodium hydroxide (NaOH) and diethanolamine (DEA) as an absorbent. It was found that the membrane resistance could be as high as 60% of total resistance in wetted mode of operation.

Atchariyawut et al. [13] studied the effect of three different PVDF membrane structures on the mass transfer coefficient in GAM systems that absorbed pure CO$_2$ into distilled water. The finger-like portion and molecular weight cut off (MWCO) of the PVDF membrane affected the overall mass transfer coefficient and CO$_2$ absorption performance. They found that PVDF membranes are an alternative membrane that could be used in GAM systems because the manufacturing and material cost is cheaper than that of the PTFE membrane. While, some authors have reported that PTFE membranes have the best performance in GAM systems, they are much more expensive than PP membranes [10,11]. Table 1 shows the cost comparison of PTFE, PP and PVDF commercial hollow fiber membranes.

**Table 1**
Cost of commercial hollow fiber membranes.

| Membrane | Cost ($US/m) | Supplier |
|---|---|---|
| PVDF | 0.36 | Wenzhou New Century International Ltd. (China) |
| PTFE | 11.50 | Sumitomo Electric Fine Polymer (Japan) |
| PP | 0.01 | Mitsubishi Rayon Ltd. (Japan) |

In this work, the performance of microporous PP, PTFE and PVDF membranes were investigated in GAM systems for CO$_2$ capture. PTFE and PP membranes were received from commercial vendors. Tailor-made PVDF membranes were prepared via a phase inversion method containing lithium chloride (LiCl) as a non-solvent additive in the manufacturing process. The membrane resistances were determined using the Wilson plot method. In addition, the CO$_2$ fluxes were determined for both physical and chemical absorption.

## 2. Theory

### 2.1. Resistance in series model

The film theory has been described in GAM systems as a resistance in series model [12]. Membrane contactors have three resistances in series including the liquid film resistance, the gas film resistance and the membrane itself. This is shown schematically in Fig. 1. The overall mass transfer coefficient can be written as follows [14]:

$$\frac{1}{K_{ol}} = \frac{1}{k_l} + \frac{Hd_o}{k_m d_{\ln}} + \frac{Hd_o}{k_g d_i} \qquad (1)$$

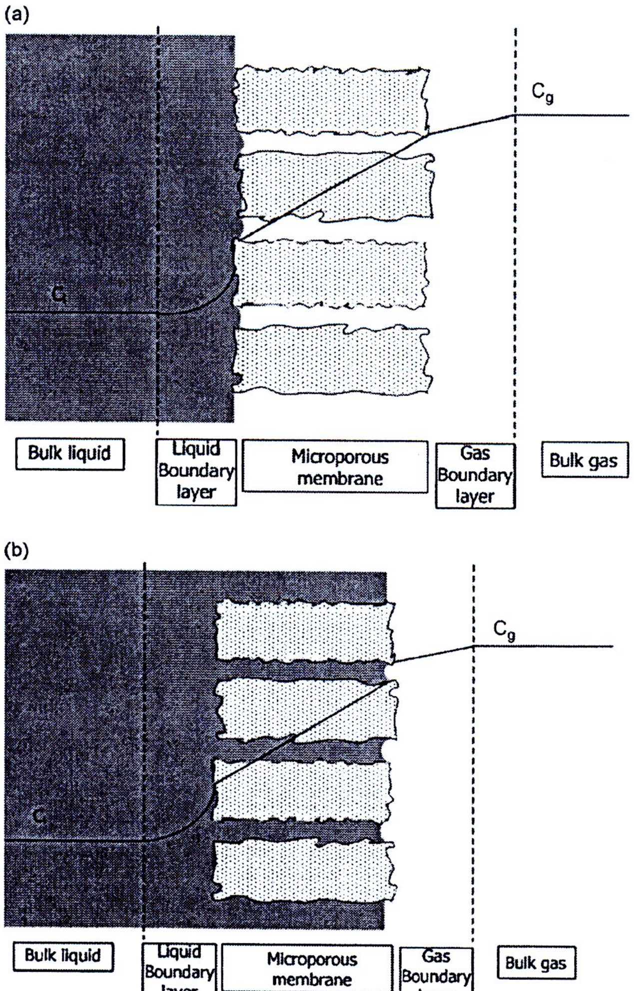

**Fig. 1.** Mass transfer resistance in series model for membrane contactors (a) non-wetted mode and (b) wetted mode.

$$\frac{1}{K_g} = \frac{1}{Hk_l} + \frac{d_o}{k_m d_{ln}} + \frac{d_o}{k_g d_i} \qquad (2)$$

where $K_{ol}$ and $K_g$ are the overall liquid and gas-phase mass transfer coefficient and $k_l$, $k_m$, and $k_g$ are the liquid, membrane and gas mass transfer coefficients, respectively. $H$ represents Henry's constant [15], and $d_o$, $d_i$, and $d_{ln}$ are the outer, inner and logarithmic mean diameters of the membrane. The $K_{ol}$ term can be calculated as follows [5]:

$$K_{ol} = \frac{Q_l(C_{l,out} - C_{l,in})}{A_T \Delta C_{l,av}} \qquad (3)$$

The logarithmic mean concentration is given by

$$\Delta C_{l,av} = \frac{(HC_{g,in} - C_{l,out}) - (HC_{g,out} - C_{l,in})}{\ln((HC_{g,in} - C_{l,out})\backslash(HC_{g,out} - C_{l,in}))} \qquad (4)$$

where $Q_l$ is the liquid flow rate, $C_{l,in}$ and $C_{l,out}$ are the inlet and outlet $CO_2$ concentration in the liquid-phase, $C_{g,in}$ and $C_{g,out}$ are the inlet and outlet $CO_2$ concentration in the gas-phase, and $A_T$ is the gas–liquid contacting area.

The overall gas-phase mass transfer coefficient was calculated using a method similar to the one used for packed columns. It can be calculated as follows [11]:

$$K_g a_v = \frac{G_I}{P(y - y^*)} \frac{dY}{dZ} \qquad (5)$$

where $K_g a_v$ is overall volumetric gas-phase mass transfer coefficient, $G_I$ is the inert gas flow rate, $dY/dZ$ is the solute concentration gradient.

In a non-wetted mode of operation, the membrane mass transfer coefficient can be calculated using the following equation [16]:

$$k_m = \frac{D_{g,eff}\,\varepsilon_m}{\tau_m l_m} \qquad (6)$$

where $D_{g,eff}$ is the effective diffusion coefficient of gas in the gas-filled membrane pore, and $\varepsilon_m$, $\tau_m$, and $l_m$ are the porosity, tortuosity, and thickness of the membrane, respectively.

### 2.2. Wilson plot

Wilson plots are an alternative technique for determining the membrane resistance [1,13]. For gas absorption in GAM systems, the gas-phase mass transfer resistance can be ignored [12] while the liquid-phase mass transfer resistance is proportional to liquid velocity. The Wilson plot equation can be plotted with $1/K_{ol}$ versus $v^{-\alpha}$ where $v$ is the liquid velocity and $-\alpha$ is the value that provides the best straight line. It can be simplified from Eq. (1):

$$\frac{1}{K_{ol}} = C_1 v^{-\alpha} + \frac{Hd_o}{k_m d_{ln}} \qquad (7)$$

From this equation, the membrane resistance is given by the interception of the $y$-axis.

## 3. Experiment

The experiments were divided into two parts: physical absorption and chemical absorption. Hollow fiber PP, PTFE and PVDF membranes were used in two experiments for comparing $CO_2$ absorption performance. PP and PTFE membranes were received from Mitsubishi Rayon Ltd. (Japan), and Sumitomo Electric Fine Polymer (Japan), respectively. PVDF membranes were made using the phase inversion method with lithium chloride as an additive. Dimethylacetamide (DMAc) was used as a solvent to dissolve the PVDF polymer and 30% dimethylacetamide/water solutions were used as an internal coagulant to form the hollow fiber lumen. The fabrication method, materials and procedure used to manufacture the PVDF hollow fiber membranes that were used in this work were reported by Xu et al. [17]. The membrane characteristics are listed in Table 2. The experimental setup is shown in Fig. 2. The GAM module was made from acrylic tubing with an inside and outside diameter of 28 and 34 mm, respectively, while the module length was roughly 0.25 m. Fig. 3 shows the schematic of the acrylic discs that were used to pot the three hollow fiber membranes. Removable membrane cartridges were designed to provide the best arrangement and position of hollow fiber membranes in the module. This design helps to control liquid channeling and dead zones when liquid is fed in the shell side. A counter current mode of operation was used in all experiments to obtain the best performance [11]. Liquid solution was pumped with a centrifugal pump to the bottom of the module and flowed upwards out the top of the module. This configuration ensured that the liquid contacted all of the membrane surface area. The liquid flow rate was controlled with a variable area flow meter. A known volume was collected over time to calibrate the liquid flow rate. The feed gas stream was controlled using a gas flow controller. The gas was introduced into the GAM module before the liquid stream in order to prevent wetting problems. Each run was operated at least 30 min before collecting any data to make sure that steady state conditions had been reached.

**Table 2**
Characteristics of hollow fiber membranes.

| Description | PVDF | PP | PTFE |
|---|---|---|---|
| Outer diameter (mm) | 0.9 | 0.300 | 2.0 |
| Inner diameter (mm) | 0.8 | 0.244 | 1.0 |
| Membrane length (m) | 0.118 | 0.146 | 0.122 |
| Membrane porosity (%) | – | 35 | 50 |
| Membrane pore size[a] (μm) | 0.5 | – | 20 |
| Fibers per module | 240 | 1550 | 57 |
| Outside fiber area (m²) | 0.080 | 0.213 | 0.044 |
| Module void fraction (%) | 75.2 | 82.2 | 70.1 |
| Reynolds number | 5–26 | 3–14 | 10–46 |
| Shell inside diameter (mm) | | 28 | |

[a] Determined from SEM images.

In the physical and chemical absorption experiments, the liquid flow rate was fed into the shell side of the GAM module while the gas stream was fed into the fiber lumen. When the fiber lumen is smaller than 100 μm, the pumping costs are excessive [18].

### 3.1. Physical absorption

The physical absorption tests were conducted with pure $CO_2$ at a constant gas flow rate of 300 ml/min. The de-ionized water flow rate was varied. The absorbent was fed into the module shell side while the pure $CO_2$ gas was fed into the membrane lumen side. At steady conditions, the feed gas stream was measured using a bubble flow meter.

### 3.2. Chemical absorption

Aqueous solutions of MEA were prepared to a desired concentration using de-ionized water. Standard hydrochloric acid solution (1 N) was used as a titrant with methyl orange as an indicator. A known volume was collected at steady state conditions for titration to determine the $CO_2$ loading in the MEA solution. $CO_2$ loading was determined to make sure that the mass balance error between the gas and liquid side was low, indicating the experiment was valid. The $CO_2$ loading procedure can be found in the Association of Official Analytical Chemists [19]. A simulated flue gas stream containing 15% $CO_2$ and 85% air was prepared as a feed gas. An infrared $CO_2$ analyzer was used to verify the desired concentration of $CO_2$

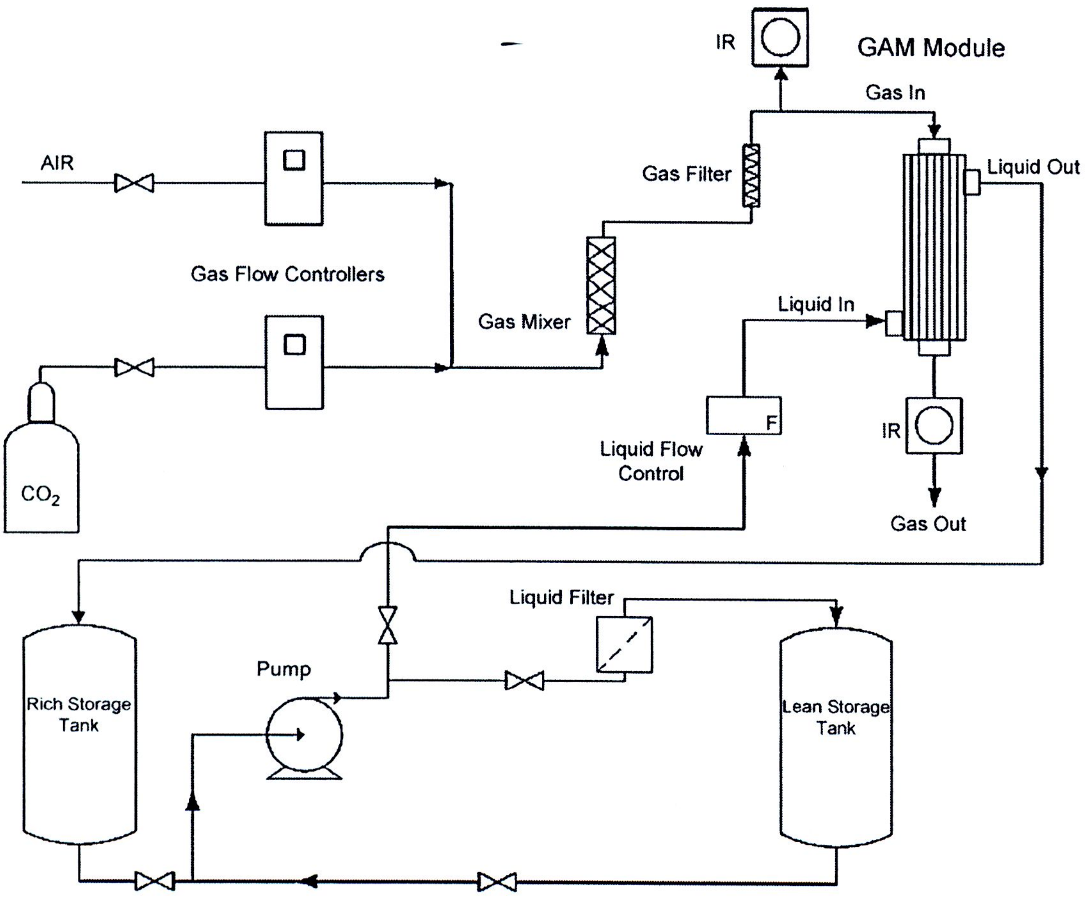

**Fig. 2.** Experimental setup for the gas absorption membrane contactor.

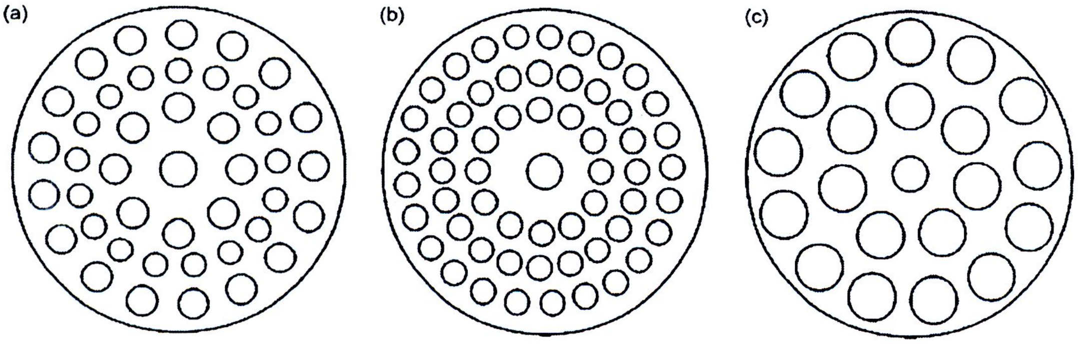

**Fig. 3.** Schematic of acrylic potting discs for hollow fiber membranes. (a) PP disc; (b) PTFE disc; (c) PVDF disc.

in the feed gas stream. At steady state conditions, the $CO_2$ outlet concentration was measured using the infrared analyzer. An MEA solution sample was taken at the top of module to find the $CO_2$ loading in liquid side to make sure that the mass balance error was not more than 10%.

## 4. Results and discussion

### 4.1. Physical absorption experiment

#### 4.1.1. Effect of gas velocity on $CO_2$ absorption flux

PTFE membranes were used to test the effect of gas velocity. Fig. 4 shows that the absorption flux remained constant while the gas velocity increased. The gas velocity has no effect on absorption flux and the overall mass transfer. This is because gas-phase mass transfer resistance is not dominant. The controlling resistance in the GAM system is the liquid side mass transfer resistance because the $CO_2$ absorption occurs in the liquid film [9].

#### 4.1.2. Membrane resistance analysis using a Wilson plot

The Wilson plot method can be used to find membrane resistance. Fig. 5 shows the Wilson plot for the three membranes. The power number of the liquid velocity was used to get the best straight line, as has been done by previous researchers [13,20]. Recently, Atchariyawut et al. [13] have used this method to describe the effect of membranes structure on membrane resistance. They

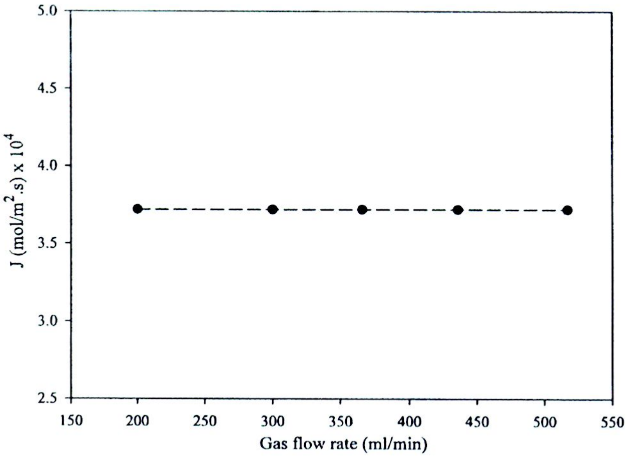

**Fig. 4.** Effect of gas flow rate on $CO_2$ flux (PTFE membrane, pure $CO_2$ and pure water system, constant water velocity at $26.10\,m^3/m^2$ h).

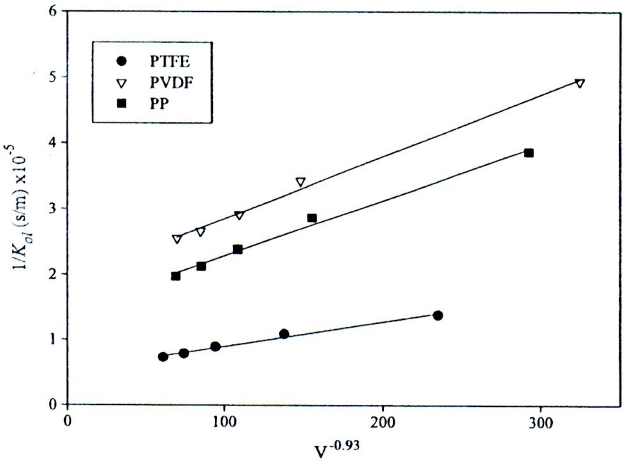

**Fig. 5.** Wilson plot (pure $CO_2$–water).

plotted $1/K_{ol}$ between $v^{-0.93}$ to analyze PVDF and PP membrane resistances when the liquid flowed in the shell side of membrane module. They found that a finger-like pore portion had a significant effect on membrane resistance. The increase of the finger-like structure provided a lower membrane resistance. The structure of the PVDF membranes used in this work will be discussed later.

Wilson equations and membrane resistances are shown in Table 3. It was found that the PTFE, PP and PVDF membranes have membrane resistances of 39%, 43% and 47%, respectively. When the membrane is partially wetted by capillary condensation in the pores, the membrane resistance increases, thus reducing the overall mass transfer coefficient [21]. The hydrophobicity of membranes is represented in terms of the contact angle between the water and membrane. The contact angle value is an angle between liquid and solid. In the case of water, a material is deemed to be hydrophobic if the contact angle is higher than 90°. In general, the hydrophobicity of the membranes is in the order of PTFE > PP > PVDF, as shown in Table 4, which indicates the resistance to wettability by water. In a non-wetted mode of operation, the pores of the membrane are completely filled by gas, and the membrane resistance should not be more than 0.12% and 0.65% for PVDF and PTFE membranes based on Eq. (6), respectively. If the membrane pores were partially wetted by capillary condensation, the membrane resistance increases [13]. From the results shown in Table 3, it was clear that all of the membranes were partially wetted by water and/or water vapor. A high contact angle can prevent a wetting problem because of its natural hydrophobicity. From Table 4, the PTFE membrane has a higher hydrophobicity than PP and PVDF membranes. It was shown that PTFE membranes can prevent water penetration into membrane pores better than PP membranes. The PTFE membrane resistance was less than the PP and PVDF membranes due to its hydrophobicity. When the liquid water penetrates into the pores, the membrane resistance is increased. From the results, the liquid water penetrated into the PP pores more than PTFE pores, and that had an effect on the membrane resistance.

**Table 3**
Wilson equation and membrane resistance analysis.

| Membrane | Equation | $R_m/R_{tot}$[a] (%) |
|---|---|---|
| PTFE | $1/K_{ol} = 364.03\ v^{-0.93} + 53566$ | 39.87 |
| PP | $1/K_{ol} = 845.15\ v^{-0.93} + 143406$ | 43.32 |
| PVDF | $1/K_{ol} = 951.49\ v^{-0.93} + 189049$ | 47.23 |

[a] $R_{tot}$ was calculated at $v = 0.003$ m/s.

**Table 4**
Contact angle between water and membranes.

| PVDF | PP | PTFE | Reference |
|---|---|---|---|
| 100° | – | – | [26] |
| 92° | – | – | [25] |
| – | 100° | | [27] |
| – | 118° | 127° | [28] |
| – | 104° | 113° | [29] |
| – | – | 133.5° | [30] |

Surprisingly, the PVDF membrane had the highest membrane resistance, but its absorption performance was higher than PP membrane. However, structure, pore size and porosity of the membrane also have an effect on membrane resistance and absorption performance [13,17,22]. The cross section of the PTFE and PVDF membranes were examined using a JSM-5600, JEOL Ltd. scanning electron microscope (SEM). Fig. 6 shows PTFE and PVDF SEM images. A microporous structure was formed in the inner surface of hollow fiber membrane when 30%DMAc was used an internal coagulant [17]. In addition, the mass transfer resistance is increased by a dense skin layer. Referring to Fig. 6, the finger-like structure in the PVDF membrane was over 50% of the membrane thickness. When the finger-like structure is increased, the absorption performance and membrane porosity increases while the membrane resistance tends to decrease [13]. In general, the phase inversion method for manufacturing membranes yields a higher membrane porosity than the sintering method. Unfortunately, there is no data for the porosity of the PVDF membrane, but it should be higher than the porosity of the PP membranes due to its manufacturing process. It can be reasonably concluded that the PVDF membrane had higher absorption flux than the PP membrane because of porosity, pore size and the structure of the hollow fiber membrane.

### 4.1.3. Comparing membrane performance

The PTFE, PP and PVDF membranes were evaluated for their $CO_2$ absorption performance with respect to each other. The PTFE and PP membranes were received from Mitsubishi Rayon Ltd. (Japan), and Sumitomo Electric Fine Polymer (Japan), respectively. The PVDF membranes were prepared by a phase inversion method with lithium chloride as an additive. All membranes had $CO_2$ flux increase with an increasing liquid velocity, due to an increase in the mass transfer coefficient. This can be seen in Fig. 7. When the liquid velocity increased, which affected the mass transfer coefficient, an increase in absorption flux was observed. This confirmed that the liquid film is the controlling step in the GAM system.

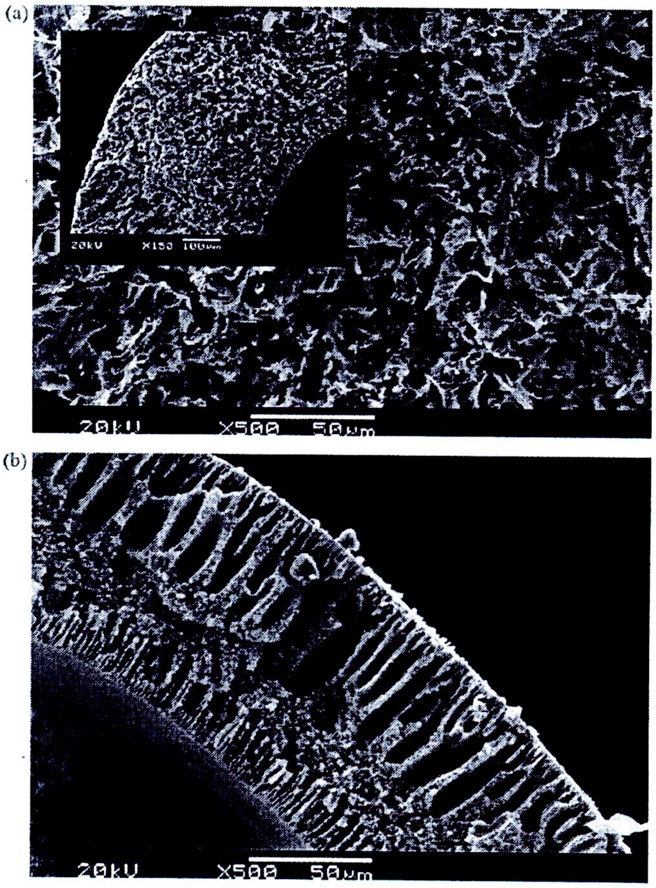

**Fig. 6.** Cross sectional SEM images of hollow fiber membranes (a) PTFE membrane and (b) PVDF membrane.

$CO_2$ flux comparisons produced surprising results for the PVDF membranes. The PVDF membrane had a higher $CO_2$ flux than the PP membrane, but it was lower than the PTFE membrane by roughly 20%. The absorption flux depends on many parameters including the membrane structure, membrane morphology, and operating parameters. Asimakopoulou and Karabelas [23] studied the effect of packing density on shell side liquid film mass transfer coefficients. They found that there was no effect on the shell side mass transfer coefficient when the packing density was less than 0.30. The packing densities used in this work, fit this criteria.

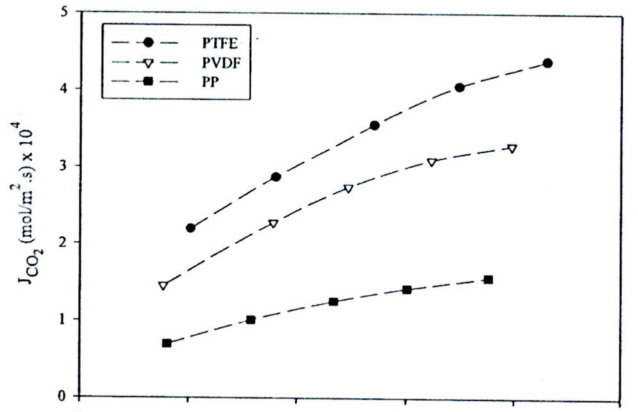

**Fig. 7.** Effect of liquid velocity on $CO_2$ flux in physical absorption experiments (pure $CO_2$–water, $Q_g$ = 300 ml/min).

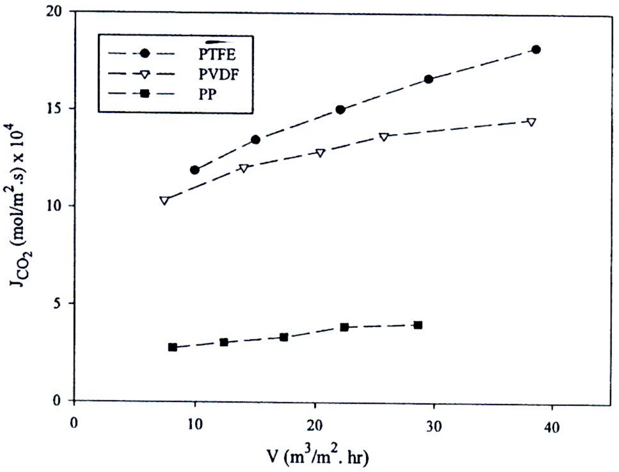

**Fig. 8.** Effect of liquid velocity in chemical absorption experiments (1.0 M aqueous MEA solution, $CO_2$ loading 0.20–0.21 mol $CO_2$/mol amine, 15% $CO_2$, inert gas flow rate 0.30 mol/min).

Membrane porosity is also a significant factor that affects the $CO_2$ absorption flux in GAM systems, as discussed before. However, the cost of the membrane should be considered. PTFE and PVDF membranes cost 11.5 $US/m (Sumitomo Electric Fine Polymer) and 0.36 $US/m (Wenzhou New Century International Ltd.), respectively. The price of the PVDF membrane is considerably cheaper than the PTFE membrane. When comparing between the price and performance of PTFE and PVDF membranes. We can see that the PVDF membrane is better than the PTFE membrane. From the results, the PVDF membranes are suitable in the GAM system because it had a $CO_2$ flux that was almost equal to the PTFE membrane. In addition, the PVDF membranes are cheaper and easier to manufacture.

### *4.2. Chemical absorption experiment*

MEA solution was used as an absorbent to test the performance of membranes. A counter-current mode of operation was used with the gas flowing inside the membrane lumen and the liquid flowing in the module shell side.

Figs. 8 and 9 show the absorption performance of PTFE, PVDF and PP membranes in terms of $CO_2$ flux and the overall volumetric gas-phase mass transfer coefficient ($K_g a_v$), respectively. It is clear that the membrane performance was in order of PTFE > PVDF > PP in terms of both the absorption flux and overall volumetric gas-phase mass transfer coefficient. It can be seen that the PTFE membranes performed better than the PVDF and PP membranes. The PTFE and PP membranes had membrane porosities of 50% and 35%, respectively. The higher membrane porosity led to a higher performance. In chemical absorption tests, such as $CO_2$–MEA and $CO_2$–NaOH, the membrane porosity had an effect on the mass transfer coefficient, as reported by Matsumoto et al. [22]. The overall mass transfer coefficient increased with an increase in the porosity because of the liquid film boundary layer in the $CO_2$–MEA system. When the ratio between the thickness of the liquid film boundary layer and the average distance between pores is small, the boundary layer is close to the membrane surface. This can increase the mass transfer coefficient in GAM systems. The PVDF membrane had the highest membrane resistance, but it had $CO_2$ fluxes higher than the PP membrane. Fig. 6(b) shows the image of the PVDF membrane.

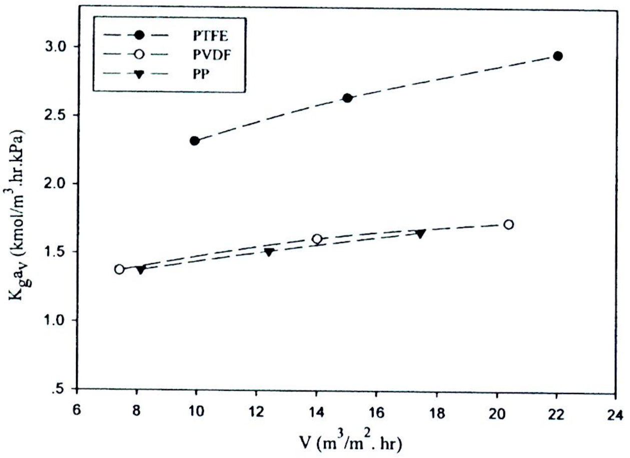

**Fig. 9.** Effect of liquid velocity on the $K_ga_v$ in a GAM system. (1.0 M aqueous MEA solution, $CO_2$ loading 0.20–0.21 mol $CO_2$/mol amine, 15% $CO_2$, inert gas flow rate 0.30 mol/min).

There is a dense skin layer on the outer surface of PVDF membrane, while the PTFE does not have any dense skin layers on either side of the membrane. The dense skin layer decreases the mass transfer coefficient. It is possible that the lower performance of the PVDF membrane came from the dense skin layer. Xu et al. [17] reported that skinless inner and outer hollow fiber membranes could enhance the absorption rate in GAM systems.

The effect of MEA concentration on the $CO_2$ flux is shown in Fig. 10. This experiment was done with PTFE membranes to study the effect of solution concentration on the absorption performance. MEA solution was used as an absorbent with concentrations of 1.0 and 3.0 M. It was clear that the $CO_2$ fluxes increased with an increasing liquid velocity and solution concentration. When the solution concentration and liquid velocity increased, more free amine was available, leading to a higher reaction rate between $CO_2$ and amine. However, solution viscosity has an effect on the absorption performance when using a high solution concentration. According to deMontigny et al. [9], absorption performance can decrease with highly concentrated MEA solutions because of the effect of viscosity.

The wettability of membranes was studied by many researchers [5,11,13]. They found that membrane wetting has a significant effect on $CO_2$ absorption flux as well as the overall mass transfer coefficient. The effect of operating time on PTFE and PVDF membranes is shown in Fig. 11. The PTFE membranes maintained the $CO_2$ absorption flux after 60 h of operating time because of its hydrophobicity. As reported by deMontigny et al. [11], the PTFE membranes could maintain the same overall mass transfer coefficient after 80 h of operation. As seen in Fig. 11, after 40 h of operation the PVDF membranes had an absorption performance that dropped by roughly 33%. After 60 h of operation the absorption performance had a reduction by roughly 40%. When the membrane pore is totally filled by liquid, the absorption flux does not increase with an increase the liquid velocity. In Fig. 11, the absorption flux of PVDF membrane decreased during operation. The reduction in absorption flux was quite high after 40 h of operation. The performance dropped slightly more after an additional 20 h of operation (60 h in total). The reduction in the PVDF membrane absorption performance indicated that the PVDF membranes were partially wetted by MEA solution. Membrane modification can increase hydrophobicity [24,25]. PVDF membranes need to be extensively studied in GAM applications because the performance is acceptable and the cost is significantly cheaper than PTFE membranes.

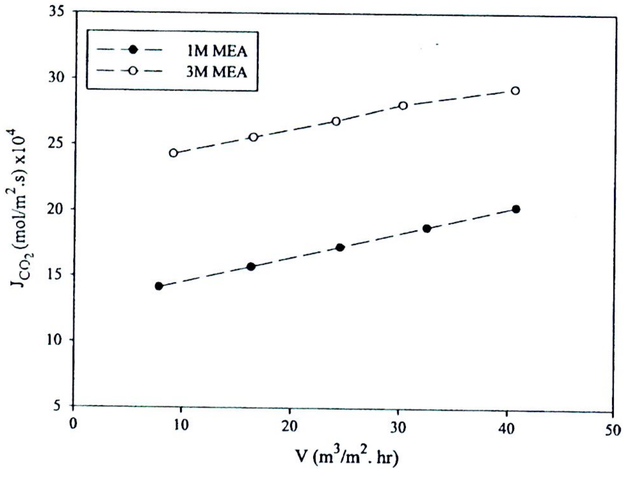

**Fig. 10.** Effect of solution concentration on $CO_2$ flux (PTFE) (fresh aqueous MEA solution, 15% $CO_2$, inert gas flow rate 0.30 mol/min).

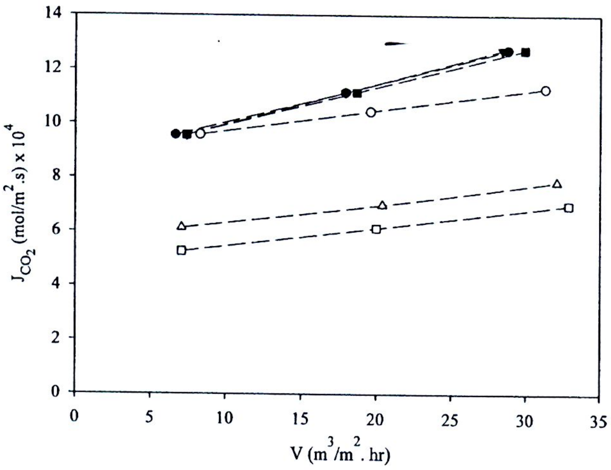

**Fig. 11.** Effect of operating time on membrane performance (1.0 M aqueous MEA solution, $CO_2$ loading 0.20–0.22 mol $CO_2$/mol amine, 15% $CO_2$, inert gas flow rate 0.30 mol/min).

## 5. Conclusions

Hollow fiber membrane contactors are an alternative technique for absorption systems. There are many membranes that have been studied in GAM systems. Recently, PVDF membranes have been investigated by many researchers. In this work, PTFE, PP and PVDF membranes were studied for comparing $CO_2$ absorption performance and membrane resistance.

In physical absorption experiments, the PVDF membrane performed better than the PP membrane. The PVDF membrane had a membrane resistance around 47% of the total resistance, whereas the PTFE and PP membranes had membrane resistances of 39% and 43%, respectively, of the total resistance. The membrane resistance increased because of membrane wetting. In chemical absorption experiments, the $CO_2$ absorption flux had the same results that were seen in the physical experiment: PTFE > PVDF > PP. The PVDF membrane performed better than PP membranes in the physical and chemical absorption experiments. In terms of stability, the PTFE membrane could maintain their performance after 60 h of operation, while the PVDF membrane had a reduction in absorption performance. However, based on the cost of PVDF membranes, and their comparable performance to PTFE membranes, they remain a membrane of interest.

## Acknowledgements

The authors gratefully acknowledge the financial support from the Thailand Research Fund (TRF), the Commission on Higher Education, Thailand through the Royal Golden Jubilee Ph.D. Program, the TRF Senior Research Scholar Grant and from the International Test Centre for $CO_2$ Capture, University of Regina. We also would like to thank Ms. Aihua Yang for helping us to manufacture the PVDF membranes and Sumitomo Electric Fine Polymer, Japan for providing PTFE membranes for research.

## References

[1] A. Gabelman, S. Hwang, J. Membr. Sci. 159 (1999) 61–106.
[2] J.L. Li, B.H. Chen, Sep. Purif. Technol. 41 (2005) 109–122.
[3] Z. Qi, E.L. Cussler, J. Membr. Sci. 23 (1985) 321–332.
[4] Z. Qi, E.L. Cussler, J. Membr. Sci. 23 (1985) 333–345.
[5] R. Wang, H.Y. Zhang, P.H.M. Feron, D.T. Liang, J. Membr. Sci. 46 (2005) 33–40.
[6] S. Karoor, K.K. Sirkar, Ind. Eng. Chem. Res. 32 (1993) 674–684.
[7] A. Malek, K. Li, W.K. Teo, Ind. Eng. Chem. Res. 36 (1997) 784–793.
[8] P. Kosaraju, A.S. Kovvali, A. Korikov, K.K. Sirkar, Ind. Eng. Chem. Res. 44 (2005) 1250–1258.
[9] D. deMontigny, P. Tontiwachwuthikul, A. Chakma, Ind. Eng. Chem. Res. 44 (2005) 5726–5732.
[10] N. Nishikawa, M. Ishibashi, H. Ohta, N. Akutsu, H. Matsumoto, T. Kamata, H. Kitamura, Energy Convers. Manage. 36 (1995) 415–418.
[11] D. deMontigny, P. Tontiwachwuthikul, A. Chakma, J. Membr. Sci. 277 (2006) 99–107.
[12] H.A. Rangwala, J. Membr. Sci. 112 (1996) 29–240.
[13] S. Atchariyawut, C. Feng, R. Wang, R. Jiraratananon, D.T. Liang, J. Membr. Sci. 285 (2006) 272–281.
[14] K.K. Sirkar, Other new membrane processes, in: W.S.W. Ho, K.K. Sirkar (Eds.), Membrane Handbook, Chapman & Hall, New York, 1992, pp. 885–899.
[15] G.F. Versteeg, W.P.M. van Swaalj, J. Chem. Eng. Data 33 (1988) 29–34.
[16] M. Mavroudi, S.P. Kaldis, G.P. Sakellaropoulos, J. Membr. Sci. 272 (2006) 103–115.
[17] A. Xu, A. Yang, S. Young, D. deMontigny, P. Tontiwachwuthikul, J. Membr. Sci. 311 (2008) 153–158.
[18] S.R. Wickramasinghe, M.J. Semmens, E.L. Cussler, J. Membr. Sci. 62 (1991) 371–388.
[19] W. Horeitz, Association of Official Analytical Chemists (AOAC) Methods, 12th ed., George Banta, 1975.
[20] M.C. Yang, E.L. Cussler, AIChE J. 32 (1986) 1910–1916.
[21] H. Mahmud, A. Kumar, R.M. Narbaitz, T. Matsuura, J. Membr. Sci. 179 (2000) 29–41.
[22] H. Matsumoto, H. Kitamura, T. Kamata, M. Ishibashi, H. Ota, N. Akutsu, J. Chem. Eng. Jpn. 28 (1995) 125–128.
[23] A.G. Asimakopoulou, A.J. Karabelas, J. Membr. Sci. 282 (2006) 430–441.
[24] S. Duan, T. Kouketsu, S. Kazama, K. Yamada, J. Membr. Sci. 283 (2006) 2–6.
[25] Y.H. Zhao, Y.L. Qian, B.K. Zhu, Y.Y. Xu, J. Membr. Sci. 310 (2008) 567–576.
[26] S. Atchariyawut, R. Jiraratananon, R. Wang, J. Membr. Sci. 304 (2007) 163–172.
[27] H. Schönherr, Z. Hruska, G.J. Vancso, Macromolecules 31 (1998) 3679–3685.
[28] V.Y. Dindore, D.W.F. Brilman, F.H. Geuzebroek, G.F. Versteeg, Sep. Purif. Technol. 40 (2004) 133–145.
[29] C.W. Extrand, Langmuir 19 (2003) 646–649.
[30] K. Gotoh, Y. Nakata, M. Tagawa, M. Tagawa, Colloids Surf. A 224 (2003) 165–173.

Separation and Purification Technology 66 (2009) 153–158

Contents lists available at ScienceDirect

Separation and Purification Technology

journal homepage: www.elsevier.com/locate/seppur

# Application of ozonation membrane contacting system for dye wastewater treatment

S. Atchariyawut[a], J. Phattaranawik[b], T. Leiknes[b], R. Jiraratananon[a,*]

[a] *Department of Chemical Engineering, King Mongkut's University of Technology Thonburi, Bangkok 10140, Thailand*
[b] *Department of Hydraulic and Environmental Engineering, NTNU Norwegian University of Science and Technology, S.P. Andersensvei 5, N-7491 Trondheim, Norway*

ARTICLE INFO

*Article history:*
Received 16 July 2008
Received in revised form 2 November 2008
Accepted 10 November 2008

*Keywords:*
Membrane contactor
Ozonation
Reactive dye
Decolorization
Auxiliary reagents

ABSTRACT

The aims of this work are to investigate the ozone mass transfer in the hollow fiber membrane contactor for ozonation of dye solution and to study the effect of dyeing auxiliary reagents on decolorization performance. Effects of hydraulic retention time (HRT) in the system and membrane on color removal were also investigated in the continuous ozonation membrane contacting system. Dye used in this experiment was C.I. Reactive Red 120 (RR 120) and sodium carbonate ($Na_2CO_3$) and sodium chloride (NaCl) were used as additives. It was found that the ozone flux increased with increasing liquid velocity for water and dye solution as a liquid phase. Change in gas velocity did not influence the ozone flux. Therefore, the main mass transfer resistance for ozonation in membrane contactor was in liquid phase for both cases. The presence of $Na_2CO_3$ in the dye solution resulted in increasing the ozone flux, conversely, the ozone flux decreased when NaCl was added. Decolorization performance by ozone was inhibited when $Na_2CO_3$ existed in the dye solution. For ozonation membrane contacting system, the dye color removal performance increased with increasing HRT of the system. Additionally, decolorization of dye solution increased with decreasing HRT in the membrane module.

## 1. Introduction

Textile industry consumes and discharges high amount of water. The effluents from textile industry contain high concentration of organic and inorganic compounds, and are strong in color. The majority of dyes used in the textile industry is the azo dyes, accounting for more than 50% of all commercial dyes. These dyes include azo groups (N=N) mainly bound to substituted benzene or naphthalene rings. In addition, they contain sulphonic acid groups in order to confirm both their solubility in the water and their ability to dye wool, silk, nylon, cotton, cellulose acetate and others. Sulphonic acid group can be deactivated by electrophilic attack and biological degradation taking place in the common wastewater treatment process. Thus, treatment of the effluents by conventional chemical coagulation and biological methods to reduce biological oxygen demand (BOD), and chemical oxygen demand (COD), and suspended solid are generally satisfactory, except the removal of dye color. The azo dye removal in biological wastewater treatment process is typically based on the anaerobic treatment concept [1]. Advanced oxidation processes (AOP) including UV/$H_2O_2$, and Fenton's reagent have been applied [2,3] to decolorize the effluents containing dyes. A comparison between different oxidants was carried out [4] and it was found that ozone generally produces nontoxic products which are finally converted to $CO_2$ and $H_2O$ if the conditions are drastic enough.

In the previous study [5], the removal of direct dye by ozonation was shown to be a promising technique. Ozonation is an attractive AOP technology because it can destroy the double bonds often related with dye colors. Ozone is a powerful oxidant for water and wastewater treatment. Once dissolved in water, ozone reacts with a great number of organic compounds in two different ways: by direct oxidation as molecular ozone or by indirect reaction through formation of secondary oxidants like free radical species, in particular, the hydroxyl radicals. Both ozone and hydroxyl radicals are strong oxidants and are capable of oxidizing compounds such as dyes. The benefit of ozone on environmental application is well known and has been extensively discussed in the previous works [6,7].

A conventional equipment to perform ozonation is a bubble column which is simple in design and operation [5,8,9]. However, the disadvantages of the bubble column have been addressed, for example, flooding, uploading, emulsion, and foaming. These problems can be avoided by using a gas–liquid membrane contactor [10]. Gas–liquid membrane contactor is a membrane process in which the hydrophobic porous membranes are employed as a barrier to separate gas and liquid phases. Fig. 1 depicts the mass transfer mechanism of the interested gas for a non-wetted (gas

---

* Corresponding author. Tel.: +66 2470 9222; fax: +66 2428 3534.
*E-mail address:* ratana.jir@kmutt.ac.th (R. Jiraratananon).

1383-5866/$ – see front matter © 2008 Elsevier B.V. All rights reserved.
doi:10.1016/j.seppur.2008.11.011

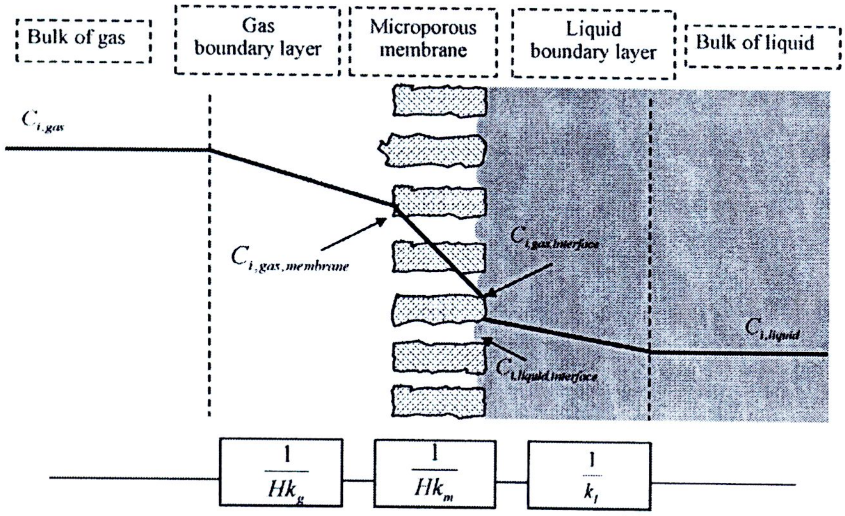

**Fig. 1.** Mass transfer regions and resistance-in-series in non-wetted membrane contactor.

filled pores) gas–liquid membrane contactor. It can be seen that the feed gas has to encounter with three resistances in series, i.e. gas phase boundary layer, membrane and liquid phase boundary layer. The advantages of the membrane contactors over conventional contactors lie in the high interfacial area and the hydrodynamic decoupling of the phases. Membrane contactors have played an important role in the processes such as liquid–liquid extraction and gas–liquid absorption. The most widely application is the absorption of $CO_2$ by both physical and chemical absorption [10,11].

The reaction kinetics of ozonation of humic substances was studied using a hollow fiber membrane contactor [12]. Leiknes et al. [13] carried out the decolorization of natural organic matter (NOM) by ozonation using a tubular membrane module to study the effects of the flow rates and temperatures of the liquid phase on ozone transfer and on the enhancement of mass fluxes. Mass transfer study on a flat-sheet membrane contactor for ozonation of NOM and indigo reagent I was also recently reported [14]. Ozonation of wastewaters by membrane contactors were also reported by few investigators [10,15].

Although there is a number of previous works on ozonation of dye solution or dyeing effluent [5,8,9], these investigations used conventional bubble columns for their studies. Due to the disadvantages of the bubble column mentioned earlier, it is the interest of this work to apply a hollow fiber membrane contactor for ozonation of dye solution. The objective of this work was to study the mass transfer in the ozonation membrane contactor by varying gas and liquid phase velocity. Effects of dyeing auxiliary reagents, i.e. $Na_2CO_3$ ad NaCl were also investigated. The continuous ozonation membrane contacting system was designed and examined for decolorization of dye solution. The results of this work were expected to provide useful experimental data for application of a membrane contactor for ozonation of dyeing effluents.

## 2. Materials and methods

### 2.1. Ozone generator

The ozone generator used in this work was developed by the Department of Hydraulic and Environmental Engineering, Norwegian University of Science and Technology (NTNU) under the Technology Enabled Universal Access to Safe Water (TECHNEAU) project funded by the European Commission for achieving the low-cost ozoniser for potable water treatment. Ozone generation technology which was employed for the generator was dielectric barrier discharge in the surface discharge configuration. It can be called as PURION technology which was extremely flexible in design, allowing easy adaptation of the generator to any specific applications. The use of surface discharge in ozone generation is relatively new, and was pioneered by Masuda et al. [16]. Under the development project, ceramic material and high purity stainless steel were selected to be used as dielectric layer and high voltage electrode, respectively, in order to provide a high efficiency and competitive price of ozoniser. Since, 68% of the energy input into ozone generators is expended as heat; the heat has to be removed from the discharge and reactor surfaces in order to enhance the ozone production and efficiency. In the PURION ozone generator, water was used to provide the more efficient cooling media.

### 2.2. Experimental setup

The Microza hollow fiber PVDF membrane module (UMP-153) used in this work was purchased from Pall Corporation. The specifications of the membrane are listed in Table 1. The azo reactive dye C.I. Reactive Red 120 manufactured and kindly provided by DyStar Textilfarben GmbH & Co. and Dystar Thai, Ltd. Molecular formula of RR 120 and its molecular weight are $C_{44}H_{24}Cl_2N_{14}O_{20}S_6H_6$ and 1337.34 g/mol, respectively. A reagent grade NaCl and $Na_2CO_3$ used as additives in dye solution were bought from Merck, Ltd. Pure oxygen (99.8%) was used to produce ozone in all experiments.

The experimental works were divided into two parts. Firstly, the mass transfer study and effect of dyeing auxiliary reagents on color removal were carried out. The experimental setup is schematically shown in Fig. 2. The ozone was produced with PURION ozone generator by pure oxygen. The ozone concentration in the gas phase was measured by the ozone analyzer, BMT 961 (UV-photometric method) with 1.5% measurement uncertainty. For all runs, the

**Table 1**
Specifications of the hollow fiber membrane module (UMP-153) used.

| | |
|---|---|
| Membranes | Polyvinylidene fluoride |
| Fiber o.d. (mm) | 3.8 |
| Fiber i.d. (mm) | 2.6 |
| Module i.d. (mm) | 35 |
| Membrane pore size (μm) | 0.2 |
| Membrane porosity | 0.7 |
| Number of fibers | 50 |
| Effective module length (mm) | 200.3 |
| Effective contact area ($m^2$) | 0.084 |

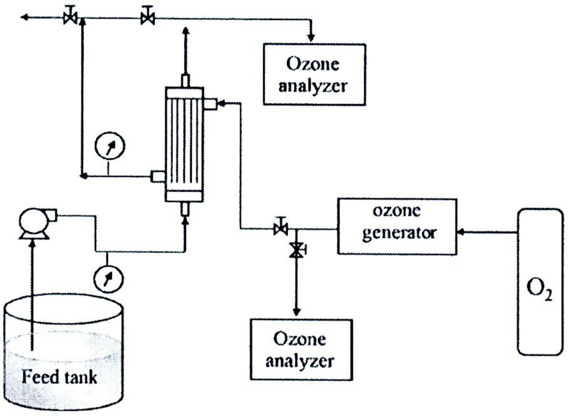

**Fig. 2.** Schematic diagrams of a gas–liquid membrane contactor unit.

ozone concentration in the feed stream was kept at 50 mg/l and it was fed through the shell side of the membrane module. The pure water or dye solution was pumped by peristaltic pump (L/S® Easy-load® II, Masterflex) from the feed tank into the lumen side of the hollow fibers. The liquid phase was fed as a single pass through and the contact time was adjusted by tuning the liquid flow rate for this part of the experiment. The second part is the study of continuous ozonation membrane contacting system on a dye decolorization performance. The experimental equipments were setup the same as the first part, besides, an additional tank namely reactor tank was added into the system as shown in Fig. 3. This reactor was used to separate the effect of system retention time and the liquid phase mass transfer coefficient. Therefore, the contact time of dye and ozone in the system and the mass transfer coefficient in the membrane can be independently controlled by using peristaltic pump P1 and P2, respectively. This conceptual design provided the continuous ozonation membrane contacting system which is suitable for the dye effluent treatment processes.

Ozone concentration in the water was measured by colorization method by indigo reagent [17]. The ozone fluxes for pure water were determined by mass balance in the liquid phase, whereas ozone fluxes for dye solution were calculated by the mass balance in the gas phase. For all experiments, the synthetic dye wastewater was used. The dye concentration was kept to be constant at 300 mg/l and the auxiliary reagents used were 40 g/l NaCl and $Na_2CO_3$. The color of the RR 120 dye was measured with U 3000 spectrophotometer, Hitachi at 535 nm wavelength. The conductivity and pH of the dye solution after ozonation were determined by LF537 Microprocessor Conductivity Meter, WTW and ION83 Ion Meter Radiometer, respectively. COD of the tested effluents were measured by COD cuvette test provided by HACH LANGE GmbH.

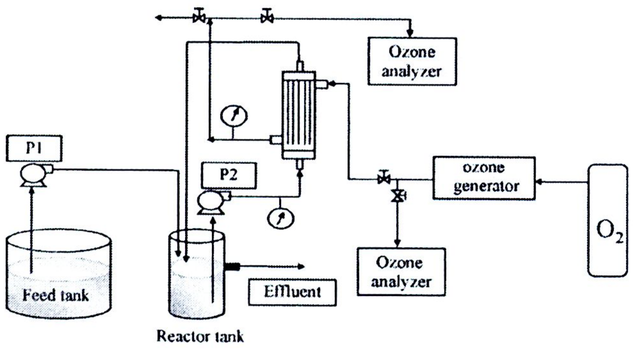

**Fig. 3.** Schematic diagrams of an ozonation membrane contacting system.

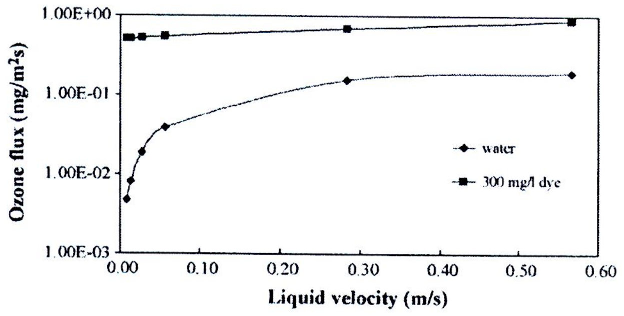

**Fig. 4.** Effect of liquid velocity on ozone flux (gas flow rate: 350 ml/min; operating temperature: 25 °C).

## 3. Results and discussion

### 3.1. Mass transfer analysis in ozonation membrane contactor

With the aim of gaining a better understanding of the ozone mass transfer phenomena in the membrane contactor, the effects of gas and liquid velocities on the ozone flux were studied for both in pure water (physical absorption) and in dye solution (chemical absorption) system.

Fig. 4 depicts the effect of liquid phase velocity on ozone flux using pure water and 300 mg/l dye solution as liquid phase. The ozone flux increased with increasing liquid velocity for physical and chemical experiments since the liquid phase mass transfer coefficient ($k_l$) was enhanced with the liquid velocity. The change of ozone flux with water velocity was larger than that of dye solution. Wang et al. [18] reported the similar trend of the results of effect of liquid phase velocity on the flux for both physical and chemical reaction systems. For the mass transfer system with the presence of chemical reaction, the mass transfer rate can be improved as the liquid mass transfer coefficient was increased. As ozone can chemically react with dye; therefore, the ozone flux in dye solution was higher than that in the pure water. The effects of gas velocity on the ozone flux for pure water and 300 mg/l dye solution were presented in Fig. 5. It can be seen that the change of gas velocity did not affect the ozone flux for both systems.

According to Fig. 1, it can be seen that there are three mass transfer steps for ozone transport in the membrane contacting process, i.e. gas phase, membrane and liquid phase. The overall mass transfer resistance is a summation of the individual mass transfer resistance in each phase, which can be shown as:

$$\frac{1}{K_{ol}} = \frac{1}{k_l} + \frac{d_o}{Hk_m d_{ln}} + \frac{d_o}{Hk_g d_i} \tag{1}$$

where $K_{ol}$ is the overall mass transfer coefficient-based liquid-phase (m/s), $k_l$, $k_m$, $k_g$ are the individual mass transfer coefficients

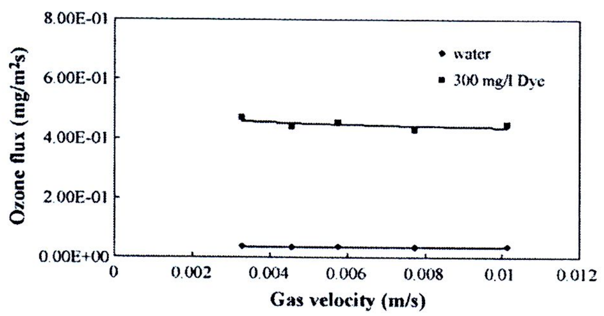

**Fig. 5.** Effect of gas velocity on ozone flux (liquid flow rate: 18 ml/min; operating temperature: 25 °C; Re: 165).

of the liquid phase, membrane and gas phase, respectively. $H$ represents Henry's constant. $d_i$, $d_o$, $d_{ln}$ are the inner, outer and logarithmic mean diameters of the fibers, respectively.

At 295 K, the Henry's constant ($H$) for ozone in water is 3.823 $(mg/l)_g/(mg/l)_l$ [14]. Therefore, for ozonation in pure water, the overall mass transfer coefficient was in the range of $5.30 \times 10^{-7}$ to $1.84 \times 10^{-5}$ m/s for these experimental conditions as the liquid velocity was varied from 0.01 to 0.5 m/s (see also Fig. 4). The overall mass transfer coefficient also increased with liquid velocity. The trend of the overall mass transfer coefficient should be the same for ozonation of dye solutions. Unfortunately, the overall mass transfer coefficient for ozone and dye solution system cannot be determined due to lack of Henry's constant data of dye and ozone. However, it would be expected that the overall mass transfer coefficient of the ozone in the dye solution should be higher than that in pure water according to the chemical reaction between ozone and dyes.

Referring to the above results and Eq. (1), it can be suggested that the main mass transfer resistance was in the liquid phase for these two cases (pure water and 300 mg/l dye solution used as liquid phase). The study of mass transfer would be useful in the operation of membrane contacting system for ozonation dye effluents.

### *3.2. Effect of auxiliary reagent on dye effluent treatment*

NaCl and $Na_2CO_3$ are generally used as the auxiliary reagents since they can act as exhausting and retarding agents. Fig. 6 shows the effect of dye additives on the ozone flux. It can be seen that the ozone flux increased when the $Na_2CO_3$ was in dye solution. The pH of dye solution was increased when $Na_2CO_3$ was added leading to decomposition of ozone molecule to be $OH^\bullet$ radical. This resulted in increasing the mass transfer coefficient in the liquid phase due to the enhancement of ozone concentration difference between gas and liquid phases. When NaCl was added into the dye solution, the ozone fluxes were found to be decreased due to the decrease of gas solubility in the salt solution (salting out effect) [19].

The effects of dye auxiliaries on the ozonation performance were presented as a function of ozonation time. The decolorization performances of ozone in dye solution with and without additive reagents are shown in Fig. 7 where $A_0$ and $A$ represent the absorbance of dye solution before and after ozonation, respectively. It was found that, after 30 min ozonation time, the color in the dye solution without any additives decreased around 64% and the decolorization of the dye solution with the presence of $Na_2CO_3$ as an additive was around 40% of the initial dye concentration. $Na_2CO_3$ in the dye solution inhibited the decolorization performance of the ozone. For the effect of NaCl in the dye solution, it can be found that the addition of NaCl slightly affected the decolorization performance of the ozone. Ozone can react with dyes in two different ways, i.e. direct ozone molecular and indirect radical type chain reactions. At the high pH of the dye solution, $O_3$ molecules can decompose into $OH^\bullet$ radical which is less selective than ozone molecule. The pH of the solution was around 11 (also see Fig. 8) when 40 g/l $Na_2CO_3$ was added into the dye solution. Therefore, when the solution was consisted of $Na_2CO_3$, the decolorization performance of the dye solution was decreased due to the decrease of the double bond selectivity. In addition, $OH^\bullet$ radical can be scavenged by $CO_3{}^{2-}$ resulted in wasting the $OH^\bullet$ oxidant with dye [8].

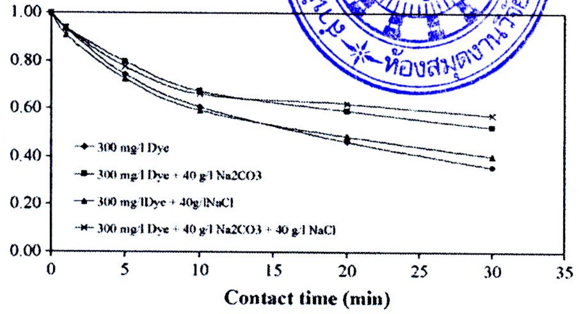

**Fig. 7.** Effects of ozonation time and dye auxiliary reagents on decolorization (gas flow rate: 350 ml/min; operating temperature: 25 °C).

The effects of ozonation time and auxiliary reagents on pH of the dye solution are presented in the Fig. 8. The pH of 300 mg/l dye solution decreased from 7.44 to 3.18 during 30 min operation time. The decrease of pH was caused by the oxidation of azo groups and aromatic rings which produced organic and inorganic acid such as oxalic and formic acid [20]. When the dye solution contained 40 g/l $Na_2CO_3$, the pH of the solution maintained roughly 11 throughout 30 min of ozonation due to the high concentration of $Na_2CO_3$. The addition of NaCl into the dye solution did not influence the change of pH solution as well as the ozonation oxidation performance.

Table 2 shows the effect of ozonation time and dye auxiliaries on the solution conductivity. For the dye solution without additives, the solution conductivity increased with operation time from $2.7 \times 10^{-4}$ to $5.8 \times 10^{-4}$ mS/cm. This is because the dye molecules were decomposed by the ozone resulting in generating small ions such as organic acids, $SO_2{}^{2-}$, $NO_2{}^-$, $NO_3{}^-$, and $NH_4{}^+$. The decomposition pathways of azo reactive dye C.I. Reactive Red 120 was presented in the literature [20]. Changing in conductivity of the dye solution can confirm that the dye molecules were decomposed by ozonation. For the dye solution in the presence of assisting reagents, the observed solution conductivity was found to be constant with the ozonation time due to the high concentration of additives.

The effect of ozonation time on COD removal of the dye solution and dye solution consisting of 40 g/l $Na_2CO_3$ were shown in Fig. 9. The COD removal of dye solution increased with increasing ozone contacting time. The COD decreased by roughly 32 and 23% of the

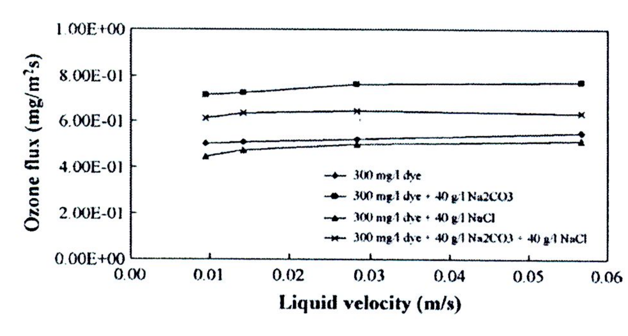

**Fig. 6.** Effects of liquid velocity and dye auxiliary reagents on ozone flux (gas flow rate: 350 ml/min; operating temperature: 25 °C).

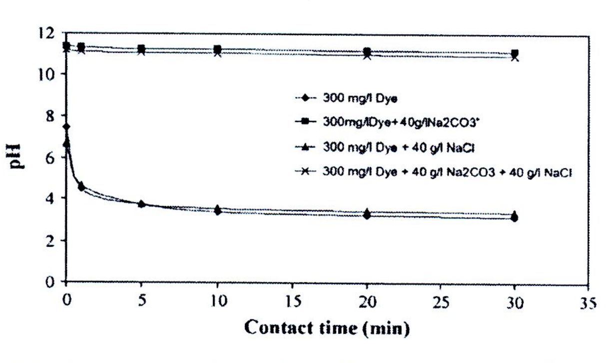

**Fig. 8.** Effects of ozonation time and dye auxiliary reagents on pH (gas flow rate: 350 ml/min; operating temperature: 25 °C).

**Table 2**
Effects of ozonation time and dye auxiliary reagents on conductivity (gas flow rate: 350 ml/min; operating temperature: 25 °C).

| Contact time (min) | Conductivity (mS/cm) | | | |
|---|---|---|---|---|
| | 300 mg/l dye | 300 mg/l dye + 40 g/l $Na_2CO_3$ | 300 mg/l dye + 40 g/l NaCl | 300 mg/l dye + 40 g/l $Na_2CO_3$ + 40 g/l NaCl |
| 0 | $2.65 \times 10^{-4}$ | 38.4 | 55.8 | 78.2 |
| 1 | $2.90 \times 10^{-4}$ | 38.6 | 55.9 | 78.1 |
| 5 | $3.70 \times 10^{-4}$ | 38.5 | 55.9 | 78.3 |
| 10 | $4.50 \times 10^{-4}$ | 38.6 | 56.0 | 78.3 |
| 20 | $5.40 \times 10^{-4}$ | 38.3 | 56.1 | 78.2 |
| 30 | $5.80 \times 10^{-4}$ | 38.3 | 56.1 | 78.2 |

initial COD for 300 mg/l dye solution and 300 mg/l dye containing 40 g/l $Na_2CO_3$ solution, respectively. The COD removal efficiency of ozonation process was inhibited when the $Na_2CO_3$ was added into the dye solution. This is because ozone was scavenged with $CO_3^{2-}$ resulted in losing ozone oxidizing power with dye in the solution [8]. The COD determination cannot be carried out when the solution composed with NaCl because of positive interference of chloride ions ($Cl^-$) with the COD measurement.

The ratio of $O_3$ used/COD eliminated is one of the appropriate parameters indicating the ozonation efficiency for COD removal in the dyeing effluent treatment processes. At 30 min residence time of 300 mg/l dye solution in the membrane module, the $O_3$ used/COD eliminated ratio was approximately 1.85 g $O_3$/g COD. It means that one gram of COD removal was required to utilize 1.85 g of ozone. The ratio of $O_3$ used/COD eliminated was 5.15 g $O_3$/g COD at 5 min residence time of dye solution. This indicated that as the residence time increased the ozonation efficiency increased. In order to gain the highest ozonation efficiency, the residence time of the dye solution has to be considered.

### 3.3. Decolorization performance in ozonation membrane contactor system

Wastewater from dyeing process is generally treated in a continuous system due to the large volume of the effluent. In this part, the study of ozonation in membrane contacting system was carried out by adding the reactor tank (see also in Fig. 3) in order to achieve the continuous concept. In addition, the effect of hydraulic retention time (HRT) in the membrane and system can be individually investigated. HRT of dye solution in the system can be varied by adjusting the dye solution flow rate using peristaltic pump P1 (see Fig. 3). The change of dye solution flow rate resulted in the ozone–dye contacting time. In addition, the HRT of the membrane was controlled by using peristaltic pump P2 (see Fig. 3). The mass transfer in the system can be individually controlled by tuning the HRT in the membrane contactor.

The effects of HRT system on dye decolorization is presented in Fig. 10. It can be found that the color removal performance decreased with decreasing the retention time in the system. The dye decolorization at steady state was found to be 44 and 68% for 2 and 4 h of HRT system at the same 0.1 min of HRT membrane, respectively. Fig. 11 shows the comparison of HRT membrane with the same 4 h HRT system on dye decolorizaiton performance. As the HRT membrane was decreased by increasing the liquid flow rate, the decolorization performance increased. It can be explained that the mass transfer coefficient was increased with increasing liquid velocity. It is clear that the decolorization performance depends upon both HRT system and membrane. Long system retention time and low retention time in the membrane were the suitable conditions for color removal by ozonation membrane contacting system.

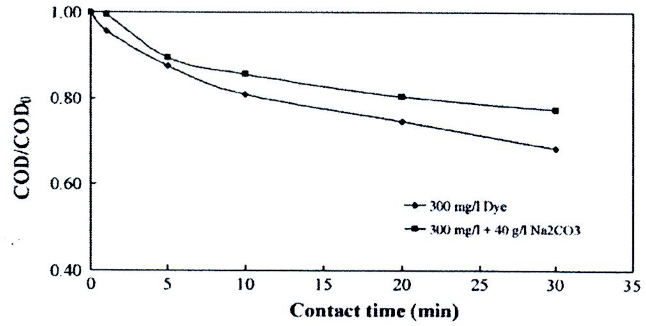

**Fig. 9.** Effects of ozonation time and $Na_2CO_3$ on COD removal (gas flow rate: 350 ml/min; operating temperature: 25 °C).

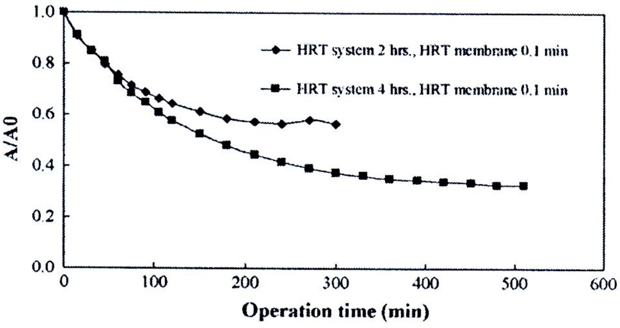

**Fig. 10.** Effects of ozonation time and HRT system on decolorization (gas flow rate: 350 ml/min; operating temperature: 25 °C).

Fig. 12 illustrates the effect of auxiliary dyeing reagents on the decolorization performance in the ozonation membrane contacting system. The experiments were performed at 4 h HRT system and 0.1 HRT membranes for both cases. The decolorization performance decreased around 10% when the auxiliary reagents existed in the dye solution as discussed in Section 3.2. Thus, the use of ozonation membrane contactor system can help to decrease the dye color in the effluent. In addition, this process can be continuously operated and provided the good performance for dye effluent decolorization.

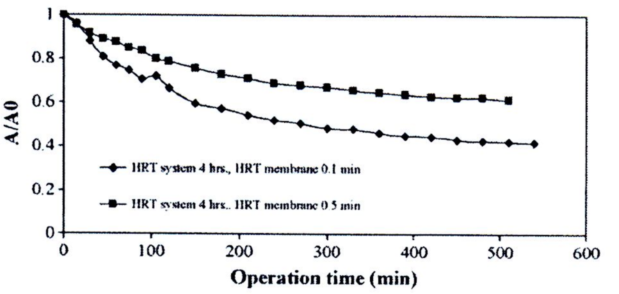

**Fig. 11.** Effects of ozonation time and HRT membrane on decolorization (gas flow rate: 350 ml/min; operating temperature: 25 °C).

Separation and Purification Technology 66 (2009) 313–321

Contents lists available at ScienceDirect

Separation and Purification Technology

journal homepage: www.elsevier.com/locate/seppur

# Experimental study on dealcoholization of wine by osmotic distillation process

Satit Varavuth, Ratana Jiraratananon*, Supakorn Atchariyawut

*Department of Chemical Engineering, King Mongkut's University of Technology Thonburi, Bangkok 10140, Thailand*

ARTICLE INFO

*Article history:*
Received 9 October 2008
Received in revised form 14 December 2008
Accepted 15 December 2008

*Keywords:*
Dealcoholization
Hollow fibers
Mass transfer study
Osmotic distillation
Stripping solutions
Wine

ABSTRACT

The types of stripping solutions and influences of operating parameters including feed and stripping velocities, system temperatures on the ethanol removal of ethanol solution and wine by using osmotic distillation (OD) process were investigated along with the mass transfer study. The experiments were performed by the membrane contactor unit using 0.2 μm pore size diameter microporous PVDF hollow fibers. Three different types of stripping solutions (pure water, 50% (w/w) glycerol, 40% (w/w) $CaCl_2$) were used to compare the dealcoholization performance of the process. Aroma loss study was also carried out by using ethyl acetate and iso-amyl alcohol solutions to represent the major aroma compounds presenting in the real wine. Long-term tests for ethanol solution and wine were also performed in order to evaluate the dealcoholization performance of OD process.

Using water as a stripper presented more promising result compared with the others because it provided higher ethanol flux and lower counter transport of water due to the water activity differences. The results of the study showed that the ethanol flux and ethanol removal performance were enhanced by the increase of feed and stripping solution velocities and system temperatures. Aroma components were significantly lost during the process operation. The ethanol concentration in the wine can be reduced to roughly 34% of the initial concentration for 360 min operation.

## 1. Introduction

Wine is the one of alcoholic beverages which is mainly made from the fermentation of grape juice. Generally, wines are composed of 10–15% (v/v) alcohol, sugars, proteins, antioxidant agents, and vitamins. Many benefits have been found in moderate drinkers of red wines such as cancer protection, cardioprotection. However, it is arguable that one of the major defects in many modern wines is excessive ethanol. There is considerable worldwide interest today, for heath reason, in the methods for selective removal of alcohol from wines with minimum effects on their taste, odor or mouthfeel [1,2].

There have been many processes applicable to produce low alcohol content beverages. Spinning cone column [3,4] is operated by two stages, i.e. aroma recovery and ethanol removal. The aroma fraction is added back into dealcoholized wines, thus, it leads to a costly process operation. The membrane processes including reverse osmosis [5,6], vacuum membrane distillation [7], pervaporation [8,9], can also be utilized in reducing alcohol in the beverages. However, the operations of these membrane processes require the high energy consumption for conditioning the suitable operating pressure.

The alternative membrane process which operates at low temperature and atmospheric pressure has been studied and it is called osmotic distillation (OD) [2]. The separation by OD depends upon the vapor pressure differences between feed and stripping streams. OD process is a membrane contactor technique in which the porous hydrophobic membrane separates two aqueous solutions and prevents the solution penetration into the membrane pores. The important advantages of this process are avoiding the thermal damage to components or aroma and flavor loss and low energy consumption. The main application of OD is to concentrate the fruit juices by using brines as stripping solutions. In fruit juice concentration by OD, water transfers from the feed side to the stripping side due to the water activity differences [10,11]. OD process can concentrate the solutions to very high concentrations (60–70° Brix) [12,13].

Due to the advantages of OD, it can be applied as alternative process for removal of alcohol from the alcoholic beverages. There are a few works focusing on the dealcoholization of wines by using OD process. Hogan et al. [2] proposed the concept of using OD for removal ethanol content from wines. It was quoted that OD of high alcohol-content wine at a temperature of 10–20 °C using plain water as the stripping agent can rapidly reduce its alcohol content to 6% with minimum loss of its flavor and fragrance components. In a recent study, Diban et al. [14] investigated the possibility of using hollow fiber membrane contactor to partial dealcoholize synthetic wine solutions at room temperature. The results showed that a partial dealcoholization of 2% (v/v) gave acceptable aroma losses that

---

* Corresponding author. Tel.: +66 2470 9222; fax: +66 2428 3534.
*E-mail address:* ratana.jir@kmutt.ac.th (R. Jiraratananon).

1383-5866/$ – see front matter © 2008 Elsevier B.V. All rights reserved.
doi:10.1016/j.seppur.2008.12.011

**Nomenclature**

| | |
|---|---|
| $A$ | constant in Antoine equation |
| $B$ | constant in Antoine equation |
| $C$ | constant in Antoine equation |
| $C_{f,b}$ | solute concentration of bulk feed stream (%, v/v) |
| $C_{f,m}$ | solute concentration at the membrane surface on feed side (%, v/v) |
| $C_{s,b}$ | solute concentration of bulk stripping stream (%, v/v) |
| $C_{s,m}$ | solute concentration at the membrane surface on stripping side(%, v/v) |
| $d_h$ | hydraulic diameter (mm) |
| $d_o$ | outside diameter of fiber (mm) |
| $D_i$ | inner diameter of module (mm) |
| $J_e$ | ethanol flux (kg/m$^2$ h) |
| $k_f$ | mass transfer coefficient in feed side(m/s) |
| $k_m$ | mass transfer coefficient in membrane (m/s) |
| $k_s$ | mass transfer coefficient in stripping side(m/s) |
| $K_{ov}$ | overall mass transfer coefficient (m/s) |
| $L$ | effective module length (mm) |
| $n$ | number of fiber |
| $P_i^{sat}$ | saturation pressure of $i$ component (Pa) |
| $P_{ef,b}$ | ethanol vapor pressure of bulk feed stream (mmHg) |
| $P_{ef,m}$ | ethanol vapor pressure at the membrane surface on feed side (mmHg) |
| $P_{es,b}$ | ethanol vapor pressure of bulk stripping stream (mmHg) |
| $P_{es,m}$ | ethanol vapor pressure at the membrane surface on stripping side (mmHg) |
| $\Delta P_b$ | ethanol vapor pressure difference (mmHg) |
| $Re$ | Reynolds number |
| $Sc$ | Schmidt number |
| $Sh$ | Sherwood number |
| $T$ | temperature (K) |
| $v_f$ | feed velocity (m/s) |
| $v_s$ | stripping solution velocity (m/s) |

*Greek letters*

| | |
|---|---|
| $\phi$ | packing density (%) |
| $\rho_e$ | ethanol density (g/cm$^3$) |

did not damage the final perceived quality of the product. However, aroma compound losses can reach almost 100% for the most volatile compound when residence time of the feed stream was larger.

The mass transfer in the dealcoholization of wines by OD is different from that of fruit juices. In the concentration of fruit juices by OD, water is the major volatile component transferred through the membrane from the feed side to the stripping side (usually brines). However, in dealcoholization of wines, there is simultaneous transport of both alcohol and water. The direction of water transport depends on the types of stripping solutions and this can affect the performance. In this work, we examined both ethanol flux and water flux of ethanol solution and wine. The main objective of the present work is to study the dealcoholization performance of OD process of ethanol solution and wine. The parameters studied were feed and stripping velocities, system temperature, and types of stripping solutions. Three kinds of stripping solutions, i.e. pure water, glycerol and $CaCl_2$ aqueous solution were selected to be used for evaluating the process performance in term of ethanol and water flux. Water can be potentially used as a stripper for dealcoholization of OD process because it is cheap, convenient, and non-corrosive [14]. $CaCl_2$ and glycerol solutions have been widely utilized in fruit juice concentration by OD process [11,15,16] since they provide the low water activity and non-toxic. However, $CaCl_2$ solution causes equipments corrosion while glycerol solution has a higher viscosity than salt solutions. These three stripping solutions presented the advantages and weaknesses, therefore, it is interesting to use them for comparison of dealcoholization performance in OD process because there is no published work reported on the comparison of ethanol and water transfer, and the analysis of mass transfer coefficients. In this work, the losses of aromas (ethyl acetate and iso-amyl alcohol) during the process operation were also investigated. In addition, the long-term performance of OD process for dealcoholization was also reported.

## 2. Theory

Osmotic distillation is an isothermal membrane transport process which can be operated at ambient temperature and atmospheric pressure. Membranes used for OD are the microporous hydrophobic membranes in order to prevent the aqueous solution penetrating into the pores. The driving force of the process is the partial pressure or vapors pressure differences of the volatile solute in feed and stripping solutions. In the present work, the performances of dealcoholization of real wine and ethanol aqueous solution were investigated. The theory involving ethanol transport in OD process is briefly reviewed as follows.

The transport mechanism of ethanol in dealcoholization by OD process can be divided into three steps: (i) evaporation of ethanol at the membrane pores on the feed side, (ii) diffusion of ethanol vapor through the membrane pores, and (iii) condensation of ethanol vapor in the stripping solution at the membrane pore exit as illustrated in Fig. 1. The flux obtained from the OD can be usually expressed by Eq. (1) in which the driving force corresponds to the bulk concentrations for both sides.

$$J_e = K_{ov}\Delta P_b \tag{1}$$

where $J_e$ is the ethanol flux, $\Delta P_b(P_{ef,b} - P_{es,b})$ is the ethanol vapor difference between bulks of feed and stripping sides, and $K_{ov}$ is the overall mass transfer coefficient which can be given by:

$$\frac{1}{K_{ov}} = \frac{1}{k_f} + \frac{1}{k_m} + \frac{1}{k_s} \tag{2}$$

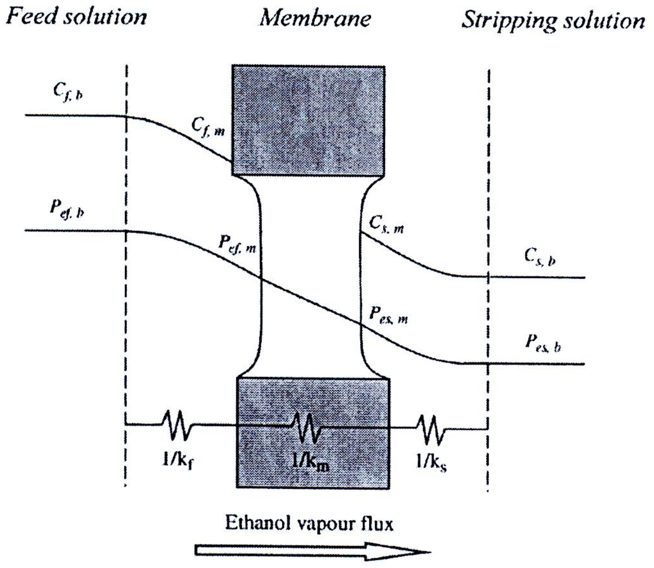

**Fig. 1.** Concentration profile of ethanol in dealcoholization process by OD.

where $k_f$, $k_m$, and $k_s$ represent the mass transfer coefficients of feed boundary layer, membrane, and stripping boundary layer, respectively.

In the dealcoholization process operation, the ethanol vapor transport from the feed side results in the decrease of ethanol concentration at the membrane surface (see Fig. 1). Therefore, it leads to a concentration difference between the bulk and the membrane surface. This phenomenon is known as concentration polarization (CP) affecting the driving force of the process. According to the mass balance across the feed boundary layer at steady state condition, the relationship between bulk concentration ($C_{f,b}$) and the concentration at membrane surface ($C_{f,m}$) is given by:

$$C_{f,m} = C_{s,b} - (C_{s,b} - C_{f,b})/\exp\left(J_e/\rho_e k_f\right) \quad (3)$$

From Eq. (3), in order to obtain $C_{f,m}$, $J_e$ and $C_{s,b}$ can be determined experimentally. The mass transfer coefficient ($k_f$) can be estimated from the appropriate mass transfer correlations.

Therefore, the concentration polarization effect can be quantitatively determined by:

$$\text{CP ratio} = \frac{C_{f,m}}{C_{f,b}} \quad (4)$$

For the mass transfer in the tube side of the hollow fiber membrane, the well-known Graetz–Leveque mass transfer correlation, Eq. (5) has been widely used to predict accurately the tube side mass transfer coefficient ($k_f$) [11,17].

$$Sh = 1.615\left(Re \cdot Sc \cdot \frac{d_h}{L}\right)^{1/3} \quad (5)$$

where *Sh*, *Re*, and *Sc* are the Sherwood number, Reynolds number, and Schmidt number, respectively.

For the mass transfer in the shell side, several correlations have been proposed [18,19]. However, those correlations were derived for evaluating the shell side mass transfer coefficients for solvent extraction or gas stripping system. Therefore, the correlations may be appropriate for those systems and for a limited range of conditions studied. In the present study, the shell side mass transfer correlation for the OD system using hollow fiber membranes presented by Thanadgunbawon et al. [20], Eq. (6) which includes the effect of membrane packing density was applied to calculate the shell side mass transfer coefficient ($k_s$).

$$Sh = \left(-0.4575\phi^2 + 0.3993\phi - 0.0475\right) Re^{(4.0108\phi^2 - 4.4296\phi + 1.5585)} Sc^{0.33} \quad (6)$$

This correlation is applicable when the membrane module packing density ($\phi$) is between 30 and 60% and for laminar flow. The packing density of the membrane module is defined below;

$$\phi = n_{\text{fibers}} \times \left(\frac{d_o}{D_i}\right)^2 \quad (7)$$

where $n_{\text{fibers}}$ is number of fibers, $d_o$ and $D_i$ are the outside diameter of fiber and inner diameter of module, respectively.

**Table 1**
Specifications of PVDF hollow fiber module.

| | |
|---|---|
| Membrane pore size (μm) | 0.2 |
| Inner diameter (mm) | 0.650 |
| Outside diameter (mm) | 1.000 |
| Membrane thickness (um) | 170 |
| Membrane porosity (ε) (%) | 64 |
| Number of fibers | 36 |
| Total length of module (mm) | 250 |
| Total effective length (mm) | 180 |
| Effective area (cm²) | 132.26 |
| Cross-section flow area of the fiber side (mm²) | 11.94 |
| Cross-section flow area of the shell side (mm²) | 20.73 |
| Packing density (%) | 57 |

## 3. Materials and methods

### 3.1. Materials

The hydrophobic porous polyvinylidenefluoride (PVDF) hollow fiber membranes kindly provided by Memcor, Australia (South Windsor, New South Wales, Australia) were used in the experiments. The specifications of the membrane and module are shown in Table 1. Red wine was purchased from Siam Winery, Thailand. Its ethanol content was determined to be 13.2% (v/v). A 99.9% grade ethanol obtained from Merck Ltd., Thailand, a 99.5% grade glycerol purchased from Ajax finechem, and a 99.5% grade $CaCl_2{\cdot}2H_2O$ (Chem-Supply Pty. Ltd., Australia) were mixed with RO water, respectively, to prepare aqueous feed and stripping solutions at desired concentrations. Ethyl acetate (supplied by Lab Scan Asia Co. Ltd., Thailand) and iso-amyl alcohol (purchased from QReC, New Zealand) were also mixed with RO water to prepare the aroma solutions at concentration of 50 and 400 mg/l, respectively. Table 2 summarizes the physical properties of both aroma compounds.

### 3.2. Experimental setup

The experimental setup of the OD system is schematically shown in Fig. 2. The membrane module was established in a vertical position. The feed and stripping solutions were fed into the module by the peristaltic pumps (Easy-Load II, Masterflex model 77201-62). Feed and stripping solutions were co-currently circulated through tube and shell side, respectively. The feed and stripping solution tanks were 1255 and 2000 ml, respectively. The temperatures of feed and stripping side were controlled by water bath (YCW-010 series, KK) attached with temperature controller. The ethanol fluxes were obtained by measuring the feed volume over 1 h operating time in the pipette connected to the feed tank.

### 3.3. Experimental conditions

The operating parameters which affect the ethanol removal performance, i.e. feed velocity, stripping solution velocity, and temperature were investigated. The feed and stripping velocities were varied in the range of 0.1–0.7 m/s (laminar flow region). In order to study the effect of temperature on the separation performance, the system temperature was adjusted at 30, 35, and 40 °C. The effect of types of stripping solutions, i.e. pure water, 50% (w/w) glycerol, and 40% (w/w) $CaCl_2$ on the ethanol removal were studied. 50 mg/l

**Table 2**
Physical properties of aromas [14,22].

| Aroma | Chemical structure | MW (kg/kg mol) | Density (kg/m³) | Boiling point (°C) | Vapor water 35 °C (Pa) | Water solubility 25 °C (mg/l) |
|---|---|---|---|---|---|---|
| Ethyl acetate | $CH_3CO_2C_2H_5$ | 88.10 | 902 | 77.10 | $2.04 \times 10^4$ | 29,930 |
| Iso-amyl alcohol | $(CH_3)CHCH_2CH_2OH$ | 88.14 | 810 | 132.00 | 942.59 | 41,580 |

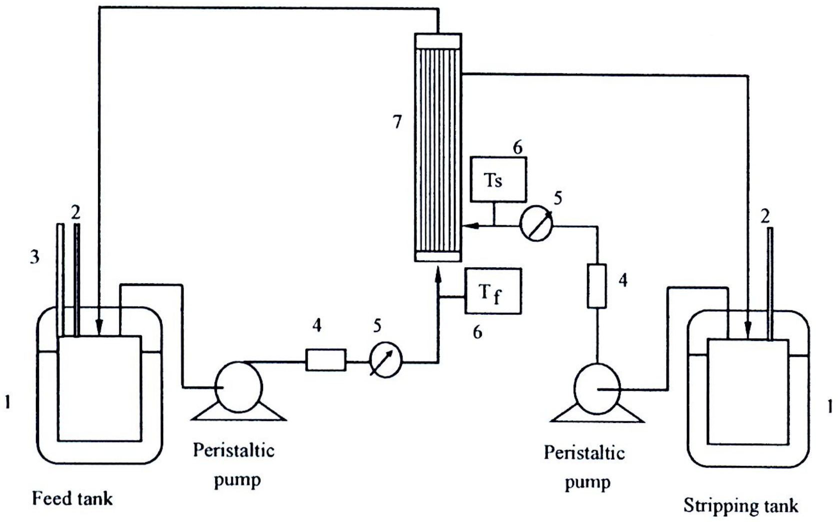

**Fig. 2.** Osmotic distillation experimental setup: (1) water bath, (2) thermometer, (3) pipette, (4) flow meter, (5) pressure gauge, (6) thermocouples, and (7) hollow fiber membrane.

ethyl acetate and 400 mg/l iso-amyl alcohol solutions were used to study the aroma loss in dealcoholization process.

### *3.4. Components analysis and physical properties*

The experiments were performed using ethanol solution (13%, v/v), red wine, and aroma solutions as feeds. Ethanol concentrations were determined by Gas Chromatograph (6890 Hewlett Packard, TCD). The concentrations of ethyl acetate and iso-amyl ethanol were also analyzed by Gas Chromatograph (6890 Hewlett Packard, FID). The physical properties (i.e. densities, viscosities, and diffusivities) of ethanol and stripping solution were obtained from literature [15,21,22].

### *3.5. Membrane cleaning*

After the membrane module was used, it was cleaned by thoroughly flushing the system with RO water both in the tube and shell side without recycling for 5 min. Subsequently, a 1% (w/w) NaOH solution was circulated for 1 h. Finally, the system was rinsed with RO water without recycling for 10 min and then it was dried by using nitrogen gas.

## 4. Results and discussion

### *4.1. Types of stripping solutions*

The performance of three stripping solution, i.e. pure water, 50% (w/w) glycerol, and 40% (w/w) $CaCl_2$, for dealcoholization of 13% (v/v) ethanol solution was compared in terms of ethanol flux, water flux and the reduction of ethanol concentration, as the followings.

### *4.1.1. Ethanol flux*

The ethanol fluxes for three stripping solutions were plotted as a function of stripping solution velocity as depicted in Fig. 3. As the stripping solution velocity was increased, the ethanol fluxes were enhanced due to the increase of Reynolds numbers (see Eq. (6)). Fig. 3 also shows that when pure water was used as a stripping solution, the ethanol flux was higher compared with those of glycerol and $CaCl_2$ solutions. This can be supported by the viscosity values of the stripping solutions. At 30 °C, the viscosity of water is 0.008 g/cm s, which is much lower than that of 50% (w/w) glycerol (0.045 g/cm s) and 40% (w/w) $CaCl_2$ (0.082 g/cm s) [21]. Therefore, at the same stripping solution velocity, the Reynolds number for water was higher, resulting in higher ethanol flux. The results can also

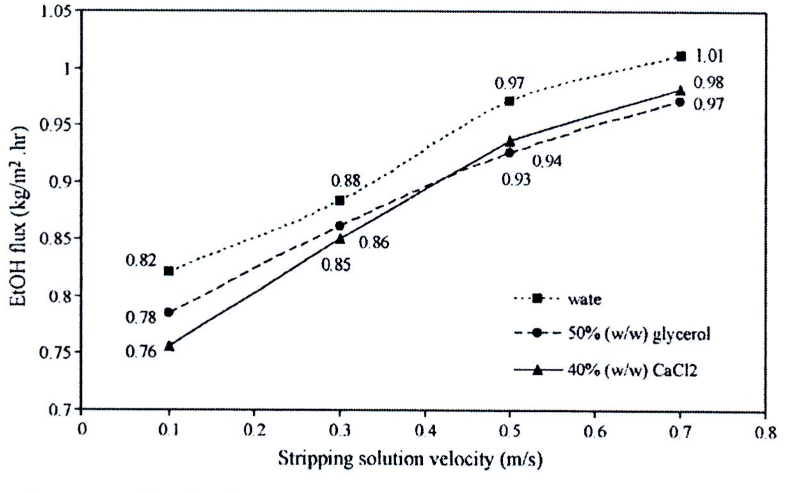

**Fig. 3.** Effects of stripping solution velocity on ethanol flux for using pure water, 50% (w/w) glycerol, 40% (w/w) $CaCl_2$ as stripping solutions (feed: 13% (v/v) ethanol solution, system temperature: 30 °C, feed velocity: 0.4 m/s).

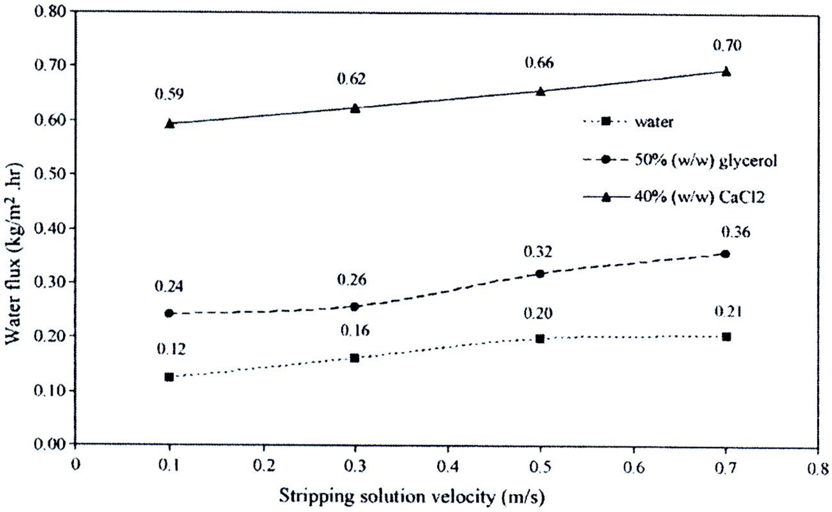

**Fig. 4.** Effects of stripping solution velocity on water flux for using pure water, 50% (w/w) glycerol, 40% (w/w) $CaCl_2$ as stripping solutions (feed: 13% (v/v) ethanol solution, system temperature: 30 °C, feed velocity: 0.4 m/s).

be explained by the diffusion coefficient of ethanol in the stripping agents. The increase of solution viscosity reduces the diffusion coefficients according to the Wilke–Chang equation [22]. This confirms that water is the most suitable stripping solution for dealcoholization when all factors (cost, non-toxicity, and availability) are taken into account.

### 4.1.2. Water flux

In the removal of ethanol by OD, there is simultaneous transfer of both ethanol and water vapor. When water is used as a stripping solution, ethanol transfers from the feed side to the stripping side due to the vapor pressure difference, while water vapor transfers in the opposite direction, i.e. from the stripping side to the feed side as a results of higher water activity of pure water (1.0) compared with that of 13% (v/v) ethanol solution (0.939) [23]. Conversely, water transfers from the feed side to the stripping side when 50% (w/w) glycerol (water activity 0.818) and 40% (w/w) $CaCl_2$ (water activity 0.387) [15] are the stripping solutions. The water fluxes increased with the stripping solution velocity (see Fig. 4) due to the increase of Reynolds numbers as mentioned earlier. The magnitudes of water fluxes were in the following order: 40% (w/w) $CaCl_2$ > 50% (w/w) glycerol > pure water. In practice, the water flux should be of low value so that it least affects the final concentration of ethanol solution or wines. Therefore, this is another advantage of using pure water as a stripping solution.

### 4.1.3. The reduction of ethanol concentration

Fig. 5 shows the effect of stripping velocity on the ethanol reduction performance for pure water, 50% (w/w) glycerol and 40% (w/w) $CaCl_2$ used as the stripping solutions. The ethanol concentration in case of using water as a stripper was lower than others. This can be explained that, apart from the ethanol transport, there was diffusion of water vapor from the stripping to feed side due to the water activity differences (as mentioned in Section 4.1.2) which resulted in decreasing ethanol concentration. Conversely, in case of glycerol and $CaCl_2$ solutions used as stripping solutions, water transferred from feed to stripping side; therefore, ethanol concentration in the feed side was increased.

According to the above results, it can be suggested that the water was more appropriate to be used as the stripping solution for dealcoholization in OD process as the water flux was lowest.

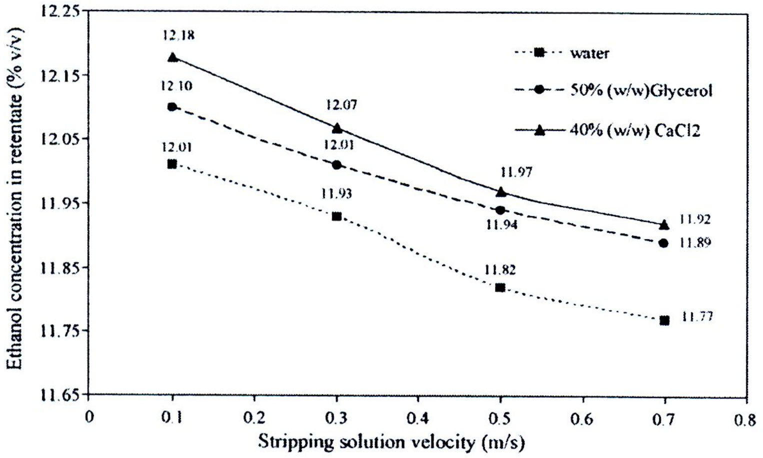

**Fig. 5.** Effects of stripping solution velocity on retentate ethanol concentration for pure water, 50% (w/w) glycerol, 40% (w/w) $CaCl_2$ as stripping solutions (feed: 13% (v/v) ethanol solution, system temperature: 30 °C, feed velocity: 0.4 m/s).

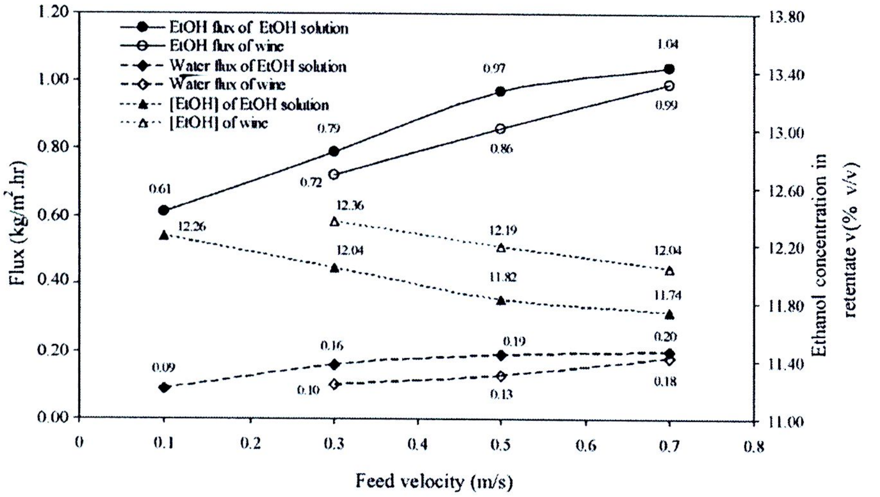

**Fig. 6.** Effects of feed velocity on ethanol and water flux, and retentate concentration of ethanol solution and wine (stripping solution: water, system temperature: 30 °C, stripping solution velocity: 0.4 m/s).

### 4.2. Effect of feed velocity

The ethanol fluxes, ethanol concentrations after 1 h of operation and the reversed water flux from the stripping side are plotted as function with feed velocity for both ethanol solution and wine as presented in Fig. 6. It can be found that the ethanol flux increased with increasing feed side velocity due to increasing the mass transfer coefficient (see also Table 3). The similar trend of the results was found in literatures [11,24]. The mass transfer coefficients were determined by using Eq. (5). Additionally, the overall mass transfer coefficients based on the experimental results were also calculated by using the following equations.

$$K_{ov} = \frac{J}{\Delta C_{av}} \tag{8}$$

The logarithmic mean concentration, $\Delta C_{l,av}$, is expressed as

$$\Delta C_{av} = \frac{(C_{f,\text{in}} - C_{s,\text{in}}) - (C_{f,\text{out}} - C_{s,\text{out}})}{\ln\left(\frac{C_{f,\text{in}} - C_{s,\text{in}}}{C_{f,\text{out}} - C_{f,\text{out}}}\right)} \tag{9}$$

The overall mass transfer coefficients of the ethanol solution were higher than those of wine. The result revealed that the mass transfer of the system was controlled by the mass transfer in the stripping side.

Ethanol fluxes of ethanol solution and wine was increased from 0.79 to 1.04 and from 0.72 to 0.99 kg/m² h, respectively, with the feed velocity varying from 0.3 to 0.7 m/s. The ethanol flux of wine was lower than that of ethanol solution. It was likely that the complex nature of wine can result in fouling on the membrane surface such that evaporation of ethanol was partially prohibited. Eq. (4) was used for evaluating the concentration polarization for both wine and ethanol solution. CP in case of ethanol solution used as feed was (0.9850–0.9870), higher than that of using wine (0.9725–0.9727). The results of CP together with the mass transfer coefficients ($k_s$) presenting in Table 3 supported the experimental results that ethanol flux for wine was lower than that of ethanol solution.

From Fig. 6, the remaining ethanol concentration in the feed tank after operation was in the range of 12.04–11.74% (v/v) for ethanol solution and 12.36–12.04% (v/v) for wine. Due to the water activity difference between the feed and stripping solution (pure water) as discussed in Section 4.1, there was the water transfer from the stripping side to the feed side. The water flux in case of ethanol solution and wine were in the range of 0.09–0.20 and 0.10–0.18 kg/m² h, respectively. It can be seen that the water flux was quite low compared with the ethanol flux because the difference in water partial pressure was low. Hogan et al. [2] reported that ethanol has the highest evaporation ability in the wines due to its lower boiling point. The vapor pressure of ethanol and water at 30 °C were 78.44 and 31.74 mmHg [25], respectively.

### 4.3. Effect of stripping solution velocity

The effect of stripping solution velocity on the ethanol flux, the water flux, and remaining ethanol concentration in the feed were shown in Fig. 7. The ethanol flux increased from 0.82 to 1.01 kg/m² h and the ethanol concentration in the feed tank decreased from 13 to 12.01 – 11.77% (v/v) with increasing stripping velocities in the range of 0.1–0.7 m/s. The countered water flux from stripping side to feed side also increased in the range of 0.12–0.21 kg/m² h with stripping velocity. The increase of stripping side velocity enhanced the mass transfer coefficient, $k_s$ in the shell side. The shell side mass transfer coefficients was estimated by using empirical correlation Eq. (6) as presented in Table 3. Comparison between the mass

**Table 3**

Calculation of tube (feed) and shell (stripping) side mass transfer coefficients (feed: 13% (v/v) ethanol solution and wine, stripping solution: water, system temperature: 30 °C).

| Tube side (feed) (stripping solution velocity: 0.4 m/s) | | | | | | | | Shell side (stripping) (feed velocity: 0.4 m/s) | | |
|---|---|---|---|---|---|---|---|---|---|---|
| Feed: ethanol 13% (v/v) | | | | Feed: wine | | | | $v_s$ (m/s) | $Re_s$ | $k_s$ (m/s) |
| $v_f$ (m/s) | $Re_f$ | $k_f$(m/s) | $K_{ov}$ (m/s) | $v_f$ (m/s) | $Re_f$ | $k_f$ (m/s) | $K_{ov}$ (m/s) | | | |
| 0.1 | 37.56 | 1.12E−05 | 1.74E−06 | | | | | 0.1 | 75.20 | 2.32E−06 |
| 0.3 | 112.68 | 1.61E−05 | 2.29E−06 | 0.3 | 110.09 | 1.59E−05 | 2.03E−06 | 0.3 | 225.61 | 3.36E−06 |
| 0.5 | 187.80 | 1.91E−05 | 2.89E−06 | 0.5 | 183.49 | 1.89E−05 | 2.49E−06 | 0.5 | 376.02 | 4.00E−06 |
| 0.7 | 262.92 | 2.14E−05 | 3.15E−06 | 0.7 | 256.88 | 2.11E−05 | 2.94E−06 | 0.7 | 526.43 | 4.48E−06 |

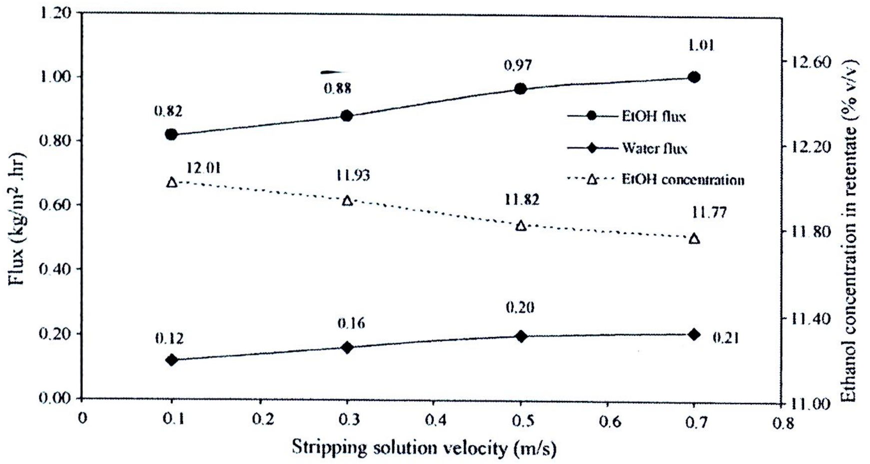

Fig. 7. Effects of stripping solution velocity on ethanol and water flux, and retentate concentration (feed: 13% (v/v) ethanol solution, stripping solution: water, system temperature: 30 °C, feed velocity: 0.4 m/s).

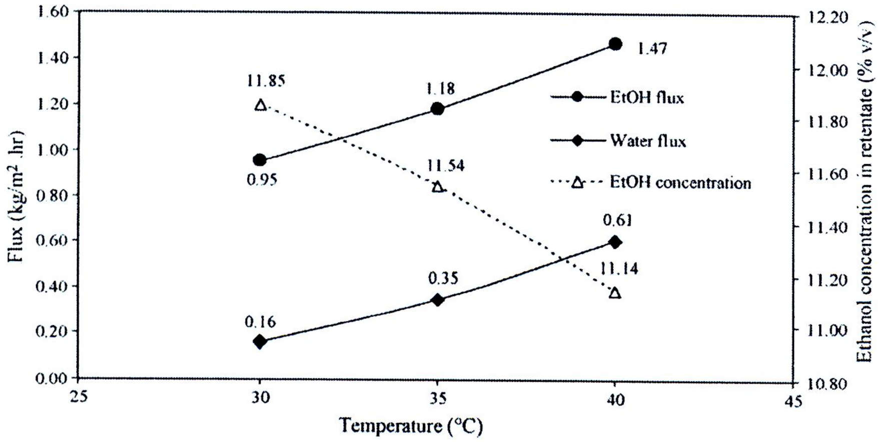

Fig. 8. Effects of system temperature on ethanol and water flux, and retentate concentration (feed: 13% (v/v) ethanol solution, stripping solution: water, system temperature: 30 C, feed velocity: 0.4 m/s, stripping solution velocity: 0.5 m/s).

transfer coefficients in the feed side to the stripping side indicated that the mass transfer coefficients in feed side were higher than those in stripping side. Hence, the change in feed velocity influenced more significantly on flux than the stripping velocity.

### 4.4. Effect of temperature

The temperature of the system was varied from 30 to 40 °C in order to investigate its effect on dealcoholization performance. The results displayed in Fig. 8 showed that ethanol flux increased from 0.95 to 1.47 kg/m$^2$ h, the water flux increased from 0.16 to 0.61 kg/m$^2$ h, while the ethanol concentration was reduced from 13 to 11.14% (v/v). The significant increase of fluxes can be supported by the exponential increase of vapor pressure with temperature as described by the Antoine's equation as follows:

$$\log P_i^{\text{sat}} = \left[A - \frac{B}{C+T}\right] \qquad (10)$$

where $P_i^{\text{sat}}$ is the saturation pressure of $i$ (mmHg), $T$ is temperature (°C) $A$, $B$, and $C$ is a constant, $A = 8.07$, $B = 1730.63$, and $C = 233.43$ for water and $A = 8.11$, $B = 1592.86$, and $C = 226.18$ for ethanol [25].

In addition, the diffusion coefficients of vapor also increase with temperature [26]. The reduction of solution viscosities with increasing system temperature also enhanced the Reynolds numbers. As a result, the mass transfer coefficients for both feed and stripping solutions can be improved. Table 4 presents the values of mass transfer coefficients for feed ($k_f$) and stripping solution ($k_s$).

### 4.5. Study of aroma losses

There are many kinds of aroma compounds presenting in the wines. Carbonyls, alcohols, esters acetic, acids, furanones are the major chemical functional groups of flavors, aromas, and fragrances of the wines [1]. In order to achieve the goal of dealcoholization of wine where the alcohol content is reduced, meanwhile other components should be not spoiled or lost.

In the present study, ethyl acetate and iso-amyl alcohol were selected to prepare the model solutions containing the aroma compounds. Figs. 9 and 10 depict the effect of operating time on the

**Table 4**
Calculation of tube (feed) and shell (stripping) side mass transfer coefficients (feed: 13% (v/v) ethanol, stripping solution: water, feed velocity: 0.4 m/s, stripping solution velocity: 0.5 m/s).

| Operating temperature (°C) | Tube side (feed) | | Shell side (stripping) | |
|---|---|---|---|---|
| | $Re_f$ | $k_f$ (m/s) | $Re_s$ | $k_s$ (m/s) |
| 30 | 150.23 | 1.77E−05 | 376.00 | 3.99E−06 |
| 35 | 175.66 | 1.87E−05 | 416.70 | 4.14E−06 |
| 40 | 201.51 | 1.96E−05 | 458.76 | 4.28E−06 |

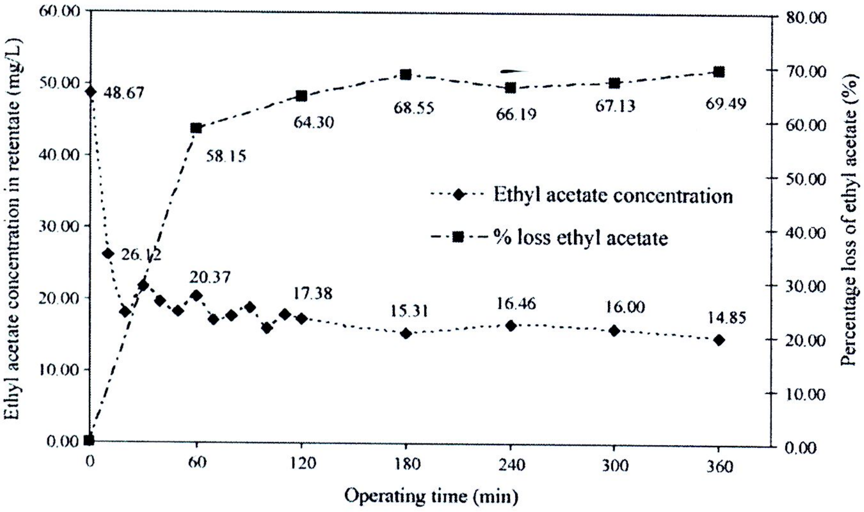

**Fig. 9.** Ethyl acetate concentration and percentage loss versus time (feed: 50 mg/l ethyl acetate, stripping solution: water, system temperature: 35 °C, feed velocity: 0.5 m/s, stripping solution velocity: 0.4 m/s).

aroma loss. For both types of aroma used, the same trends of the results were found. The reduction of aroma concentration increased with operating time. The concentrations rapidly decreased in the first 10 min of operation due to the high concentration difference (driving force). The percentages of ethyl acetate and iso-amyl alcohol loss were approximately 47 and 23%, respectively, in the early stage. At the end of the operation (360 min), the reduction of ethyl acetate and iso-amyl alcohol were found to be roughly 70 and 44% of the initial concentrations, respectively. The decrease of ethyl acetate concentration was higher than that of iso-amyl alcohol due to the higher vapor pressure as presented in Table 2.

Similar trend of the aroma loss results were also reported by other researchers. Diban et al. [14] also investigated the loss of aroma compound, i.e. ethyl acetate and iso-amyl alcohol by using OD process using water as stripping solution. The losses of ethyl acetate and iso-amyl alcohol were in the range of 37.4–65.2 and 13.7–50.9%, respectively, at 25 °C. The performance of orange juice concentration by using osmotic distillation and membrane distillation were compared by Alves and Coelhoso [27]. The model solution consisting of 45% (w/w) sucrose and 18 ppm aroma compounds, i.e. citral and ethyl butyrate were studied. The percentage losses of citral and ethyl butyrate were 49 and 51%, respectively. In order to minimize the loss of aroma in OD process, it is necessary to reduce the system temperature. However, this will be traded off by the reduction of fluxes which may be compensated by the increase of the membrane area. The low system temperature will also guarantee the product quality.

### *4.6. Long-term performance of OD process for dealcoholization*

The dealcoholization performance of 13% (v/v) ethanol solution and real wine (13.20% (v/v) ethanol) at 35 °C over 360 min of operation is presented in Fig. 11. In the beginning of the operation, the ethanol concentration for both cases rapidly decreased due to the higher driving force (ethanol concentration differences between feed and stripping sides). At the end of the experiment, the concentration of ethanol solution and wine can be reduced roughly 38 and 34% of the initial concentration, respectively. It can be seen that the ethanol removal performance in case of using 13% (v/v) ethanol solution as feed was slightly higher than that of using real wine. As mentioned earlier (see Section 4.2), this could be due to the difference in composition of ethanol solution and wine. At the end of

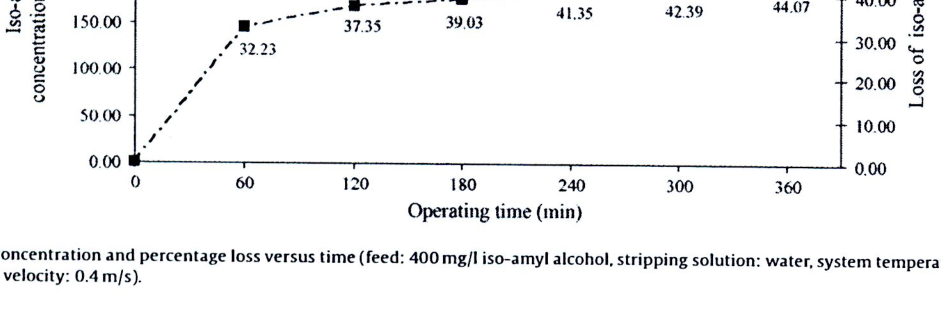

**Fig. 10.** Iso-amyl alcohol concentration and percentage loss versus time (feed: 400 mg/l iso-amyl alcohol, stripping solution: water, system temperature: 35 °C, feed velocity: 0.5 m/s, stripping solution velocity: 0.4 m/s).

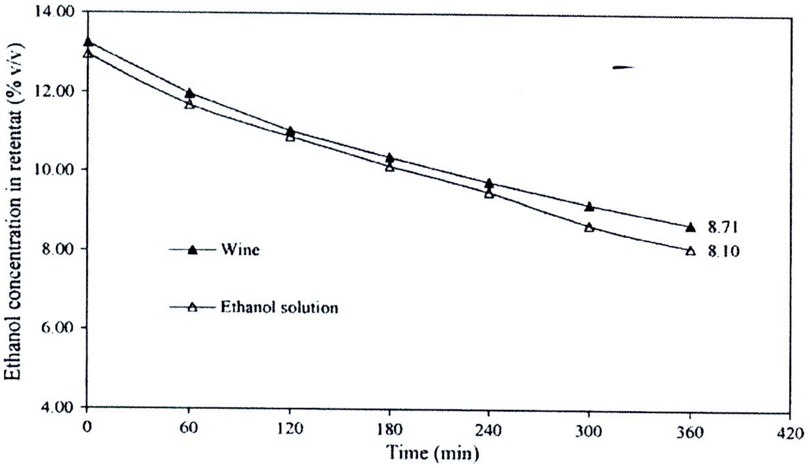

Fig. 11. Dealcoholization performance of ethanol solution and wine in OD process (stripping solution: water, system temperature: 35 °C, feed velocity: 0.5 m/s, stripping solution velocity: 0.4 m/s).

the experiments, the total solid in the wine was approximately the same as its initial value (0.80 g/30 ml) while its turbidity increased from 0.48 NTU to 1.31 NTU. The increase in turbidity could be due to the reaction between wine and sunlight responsible the off-flavor that the beverages can develop when they are exposed to light [28].

## 5. Conclusion

The potential of wine dealcoholization by using osmotic distillation process was evaluated via a series of experimental studies in a combination with mass transfer analysis. Three different types of stripping solution were selected to be used for comparison the ethanol removal performance. The use of water as the stripper provided the better performance in term of ethanol flux, removal ethanol performance and water flux than others. It was also found that the increase of feed and stripping velocity, and operating temperature resulted in increasing the ethanol flux as well as ethanol removal performance. For aroma losses study, the reduction of ethyl acetate and iso-amyl alcohol were approximately 70 and 44%, respectively after 360 min of operation. The ethanol removal performance in the long-term test of OD was performed over 360 min operating time for both ethanol solution and wine. The ethanol content in ethanol solution and wine can be reduced around 38 and 34% of the initial concentration, respectively.

## Acknowledgements

The authors would like to thank Thailand Research Fund (TRF) and the Commission on Higher Education, Thailand through the TRF senior research scholar grant for the financial support.

## References

[1] R.J. Clarke, J. Bakker, Wine Flavour Chemistry, Blackwell Publishing, Australia, 2004.
[2] P.A. Hogan, R.P. Canning, P.A. Peterson, R.A. Johnson, A.S. Michaels, A new option: osmotic distillation, Chem. Eng. Prog. (July 1998).
[3] S.V. Makarytchev, T.A.G. Languish, D.F. Fletcher, Mass transfer analysis of spinning cone columns using CFD, Chem. Eng. Res. Des. 82 (6) (2004) 752–761.
[4] S.J. Sykes, D.J. Casimir, R.G.H. Prince, Recent advances in spinning cone technology, Food Aust. 44 (10) (1992) 462–464.
[5] J. Westbrook, Dealcoholization of wine by reverse osmosis, Aust. Grapegrower Winemaker 316 (1990) 110–111.
[6] M.V. Pilipovik, C. Riverol, Assessing dealcoholization systems based on reverse osmosis, J. Food Eng. 68 (2005) 437–441.
[7] E. Gomez-Plaza, A. Martinez-Cutillas, J.M. Lopez-Nicolas, J.M. Lopez-Roca, Dealcoholization of wine. Behaviour of the aroma components during the process, Lebensm.-Wiss. U.-Technol. 32 (1999) 384–386.
[8] H.O.E. Karlsson, G. Trägårdh, Applications of pervaporation in food processing, Trends Food Sci. Technol. 7 (1996) 78–83.
[9] L. Takács, G. Vatai, K. Korány, Production of alcohol free wine by pervaporation, J. Food Eng. 78 (1) (2007) 118–125.
[10] W. Kunz, A. Benhabiles, R. Ben-Aim, Osmotic evaporation through macroporous hydrophobic membranes: a survey of current research and applications, J. Membr. Sci. 121 (1996) 25–36.
[11] R. Thanedgunbaworn, R. Jiraratananon, M.H. Nguyen, Mass and heat transfer analysis in fructose concentration by osmotic distillation process using hollow fibre module, J. Food Eng. 78 (2007) 126–135.
[12] F.G. Bailey, A.M. Barbe, P.A. Hogen, R.A. Johnson, J. Sheng, The effect of ultrafiltration on the subsequent concentration of grape juice by osmotic distillation, J. Membr. Sci. 164 (2000) 195–204.
[13] F. Vaillant, E. Jeanton, M. Dornier, G.M. O'Brien, M. Reynes, M. Decloux, Concentration of passion fruit juice on an industrial pilot scale using osmotic evaporation, J. Food Eng. 47 (2001) 195–202.
[14] N. Diban, V. Athes, M. Bes, I. Souchon, Ethanol and aroma compounds transfer study for partial dealcoholization of wine using membrane contactor, J. Membr. Sci. 311 (2008) 136–146.
[15] M. Celere, C. Gostoli, Heat and mass transfer in osmotic distillation with brines, glycerol and glycerol-salt mixtures, J. Membr. Sci. 257 (2005) 99–110.
[16] V.D. Alves, I.M. Coelhoso, Mass transfer in osmotic evaporation: effect of process parameters, J. Membr. Sci. 208 (2002) 171–179.
[17] R. Gawronski, B. Wrzesinska, Kinetics of solvent extraction in hollow-fiber contactors, J. Membr. Sci. 168 (2000) 213–222.
[18] M.J. Costello, A.G. Fane, P.A. Hogan, R.W. Schofield, The effect of shell side hydrodynamics on the performance of axial flow hollow fibre modules, J. Membr. Sci. 80 (1993) 1–11.
[19] R.M.C. Viegas, M. Rodriguez, S. Luque, J.R. Alvarez, I.M. Coelhoso, J.P.S.G. Crespo, Mass transfer correlations in membrane extraction: analysis of Wilson-plot methodology, J. Membr. Sci. 145 (1998) 129–142.
[20] R. Thanedgunbaworn, R. Jiraratananon, M.H. Nguyen, Shell-side mass transfer of follow fibre modules in osmotic distillation process, J. Membr. Sci. 290 (2007) 105–113.
[21] B. Gonzalez, N. Calvar, E. Gomez, A. Domınguez, Density, dynamic viscosity, and derived properties of binary mixtures of methanol or ethanol with water, ethyl acetate, and methyl acetate at $T$ = (293.15, 298.15, and 303.15) K, J. Chem. Thermodyn. 39 (2007) 1578–1588.
[22] R.H. Perry, D.W. Green, Perry's Chemical Engineers' Handbook, seventh ed., McGraw-Hill, Australia, 1998.
[23] M.E. Guerzoni, M.C. Nicoli, R. Massini, C.R. Lerici, Ethanol vapour pressure as a control factor during alcoholic fermentation, World J. Microb. Biot. 13 (1997) 11–16.
[24] M. Courel, M. Dornier, J.M. Herry, G.M. Rios, M. Reynes, Effect of operating condition of sucrose solutions by osmotic distillation, J. Membr. Sci. 170 (2000) 281–289.
[25] W. Feng, Vapor pressure measurement for water, methanol, ethanol, and their binary mixtures in the presence of an ionic liquid 1-ethyl-3-methylimidazolium dimethylphosphate, Fluid Phase Equilib. 225 (2007) 186–192.
[26] J.R. Welty, C.E. Wicks, R.E. Wilson, G.L. Rorrer, Fundamentals of Momentum, Heat, and Mass Transfer, fifth ed., John Wiley & Sons, Hoboken, NJ, p. 711.
[27] V.D. Alves, I.M. Coelhoso, Orange juice concentration by osmotic evaporation & membrane distillation cooperative study, J. Food Eng. 74 (2005) 125–133.
[28] F. Mattivi, A. Monetti, U. Vrhovsek, D. Tonon, C. Andrés-Lacueva, High-performance liquid chromatographic determination of the riboflavin concentration in white wines for predicting their resistance to light, J. Chromatogr. A 888 (2000) 121–127.

Journal of Membrane Science 342 (2009) 97–104

Contents lists available at ScienceDirect

Journal of Membrane Science

journal homepage: www.elsevier.com/locate/memsci

# Modification of PVDF membrane by chitosan solution for reducing protein fouling

Somnuk Boributh, Ampai Chanachai, Ratana Jiraratananon*

*Department of Chemical Engineering, King's Mongkut University of Technology Thonburi, 91 Prachautit Road, Tungkru, Bangkok 10140, Thailand*

ARTICLE INFO

*Article history:*
Received 4 May 2009
Received in revised form 11 June 2009
Accepted 15 June 2009
Available online 21 June 2009

*Keywords:*
Chitosan
Membrane modification
Protein fouling
PVDF membrane

## ABSTRACT

This work studied modification of hydrophobic membrane by chitosan solution for the purpose of reducing protein fouling. The membrane used was flatsheet polyvinylidenefluoride (PVDF) of 0.22 μm pore size. The membranes were modified by 3 different methods, i.e. immersion method, flow through method and the combined flow through and surface flow method. Chitosan solution concentration and modification time were varied. The modified membranes were then neutralized with NaOH solution. The results of scanning electron microscopy (SEM) and Fourier transform infrared spectroscopy (FTIR) study of modified membranes compared to unmodified membranes confirmed that there was chitosan coated on the membrane surfaces. The water contact angles and water fluxes decreased with increasing chitosan concentration and modification time. The result also indicated that modified membranes had higher hydrophilicity than unmodified membrane. In protein fouling experiment, bovine serum albumin (BSA) was used as a protein model solution. Modified membranes exhibited good anti-fouling properties in reducing the irreversible membrane fouling. The membrane modified by a combined flow through and surface flow method showed the best anti-fouling properties compared with other methods. Protein adsorption on the modified membrane was highest at the isoelectric point (IEP) of BSA solution and decreased as the solution pH was far from the IEP.

## 1. Introduction

Poly(vinylidene fluoride) (PVDF) membrane is widely used in microfiltration, ultrafiltration and nanofiltration due to its excellent chemical resistance, good thermal and mechanical properties [1–3]. However, in the application involving protein solution, the protein adsorption on the membrane surface and in the membrane pores due to the inherent hydrophobic characteristic of PVDF often causes serious membrane fouling and a rapid decline of permeation flux.

Protein fouling in membrane processes is a complicated mechanism due to many factors affecting fouling formation. It is known that the electrostatic force and the hydrophobic interaction between certain domains in protein molecules and the hydrophobic membrane surfaces as well as between protein molecules are the main factors affecting membrane fouling [4,5]. Huisman et al. [6] reported that membrane–protein interactions influenced the fouling behavior in the initial stage of filtration and in the later stage of filtration, protein–protein interactions dictated the overall performance. The interactions also depend on other parameters such as membrane materials, solution type and operating conditions.

Solution pH is an important factor which can strongly affect membrane fouling and filtration performance. It was reported that change in pH could cause fouling in protein filtration. Zhao et al. [7] found that BSA adsorption on chitosan/PES (polyethersulfone) composite MF membrane was highest at the IEP (isoelectric point) and at low pH (3.0–4.7), the MF composite membranes had higher adsorption capacities of BSA than at higher pH range (6.0–8.0). Mo et al. [8] emphasized the effect of pH on BSA fouling in RO process. The study found that the most severe BSA fouling occurred at pH near IEP of BSA, where the electrostatic repulsion between BSA molecules was weakest.

To obtain a hydrophilic surface with anti-fouling property, several techniques have been studied. The modification by adsorbing suitable hydrophilic polymer on the membrane surface can introduce the repulsive force between membrane surface and protein molecules. Previous works reported that increasing membrane surface hydrophilicity such as modification by hydrophilic polymer through blending, coating and surface grafting could effectively reduce irreversible membrane fouling [9,10]. Many hydrophilic polymers have been coated on different base membranes, for examples, chitosan/poly(acrylonitrile) [11], carboxylmethyl chitosan/poly(ethersulfone) [7], chitosan/polystyrene [12] and polyvinyl alcohol/polypropylene [13]. The hydrophilic polymers may be casted onto the membrane surfaces [14] or the membranes were immersed in the hydrophilic polymer solution

---

* Corresponding author. Tel.: +66 2470 9222; fax: +66 2428 3534.
*E-mail address:* ratana.jir@kmutt.ac.th (R. Jiraratananon).

0376-7388/$ – see front matter © 2009 Elsevier B.V. All rights reserved.
doi:10.1016/j.memsci.2009.06.022

[7]. These methods are limited by the fact that the hydrophilic modification occurs only on the membrane surface, while internal pores remain susceptible to fouling. A promising method to modify surface of internal pores is to force the hydrophilic polymer solution to flow through the membrane pores.

Chitosan is the hydrophilic polymer of interest for modifying the membrane in this work. Chitosan has been identified as hydrophilic, non-toxic, biodegradable, antibacterial, and biocompatible. It has been widely used for coating on hydrophobic membranes to increase hydrophilicity [11,12].

Only a few studies of coating hydrophilic polymer on PVDF membrane have been reported [15]. It may be because PVDF membranes are highly hydrophobic which make them difficult to be coated by hydrophilic polymers. The complicated methods are often applied in PVDF membranes modification such as UV-modification and grafting [15].

The present work focuses on modification of hydrophobic microfiltration PVDF membrane to obtain the hydrophilic ultrafiltration membrane with anti-fouling properties. In this work, the PVDF commercial membrane was modified by chitosan solution using 3 different methods, i.e. (1) an immersion method, (2) a flow through method and (3) a combined flow through and surface flow method. The effects of chitosan concentration, modification time were investigated. In addition, protein fouling and adsorption behavior of the modified membranes at various pH were also reported.

## 2. Methodology

### 2.1. Materials

PVDF flat sheet membrane with reported pore size of 0.22 μm was purchased from the Millipore Co. Ltd. Chitosan ($M_n$ = 50,000 Da, 85% deacetylation) was procured from NNC Production Co. Ltd., Thailand. Polyethylene glycols (PEG) with molecular weights 4, 15, 35, 100 and 400 kDa were supplied by Fluka. Dextran with molecular weight of 162 kDa was obtained from Sigma. Bovine serum albumin (BSA) was purchased from Fluka. It's molecular weight and IEP were 67,000 Da and 4.7, respectively. All chemicals were analytical grade. Deionized (DI) water was used for preparing all solutions.

### 2.2. Experimental setup

The schematic diagram for the filtration experiments is displayed in Fig. 1. The feed solution was supplied from the feed tank (2 l in volume) by a peristaltic pump (Masterflex, Model 77201-62) through the flow meter and a pressure gauge before entering the membrane module. The module was a radial cross flow type that can be equipped with a circular flat sheet membrane with an effective area of 19.638 cm². When the experimental setup was applied for membrane modification, both permeate and retentate were returned to the feed tank. For filtration experiments, the permeate was collected at different time intervals (to determine flux) and was then returned to the feed tank. The feed flow rate was fixed to 0.877 l/min for all experiments.

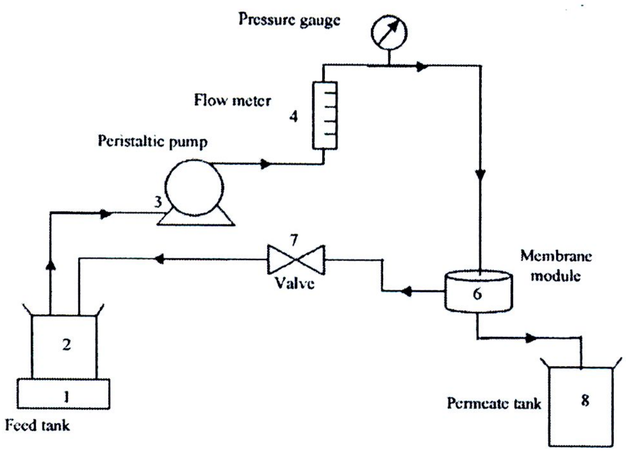

**Fig. 1.** Schematic diagram of the radial cross flow ultrafiltration (UF) unit.

### 2.3. Membrane modification

Prior to modification, the water flux of the original membrane was determined at fixed conditions (flow rate of 0.877 l/min, applied pressure 1.5 bar, temperature 25 °C). We noticed variation in water flux for different pieces of membrane. Therefore, the membranes with water flux in range of 1510 ± 100 l/m² h were selected for further modification. Before modification process, the membranes were wetted by filtering DI water for 5 min.

The chitosan was dissolved in 2 wt% aqueous acetic solution. The amount of chitosan was varied to obtain the chitosan solution with concentrations between 0.1 and 2.5 wt%. Three methods of modification were studied. For each method, chitosan concentration and time were varied.

- Method 1: Immersion method. The membrane was immersed in the chitosan solution with specific concentration and time.
- Method 2: A flow through method. The chitosan solution was fed at an applied pressure of 2 bar, through the membrane module.
- Method 3: A combined flow through and surface flow method. This method involved 2 steps of modification, each with equal time. The chitosan was fed through the membrane at an applied pressure of 2 bar. The operation was then switched to a surface flow mode in which the chitosan solution flowed (without applying any pressure) tangentially over the membrane surface.

The modified membranes from methods 1, 2 and 3 were dried by annealing in a vacuum oven at 60 °C for 45 min. After that the dried membranes were neutralized by filtering NaOH solution (1.0 M in 50%v water–ethanol mixture) for 30 min to ensure that all chitosan acetate was converted to chitosan. Then the membranes were cleaned by filtering 50%v ethanol solution for 10 min to remove the remaining NaOH and to prevent the osmotic crack, and followed by washing with DI water for 30 min. Finally, the membranes were dried at 25 °C.

### 2.4. Analysis

The concentrations of PEG and dextran were analyzed by Gel Permeation Chromatography (GPC) column (Polysep 4000) with HPLC [16,17]. UV–vis spectrometer (HP 8433) was used for analyzing BSA concentration.

### 2.5. Membrane characterizations

#### 2.5.1. Fourier transform infrared spectroscopy (FTIR) study

To investigate the chemical structures of PVDF membrane, chitosan and modified membranes, Thermo-Nicolet Magna 550 FTIR was used with 50° angle of incidence. Each spectrum was collected by cumulating 32 scans at a resolution of 4 cm⁻¹.

#### 2.5.2. Membrane morphology study

The surface and the cross-sectional morphology of the membranes were characterized by scanning electron microscopy (SEM, LEO model 1455VP). All samples were dried in vacuum for 12 h at room temperature and were gold-coated. The scanning was performed at an accelerating voltage of 10 kV. The cross-section of membranes was prepared by fracturing in liquid nitrogen.

### 2.5.3. *Water contact angle*

Membrane hydrophilicity was studied by measuring contact angles (Kruss, Model DSA 10 MK 2) of the membranes at 25 °C. The DI water was dropped on the membrane sample surface at 5 different points, the average of measured values was taken as its water contact angle.

### 2.5.4. *Flux measurement*

The experiment setup depicted in Fig. 1 was used for determining water flux, solution flux of the base membrane and modified membranes. The operating conditions were at a flow rate of 0.877 l/min, 25 °C and an applied pressure of 1.5 bar. The steady state values were recorded.

### 2.5.5. *Determination of molecular weight cut offs (MWCO)*

In order to estimate the MWCO of the modified membranes, rejections of PEG solution (2 wt% concentration), BSA solution (1 wt% concentration, pH 7) and 0.25 wt% of dextran solution were determined.

### 2.5.6. *Membrane stability test*

The stability of the modified membrane was tested by the following steps. The modified membranes were applied for filtering DI water for 20 h. The water flux was measured every 2 h during the operation. The modified membranes after filtration of water were then dried at the room temperature for 12 h. In order to compare the membrane structure with the newly modified membrane (without water filtration), the SEM images were taken, the FTIR study and the contact angle measurement were also performed.

## 2.6. *Fouling study*

### 2.6.1. *Protein filtration*

The objective of this part of the experiments was to assess the performance of the modified membranes on protein fouling. BSA protein was used as a protein model solution in order to compare the protein fouling on the unmodified and modified membranes. BSA (1.0 g/l) was dissolved in phosphate buffered saline solution consisting of 0.03 M $Na_2HPO_4$, 0.03 M $KH_2PO_4$ and 0.03 M NaOH in DI water [16]. The pH was adjusted to IEP of BSA (pH 4.7). The fouling experiment was performed using the experimental setup in Fig. 1. The phosphate buffered saline solution (without BSA) flux was also measured under fixed conditions (flow rate 0.877 l/min and 1.5 bar pressure) until the steady state flux ($J_0$) was obtained. Then, BSA solution flux ($J_t$) was determined. After that, the fouled membrane was cleaned by filtration of DI water for 30 min, and then the phosphate buffered saline solution flux of cleaned membrane was measured for period of 30 min. Next, the membrane was chemically cleaned by 0.1 wt% NaOH for 30 min. Then the permeation flux of buffer solution was measured for another 30 min. Finally, BSA flux was again determined. These procedures allowed for the observation of flux recovery of the membranes.

### 2.6.2. *Protein adsorption*

BSA (1.0 g/l) in phosphate buffered saline solution was prepared to carry out the static adsorption of protein on the membrane surface. Sodium azide (0.02 wt%) was used as a bactericide [7]. The pH was adjusted to 3.0, 4.7, 5.0, 7.0 and 9.7 by adding 0.1 M NaOH or 0.1 M HCl solution. The membrane samples were cut into small pieces (1 cm × 2 cm) and were immersed in the BSA solution in test tubes at 25 °C for 24 h to allow for adsorption equilibrium. The amount of BSA adsorbed on the membrane samples was calculated by a mass balance using initial and final solutions of BSA concentrations measured by UV–vis. spectrometer (HP 8453) at the wavelength of 280 nm.

## 3. Results and discussions

### 3.1. *Membrane characterizations*

### 3.1.1. *Chemical structures on membrane surface*

The chemical structures of the modified and unmodified membranes were characterized by FTIR. Fig. 2 presents the FTIR spectra for chitosan, unmodified PVDF membrane and modified membrane with chitosan concentration of 0.5 and 1.0 wt% (method 2). For the FTIR spectra of chitosan, the bands at 900 and 1150 $cm^{-1}$ referred to –N–H wagging mode and =C–O–C stretching, respectively. The absorption peaks appearing at 1030 and 1050 $cm^{-1}$ were assigned to –C–O stretching in cyclic alcohols. Also, the bands at 1590 and 1650 $cm^{-1}$ were the characteristics of –N–H deformation in amino group and >C=O stretching of N-acetyl group, respectively. The broad and strong band ranging from 3200 to 3600 $cm^{-1}$ indicated the presence of –O–H and $-NH_2$ groups in chitosan.

For the unmodified PVDF membrane, the absorption peaks of $-CF_2$ stretching and C=C stretching modes of PVDF were shown at 1200 and 1475 $cm^{-1}$, respectively [18]. The absorption peaks at 795, 850 and 1280 $cm^{-1}$ were the typical characteristic of PVDF.

Comparing between unmodified membrane and two modified membranes (at 0.5 and 1.0 wt% chitosan solution), the six new absorption peaks (900, 1030, 1050, 1150, 1590 and 1650 $cm^{-1}$) were shown in the FTIR spectra of the modified PVDF membranes. The new peaks were the typical peaks of chitosan as described previously [11]. The results confirmed that, there was chitosan coated on the PVDF membrane surface. In addition, an increase of chitosan concentration also led to an increase in the amount of chitosan depositing on the membrane surface which can be seen from the higher chitosan peaks.

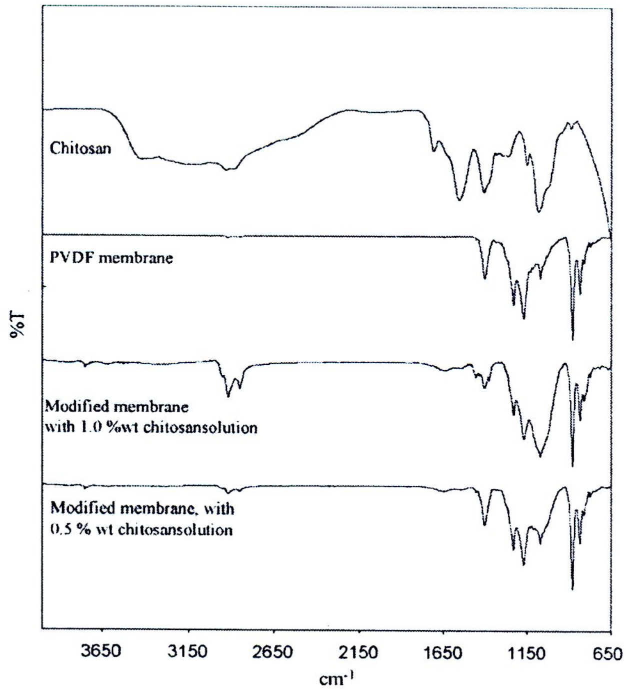

**Fig. 2.** FTIR spectra of the chitosan, unmodified PVDF membrane and membranes modified (by method 2, a flow through method) with 0.5 and 1.0 wt% chitosan, 90 s modification time.

### 3.1.2. *Morphology of the modified PVDF membranes*

The membrane morphologies were shown by SEM images as presented in Fig. 3. Compared to porous top surface of unmodified membrane (Fig. 3a), the membranes modified by method 2 with 0.5 wt% chitosan (Fig. 3c) and 2.0 wt% chitosan (Fig. 3e) showed dense layers of chitosan blocking the surface pores. In addition, modification with high concentration (2.0 wt% chitosan) gave denser coated layer than that at low chitosan concentration. From cross-sectional SEM images, there was no difference between skin layer thickness of the modified and unmodified membranes which means that the chitosan layer on membrane surface was very thin. It seemed that there was some chitosan in the membrane pores when modified by high chitosan concentration (2.0 wt%, Fig. 3f). However, we have found that the SEM images of the membrane structure modified with three different methods were not significantly different. Therefore, the membrane hydrophilicity was compared in terms of water contact angle and water flux.

### 3.1.3. *Hydrophilicity of modified membranes*

The water contact angle measurement is one of the methods for characterization the hydrophilic property of the membrane surface. Theoretically, a hydrophilic surface gives a low contact angle (less than 90°), while a hydrophobic surface provides a high contact angle [19]. The results of contact angle measurement showed that the base membrane had a contact angle of 115 ± 2°. The membrane modified by method 2 for 90 s using the chitosan concentrations of 0.1, 0.5, 1.0 and 1.5 wt% gave the contact angles of 77°, 70°, 65° and 61°, respectively. Thus, the hydrophilicity of the membranes increased with chitosan concentration due to the increased amount of chitosan deposit. The dependence of contact angle on the modification time also showed the same trend. Increasing the modification time from 30 to 120 s (1.0 wt% chitosan) resulted in the decreased of contact angles from 70° to 57°. The increased amount of chitosan deposit was responsible for the increased hydrophilicity of the modified membranes. The contact angles of membranes

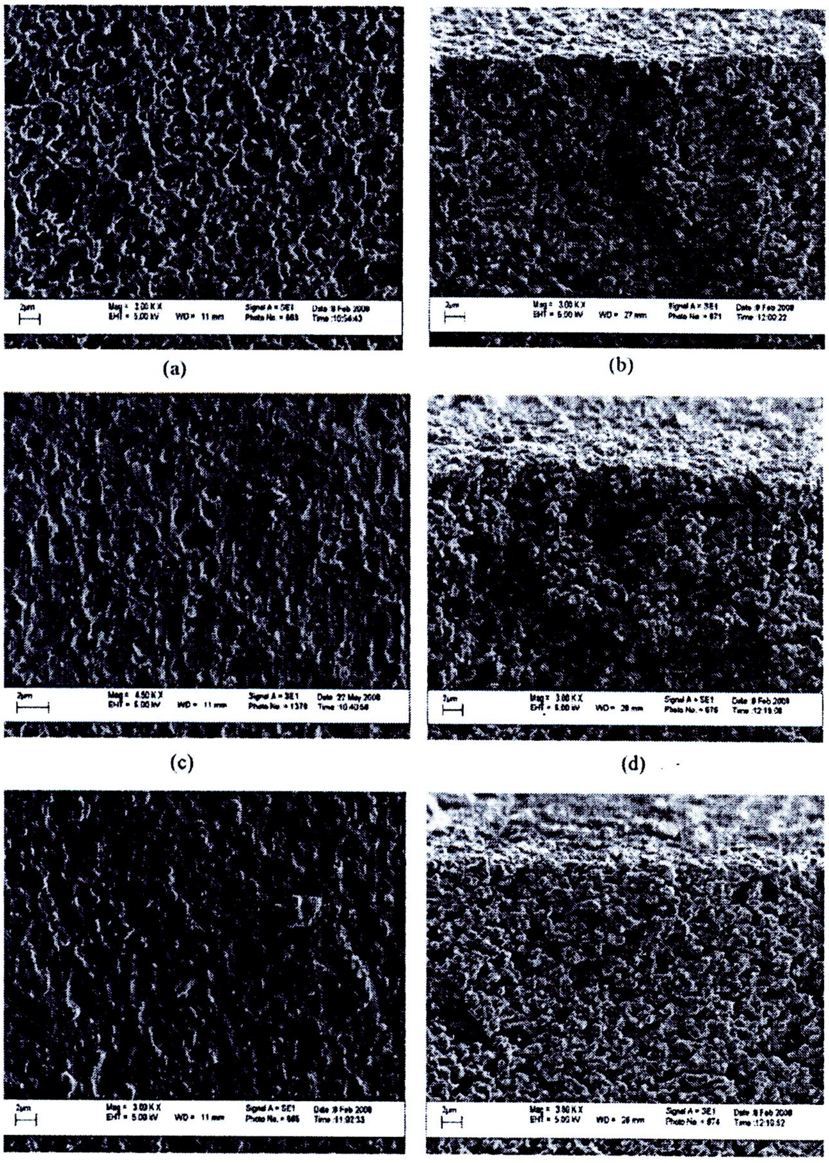

**Fig. 3.** SEM images of top surface and cross-section of unmodified membrane (a and b), modified membranes (method 2) 0.5 wt% chitosan (c and d), and 2.0 wt% chitosan (e and f). Modification time 90 s.

**Table 1**
Characterization of membranes modified with 3 different methods using 1.0 wt% chitosan, 90 s modification time.

| Method | Contact angle (theta) | Water flux (l/m² h)[a] | MWCO (kDa)[b] |
|---|---|---|---|
| 1. Immersion | 73 | 972 ± 105 | >162 |
| 2. A flow through | 65 | 444 ± 50 | >162 |
| 3. A combined flow through and surface flow | 61.5 | 247 ± 55 | >162 |

[a] Measured at 1.5 bar.

[b] Measured using PEG and dextran solutions.

modified with different methods were shown in Table 1. The membrane modified by method 3 gave the highest hydrophilicity with contact angle of 61.5° while the membrane modified by immersion method (method 1) provided the lowest hydrophilicity. It can be explained that for the membranes modified by a flow through method (method 2), chitosan was deposited on both surface and pore wall. For the membranes modified by method 3, it was possible chitosan deposit on membrane surface was thicker compared with method 2, while for method 1, chitosan was only coated on the membrane surface. From the results, it can be concluded that the hydrophilicity of modified membranes increased with chitosan concentration and modification time. By using method 3, chitosan which is a highly hydrophilic polymer can deposit on both the membrane surface and in the membrane pores, resulting in higher hydrophilicity.

The results of water fluxes of the modified membranes depicted in Table 1 indicated that the membrane modified by method 1 gave highest flux, followed by those of method 2 and method 3, respectively. The membrane modified by method 3 had lowest contact angle (more hydrophilic), but its water flux was also lowest. This is not surprising because for modification by method 3, chitosan can be accumulated both on the membrane surface and in the membrane pores. These increased the membrane thickness, reduced the pore volume, resulting in the decreased of water flux due to the increase of membrane resistance.

### 3.1.4. *Molecular weight cut offs (MWCO)*

In this work, the MWCO is defined as MW which is 90% rejected. The experiments were carried out using solutes of different molecular weights which were PEG, BSA and dextran. Fig. 4 shows the effect of chitosan concentration on solute rejections for membranes modified by a flow through method. It can be seen that the unmodified PVDF base membrane did not reject any solutes in range of 0–162 kDa. In case of membranes modified with low chitosan concentration (0.5 and 1.0 wt%), the MWCO of modified membranes were still larger than 162 kDa due to the small amount of chitosan deposit on the membrane surface and pore wall, while the membranes modified with 1.5, 2.0 and 2.5 wt% gave MWCO of 152.5, 90 and 63.5 kDa, respectively. This suggested that the increase of chitosan concentration caused a reduction of membrane pore sizes.

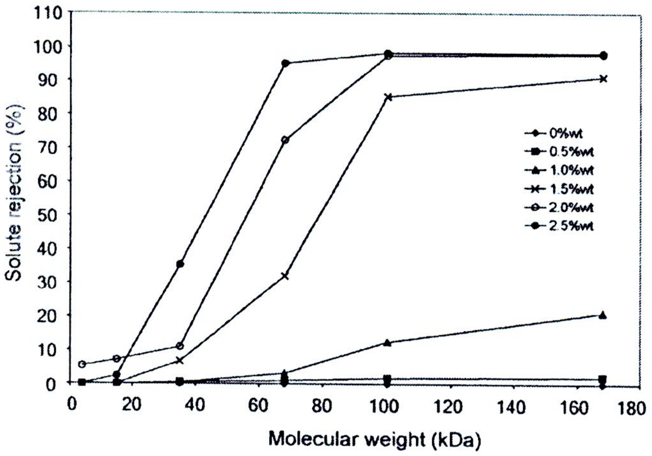

**Fig. 4.** Solute rejection of membranes modified by a flow through method using different chitosan concentrations, 90 s modification time.

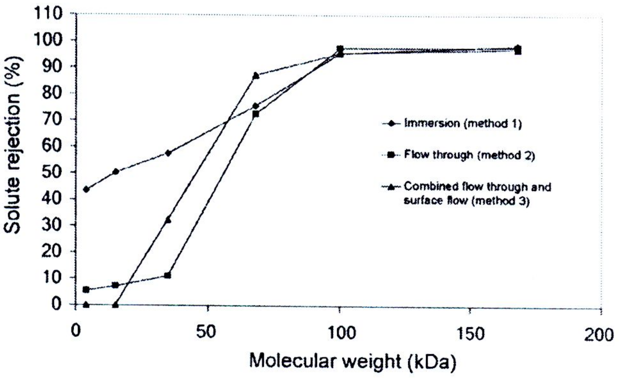

**Fig. 5.** Solute rejection of membranes modified with different methods, 2.0 wt% chitosan concentration, 90 s modification time.

The MWCO curves of membranes modified with different methods at 2.0 wt% chitosan was shown in Fig. 5. The modification of membrane by methods 1, 2 and 3 gave MWCO of 91, 90 and 72 kDa, respectively. Interestingly, the solute rejection curves of the membrane modified by methods 2 and 3 were sharper than that of membrane modified by immersion technique. The shape of solute rejection curve can reflect the pore size distribution of modified membranes. The sharper curve means more narrow pore size distribution [11]. From the results, it can be explained that for the membrane modified by methods 2 and 3, the chitosan solution was coated uniformly on surface and pore wall. In case of immersion method (method 1), the base membrane was only immersed in chitosan solution without giving any pressure, chitosan can be only coated on membrane surface.

### 3.1.5. *Membrane stability*

In order to verify the integrity of chitosan deposit on the membrane surface and pores, the modified membranes were tested by water filtration. The water fluxes for period of 20 h of modified membranes were depicted in Fig. 6. It was observed that the flux decline was not significant.

To confirm the existence chitosan layer coated on membrane surface after 20 h water filtration, the contact angle of used membrane was again measured, together with the FTIR study. The result of FTIR measurement showed insignificant change of the FTIR peaks (positions and heights) of modified membrane before and after filtration test. The contact angles of membranes modified by flow through method with 0.5 wt% chitosan before and after filtration test were 70° and 73°, respectively. It clearly showed that only the small amount of chitosan might be lost by filtration with water. Fig. 7 shows the SEM pictures of the membranes modified by method 2 with 0.5 wt% chitosan before and after 20 h filtration of water. It is shown that the coated chitosan layer was stable on membrane surface. The results of water flux, contact angle, FTIR study and SEM images confirmed that chitosan was strongly deposited on PVDF membrane. The stabilization of chitosan layer on base membrane by neutralizing with 1.0 M NaOH was an effective method to provide the chitosan layer stability on the base membrane.

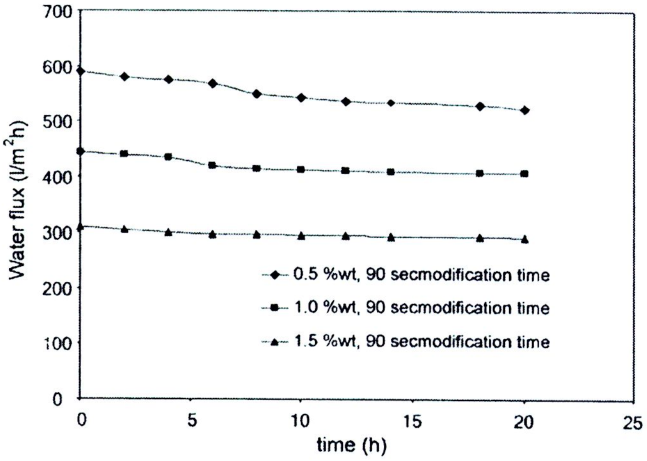

**Fig. 6.** Water fluxes of membranes modified by flow through method for a period of 20 h.

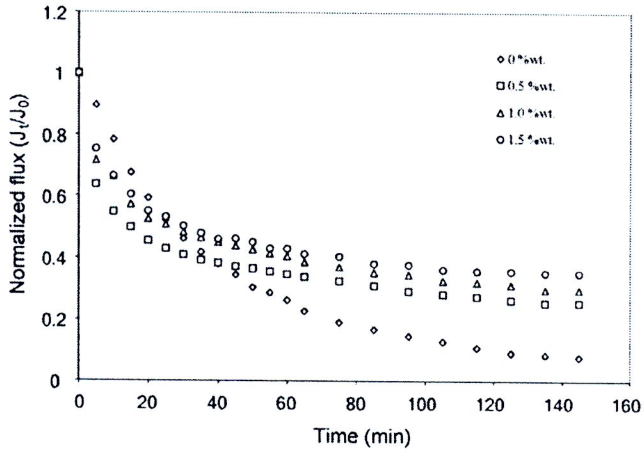

**Fig. 8.** Normalized fluxes of BSA solution of membranes modified with different chitosan concentrations (method 2); 90 s modification times, pH 4.7 (IEP of BSA).

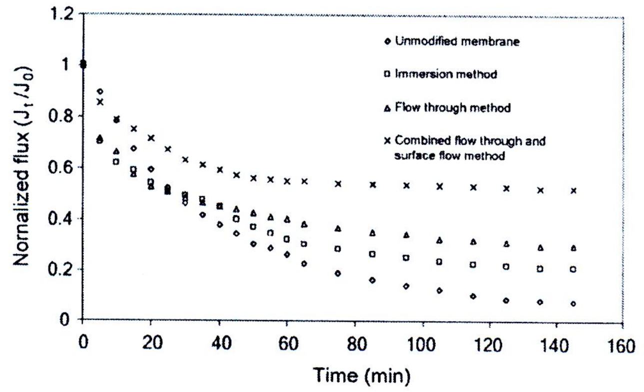

**Fig. 9.** Normalized fluxes of BSA solution of membranes modified with different techniques, 1.0 wt% chitosan, 90 s modification time at IEP of BSA.

## 3.2. *Fouling of membrane by protein*

### 3.2.1. *Effect of chitosan concentration on protein fouling*

To investigate the anti-fouling properties of the modified membranes, filtration of BSA solution by unmodified membrane and membranes modified with different chitosan concentrations were performed. Fig. 8 shows normalized flux of unmodified and membranes modified with 0.5, 1.0 and 1.5 wt% chitosan. The normalized flux is the ratio of instantaneous BSA flux ($J_t$) divided by flux of buffer solution ($J_0$). It is clearly shown that the flux decline of unmodified membrane was higher than those of modified membranes indicating higher fouling of unmodified membrane. In case of modified membranes, it appeared that the fouling of BSA decreased with increasing chitosan concentration due to an increase of hydrophilicity (Section 3.1.3).

### 3.2.2. *Effect of modification method on protein fouling*

Fig. 9 shows BSA normalized flux of unmodified PVDF membrane and modified with different methods. The unmodified membrane had the highest normalized flux decline during protein filtration. In case of modified membranes, the modification methods significantly affected flux decline. The lowest flux declined appeared in case of membrane modified by method 3 and the membrane modified by immersion (method 1) had highest flux decline. For the membrane modified by a flow through and surface flow method, the chitosan was forced to flow though the membranes under a given pressure (2 bar). Chitosan can deposit on both surface and in the pores, resulting in prevention of BSA adsorption. While, the membrane modified by immersion, chitosan deposited only on the membrane surface. Therefore, BSA could be adsorbed easily on the

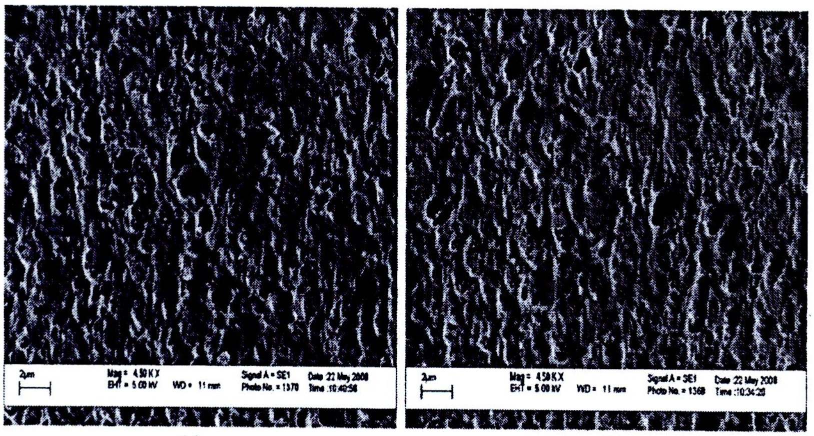

(a) (b)

**Fig. 7.** SEM images of the top surface of membranes modified (by method 2) with 0.5 wt% chitosan concentration, 90 s modification time (a) before filtering with water, (b) after 20 h filtration of water.

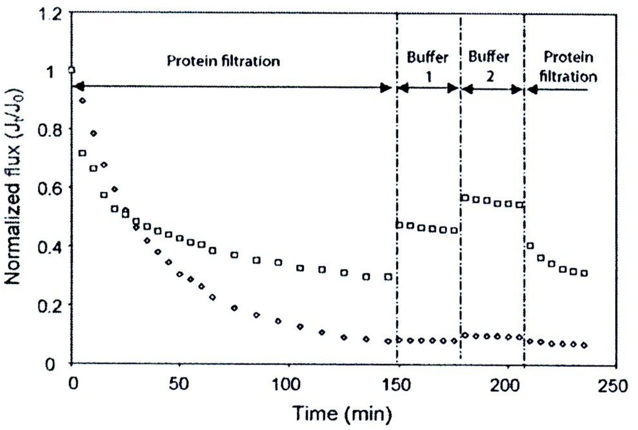

**Fig. 10.** Normalized flux recovery of (◇) unmodified and (□) modified membrane (method 2) with 1.0 wt% chitosan, 90 s modification time at IEP of BSA. Buffer 1—after cleaning with DI water; Buffer 2—after cleaning with 0.1 M NaOH.

pore walls which led to high flux decline and irreversible fouling (see Section 3.2.4).

### 3.2.3. Flux recovery of protein filtration

The results from the experimental procedure described in Section 2.6.1 are displayed in Fig. 10. The first zone, on the left hand side, compares the normalized fluxes between unmodified and modified membranes. Flux recoveries after cleaning with DI water (Buffer 1) for unmodified and modified membranes were 8% and 45%, respectively. After cleaning with 0.1 M NaOH solution, the recoveries (Buffer 2) were 10 and 57%. The normalized flux of protein filtration in the last stage was comparable to that of the first stage. The higher flux recovery of modified membrane suggested that protein fouling on chitosan layer was partially reversible because of the hydrophilicity of modified membrane.

### 3.2.4. Resistance analysis

In order to investigate the anti-fouling property of the modified membrane, resistance in series model was used to characterize the degree of membrane fouling [16,20]. The permeation flux is define as

$$J = \frac{\Delta P}{\mu R_t} \tag{1}$$

where

$$R_t = R_m + R_{cp} + R_f \tag{2}$$

and

$$R_f = R_{rf} + R_{irf} \tag{3}$$

where $J$ is the permeation flux, $\Delta P$, the trans-membrane pressure, $R_t$, the total resistance, $R_m$, the inherent membrane resistance, and $R_{cp}$ is the concentration polarization resistance which can be removed by washing with DI water. $R_f$ is the fouling resistance consisted of reversible fouling resistance ($R_{rf}$) which can be cleaned by chemical cleaning (0.1 M NaOH) and irreversible fouling resistance ($R_{irf}$). These resistances can be calculated from the solution flux data and from clean water flux before and after membrane cleaning. The details were described elsewhere [21,22]

As shown in Fig. 11, the resistances $R_t$, $R_{rf}$ and $R_{irf}$ decreased with increasing chitosan concentration. The value of $R_{irf}$ for membrane modified with 1.5 wt% chitosan was $1.22 \times 10^{12}\ \mathrm{m}^{-1}$, which was only 21.32% of that of unmodified membrane while, $R_{rf}$ was half of unmodified membrane. Both $R_{rf}$ and $R_{irf}$ indicate the degree of fouling and overall performance during protein filtration. The value of $R_{irf}$ reflects the degree of irreversible fouling. The sharp decrease of $R_{irf}$ with increasing chitosan concentration indicated that the amount of chitosan on membrane surface and pores help protect the irreversible fouling of the modified membranes. The increase of membrane resistance $R_m$ with chitosan concentration confirmed the previous discussion (Section 3.1.3) that accumulation of chitosan on the membrane surface and in the pores increased the membrane thickness, reduced the pore volume, leading to the increase of membrane resistance.

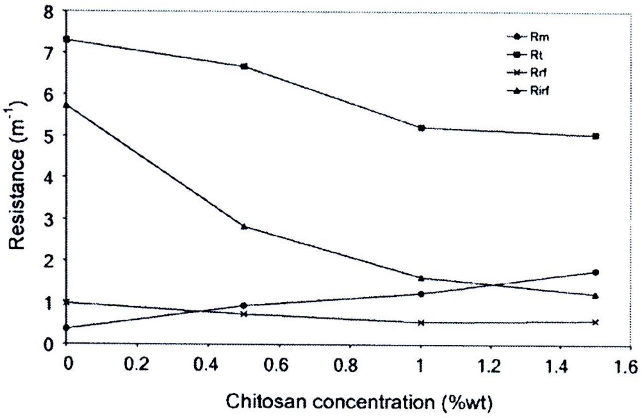

**Fig. 11.** Transport resistances due to BSA filtration of the membrane modified by a flow through method using different chitosan concentrations, 90 s modification time.

### 3.2.5. Protein adsorption

Fig. 12 shows the results of static BSA adsorption on the membrane surface at different pH of BSA solutions. It can be seen that the unmodified PVDF membrane had higher amount of BSA adsorption than the modified membranes due to high hydrophobicity of the PVDF membrane. In addition, the membrane modified with higher chitosan concentration gave lower BSA adsorption since chitosan can improve the hydrophilicity of the membrane.

The highest BSA adsorption appeared at pH 4.7 (isoelectric point, IEP of BSA) for all membranes. At IEP of BSA, the repulsive force between membrane surface and BSA is weakest and BSA can be easily adsorbed on the membrane surface. The extent of electrostatic repulsion was dependent on the magnitude of membrane surface charge [7] which was a function of the difference between BSA solution pH and IEP. In addition the change in pH causes the changes in structure and conformation of protein, which also affect

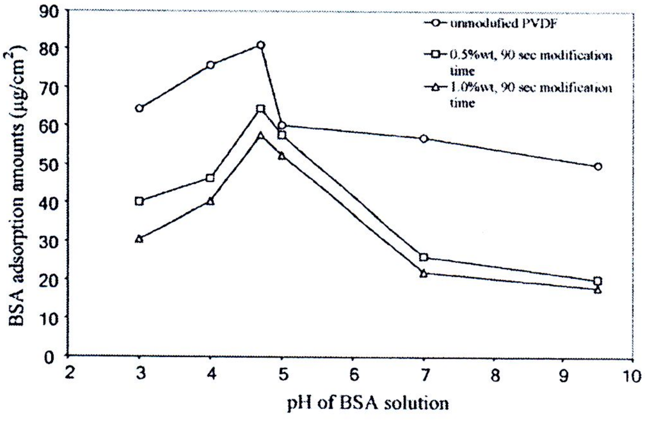

**Fig. 12.** The amount of BSA adsorbed on unmodified membrane and membrane modified by a flow through method using two different chitosan concentrations.

adsorption mechanisms. For the pH which was far from BSA IEP, the electrostatic repulsion was high, BSA adsorption was small. When pH of solution was adjusted to below BSA IEP and above chitosan IEP, the charges of both membrane surface and BSA were positive and negative, respectively. This induced strong repulsive force between membrane and BSA. Therefore, a small amount of BSA was adsorbed on membrane. It can be concluded that, the amount of BSA adsorption can be reduced by adjusting the pH of the solution.

## 4. Conclusion

The modification of hydrophobic PVDF membrane with chitosan was performed in order to increase the hydrophilicity and to reduce protein fouling. From the SEM and FTIR results, it confirmed that there was chitosan deposited on the membrane surfaces and in the pores. The hydrophilicity of the modified membrane increased (water contact angle decreased) with increasing chitosan concentration and modification time. However, as the chitosan concentration and modification time was increased, the water permeate flux was decreased. Moreover, the modification method significantly affected the deposition of chitosan on membrane surface and pore wall.

In the protein fouling study, the normalized flux during the BSA filtration slightly declined when membrane was modified with high chitosan concentration. The modification of PVDF membrane with chitosan could effectively prevent protein fouling on membrane. Fluxes recovery of modified membrane was better than the unmodified membrane. The membrane modified by a combined flow through and surface flow method showed the best anti-fouling properties compared with other methods. Protein adsorption on the modified membrane was highest at the BSA IEP while the adsorption decreased at the BSA solution pH was far from the IEP.

## Acknowledgments

The authors gratefully acknowledge the financial support from the Thailand Research Fund (TRF) and from the Commission on Higher Education, Thailand.

## References

[1] P. Wang, K.L. Tan, E.T. Kang, K.G. Neoh, Synthesis, characterization and anti-fouling properties of poly(ethylene glycol) grafted poly(vinylidene fluoride) copolymer membranes, J. Mater. Chem. 11 (2001) 783.
[2] A. Akthakul, R.F. Salinaro, A.M. Mayes, Antifouling polymer membranes with subnanometer size selectivity, Macromolecules 37 (2004) 7663.
[3] Y. Chang, Y.-J. Shih, R.-C. Ruaan, A. Higuchi, W.-Y. Chen, J.-Y. Lai, Preparation of poly(vinylidene fluoride) microfiltration membrane with uniform surface-copolymerized poly(ethylene glycol) methacrylate and improvement of blood compatibility, J. Membr. Sci. 309 (2008) 165–174.
[4] G.B. Sigal, M. Mrksich, G.M. Whitesides, Effect of surface wettability on the adsorption of proteins and detergents, J. Am. Chem. Soc. 120 (1998) 3464.
[5] F. Fang, I. Szleifer, Effect of molecular structure on the adsorption of protein on surfaces with grafted polymers, Langmuir 18 (2002) 497.
[6] I.H. Huisman, P. Prádanos, A. Hernández, The effect of protein–protein and protein–membrane interactions on membrane fouling in ultrafiltration, J. Membr. Sci. 179 (2000) 79.
[7] Z.-P. Zhao, Z. Wang, S.-Ch. Wang, Formation, charged characteristic and BSA adsorption behavior of carboxymethyl chitosan/PES composite MF membrane, J. Membr. Sci. 217 (2003) 151–158.
[8] H. Mo, K.G. Tay, H.Y. Ng, Fouling of reverse osmosis membrane by protein (BSA): effects of pH, calcium, magnesium, ionic strength and temperature, J. Membr. Sci. 315 (2008) 28–35.
[9] J.F. Hester, P. Banerjee, A.M. Mayes, Preparation of protein-resistant surfaces on poly(vinylidene fluoride) membranes via surface segregation, Macromolecules 32 (1999) 1643–1650.
[10] M. Taniguchi, J.E. Kilduff, G. Belfort, Low fouling synthetic membranes by UV-assisted graft polymerization: monomer selection to mitigate fouling by natural organic matter, J. Membr. Sci. 222 (2003) 59–70.
[11] D.A. Musale, A. Kumar, G. Pleizier, Formation and characterization of poly(acrylonitrile)/chitosan composite ultrafiltration membranes, J. Membr. Sci. 154 (1999) 163–173.
[12] U.K. Aravind, Ji. Mathew, C.T. Aravindakumar, Transport studies of BSA, lysozyme and ovalbumin through chitosan/polystyrene sulfonate multilayer membrane, J. Membr. Sci. 299 (2007) 146–155.
[13] C.-H. Zhang, F.-L. Yang, W.-J. Wang, B. Chena, Preparation and characterization of hydrophilic modification of polypropylene non-woven fabric by dip-coating PVA (polyvinyl alcohol), Sep. Purif. Technol. 61 (2008) 276-286.
[14] K. Yoon, K. Kim, X.F. Wang, D.F. Fang, B.S. Hsiao, B. Chu, High flux ultrafiltration membranes based on electrospun nanofibrous PAN scaffolds and chitosan coating, Polymer 47 (2006) 2434.
[15] N. Singh, S.M. Husson, B. Zdyrko, I. Luzinov, Surface modification of microporous PVDF membrane by ATRP, J. Membr. Sci. 262 (2005) 81–90.
[16] B. Jung, Preparation of hydrophilic polyacrylonitrile blend membranes for ultrafiltration, J. Membr. Sci. 229 (2004) 129–136.
[17] S. Atchariyawut, C. Feng, R. Wang, R. Jiraratananon, D.T. Liang, Effect of membrane structure on mass-transfer in the membrane gas–liquid contacting process using microporous PVDF hollow fibers, J. Membr. Sci. 285 (2006) 272–281.
[18] S. Rajendran, M. Sivakumar, R. Subadevi, M. Nirmala, Characterization of PVA–PVDF based solid polymer blend electrolytes, Physica B 348 (2004) 73–78.
[19] Z.-K. Xu, J.-L. Wang, L.-Q. Shen, D.-F. Nen, Y.-Y. Xu, Microporous polypropylene hollow fiber membrane. Part I. Surface modification by the graft polymerization of acrylic acid, J. Membr. Sci. 196 (2002) 221–229.
[20] L.-P. Zhu, H.-B. Dong, X.-Z. Wei, Z. Yi, B.-K. Zhu, Y.-Y. Xu, Tethering hydrophilic polymer brushes onto PPESK membranes via surface-initiated atom transfer radical polymerization, J. Membr. Sci. 320 (2008) 407–415.
[21] R. Jiraratananon, A. Chanachai, A study of fouling in the ultrafiltration of passion fruit juice, J. Membr. Sci. 111 (1996) 39–48.
[22] R. Jiraratananon, D. Uttapap, P. Sampranpiboon, Cross flow microfiltration of a colloidal suspension with the presence of macromolecules, J. Membr. Sci. 140 (1998) 57–66.

Separation and Purification Technology 69 (2009) 118–125

Contents lists available at ScienceDirect

Separation and Purification Technology

journal homepage: www.elsevier.com/locate/seppur

# Experimental study on membrane wetting in gas–liquid membrane contacting process for $CO_2$ absorption by single and mixed absorbents

Wichitpan Rongwong[a], Ratana Jiraratananon[a,*], Supakorn Atchariyawut[b]

[a] Department of chemical engineering, King Mongkut's University of Technology Thonburi, Bangkok 10140, Thailand
[b] WorleyParsons (Thailand) Limited, Sriracha, Chonburi, 20110, Thailand

ARTICLE INFO

*Article history:*
Received 29 April 2009
Received in revised form 7 July 2009
Accepted 9 July 2009

*Keywords:*
Amine solution
$CO_2$ absorption
Membrane contactors
Membrane wetting
PVDF hollow fiber

ABSTRACT

The membrane wetting by the liquid absorbents is an important problem in the operation of gas–liquid membrane contacting process. In order to gain a better understanding on the role of absorbents on membrane wetting, monoethanolamine (MEA, primary amine), diethanolamine (DEA, secondary amine), and 2-amino-2-methyl-1-propanol (AMP, sterically hindred amine) were applied as absorbent solutions. The membrane used for the experiments was the hollow fiber polyvinylidenefluoride (PVDF) membrane. The performance of both single and mixed amine solutions on the $CO_2$ absorption capacity and membrane wetting potential were investigated. In addition, sodium chloride (NaCl, inorganic salt) and sodium glycinate (SG, organic salt) were added into the MEA aqueous solution to observe $CO_2$ flux and membrane wetting.

The results revealed that the use of MEA solution and SG as absorbents gave highest $CO_2$ flux. The overall mass transfer coefficients obtained from the experiments also showed the same trend as $CO_2$ flux, i.e, the values were in the following order: MEA> AMP > DEA. However, the long-term flux was monitored and it was found that MEA also gave lowest flux decline due to the membrane wetting. The use of mixed amine solutions and the addition of NaCl did not help protect the membrane wetting. On the contrary, the addition of SG in to MEA solution can improve flux and resulted in stable $CO_2$ flux indicating that the membrane wetting was negligible.

## 1. Introduction

Carbon dioxide ($CO_2$) is the main gaseous component of the greenhouse gases in the atmosphere, representing about 80%. $CO_2$ has been known to contribute significantly to global warming. The effective and economical technology for $CO_2$ capture is, thus, necessary. Conventional gas absorption process for removal of $CO_2$, including chemical absorption by reactive absorbents, is normally carried out by packed and spray columns. The methods suffer many drawbacks such as flooding, foaming, and high capital and operating costs. These problems can be overcome by using hollow fiber membrane contactors [1].

Membrane contactors are devices that employ porous hydrophobic membrane as a phase barrier allowing two fluids to come to contact with each other for the purpose of mass transfer without dispersion of one phase into the other. This typical process offers several practical advantages including high surface area per unit volume, especially, when the hollow fiber membrane modules are used. Recent reviews of $CO_2$ absorption using hollow fiber membrane contactors are given in the literature [1,2].

Although the membrane contactors offer many advantages over the conventional contacting equipment, additional mass transfer resistance is introduced due to the membrane. Depending on the membrane material, the liquid absorbent nature and the pressure of the two phases, the membrane pores may be filled with gas or liquid, which corresponds to the non-wetted mode and the wetted mode. In the gas absorption case, the non-wetted mode is preferred because if the membrane pores are wetted by liquid the membrane resistance will increase, resulting in low flux. Wang et al. [3] reported that the reduction of the overall mass transfer coefficient may reach 20% even if the membrane pores were 5% wetted. The study of membrane wetting has been the subject of interest [3–5]. The membrane with high hydrophobicity is more resistant to wetting. The hydrophobicity of membranes is represented in terms of the contact angle between the liquid absorbent and membrane. In general, the hydrophobicity of the membranes is in the order of PTFE (polytetrafluoroethelene) > PP (polypropylene) > PVDF (polyvinylidenefluoride) based on the contact angle data [6]. For a given membrane material and structure,

---

* Corresponding author. Tel.: +66 2470 9222; fax: +66 2428 3534.
*E-mail address:* ratana.jir@kmutt.ac.th (R. Jiraratananon).

1383-5866/$ – see front matter © 2009 Elsevier B.V. All rights reserved.
doi:10.1016/j.seppur.2009.07.009

**Nomenclature**

| | |
|---|---|
| $A_T$ | mass-transfer area based on inside surface area of gas–liquid contact ($m^2$) |
| $C_l$ | concentration of carbon dioxide in the liquid phase ($mol\,m^{-3}$) |
| $C_g$ | concentration of carbon dioxide in the gas phase ($mol\,m^{-3}$) |
| $\Delta C_{l,av}$ | logarithmic mean concentration difference of carbon dioxide in the liquid phase ($mol\,m^{-3}$) |
| $C_{CO_2,F}$ | concentration of carbon dioxide in feed stream ($mol\,mol^{-1}$) |
| $C_{CO_2,R}$ | concentration of carbon dioxide in retentate stream ($mol\,mol^{-1}$) |
| $D$ | diffusion coefficient of carbon dioxide in the liquid phase ($m^2\,s^{-1}$) |
| $D_{g,eff}$ | effective diffusion coefficient of gas in the pores ($m^2\,s^{-1}$) |
| $d_i$ | inside diameter of membrane (m) |
| $d_{ln}$ | logarithmic mean diameter of membrane (m) |
| $d_o$ | outside diameter of membrane (m) |
| $H$ | Henry's constant |
| $J_{CO_2}$ | $CO_2$ flux ($mol\,m^{-2}\,s^{-1}$) |
| $K_{Ol}$ | overall mass transfer coefficient ($m\,s^{-1}$) |
| $k_l$ | individual mass transfer coefficient of liquid phase ($m\,s^{-1}$) |
| $k_m$ | individual mass transfer coefficient of membrane ($m\,s^{-1}$) |
| $k_g$ | individual mass transfer coefficient of gas phase ($m\,s^{-1}$) |
| $L$ | effective length of the membrane module (m) |
| $l_m$ | thickness of the hollow fiber (m) |
| $\Delta P$ | penetration pressure (Pa) |
| $Q_F$ | total gas flow rate in feed stream ($m^3\,s^{-1}$) |
| $Q_l$ | liquid flow rate ($m^3\,s^{-1}$) |
| $Q_R$ | total gas flow rate in retentate stream ($m^3\,s^{-1}$) |
| $r_p$ | membrane pore radius (m) |
| $Sh$ | Sherwood number |
| $T_g$ | gas temperature (K) |
| $V$ | velocity ($m\,s^{-1}$) |

*Greek letters*

| | |
|---|---|
| $\varepsilon_m$ | membrane porosity |
| $\theta$ | contact angle (°) |
| $\sigma$ | surface tension ($mN\,m^{-1}$) |
| $\tau_m$ | membrane tortuosity |

its hydrophobic character may be altered due to morphological change by the interaction of liquid. Khaisai et al. [6] compared the $CO_2$ absorption performance of PTFE, PP, and PVDF membranes. They concluded that based on the cost of PVDF membranes, and its comparable performance to PTFE membrane, PVDF remains a membrane of interest.

Important measures to prevent the wetting problem include the selection of liquids with suitable surface tension. It was reported that when the liquid surface tension decreased (which may be due to the presence of organic compounds) from about 33 mN/m to 30 mN/m, the transmembrane pressure difference of the PP membrane was decreased from about 0.9 bar to 0.1 bar leading to the rapid increase of membrane wetting [7]. The study of Yan et al. [4] on $CO_2$ removal using PP membrane by aqueous solutions of potassium glycinate (PG), monoethanolamine (MEA), and methyldiethanolamine (MDEA) revealed that aqueous PG solution has a lower potential of membrane wetting due to its suitable physical properties (e.g. surface tension). PG also has good reactivity towards $CO_2$ compared with MEA and MDEA.

To achieve high $CO_2$ absorption rate, reactive absorbents are widely employed in practice. The commonly used absorbents for $CO_2$ capture are aqueous solutions of amines which are weak bases that react with $CO_2$ to form complexes with weak chemical bonds. These chemical bonds are easily broken upon mild heating, leading to absorbent regeneration. The preferred amines are MEA, diethanolamine (DEA), and MDEA in terms of high $CO_2$ loading capacity, rapid absorption rate and low cost for regeneration. MEA, a primary amine, has been used extensively because of its high reactivity and low cost. However, its maximum loading is limited by stoichiometry to 0.5 mol $CO_2$ per mole of amine. DEA is less corrosive with reasonable $CO_2$ absorption rate. The advantages of MDEA, a tertiary amine, over MEA include its higher loading capacity and its low heat of reaction leading to low energy requirement for regeneration.

The use of mixed absorbents for $CO_2$ removal is of increasing interest. Glasscock et al. [8] investigated $CO_2$ absorption by mixed amines in a batch liquid continuous gas-stirred cell reactor. The simulation of $CO_2$ absorption was carried out. A differential equation based model was developed and used to study the reaction kinetics for $CO_2$ with MEA, DEA, MDEA and the mixtures of MEA/MDEA and DEA/MDEA. It was demonstrated that MDEA participated in the DEA kinetics, but not the MEA kinetics. Finally, it was concluded that the performance of the MEA/MDEA system was much more sensitive to loading than the DEA/MDEA system. The absorption of $CO_2$ into aqueous solution of amine mixtures was also reported by Mandol et al. [9]. It was found that the addition of small amount of MEA to aqueous solutions of MDEA or AMP significantly enhanced the enhancement factor and rate of absorption for both solvents. Apart from the mixtures of MEA, DEA, AMP and MDEA, the use of piperazine (PZ) as the activator for those amines is also the subject of interest [10–12].

The use of mixed amines is an interesting and promising approach since it may bring about improvement in gas absorption and in reducing energy requirement for regeneration. However, previous works [9–12] on using mixed absorbents did not include the long-term flux, wetting characteristics, and there was a lack of important data (contact angle, surface tension, and viscosity) influencing the membrane wetting. Mixed amines may also result in different membrane wetting characteristics of the system. Accordingly, it is the interest of the present work to systematically investigate the removal of $CO_2$ by a hollow fiber membrane contactor using both single and mixed amine solutions. PVDF membrane was selected for the study. Mixed amines of MEA, DEA, and AMP including SG (sodium glycinate) as well as inorganic salt, sodium chloride (NaCl), at different compositions were used for $CO_2$ removal. The wetting study was carried out by monitoring the long-term $CO_2$ flux of the mixed amine solutions. In addition, the effect of salts, i.e. SG and NaCl on $CO_2$ flux and on membrane wetting was also presented.

## 2. Theory

### 2.1. Basic principle of mass transfer in gas–liquid membrane contactor

The resistance-in-series model has been widely applied to describe the mass transfer mechanism in the gas–liquid membrane contacting process. Fig. 1 illustrates the mass transport of the interested gas for non-wetted operating mode of membrane contactors, i.e., diffusion from the bulk gas through the membrane pores and dissolution in the liquid absorbent. The resistance-in-series model

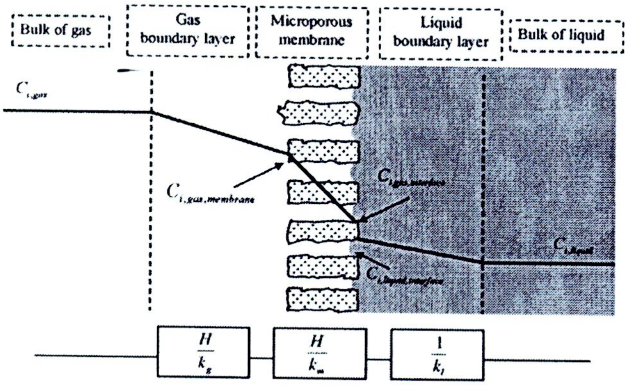

**Fig. 1.** Schematic drawing of mass transfer regions and resistance-in-series in non-wetted membrane contactor.

can be expressed as Eq. (1).

$$\frac{1}{K_{ol}} = \frac{1}{k_l} + \frac{Hd_o}{k_m d_{ln}} + \frac{Hd_o}{k_g d_i} \tag{1}$$

where $K_{ol}$ is the overall mass transfer coefficient based liquid phase (m/s), $k_l$, $k_m$, $k_g$ are the individual mass transfer coefficients of the liquid phase, membrane and gas phase, respectively. $d_l$, $d_o$, $d_{ln}$ are the inner, outer and logarithmic mean diameters of the fibers, respectively. $H$ represents Henry's constant. For the dissolution of $CO_2$ in 1 M MEA, 1 M DEA, and 1 M AMP, the Henry's constants were reported to be 0.831 [13], 0.665 [14], 0.767 [15], and 0.689 [16], respectively.

The overall mass transfer coefficient, $K_{ol}$, can be calculated based on the experiments by the following equation [13]:

$$K_{ol} = \frac{Q_l(C_{l,out} - C_{l,in})}{A_T \Delta C_{l,av}} \tag{2}$$

The logarithmic mean concentration, $\Delta C_{l,av}$, is expressed as

$$\Delta C_{l,av} = \frac{(HC_{g,in} - C_{l,out}) - (HC_{g,out} - C_{l,in})}{\ln\left(HC_{g,in} - C_{l,out}/HC_{g,out} - C_{l,in}\right)} \tag{3}$$

where $A_T$ is the gas–liquid contact area, $C_{l,in}$, $C_{l,out}$ are the liquid phase inlet and outlet concentrations, $C_{g,in}$, $C_{g,out}$ are the gas phase inlet and outlet concentrations, $Q_l$ is the liquid volumetric flow rate.

In the operation of a membrane contactor, either the gas phase or liquid phase can be fed through the shell side or tube side of the hollow fiber membrane module. However, flow of liquid in the tube side takes more advantage than that in the shell side [17] which also depends on the packing density of the membrane module used. In addition, when asymmetric membranes are used, the location of the skin layer has to be considered in order to decide the flow configuration. For the tube side, the well-known Graetz-Lévêque mass transfer correlation was widely used to predict the tube side mass-transfer coefficient [1,18];

$$Sh = \frac{k_l d_i}{D} = 1.62\left(\frac{d_i^2 V}{LD}\right)^{1/3} \tag{4}$$

where $Sh$ is Sherwood number, $D$ is the diffusion coefficient, $L$ is the tube length and $V$ is the fluid velocity.

Many correlations have been proposed to determine the shell side mass transfer coefficient [18–20]. However, each of them is applicable to a certain limited range of operation. In general, it can be expressed in the following form:

$$Sh = aRe^{\alpha}Sc^{\beta} \tag{5}$$

where $Re$ and $Sc$ are Reynolds and Schmidt numbers, respectively.

The membrane mass transfer coefficient in a completely non-wetted case can be calculated using the following equation [21]:

$$k_m = \frac{D_{g,eff}\varepsilon_m}{\tau_m l_m} \tag{6}$$

where $D_{g,eff}$ is the effective diffusion coefficient of pure gas filled in the pores. It is calculated from the summation between the molecular self-diffusion coefficient and the diffusion coefficient which is the interaction of gas molecules and membrane wall [21]. $\varepsilon_m$, $l_m$ are the porosity, thickness of the membrane provided by the manufacturer, respectively. $\tau_m$ is the tortuosity achieving from the correlation [22]. In order to estimate the overall mass transfer coefficient based on Eq. (1), Eqs. (4) and (6) were used to determine the liquid phase and membrane mass transfer coefficients.

In this study, the $CO_2$ flux which was used to indicate the process efficiency can be estimated by the following Eq. [4];

$$J_{CO_2} = \frac{(Q_F \times C_{CO_2,F} - Q_R \times C_{CO_2,R}) \times 273.15 \times 1000}{22.4 \times T_g \times A_T} \tag{7}$$

where $J_{CO_2}$ is the $CO_2$ flux. $C_{CO_2,F}$ and $C_{CO_2,R}$ are the $CO_2$ concentrations in the feed and retentate streams, respectively. $Q_F$ and $Q_R$ are the gas flow rates at the inlet and outlet of the membrane module, respectively. $T_g$ is the gas temperature. $A_T$ is the mass transfer area.

### 2.2. Penetration pressure

There are two possible operating modes in the gas–liquid membrane contacting process, i.e. dry and wet modes. The operation in dry mode (gas-filled membrane pore) is more advantageous than that in the wet mode (liquid-filled membrane pore) owing to the higher gas diffusivity. The liquid will not penetrate into the membrane pores when pressure difference between liquid and gas phase stream in membrane pores is lower than the penetration pressure [1] defined as follows:

$$\Delta P = \frac{-2\sigma\cos\theta}{r_p} \tag{8}$$

where $\Delta P$ is the penetration pressure or wetting pressure. $\sigma$ is the surface tension of the liquid. $\theta$ is the contact angle formed between fluid and the membrane pore. $r_p$ is the membrane pore radius.

## 3. Experimental

Hydrophobic porous polyvinylidenefluoride (PVDF) hollow fiber membrane used in all experiments was supplied by Memcor Australia (South Windsor, New South Wales, Australia). The membrane characteristics are shown in Table 1. Carbon dioxide (99.8%) and nitrogen gases (99%) were obtained from Thai Industrial Gases PLC, Thailand. All chemicals used in the experiment are analytical grade. The purities and suppliers of the chemicals are; monoethanolamine (MEA) 97% (Unilab), diethanolamine (DEA) 99% (Fisher scientific), 2-amino-2-methyl-1-propanol (AMP) 90% (Fluka), sodium glycinate (SG) 99% (Sigma, for use as standard solution), sodium chloride (NaCl) 99.5% (Carlo Ebra), glycinate (for synthesis of sodium glycinate) 99% (Merck), and sodium hydroxide (NaOH) 97% (Carlo Ebra).

**Table 1**
Specifications of the hollow fiber membrane module.

| | |
|---|---|
| Fiber o.d. (um) | 1300 |
| Fiber i.d. (urn) | 800 |
| Module i.d. (mm) | 10 |
| Membrane pore size (urn) | 0.2 |
| Membrane porosity | 0.60 |
| Number of fibers | 35 |
| Effective module length (mm) | 295 |
| Effective contact area (m$^2$) | 0.0207 |

**Table 2**
Surface tensions, viscosities of the absorbents and the contact angles of the absorbents and membrane.

| Absorbents | Surface tension (mN/m) | Viscosity (mPa s) | Contact angle (degree) |
|---|---|---|---|
| Water | 70.98 | 0.91 | 91.77 |
| MEA0.1M | 70.58 | 0.924 | 91.50 |
| MEA 0.25 M | 64.25 | 0.95 | – |
| MEA0.5M | 63.96 | 1.006 | 91.27 |
| MEA1M | 61.54 | 1.119 | 90.12 |
| Pure MEA | 48.55 | – | – |
| DEA1M | 59.12 | 1.22 | 87.92 |
| AMP1M | 58.81 | 1.426 | 86.95 |
| SG1M | 63.95 | 1.186 | 93.91 |
| DEA 0.25 M + AMP 0.25 M | 58.28 | 1.113 | 85.18 |
| MEA 0.25 M + AMP 0.25 M | 60.96 | 1.051 | 87.64 |
| MEA 0.25 M + DEA 0.25 M | 61.96 | 1.046 | 89.62 |
| MEA 0.25 M + NaCl 0.125 M | 64.16 | 0.974 | 91.28 |
| MEA 0.25 M + NaCl 0.25 M | 64.08 | 0.976 | 88.34 |
| MEA 0.25 M + SG0.125 M | 64.21 | 0.99 | 88.94 |
| MEA 0.25 M + SG 0.25 M | 64.03 | 1.015 | 91.1 |

**Table 3**
Experimental plan. All experiments were carried out at room temperature (30 °C) and at a constant gas flow rate of 200 ml/min.

| Experiment | Concentration of absorbents and salts (mol/L) | | | | | Absorbent flow rate |
|---|---|---|---|---|---|---|
| | MEA | DEA | AMP | SG | NaCl | (ml/min) |
| 1 | 0.25 | | | | | 400, 560760, 1000 |
| 2 | 0.5 | | | | | |
| 3 | 1.0 | | | | | |
| 4 | | 1.0 | | | | |
| 5 | | | 0.5 | | | |
| 6 | | | 1.0 | | | |
| 7 | | | | 1.0 | | |
| 8 | 0.25 | 0.25 | | | | |
| 9 | 0.25 | | 0.25 | | | |
| 10 | | 0.25 | 0.25 | | | |
| 11 | 0.25 | | | | 0.125 | |
| 12 | 0.25 | | | | 0.25 | |
| 13 | 0.25 | | | 0.125 | | |
| 14 | 0.25 | | | 0.25 | | |
| 15 | DI water | | | | | |

De-ionized (DI) water was used for preparation of all solutions.

Sodium glycinate (1 mol/l, 20 l) was prepared from the reaction between glycine and sodium hydroxide [23,24]. Ten liters of NaOH solution (2 mol/l) was mixed with 10 l of standard glycine solution (2 mol/l) and stirred at room temperature for 20 min. The conductivity and pH of the mixture were measured and compared with those of standard sodium glycinate solution to ensure that the reaction was completed.

The viscosity, surface tension of the absorbents, and the contact angle of the membrane and the absorbents were also measured by the viscometer (C-75, Canon), surface tension meter (TD2, Laude) and contact angle meter (DCAT 11, Dataphysics), respectively. These values are reported in Table 2.

Fig. 2 shows the experimental setup of a gas–liquid membrane contacting process. The mixture of $N_2/CO_2$ with a volume ratio of 80:20, which is in the composition range of flue gas was used as the feed gas composition whereas DI water, MEA, DEA, AMP and their blended aqueous solutions were employed as absorbents. The effect of addition of organic salt (SG) and inorganic salt (NaCl) into the MEA solution on the $CO_2$ separation performance were also investigated. Table 3 summarizes the experimental plan. All experiments were carried out at room temperature (30° C). The liquid flow rates were at 400 ml/min, 560 ml/min, 760 ml/min, and 1000 ml/min whereas the gas flow was fixed at 200 ml/min. In the experiment, the feed gas flow rate supplied from compressed gas cylinders was adjusted and controlled by Aalborg (GFC model) mass flow controllers, and then it was fed through the shell side of the membrane module. Digital bubble meter was used to determine the inlet and outlet gas volume flow rates. The liquid absorbent was pumped by a peristaltic pump (L/S® Easy-load® II, Masterflex model 77201-62) from the feed tank through a rotameter, after that it was fed into the tube side of the hollow fibers. The pressure gauges were used to indicate the inlet and outlet pressures of the gas and liquid phase. Gas Chromatograph (6890 Hewlett Packard, TCD) was used to analyze the inlet and outlet gas compositions. All of experimental results data were collected after the experiment had been operated for 30 min in order to ensure that the system reached the steady state. The results of each run were averaged from five times of sampling.

## 4. Results and discussion

### 4.1. $CO_2$ absorption performance with various absorbents

#### 4.1.1. Single absorbents

Fig. 3 shows the effects of liquid phase velocity and types of absorbent on the $CO_2$ absorption flux. It can be found that the $CO_2$ absorption flux increased with increasing liquid phase velocity since the mass transfer coefficient in the liquid phase was enhanced [13]. In the experiments, high absorbent flow rate was used compared with the gas flow rate. For the gas–liquid membrane contacting process, the ratio of liquid and gas flow rate does not much affect the operability of the system since gas and liquid flow rate can be independently controlled. In this process, the mass transfer resistance in the liquid phase is high or controls the system. The increase in the liquid flow rate does not cause flooding as commonly found in a usual absorption process, but benefits or increases the system performance. It should also be noted that the ratio of mole of $CO_2$ to mole of liquid absorbent was low. We used many single and mixed amine solutions. These amines are different

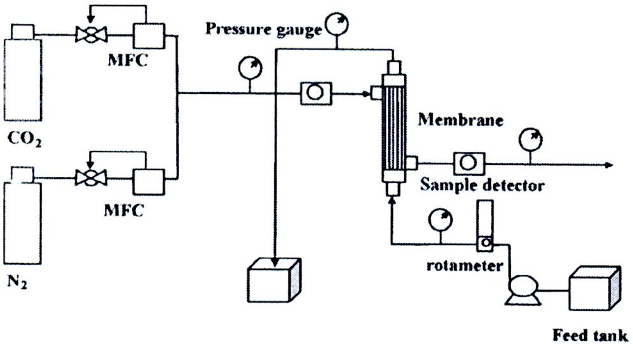

Fig. 2. Experimental setup of a gas–liquid membrane contactor unit.

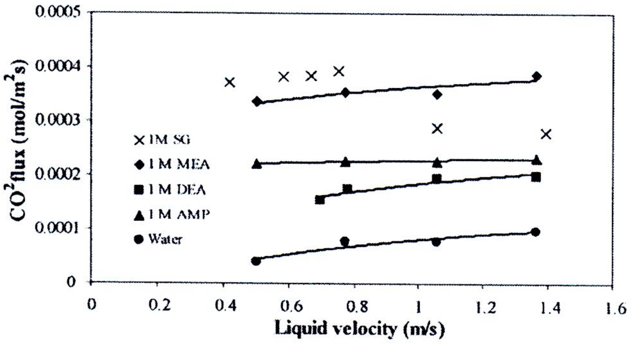

Fig. 3. Effects of absorbent velocity and types of amine solutions on $CO_2$ flux.

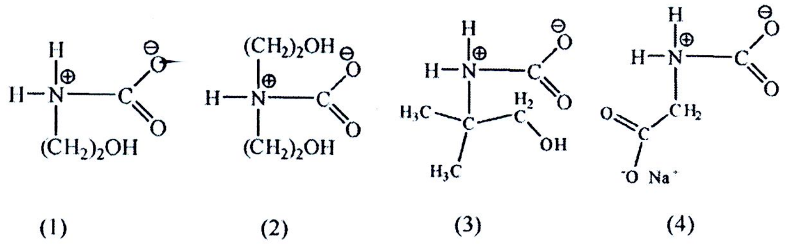

**Fig. 4.** Intermediates produced from the reaction between $CO_2$ and (1) MEA, (2) DEA, (3) AMP, and (4) SG.

in rates of reactions and absorption capacity, varying from low to high. The low ratio (mole of $CO_2$/mole of absorbent) allowed for better comparison of the results. In case of SG used as an absorbent, at low liquid velocity, the $CO_2$ flux slightly changed with the liquid velocity. This corresponds with the study of Yan et al. [4]. They reported that the $CO_2$ flux obtained from using potassium glycinate (PG) as an absorbent increased slightly in the low liquid velocity range (0.025–0.1 m/s). Although, at high liquid velocity, the $CO_2$ flux decreased with increasing liquid velocity due to the decrease in contact time between gas and liquid phase. Another possible reason for the unsuccessive decrease of $CO_2$ flux was the change of mass transfer resistance from the liquid phase to the gas phase.

From the above results, it was found that the $CO_2$ absorption fluxes of the different absorbents at 1 M concentration were in the sequence of SG (amino acid salt) > MEA (primary amine) > AMP (sterically hindered primary amine) > DEA (secondary amine) > water (physical absorbent). The results can be explained by the chemical reaction mechanism between $CO_2$ and amine. The example of reaction mechanism between amine solution and $CO_2$ is as follows [11]:

$$R^{(1)}R^{(2)}NH + CO_2 \leftrightarrow \underset{\text{(zwitterion intermediate)}}{R^{(1)}R^{(2)}NH^{+}COO^{-}} \tag{9}$$

$$R^{(1)}R^{(2)}NH + COO^{-} + B \leftrightarrow R^{(1)}R^{(2)}NCOO^{-} + \underset{\text{(carbamate ion)}}{BH^{+}} \tag{10}$$

For MEA, $R^{(1)} = (CH_2)_2OH$, $R^{(2)} = H$ and B denotes $OH^-$ or $H_2O$.

The above chemical reaction mechanism between amine and $CO_2$ is called zwitterion reaction which produces the intermediate, i.e. $R^{(1)}R^{(2)}NH^{+}COO^{-}$. $R^{(1)}$ and $R^{(2)}$ are hydrogen or alkyl group as shown in Fig. 4. This intermediate can react with B to create the carbamate ion. Therefore, the chemical reaction rate between $CO_2$ and amine depends on the stability of the intermediate. If the intermediate is not stable, it would be easier to continuously react as in Eq. (10), giving the carbamate ion which provides higher chemical reaction rate constant.

From Fig. 3 the $CO_2$ flux in case of using MEA as absorbent was higher than those of using AMP and DEA. For MEA used as absorbent, $R^{(2)}$ in Eq. (9) stands for hydrogen atom which is an electron-withdrawing group attached at the nitrogen atom of the intermediate. This induces a cation at the nitrogen atom. The intermediate from the reaction between $CO_2$ and MEA is not stable and it can instantaneously react, as in Eq. (10) to form a carbamate ion. Therefore, the chemical reaction rate between $CO_2$ and MEA is high leading to the high $CO_2$ absorption flux.

For using DEA as an absorbent, $R^{(2)}$ in Eq. (9) represents the ethanol group ($(CH_2)_2OH$) which is called an electron-donating group. The intermediate resultant from DEA is thus, more stable than that from reaction between MEA and $CO_2$. Therefore, $CO_2$ flux of DEA was lower. In case of using AMP, $R^{(1)}$ in Eq. (9) represents hydrogen atom. However, $R^{(2)}$ of AMP molecule ($C(CH_2)_2CH_3OH$) is larger than that of MEA. This can introduce the steric effect. Therefore, the $CO_2$ absorption flux of using AMP absorbent was lower than that of using MEA absorbent. Wang et al. [25] and deMontigny et al. [17] reported the same trend of the results. Moreover, the results can also be supported that by the values of rate constant of the reactions between MEA/DEA/AMP with $CO_2$ available in the literature [26] which reported that the rate constants of MEA > AMP > DEA.

The $CO_2$ flux in case of using SG as absorbent was higher than that of using MEA since the pH of 1 M SG solution (pH 12.87) is higher than that of 1 M MEA solution (pH 11.91). The higher pH value of the SG solution may result in higher $OH^-$ concentration than that in MEA solution. Thus, the chemical reaction rate between $OH^-$ and $CO_2$ of SG solution was higher than that of MEA solution resulting in higher $CO_2$ flux. Yan et al. [4] presented the similar results when PG (potassium glycinate) was used as an absorbent. In other words, SG gave higher flux than MEA because the carboxylic group attached to the nitrogen atom of the intermediate has a higher electro-negativity than the ethanol group of MEA.

From the above experimental results, the overall mass transfer coefficient ($K_{ol}$) can also be estimated based on Eqs. (2) and (3). Fig. 5 depicts the effects of different types of amine used and solution velocity on the calculated $K_{ol}$. The $K_{ol}$ values showed the same trend with measured $CO_2$ absorption flux or they were in the order of MEA > AMP > DEA > water. Unfortunately, the $K_{ol}$ of the SG solution cannot be estimated due to the lack of Henry's constant for SG. The $K_{ol}$ for all amine solutions increased with increasing in liquid velocity due to the increasing in mass transfer coefficient in the liquid phase (see also Eq. (1)).

Fig. 6 shows the effect of MEA solution concentrations on the $CO_2$ flux. The higher MEA concentration used, the higher the $CO_2$ flux achieved. This is because the increase in absorbent concentration resulted in increasing the chemical reaction rate between $CO_2$ and MEA. Similar observations on the effect of absorbent concentration on the mass transfer rate were reported in literatures [4,25].

### 4.1.2. Mixed absorbents

*4.1.2.1. Absorption capacity of mixed absorbents.* The comparison of $CO_2$ flux by using single amine solutions, i.e. MEA, AMP, and DEA at 0.5 M concentration and mixed amine solutions, i.e. MEA/DEA, DEA/AMP, and MEA/AMP of 1:1 mole ratio at 0.5 M total concentra-

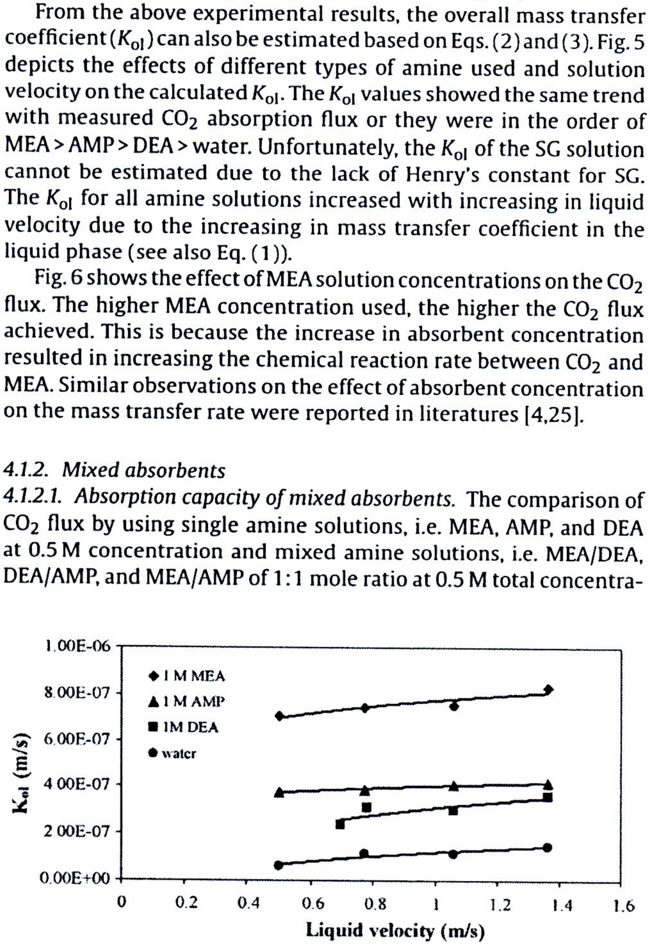

**Fig. 5.** Effects of absorbent solution velocity and various types of amine solutions on overall mass transfer coefficient ($K_{ol}$).

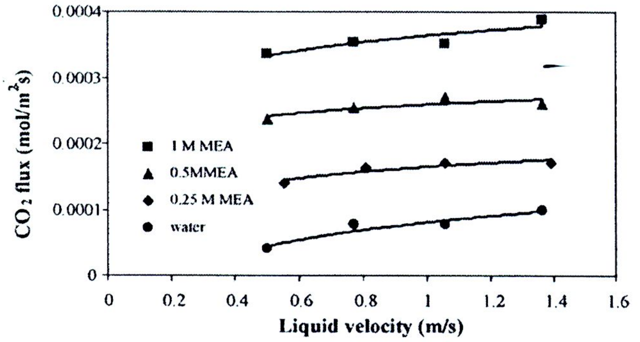

**Fig. 6.** Effects of absorbent solution velocity and MEA solution concentrations on $CO_2$ flux.

tion is shown in Fig. 7. The aim of this figure was to present the effect of mixed amine solution type on the absorption performance. These results were as expected. We expected that the absorption performance would be controlled by the amine with the higher reaction rate and absorption capacity. The $CO_2$ flux for mixed absorbents used was in the sequence of MEA/AMP > MEA/DEA > DEA/AMP. The mixed absorbent which was composed of MEA provided the high capacity in $CO_2$ absorption since the MEA is a primary amine having the higher chemical reaction rate constant with $CO_2$ than DEA and AMP (see also Section 4.1.1). The $CO_2$ flux when MEA/AMP and MEA/DEA of 0.5 M total concentration were used as absorbents were close to the $CO_2$ flux of using 1 M AMP and DEA. The similar observations were also reported by Mandal and Bandyopadhyay [9] and Paul et al. [27].

When the price and $CO_2$ absorption capacity of each amine solution are considered, the mixed amine solution of MEA/AMP shows the better potential to be used as absorbent solution in gas-liquid membrane contacting process. In addition, Pei et al. [28] reported that the mixed absorbent of MEA/AMP required less energy consumption in solution recovery than MEA solution.

*4.1.2.2. Organic and inorganic salt addition into amine solution.* In order to investigate the absorption performance affected by the presence of salt, the inorganic and organic salts were added into the amine absorbent (MEA). The organic and inorganic salts used in this study were sodium glycinate (SG) and sodium chloride (NaCl), respectively. Salts concentration was varied with the intention of investigating its influences on the $CO_2$ absorption performance. For NaCl addition, previous results [13] which showed the reduced flux was expected. For the addition of SG, the increase of flux was expected since SG can react with $CO_2$. Fig. 8 shows the effect of NaCl and SG in 0.25 M MEA solution on the $CO_2$ absorption flux. It was found that $CO_2$ flux decreased with increasing the NaCl concentration as a result of salting out effect. The salting out effect is the phenomenon which gas solubility in the liquid is decreased with increasing salt concentration. Atchariyawut et al. [13] reported that the presence of NaCl in NaOH solution resulted in decreasing $CO_2$ absorption flux and product gas humidity.

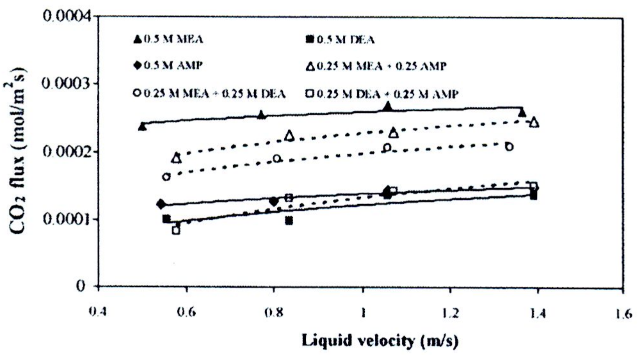

**Fig. 7.** Effects of absorbent solution velocity of single amines and mixed amines on $CO_2$ flux.

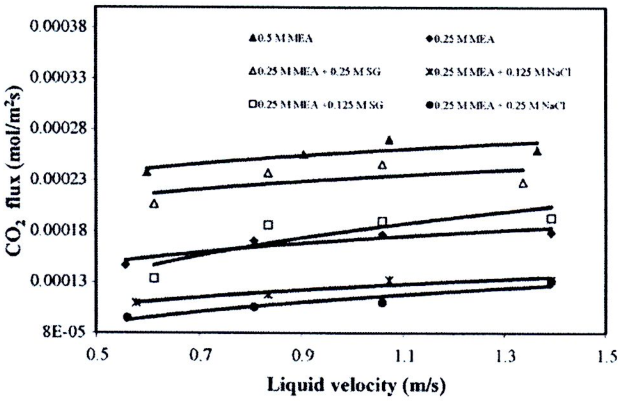

**Fig. 8.** Effects of NaCl and SG addition into MEA solution on $CO_2$ flux.

The effect of SG presence in 0.25 M MEA solution on the $CO_2$ flux is also depicted in Fig. 8. It can be seen that the $CO_2$ flux increased with increasing SG concentration. SG is an organic salt which can also lead to the salting effect, and the decrease of gas solubility. Nevertheless, the result indicated that the addition of SG could improve the $CO_2$ flux since SG can chemically react with $CO_2$ as described previously.

### *4.2. Long-term performance of gas–liquid membrane contacting process with various absorbents*

The membrane wetting by liquid absorbent is one of the significant problems in gas–liquid membrane contacting process operation. Wetting of membrane may occur after a certain period of operation due to a number of reasons. In the wetted membrane, the gas absorption flux is decreased as the membrane resistance is increased. Various type of liquid absorbents used in membrane contacting process may exhibit different phenomena of membrane wetting. In this section, the effects of various types of liquid absorbents and additives on the long-term $CO_2$ absorption performance are presented.

### *4.2.1. Effect of amine solution concentration*

Fig. 9 shows the effect of MEA concentrations on $CO_2$ flux throughout 12 days of operation. It was found that the $CO_2$ flux

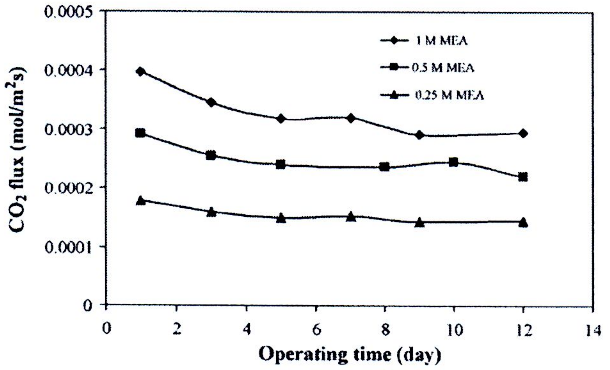

**Fig. 9.** Effects of MEA concentration on long-term performance of membrane contacting process.

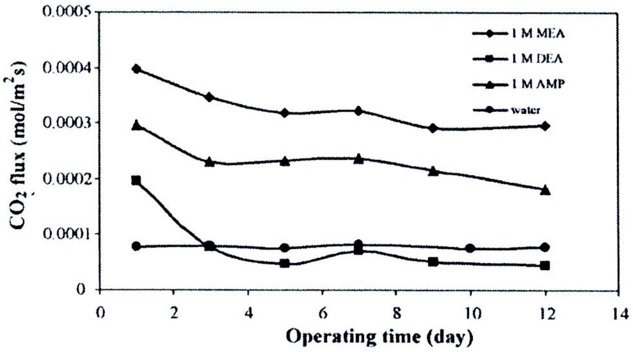

Fig. 10. Effects of various types of amine solutions on long-term performance of membrane contacting process.

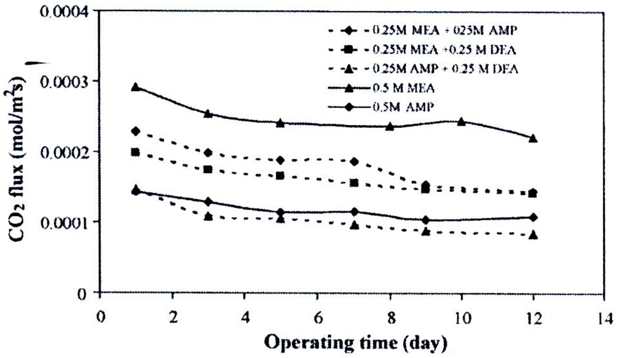

Fig. 11. Effects of mixed amine solutions on long-term performance of membrane contacting process.

decline increased obviously with increasing MEA concentration. The $CO_2$ flux of using 0.25 M, 0.5 M, and 1 M MEA solution as absorbent continuously decreased about 19%, 23%, and 26% of the initial flux, respectively. The decrease of $CO_2$ flux reflected the increase in the membrane mass transfer resistance due to membrane wetting. According to Eq. (8) and Table 2, the contact angle ($\theta$) and surface tension ($\sigma$) can be used to assess the possibility of membrane wetting. As the MEA concentration was increased, the contact angle and surface tension decreased. In the literature [4] it was also reported that the surface tension of MEA and MDEA solution decreased with concentration. Therefore, the probability of membrane wetting was more pronounced at high concentration, leading to higher flux decline.

### 4.2.2. *Effect of different types of amine solutions*

The influence of different types of amine solutions used as liquid absorbent on the $CO_2$ long-term flux was shown in Fig. 10. The MEA, DEA, and AMP solutions of 1 M were used for comparison during 12 days of operation. $CO_2$ flux of MEA, AMP, and DEA used as absorbents continuously declined roughly 26%, 39%, and 78% of initial flux, respectively. The decrease in $CO_2$ flux for 1 M MEA was lowest. The data on contact angle and surface tension of 1 M MEA (see Table 2) in comparison with those of 1 M AMP and 1 M DEA well supported the results. It was also found that when pure water used as absorbent, the $CO_2$ flux seemed to be constant during 12 days of operating period. Similar result was reported in the literature [13].

However, for comparison between DEA and AMP solutions used as absorbents, the percentage of $CO_2$ flux reduction of 1 M DEA was higher than that 1 M AMP. Nevertheless, the measured surface tension and contact angle of AMP were slightly lower than DEA. The result may be explained by the value of viscosity. The viscosity of 1 M AMP was higher than that of 1 M DEA, therefore, it was more difficult for AMP to penetrate into the membrane pores, leading to less membrane wetting. Similar explanation related to the viscosity and wetting ability of liquid absorbent was published by Lin et al. [12]. They found that the increase of piperazine concentration in AMP solution resulted in the increase of liquid absorbent viscosity and led to the decrease wetting ratio of PVDF membrane.

According to above $CO_2$ flux results, the overall mass transfer coefficient ($K_{ol}$) can be estimated based on Eqs. (2) and (3). The similar trend between the $CO_2$ flux and $K_{ol}$ was found. The overall mass transfer coefficients ($K_{ol}$) of MEA, AMP and DEA used as absorbents continuously dropped approximately 38%, 41%, and 78% of initial value during 12 days of operating time, respectively. The decrease of $K_{ol}$ was due to the increase of membrane mass transfer resistance caused by the membrane wetting.

Fig. 11 illustrates the effect of using mixed absorbents on long-term flux of $CO_2$. The mixed absorbents used in the study included MEA/DEA, DEA/AMP, and MEA/AMP of 1:1 mole ratio at 0.5 M of total concentration. The results indicated that the use of mixed absorbent solutions could not protect the membrane wetting. The reduction of $CO_2$ flux using mixed amine solutions was in the following order; of DEA/AMP > MEA/AMP > MEA/DEA. The experimental results were consistent with the measured contact angles and surface tensions according to Table 2. However, the viscosities of these mixed absorbents were close in values. Therefore, in this case the membrane wetting was not affected by viscosity.

### 4.2.3. *Effect of salt addition*

There was no previous report on the effect of salt addition on the long-term performance or the membrane wetting. NaCl and SG which are inorganic and organic salts, respectively, were used as additives in 0.25 M MEA solution in order to observe $CO_2$ flux and membrane wetting. According to Fig. 12, the addition of NaCl reduced flux due to salting out effect discussed previously. From Table 2, the surface tension of 0.25 M MEA solution, with the presence of NaCl, did not seem to change. However, the addition of NaCl into 0.25 M MEA solution increased the viscosity; thus, flux decline was not significant since membrane wetting was less important when the viscosity of the absorbent was increased [12]. From the results, the increase of salt (NaCl) concentrations from 0.125 M to 0.25 M slightly reduced flux decline (16%, 14%, respectively).

When SG was mixed with 0.25 M MEA solution the $CO_2$ flux was enhanced due to the chemical reaction between SG and MEA (see also Fig. 8). $CO_2$ flux decline was also negligible or it was less than the case of NaCl addition. The reason for this can be found from Table 2 in which the surface tension, viscosity, and the contact angle of the two cases are compared.

The results presented in Figs. 9–12 showed that flux decline, for several cases studied, was due to the membrane wetting since

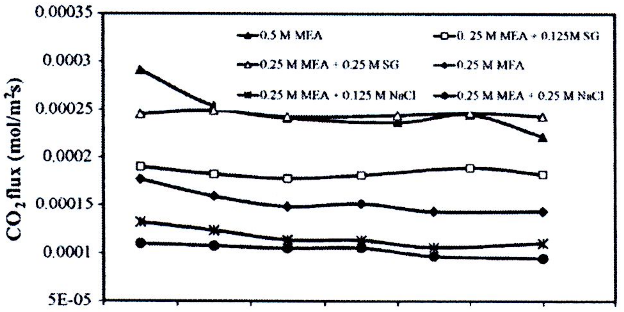

Fig. 12. Effects of NaCl and SG addition into MEA solution on long-term performance of membrane contacting process.

other experimental parameters were maintained constant, or only operating time was varied. It was also observed that the color of wetted PVDF membrane changed from the white to gray after the PVDF membrane contacted with MEA solution for about 2 days. On the other hand, the color of non-wetted PVDF membrane when using SG with MEA solution as absorbent did not change during long-term performance test period.

## 5. Conclusions

The $CO_2$ absorption capability and membrane wetting of various types of amine absorbents were investigated. Single and mixed amine solutions of MEA, DEA and AMP were selected to be used. NaCl and SG are the inorganic and organic salts, respectively, were employed as additives in the amine solutions. It was found that the absorption performance of single absorbents was in the order of MEA> AMP > DEA > water. The mixed amine absorbents consisted of MEA provided higher absorption flux and $CO_2$ flux was in the sequence of MEA/AMP > MEA/DEA > DEA/AMP. The addition of NaCl in to MEA introduced the salting out effect leading to the decrease of $CO_2$ flux. Conversely the addition of SG into MEA solution enhanced $CO_2$ flux due to the chemical reactions of both SG and MEA with $CO_2$.

The long-term $CO_2$ flux was investigated for single absorbent, mixed absorbent and absorbent with the presence of salts. The use of mixed absorbents was not able to protect the membrane wetting. The order of flux reduction of mixed absorbent was in the order of DEA/AMP > MEA/AMP > MEA/DEA. The addition of NaCl into 0.25 M MEA solution reduced $CO_2$ flux, but flux decline was improved. The addition of SG into 0.25 M MEA solution showed promising result since $CO_2$ flux was enhanced and flux decline due to the membrane wetting was not significant.

## Acknowledgement

The authors wish to thank Thailand Research Fund (TRF) and the Commission on Higher Education, Thailand through the TRF senior research scholar grant for the financial support.

## References

[1] A. Gabelman, S.T. Hwang, Hollow fiber membrane contactors, J. Membr. Sci. 159 (1999) 61–106.

[2] J.L. Li, B.H. Chen, Review of CO2 absorption using chemical solvent in hollow fiber membrane contactors, Sep. Purif. Technol. 41 (2005) 109–122.

[3] R. Wang, H.Y. Zhang, P.H.M. Feron, D.T. Liang, Influence of membrane wetting on $CO_2$ capture in microporous hollow fiber membrane contactors, Sep. Purif. Technol. 46 (2005) 33–40.

[4] S.P. Yan, M.X. Fang, W.F. Zhang, S.Y. Wang, Z.K. Xu, Z.Y. Luo, K.F. Cen, Experimental study on the separation of $CO_2$ from flue gas using hollow fiber membrane contactors without wetting, Fuel Process. Technol. 88 (2007) 501–511.

[5] H.Y. Zhang, R. Wang, D.T. Liang, J.H. Tay, Theoretical and experiment studies of membrane wetting in the membrane gas-liquid contacting process for $CO_2$ absorption, J. Membr. Sci. 308 (2008) 162–170.

[6] S. Khaisri, D. deMontigny, P. Tontiwachwuthikul, R. Jiraratananon, Comparing membrane resistance and absorption performance of three different membranes in gas absorption membrane contactor, Sep. Purif. Technol. 65 (2009) 290–297.

[7] V.Y. Dindore, D.W.F. Brilman, F.H. Geuzebroek, G.F. Versteeg, Membrane-solvent selection for $CO_2$ removal using gas-liquid contactors, Sep. Purif. Technol. 40 (2004) 133–145.

[8] D.A. Glasscock, J.E. Critchfield, G.T. Rochelle, $CO_2$ absorption/desorption in mixtures of methyldiethanolamine with monoethanolamine or diethanolamine, Chem. Eng. Sci. 46 (1991) 2829–2845.

[9] B.P. Mandal, M. Guha, A.K. Biswas, S.S. Bandyopadhyay, Removal of carbon dioxide by absorption in mixed amines: modelling of absorption in aqueous MDEA/MEA and AMP/MEA solutions, Chem. Eng. Sci. 56 (2001) 6217–6224.

[10] C.S. Tan, J.E. Chen, Absorption of carbon dioxide with piperazine and its mixtures in a rotating packed bed, Sep. Purif. Technol. 49 (2006) 174–180.

[11] J.G. Lu, Y.F. Zheng, M.D. Cheng, L.J. Wang, Effects of activators on mass-transfer enhancement in a hollow fiber contactor using activated alkanolamine solutions, J. Membr. Sci. 289 (2007) 138–149.

[12] S.H. Lin, P.C. Chiang, C.F. Hsieh, M.H. Li, K.L. Tung, Absorption of carbon dioxide by the absorbent composed of piperazine and 2-amino-2-methyl-1-propanol in PVDF membrane contactor, J. Chin. Inst. Chem. Eng. 39 (2008) 13–21.

[13] S. Atchariyawut, R. Jiraratananon, R. Wang, Effect of membrane structure on mass-transfer in the membrane gas-liquid contacting process using microporous PVDF hollow fibers, J. Membr. Sci. 285 (2006) 272–281.

[14] R. Maceiras, E. Aĩlvarez, M.A. Cancela, Effect of temperature on carbon dioxide absorption in monoethanolamine solutions, Chem. Eng. J. 138 (2008) 295–300.

[15] G.F. Versteeg, W.V. Swaalj, Solubility and diffusivity of acid gases (carbon dioxide, nitrous oxide) in aqueous alkanolamine solutions, Chem. Eng. J. 33 (1988) 29–34.

[16] A.K. Saha, Bandyopadhyay, Solubility and diffusivity of $N_2O$ and $CO_2$ in aqueous solutions of 2-amino-2-methyl-1-propanol, Chem. Eng. J. 38 (1993) 78–92.

[17] D. deMontigny, P. Tontiwachwuthikul, A. Chakma, Using polypropylene and polytetrafluoroethylene membranes in a membrane contactor for $CO_2$ absorption, J. Membr. Sci. 277 (2006) 99–107.

[18] M.C. Yang, E.L. Cussler, Designing hollow-fiber contactors, AIChE. J. 32 (11) (1986) 1910–1916.

[19] R. Prasad, K.K. Sirkar, Dispersion-free solvent extraction with microporous hollow-fiber modules, AIChE. J. 34 (1988) 177–188.

[20] S.R. Wickramasinghe, M.J. Semmens, E.L. Cussler, Mass transfer in various hollow fiber geometries, J. Membr. Sci. 69 (1992) 235–250.

[21] M. Mavroudi, S.P. Kaldis, G.P. Sakellaropoulos, A study of mass transfer resistance in membrane gas-liquid contacting processes, J. Membr. Sci. 272 (2006) 103–115.

[22] S.B. Iversen, V.K. Bhatia, K. Dam-Johansen, G. Jonsson, Characterization of microporous membranes for use in membrane contactors, J. Membr. Sci. 130 (1997) 205–217.

[23] S.P. Ziemer, T.L. Niederhauser, E.D. Merkley, J.L. Price, E.C. Sorenson, B.R. McRae, B.A. Patterson, M.L. Origlia-Luster, E.M. Woolley, Thermodynamics of proton dissociations from aqueous glycine at temperatures from 278.15 to 393.15 K, molalities from 0 to 1.0 mol/kg₋1, and at the pressure 0.35 MPa: Apparent molar heat capacities and apparent molar volumes of glycine, glycinium chloride, and sodium glycinate, J. Chem. Thermodynamics 38 (2006) 467–483.

[24] N. Matubayasi, J. Namihira, M. Yoshida, Surface properties of aqueous amino acid solutions I. Surface tension of hydrochloric acid-glycine and glycine-sodium hydroxide systems, J. Colloid Interface Sci. 267 (2003) 144–150.

[25] R. Wang, D. Li, D.T. Liang, Modeling of $CO_2$ capture by three typical amine solutions in hollow fiber membrane contactor, Chem. Eng. Process. 43 (2003) 849–856.

[26] J.A. Meisen, C.J. Lim, Kinetics of carbon dioxide absorption and desorption in aqueous alkanolamine solutions using a novel hemispherical contactor – II: Experimental results and parameter estimation, Chem. Eng. Science 61 (2006), 6950-6603.

[27] S. Paul, A.K. Ghoshal, B. Mandal, Theoretical studies on separation of $CO_2$ by single and blended aqueous alkanolamine solvents in flat sheet membrane contactor (FSMC), Chem. Eng. Process. 144 (2008) 352–360.

[28] Z. Pei, S. Yao, W. Jianwen, Z. Wei, Z. Qing, Regeneration of 2-amino-2-methyl-1-propanol used for carbon dioxide absorption, J. Environ. Sci. 20 (2008) 39–44.

Journal of Membrane Science 347 (2010) 228–239

Contents lists available at ScienceDirect

Journal of Membrane Science

journal homepage: www.elsevier.com/locate/memsci

# A mathematical model for gas absorption membrane contactors that studies the effect of partially wetted membranes

Sakarin Khaisri[a], David deMontigny[b,*], Paitoon Tontiwachwuthikul[b], Ratana Jiraratananon[a]

[a] Department of Chemical Engineering, King Mongkut's University of Technology Thonburi, Bangkok 10140, Thailand
[b] International Test Centre for $CO_2$ Capture, Faculty of Engineering and Applied Science, University of Regina, Regina, SK, Canada S4S 0A2

ARTICLE INFO

*Article history:*
Received 30 June 2009
Received in revised form 13 October 2009
Accepted 15 October 2009
Available online 27 October 2009

*Keywords:*
Carbon dioxide capture
Membrane contactors
Mathematical model
Partial wetting
Membrane resistance

ABSTRACT

A mathematical model was developed to simulate the concentration profile in a gas absorption membrane (GAM) system. Carbon dioxide ($CO_2$) absorption into an aqueous solution of monoethanolamine (MEA) was investigated in the GAM system. Three GAM modules were potted with polytetrafluoroethylene (PTFE) membranes and connected in series to measure $CO_2$ concentration and $CO_2$ loading profiles along the length of the GAM system. The model predictions for $CO_2$ concentration and $CO_2$ loading profiles along the length of GAM column were in excellent agreement with the experimental results. The average absolute deviation between the model and experimental results was 1.49%. The Wilson plot method was used to determine the membrane resistance, which was compared with a theoretical membrane resistance. It was found that the membrane mass transfer resistance calculated using the Wilson plot method could predict the $CO_2$ concentration profile with a higher accuracy than the theoretical method. Partial membrane wetting was modeled to investigate the effect of membrane mass transfer resistance on the absorption performance and the overall mass transfer coefficient. The results showed that an acceptable membrane wetting for $CO_2$ absorption in MEA solutions in GAM systems was 40%. A higher lean solution temperature increased the membrane wetting in the GAM system. The membrane mass transfer resistance in completely liquid-filled membrane pores accounted for 92% of overall mass transfer resistance.

## 1. Introduction

Carbon dioxide ($CO_2$) is a major greenhouse gas that is released to the environment during the combustion of fossil fuels. There are many methods for removing $CO_2$ from flue gas streams such as packed columns, bubble columns, and membrane contactors. Gas absorption membrane (GAM) systems are an alternative method that has seen increasing development in the past decade. GAM systems have advantages over conventional equipment because they do not suffer from flooding, channeling, entrainment, and foaming [1]. A microporous membrane is used in GAM systems to separate the gas and liquid-phases. Mass transfer in GAM systems is shown in Fig. 1. Mass transfer occurs when $CO_2$ diffuses across the membrane and is absorbed into the absorbent. The disadvantage of GAM systems is the membrane itself adds to the overall mass transfer resistance. Wang et al. [2] reported that the membrane mass transfer resistance had a significant effect on the overall mass transfer coefficient when the membrane was wetted by the absorbent solution. They found that the non-wetted mode of operation had an absorption rate that was about six times higher than the wetted mode of operation. deMontigny et al. [3] compared the performance between packed columns and GAM systems. Polytetrafluoroethylene (PTFE) and polypropylene (PP) membranes were used in the GAM system and were compared with Sulzer DX structured packing in a packed column. The overall mass transfer coefficient in the GAM system was found to be higher than the packed column by the factor of three. They reported that the PTFE membranes maintained their overall mass transfer coefficients in GAM systems with monoethanolamine (MEA) as the absorbent solution for over 85 h of operation time while the PP membranes suffered a loss in performance due to membrane wetting. Atchariyawut et al. [4] also studied mass transfer in GAM systems. The membrane mass transfer resistance was determined by the Wilson plot method. Physical and chemical absorption were predicted with a mathematical model. Polyvinylidene fluoride (PVDF) membranes were used in their work. Sodium hydroxide solution (2 M) and water were used as the absorbent solutions in the chemical and physical absorption experiments, respectively. The simulated results that used the mass transfer coefficient from the experiments were in good agreement with the experimental

---

* Corresponding author at: University of Regina, Faculty of Engineering and Applied Science, 3737 Wascana Parkway, Regina, Saskatchewan, Canada S4S 0A2. Tel.: +1 306 337 2277; fax: +1 306 585 4855.
*E-mail address:* david.demontigny@uregina.ca (D. deMontigny).

0376-7388/$ – see front matter © 2009 Elsevier B.V. All rights reserved.
doi:10.1016/j.memsci.2009.10.028

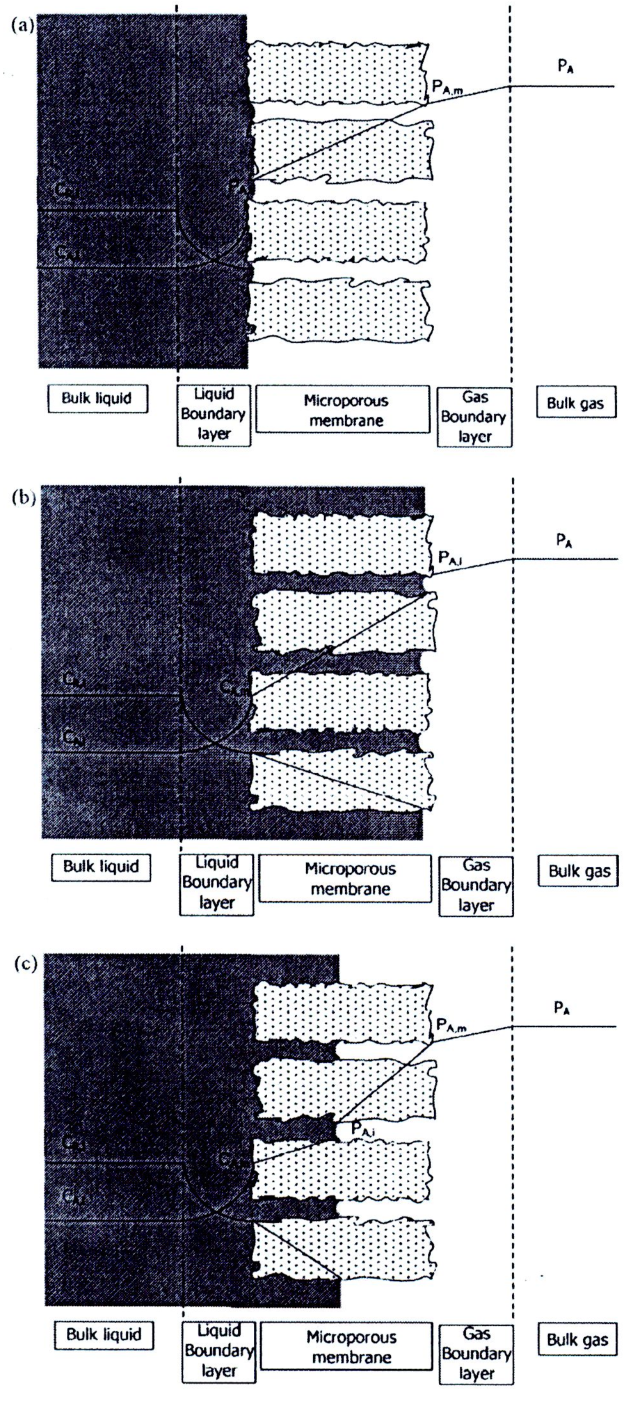

**Fig. 1.** Mass transfer resistance in series model for membrane contactors (adapted from Atchariyawut et al. [4]): (a) non-wetted, (b) wetted and (c) partially wetted.

results. They found that the membrane mass transfer resistance in the physical and chemical tests represented, 36% and 99% of the overall mass transfer resistance in the GAM systems, respectively. The high membrane mass transfer resistance in both cases was attributed to a membrane wetting problem because PVDF membranes were used in their work.

The membrane wetting mechanism for $CO_2$-alkanolamine absorption in GAM systems was investigated by Lu et al. [5]. The experimental results were validated with a mathematical model. A resistance in series model, the Laplace equation, and pore size distributions were used to study the effect of membrane wetting on mass transfer coefficients. The porosity, type of absorbent, and operation temperature had an effect on the wetting problem in the hydrophobic membranes. The temperature of the absorbent had a big effect on the wetting problem. They also reported that high membrane porosity had a significant effect on the mass transfer coefficient. Mavroudi et al. [6] developed a mathematical model based on a resistance in series model to study membrane wetting in GAM systems. In the case of liquid-filled membrane pores, the membrane mass transfer resistance accounted for 20–50% of the total resistance.

In this work, a mathematical model was developed to simulate concentration profiles and absorption performance in GAM systems. The model took into account the individual gas, liquid, and membrane mass transfer resistances, the heat transfer resistance and heat effects from the absorption, solvent evaporation, and condensation. The Wilson plot method was used to determine the membrane mass transfer resistance, which was compared with a calculated theoretical membrane mass transfer resistance. A partially wetted membrane was simulated to study the effect of membrane wetting on the absorption performance and overall mass transfer coefficient. From previous work [7], the PTFE membranes were shown to maintain their absorption performance over 60 h of operation time in the MEA-$CO_2$ system. PTFE hollow fiber membranes were used in this work to ensure that a non-wetted mode of operation was achieved during the experiments.

## 2. Theory

### 2.1. Resistance in series model

Film theory has been used to describe a resistance in series model in gas–liquid systems. Fig. 1 shows the concentration profile for the transport of gas to the liquid-phase in GAM systems. There are three resistances in the resistance in series model including gas film resistance, liquid film resistance, and the membrane itself. The resistance in series model for three modes of operation including non-wetted, wetted, and partially wetted can be written as follows [8]:

Non-wetted mode:

$$\frac{1}{K_G d_i} = \frac{H}{E k_L^0 d_i} + \frac{1}{k_M d_{ln}} + \frac{1}{k_G d_o} \quad (1)$$

Wetted mode:

$$\frac{1}{K_G d_o} = \frac{H}{E k_L^0 d_i} + \frac{H}{E k'_M d'_{ln}} + \frac{1}{k_G d_o} \quad (2)$$

Partially wetted mode:

$$\frac{1}{K_G d_{int}} = \frac{H}{E k_L^0 d_i} + \frac{H}{E k'_M d'_{ln}} + \frac{1}{k_M d_{ln}} + \frac{1}{k_G d_o} \quad (3)$$

where $K_G$ is the overall gas-phase mass transfer coefficient and $k_L$, $k_G$, $k_M$, and $k'_M$ are the liquid, gas, membrane for gas-filled pores, and membrane for liquid-filled pores mass transfer coefficients, respectively. $H$ represents Henry's constant, and $d_o$, $d_i$, $d_{int}$, $d_{ln}$, and $d'_{ln}$ are the outer, inner, interfacial, and logarithmic mean diameters of non-wetted and wetted of the membrane, respectively. $E$ is the enhancement factor.

### 2.2. Individual mass transfer coefficients

The correlations used for predicting mass transfer coefficients are important in mathematical models used for mass transfer

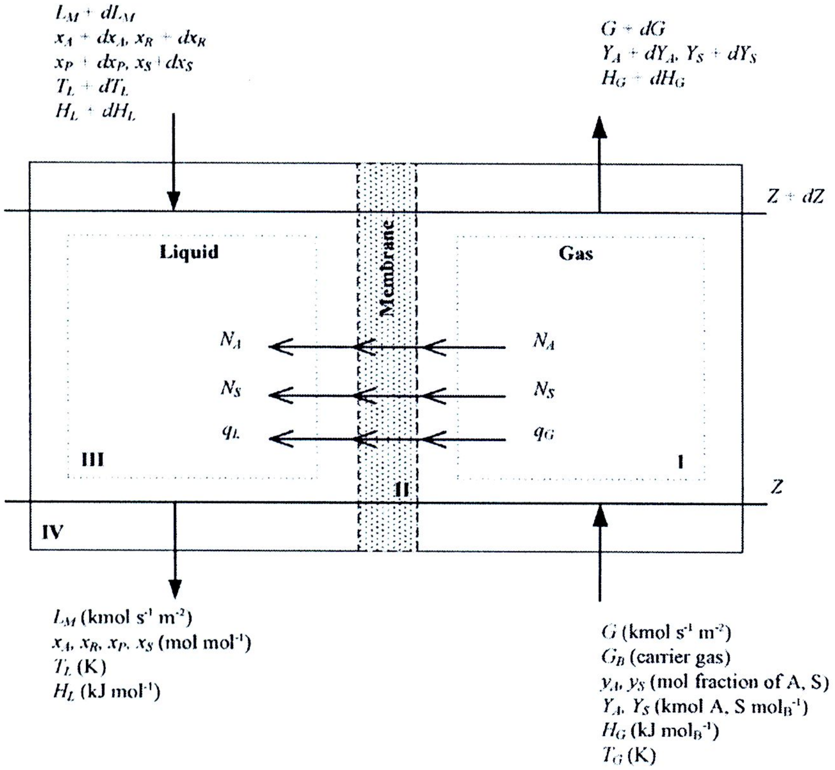

**Fig. 2.** Differential section of the GAM system (adapted from Pandya [13]).

equipment design, including GAM systems. Mass transfer coefficients can be predicted from a general equation of the form:

$$Sh = f(Re, Sc) \tag{4}$$

where *Sh* is the Sherwood number, *Re* is the Reynolds number, and *Sc* is the Schmidt number.

For liquid flowing in the fiber lumen, the liquid film mass transfer coefficient in physical absorption can be calculated by using the Leveque correlation as reported by Yang and Cussler [9]:

$$Sh = \frac{k_L^0 d_i}{D_{i,L}} = 1.62\left(\frac{d_i}{L} Re\, Sc\right)^{0.33} \tag{5}$$

Eq. (5) is valid for $Gz > 20$ to predict the tube side mass transfer.

For gas flowing in the shell-side, Yang and Cussler [9] also proposed the correlation to predict the gas side mass transfer coefficient for gas absorption and stripping:

$$Sh = \frac{k_G d_h}{D_{i,G}} = 1.25\left(Re\frac{d_h}{L}\right)^{0.93} Sc^{0.33} \tag{6}$$

where $d_h$ and $L$ are the hydraulic diameter and membrane length. Eq. (6) is valid for $0.5 < Re < 500$. Packing densities of 0.03 and 0.26 were tested in their work.

The membrane mass transfer coefficient depends on the mode of operation, i.e. non-wetted, wetted or partially wetted. For entirely gas-filled membrane pores, the membrane mass transfer resistance is the non-wetted mode. On the other hand, completely liquid-filled membrane pores represent the wetted mode. For the non-wetted mode of operation, the membrane mass transfer coefficient can be calculated by [10]:

$$k_M = \frac{D_{G,eff}\,\varepsilon}{\tau \delta_{dry}} \tag{7}$$

where $D_{G,eff}$ is the effective diffusion coefficient of gas in the gas-filled membrane pores, and $\varepsilon$, $\tau$, and $\delta_{dry}$ are the porosity, tortuosity, and dry thickness of the membrane, respectively.

The effective diffusion coefficient is a combination of molecular and Knudsen diffusivity. The effective diffusion coefficient in gas-filled membrane pores is given as:

$$\frac{1}{D_{G,eff}} = \frac{1}{D_{i,M}} + \frac{1}{D_{i,Kn}} \tag{8}$$

where $D_{i,M}$ and $D_{i,Kn}$ are the molecular and Knudsen diffusion coefficients, respectively.

For the wetted mode of operation, the membrane mass transfer coefficient depends on the diffusion coefficient of species *i* into the liquid.

$$k'_M = \frac{D_{i,L}\,\varepsilon}{\tau \delta_{wetted}} \tag{9}$$

where $D_{i,L}$ is the diffusion coefficient of species *i* in the liquid-phase, and $\delta_{wetted}$ is the wetted thickness of the membrane.

The partially wetted membrane mass transfer coefficient is a combination of the non-wetted and wetted membrane mass transfer coefficients [11]. As shown in Fig. 1(C), there are four resistances during the transport process: liquid film resistance, partially liquid-filled membrane pores resistance, partially gas-filled membrane pores resistance, and gas film resistance. The partially wetted membrane mass transfer resistance can be calculated from:

$$\frac{1}{k_M^P} = \frac{1}{k_M} + \frac{1}{k'_M} \tag{10}$$

where $k_M^P$ is the partially wetted membrane mass transfer coefficient.

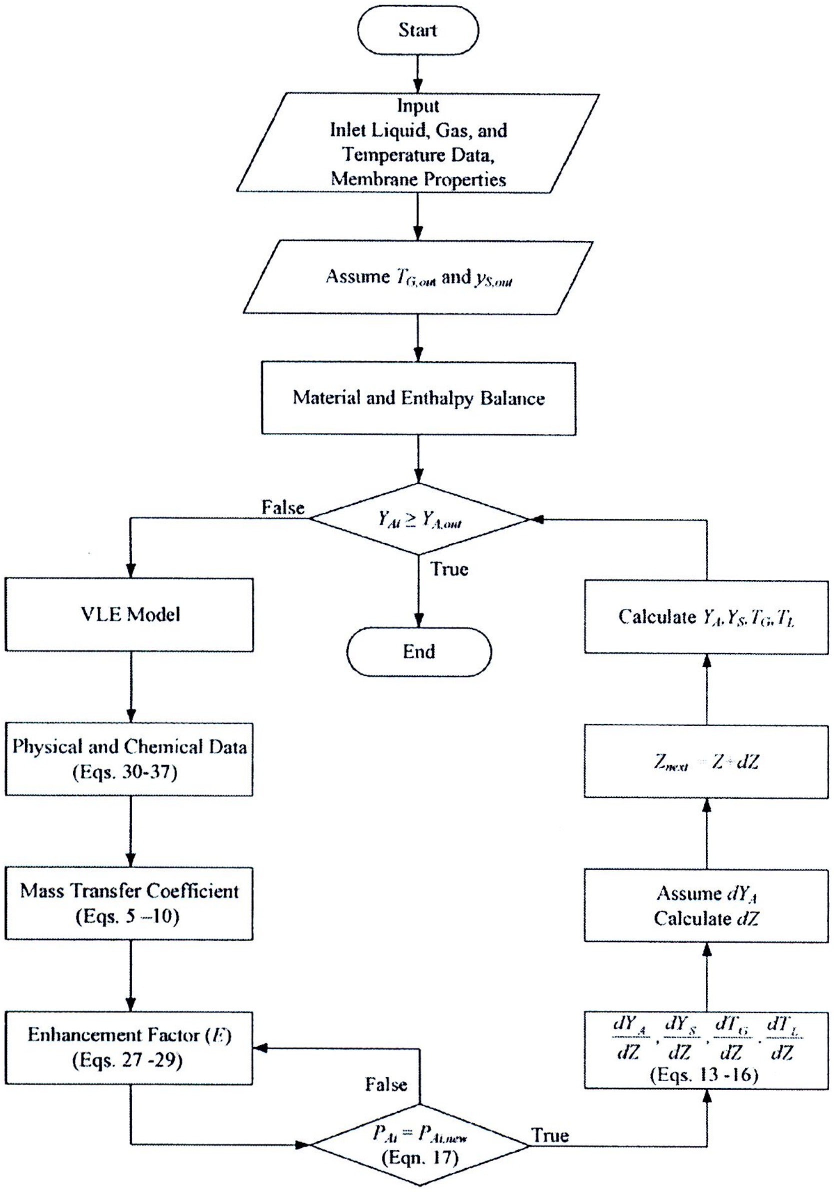

**Fig. 3.** Flowchart diagram for the GAM simulation model.

### 2.3. Wilson plots

The Wilson plot method is an effective technique for determining membrane resistance from experimental results [1]. From the resistance in series model, the overall gas-phase mass transfer resistance is proportional to liquid velocity. Using Eqs. (1) and (4), we can get the following expression:

$$\frac{1}{K_G} = C_1 \nu^{-\alpha} + d_i \left( \frac{1}{k_M d_{ln}} + \frac{1}{k_G d_o} \right) \tag{11}$$

From this equation, a plot of $1/K_G$ versus $\nu^{-0.33}$ should thus give a straight line with a $y$-intercept equal to the sum of the gas-phase and membrane resistance.

The overall gas-phase mass transfer coefficient in the membrane contactor was calculated using a method similar to the one used for packed columns. It can be calculated as follows [12]:

$$K_G a = \frac{G_B}{P(y_A - y_A^*)} \frac{dY_A}{dZ} \tag{12}$$

where $K_G a$ is the overall volumetric gas-phase mass transfer coefficient, $G_B$ is the inert gas flow rate, and $dY_A/dZ$ is the solute concentration gradient.

## 3. Mathematical model development

A mathematical model for gas absorption with chemical reaction in adiabatic packed towers was introduced by Pandya [13]. Pandya's model examined the heat effect from absorption, chemical reaction, solvent evaporation, and condensation as well as heat and mass transfer resistance in both phases. Aboudheir et al. [14] developed a rigorous model from Pandya's model to simulate the $CO_2$ absorption in 2-amino-2-methy-1-propanol (AMP) aqueous solutions in packed columns. A vapor–liquid equilibrium (VLE) and termolecular-kinetics model were developed by Aboudheir et al. [15] for use in the rigorous packed towers model. The termolecular mechanism assumes that the reaction between amine and $CO_2$ is a single step. The initial product is not a zwitterion but the

**Table 1**
Physical and chemical property equations.

| Parameter | Equation | |
|---|---|---|
| Liquid density ($g\,cm^{-3}$) [18] | $\rho = \frac{x_{MEA}M_{MEA} + x_{H_2O}M_{H_2O} + x_{CO_2}M_{CO_2}}{V}$ | (30) |
| Liquid viscosity (mPa s) [18] | $\frac{\eta}{\eta_{H_2O}} = \exp\frac{[(a\Omega + b)T + (c\Omega + d)][\alpha(e\Omega + fT + g) + 1]\Omega}{T^2}$ | (31)* |
| Solubility of $CO_2$ in MEA solution ($kPa\,m^3\,kmol^{-1}$) [19–21] | $H_{CO_2,MEA} = H_{N_2O,MEA}(H_{CO_2}/H_{N_2O})_{\text{in water}}$<br>$H_{N_2O,MEA} = \exp\left(R + \sum_{j=2}^{3}\Phi_j \ln H_{N_2O,i}\right)$ | (32)* |
| Diffusivity of $CO_2$ in MEA solution ($cm^2\,s^{-1}$) [21,22] | $D_{CO_2,MEA} = D_{N_2O,MEA}(D_{CO_2}/D_{N_2O})_{\text{in water}}$<br>$D_{N_2O,MEA} = (b_0 + b_1[MEA] + b_2[MEA]^2)\exp\left(\frac{b_3 + b_4[MEA]}{T}\right)$ | (33)* |
| Diffusivity of MEA in MEA solution ($cm^2\,s^{-1}$) [21,23] | $D_{MEA,H_2O} = \frac{13.26 \times 10^{-5}}{\eta_{H_2O}^{1.4} V_{MEA}^{0.589}}$<br>$D_{MEA} = D_{MEA,H_2O}\left(\frac{\eta_{H_2O}}{\eta_{MEA}}\right)^{0.6}$ | (34) |
| Molecular diffusivity ($cm^2\,s^{-1}$) [24] | $D_M = \frac{0.002625\,T^{3/2}}{PM_A^{1/2}\sigma_{AA}^2\Omega_D}$ | (35) |
| Knudsen diffusivity ($cm^2\,s^{-1}$) [25] | $D_{Kn} = 4850\,d_{\text{pore}}\sqrt{\frac{T}{M_A}}$ | (36) |
| Second-order reaction rate constant ($m^3\,kmol^{-1}\,s^{-1}$) [15] | $k_2 = k_{RNH_2}[RNH_2] + k_{H_2O}[H_2O]$<br>$k_{RNH_2} = 4.61 \times 10^9 \exp\left(\frac{-4412}{T}\right)$<br>$k_{H_2O} = 4.55 \times 10^6 \exp\left(\frac{-3287}{T}\right)$ | (37) |

*Please refer to the individual publications for the values of parameters.

reaction proceeds via a loosely bound encounter complex as an initial product. The simulation results agreed well with the experimental results from the pilot plant data.

In this work, a mathematical model was developed from Aboudheir's model and Pandya's model to simulate the $CO_2$ concentration profiles in GAM systems. The VLE and termolecular model that were developed by Aboudheir et al. [15] were used in this work. Most researchers [4–6] ignored the gas-phase mass transfer resistance in their mathematical model. Rangwala [11] reported that the gas-phase mass transfer resistance had a very small value in comparison with that of liquid-film mass transfer resistance. However, in this work the gas-phase mass transfer resistance was included in the mathematical model to develop a rigorous mathematical model for a GAM system. The Wilson plot method was used to determine the membrane mass transfer coefficient from the experimental results. Partially wetted membranes were investigated and simulated to study the effect of membrane mass transfer resistance on the absorption performance and overall mass transfer coefficient.

Fig. 2 shows a differential section of a GAM system. The mass transfer process has three steps in GAM systems: (1) diffusion from the gas-phase (Section 1) to the outer surface of membrane, (2) diffusion through the membrane pores (Section 2), and (3) diffusion into the liquid-phase (Section 3). For the non-wetted mode, the reaction between $CO_2$ and absorbent occurs in the liquid-phase. For the wetted and partially wetted mode, the reaction between $CO_2$ and absorbent occurs in the liquid-phase and wetted membrane pores where the liquid solution penetrates into the membrane pores.

The assumptions used in this work were developed from Pandya's model to write the main equations for mass and energy balances. The assumptions are based on the film theory [14]:

(1) The reaction is fast and takes place in the liquid film and wetted membrane pores.
(2) The heat transfer resistance in the liquid-phase is small compared to that in the gas-phase.
(3) The liquid-phase mass transfer resistance of volatile solvent (water) is negligible.
(4) The interfacial area of heat and mass transfer is the same.
(5) The $CO_2$ and water vapor can only transport across the interface.

The system is assumed to be under steady state conditions. Based on the assumptions, the main equations for mass and energy balances were written for the GAM system. Considering the gas-phase, only $CO_2$ (component $A$) and water vapor (component $S$) can transfer across the interface. The concentration gradients for both solute gas ($A$) and water vapor ($S$) are calculated from following two equations:

$$\frac{dY_A}{dZ} = \frac{-k_{G,ext}\,a\,P(y_{A,G} - y_{A,i})}{G_B} \tag{13}$$

$$\frac{dY_S}{dZ} = \frac{-k_{S,ext}\,a\,P(y_{S,G} - y_{S,i})}{G_B} \tag{14}$$

The temperature gradients for the gas and liquid-phases are given as follows:

$$\frac{dT_G}{dZ} = \frac{-h_G a(T_G - T_L)}{G_B(C_{PB} + Y_A C_{PA} + Y_S C_{PS})} \tag{15}$$

$$\frac{dT_L}{dZ} = \frac{G_B}{L_M C_{PL}}\left((C_{PB} + Y_A C_{PA} + Y_S C_{PS})\frac{dT_G}{dZ} + (C_{PS}(T_G - T_0) + \lambda_S)\frac{dY_S}{dZ} + (C_{PA}(T_G - T_0) - \Delta H_R(T_0, P))\frac{dY_A}{dZ}\right) \tag{16}$$

where $h$, $C_p$, $\lambda$, and $\Delta H_R$ are the heat transfer coefficient, heat capacity, latent heat of vaporization, and heat of chemical reaction, respectively. This data can be found in Pandya [13] for the $CO_2$ and MEA system.

The gas concentration at the interface can be obtained from the combination of mass balance equations in the gas, membrane, and liquid-phases:

$$p_{A,i} = \frac{p_A + (k_{L,ext}(d_i/d_o)E)/(k_{G,ext})C_{Ae}}{1 + (k_{L,ext}(d_i/d_o)E)/Hk_{G,ext}} \tag{17}$$

where $p_{Ai} = H \times C_{Ai}$; $C_{Ae}$, and $E$ are the equilibrium concentration and enhancement factor, respectively. The $k_{G,ext}$, $k_{S,ext}$ and $k_{L,ext}$ are defined for three cases including non-wetted, wetted, and partially wetted as follows:

Non-wetted mode:

$$k_{G,ext} = \frac{k_{A,G}}{1 + (k_{A,G}/k_M)(d_o/d_{ln})} \tag{18}$$

$$k_{S,ext} = \frac{k_{S,G}}{1 + (k_{S,G}/k_M)(d_o/d_{ln})} \tag{19}$$

$$k_{L,ext} = k_L^0 \tag{20}$$

Wetted mode:

$$k_{G,ext} = k_{A,G} \tag{21}$$

$$k_{S,ext} = k_{S,G} \tag{22}$$

$$k_{L,ext} = \frac{k_L^0}{1 + (k_L^0/k'_M)(d_i/d'_{ln})} \tag{23}$$

Partially wetted mode:

$$k_{G,ext} = \frac{k_{A,G}}{1 + (k_{A,G}/k_M)(d_o/d_{ln})} \tag{24}$$

$$k_{S,ext} = \frac{k_{S,G}}{1 + (k_{S,G}/k_M)(d_o/d_{ln})} \tag{25}$$

$$k_{L,ext} = \frac{k_L^0}{1 + (k_L^0/k'_M)(d_i/d'_{ln})} \tag{26}$$

where $k_{A,G}$ and $k_{S,G}$ are the gas-phase and water vapor mass transfer coefficient, respectively.

The enhancement factor is the ratio of the absorption flux in the presence of chemical reaction to the absorption flux in the absence of chemical reaction. The enhancement factor for gas absorption with second-order irreversible reaction is given by [16]:

$$E = \frac{-Ha^2}{2(E_\infty^* - 1)} + \sqrt{\frac{Ha^4}{4(E_\infty^* - 1)^2} + \frac{E_\infty^* Ha^2}{(E_\infty^* - 1)} + 1} \tag{27}$$

The asymptotic infinite enhancement factor based on Leveque's model is given by the following:

$$E_\infty^* = \left(1 + \frac{C_{R,0} D_R}{\nu_R C_{A,i} D_A}\right) \left(\frac{D_A}{D_R}\right)^{1/3} \tag{28}$$

where $\nu_R$ is a stoichiometric coefficient of reaction and $C_{R,0}$ is the amine concentration at the inlet. $D_A$ and $D_R$ are the diffusivity of $CO_2$ and amine in amine solution, respectively.

The Hatta number ($Ha$) is the ratio of maximum possible conversion to maximum transportation. The Hatta number is given as:

$$Ha = \frac{\sqrt{k_{2,MEA} D_A C_R}}{k_{L,ext}} \tag{29}$$

where $k_{2,MEA}$ is the second-order reaction rate constant.

For a counter-current mode of operation in absorption columns and GAM systems, the gas and liquid conditions at the inlet of the absorber are known, while the liquid and gas outlet conditions are unknown. This boundary value problem was solved with the shooting method [17]. The model begins by assuming that the temperature and moisture content of the outlet gas is in equilibrium with the inlet gas. The outlet liquid compositions are determined by applying mass and energy balances around the absorber. The shooting method starts from the top of the column and moves downward along the column. The temperature and concentration profiles are computed until the desired outlet $CO_2$ concentration is reached. The new gas outlet conditions are guessed and the calculation procedures are repeated if the results at the bottom of column do not converge with the initially assumed conditions. Fig. 3 shows the flowchart methodology used to solve the equations. The system of equations (Eqs. (13)–(29)) was solved using MATLAB. The physical and chemical properties are called as a function for use in the main program at each operating condition. The physical and chemical

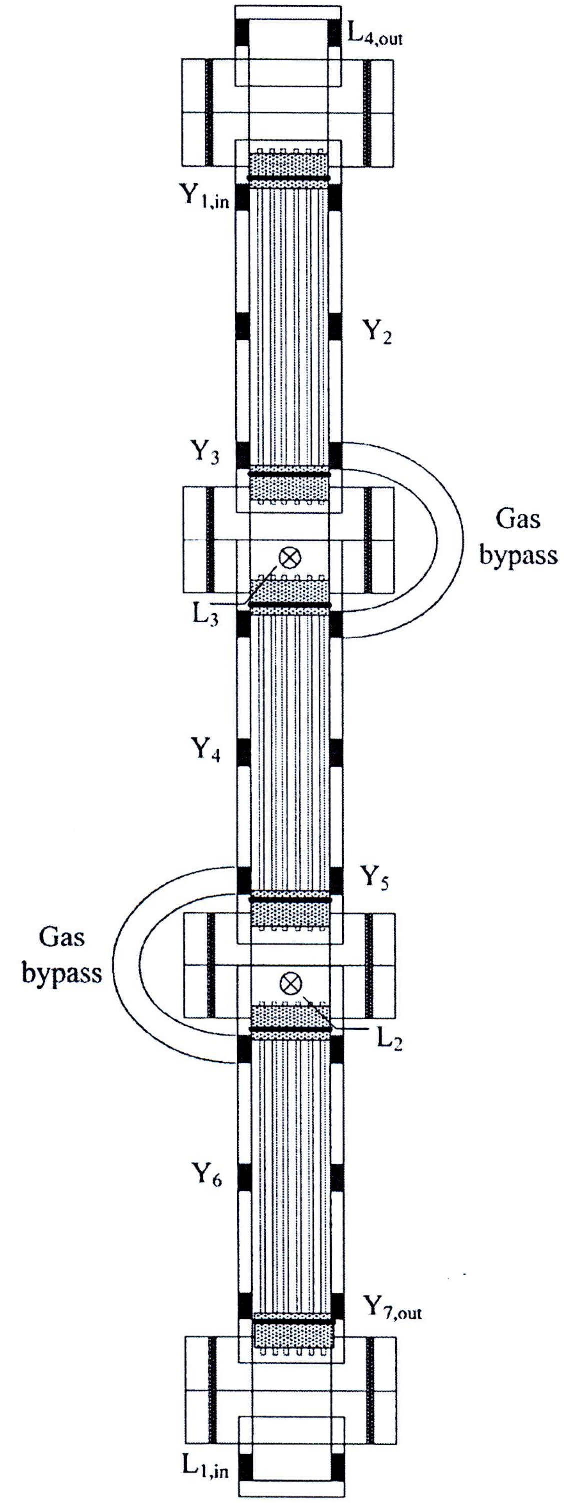

**Fig. 4.** Schematic of three GAM modules in series.

**Table 2**
Hollow fiber membrane and membrane module characteristics.

| Description | PTFE membrane |
|---|---|
| Outer diameter (mm) | 2.0 |
| Inner diameter (mm) | 1.0 |
| Membrane porosity (%) | 50 |
| Membrane length per module (mm) | 122 |
| Membrane tortuosity[a] | 3.0 |
| Membrane pore diameter[b] (μm) | 2.50 |
| Fibers per module | 57 |
| Shell inside diameter (mm) | 28 |
| Module void fraction (%) | 70.9 |

[a] Reported by Rangwala [11].
[b] Determined from SEM image.

properties that are required in the model include density, viscosity, diffusivity, solubility, and the kinetic reaction rate constant. Table 1 lists the references and equations that were used as parameters in the main program.

## 4. Experimental work

The GAM system used in this work was originally developed by deMontigny et al. [12] and connects three membrane cartridges in series, as shown in Fig. 4. This design provides gas and liquid sampling points along the column. The GAM module was made from acrylic tubing with an inside and outside diameter of 28 and 34 mm, respectively. The PTFE hollow fiber membranes were potted with 57 fibers per cartridge. Each membrane cartridge has a membrane length of 122 mm. Table 2 shows the characteristics of the PTFE membrane and modules used in the experiment and mathematical model.

A counter-current mode of operation was used in all experiments to obtain the best performance. Liquid solution was pumped with a centrifugal pump to the bottom of the module and flowed upwards out the top of the module. The liquid flow rate was controlled with a variable area flow meter. An absorbent solution was fed into the lumen while a gas stream was fed through the shell-side. A known volume of liquid was collected over time to calibrate the liquid flow rate. The feed gas stream was controlled using a gas flow controller. The gas was introduced into the GAM module before the liquid stream in order to prevent wetting problems. Each run was operated at least 30 min before collecting any data to make sure that steady state conditions had been reached. The experimental set up is shown in Fig. 5.

**Table 3**
Experimental operating conditions.

| Operating condition | Range |
|---|---|
| Inert gas flow rate (kmol m$^{-2}$ h$^{-1}$) | 41.8 |
| $CO_2$ feed concentration (%) | 15.0 |
| Liquid velocity (m$^3$ m$^{-2}$ h$^{-1}$) | 52.3–265.0 |
| MEA concentration (kmol m$^{-3}$) | 3.0 |
| Lean $CO_2$ loading (mol$_{CO_2}$ mol$^{-1}_{MEA}$) | 0.15–0.30 |

Aqueous monoethanolamine (MEA) solution was used as an absorbent. Solutions were prepared to a concentration of 3.0 kmol/m$^3$ using de-ionized water. Standard hydrochloric acid solution (1N) was used as a titrant with methyl orange as an indicator. A known volume was collected at steady state conditions for titration to determine the $CO_2$ loading in the MEA solution. $CO_2$ loading was determined to make sure that the mass balance error between the gas and liquid side was low, indicating the experiment was valid. The $CO_2$ loading procedure can be found in the Association of Official Analytical Chemists [26]. A simulated flue gas stream containing 15% $CO_2$ and 85% air was prepared as a feed gas. An infrared $CO_2$ analyzer was used to verify the desired concentration of $CO_2$ in the feed gas stream. At steady state conditions, the $CO_2$ concentrations along the length of column were measured using the infrared analyzer. The experimental procedure was provided

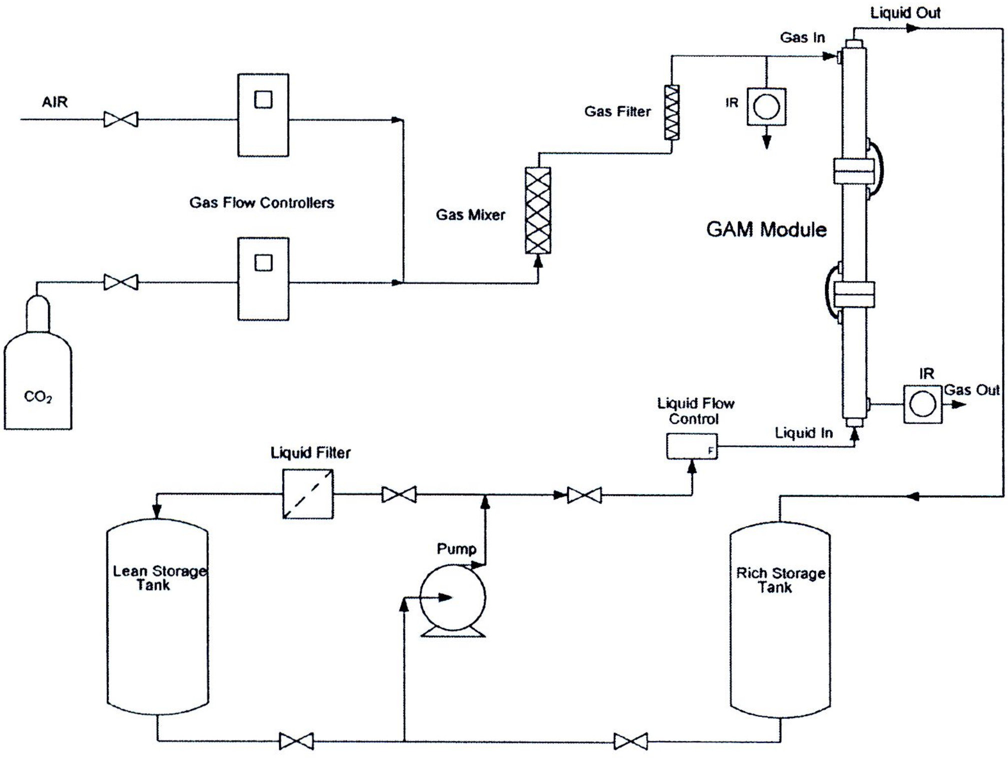

**Fig. 5.** Experimental set up for the GAM contactor.

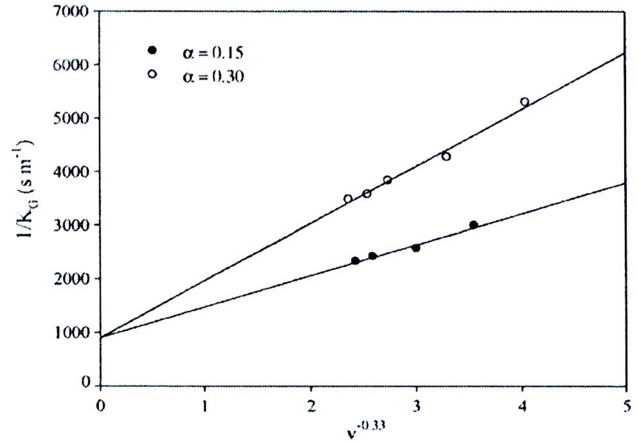

**Fig. 6.** Wilson plot of two different $CO_2$ loading lean solutions.

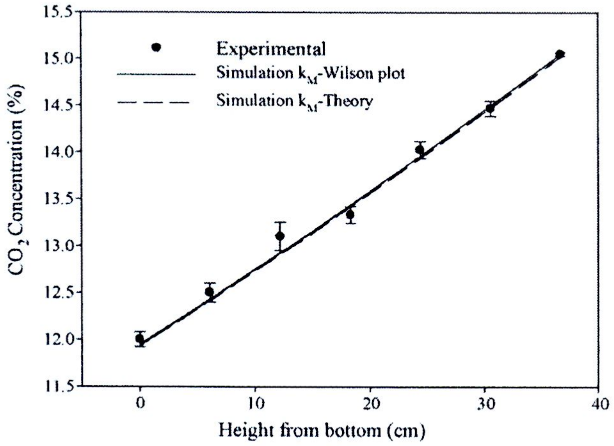

**Fig. 7.** Comparing the membrane resistance from the Wilson plot and the theoretical method ($\nu = 97.0\,m^3\,m^{-2}\,h^{-1}$, $\alpha = 0.30$).

in detail elsewhere [7]. Table 3 lists the experimental operating conditions in this work.

## 5. Results and discussion

### 5.1. Wilson plot analysis

An effective method to determine the membrane mass transfer coefficient is the Wilson plot method. Fig. 6 shows the Wilson plot analysis for the experiments in this study. When the membrane and gas mass flow rate are the same, the $y$-intercept that represents the membrane and gas-phase mass transfer resistance should also be the same. The same $y$-intercept can be seen in Fig. 6 for two different solution $CO_2$ loadings. The free amine in the system decreases with an increase in $CO_2$ loading in the solution, which affected the enhancement factor but did not have any effect on the gas-phase mass transfer coefficient. The $CO_2$ loading only has an effect on a chemical liquid mass transfer coefficient. The gas-phase mass transfer coefficient can be calculated from Eq. (6). Thus, the membrane resistance from the Wilson plot method can be calculated from the $y$-intercept in Fig. 6. Previous work [7,12] showed that the PTFE membrane system could maintain its performance over prolonged periods of operation time. It can be confirmed that membrane mass transfer resistance from the Wilson plot method represents a totally gas-filled membrane pore system.

### 5.2. Comparing membrane resistances

A theoretical non-wetted membrane mass transfer coefficient was calculated from Eq. (7) and compared to the value determined by the Wilson plot method. Table 4 shows the calculation results for both cases. Fig. 7 shows simulation results using two different membrane resistances. The $CO_2$ concentrations in the gas-phase were simulated along the column and were compared with experimental data. The average absolute deviation (AAD), for $N$ data points, used to measure an error between the predicted and experimental results can be calculated as follows:

$$\mathrm{AAD\%} = 100\left[\sum_{i=1}^{N}\frac{|(y_{\mathrm{exp}} - y_{\mathrm{calc}})/y_{\mathrm{exp}}|}{N}\right] \tag{38}$$

The membrane mass transfer resistance from the Wilson plot method had an AAD of 0.60% while the theoretical membrane mass transfer resistance had an AAD 0.80%. When the membrane mass transfer coefficient from the Wilson plot method was used in the mathematical model, the prediction results of the $CO_2$ concentration profile were in excellent agreement with the experimental data. The membrane mass transfer resistance from theory was calculated by approximating the tortuosity and membrane pore diameter. A tortuosity of 3.0 was reported by Rangwala [11], and the PTFE membrane pore diameter was determined by scanning electron microscope (SEM), JSM-5600, JEOL Ltd. The membrane and module properties were shown in Table 2.

Figs. 8 and 9 show the parity plot obtained using the membrane mass transfer resistance from the Wilson plot and theoretical methods, respectively. A slight improvement of the simulation results can be seen in Fig. 8 when the membrane mass transfer coefficient from the Wilson plot method was used in the model. Higher accuracy predictions were obtained with the membrane mass transfer resistance that came from the Wilson plot method. The theoretical membrane mass transfer resistance was calculated from Eq. (7).

**Table 4**
Comparing membrane mass transfer coefficients from the Wilson plot and theoretical methods.

| Calculation method | Membrane coefficient (cm $s^{-1}$) | AAD% |
|---|---|---|
| Wilson plot | 0.0770 | 0.60 |
| Theoretical method[a] (Eq. (7)) | 0.3370 | 0.80 |

[a] Calculated at 20 °C.

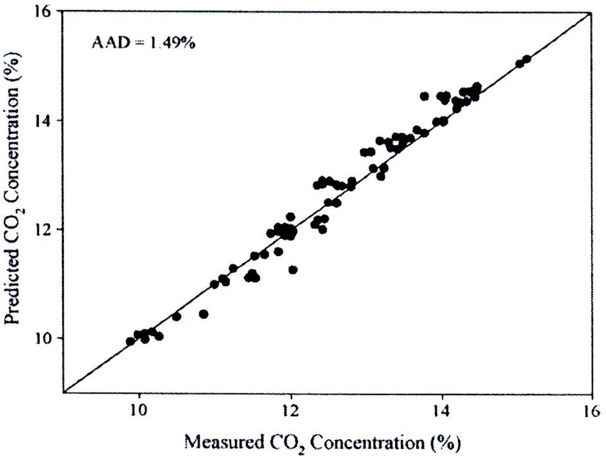

**Fig. 8.** Parity plot for the model using the Wilson plot membrane resistance.

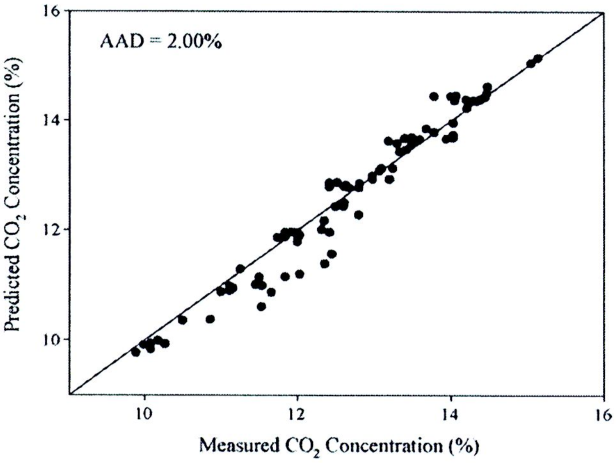

**Fig. 9.** Parity plot for the model using the theoretical membrane resistance.

The assumptions in this equation are cylindrical membrane pores, constant tortuosity and lognormal distribution of membrane pore size [5,27]. These assumptions likely led to an overestimation of the membrane mass transfer resistance. In short, the membrane mass transfer resistance that was determined experimentally produced more accurate results than the theoretical value.

The effect of $CO_2$ loading in the MEA solution on the physical and chemical properties was taken into account in the mathematical model. The $CO_2$ loading in the liquid-phase has a significant effect on physical and chemical properties including viscosity, density, diffusivity, and reaction rate constant. The top and bottom of the GAM column represent the high and low $CO_2$ loading regions, respectively, in the liquid-phase. The model predictions agreed well with the experimental data at high and low $CO_2$ loadings in the solution when the membrane resistance value from the Wilson plot method was used in the model, as seen in Fig. 8.

The $CO_2$ concentration profiles in the liquid-phase along column were simulated and compared with the experimental data, as shown in Fig. 10. The model predictions agreed well with the experimental results. The average absolute deviation of the predicted $CO_2$ loading from the measured $CO_2$ loading was 0.65%. The $CO_2$ loading in the liquid-phase increased along the column because of the reaction between $CO_2$ and MEA solution. The model predictions were in excellent agreement with experimental results when the membrane mass transfer resistance from the Wilson plot method was used to simulate the $CO_2$ loading in the model.

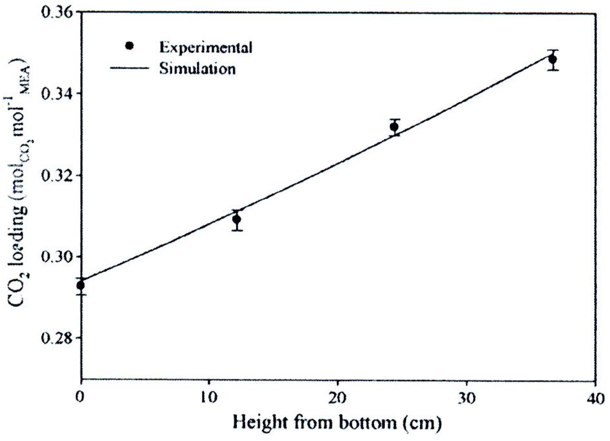

**Fig. 10.** Comparing $CO_2$ loading profiles from the simulation and experimental results using the Wilson plot membrane resistance ($\nu = 97.0\,m^3\,m^{-2}\,h^{-1}$, $\alpha = 0.30$).

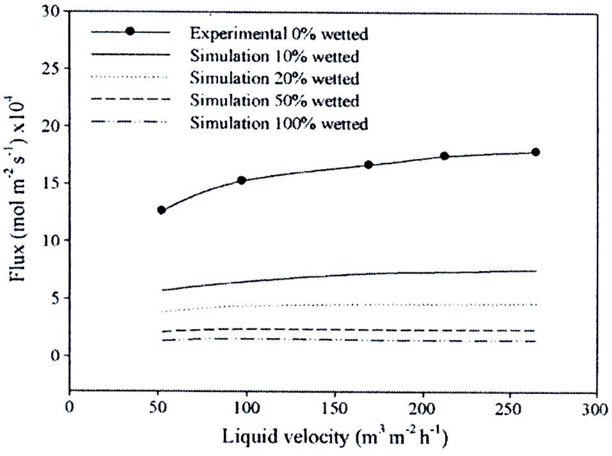

**Fig. 11.** Simulation of the effect of membrane wetting on the absorption performance ($\nu = 97.0\,m^3\,m^{-2}\,h^{-1}$, $\alpha = 0.30$).

### 5.3. *Effect of membrane wetting on absorption performance*

Membrane wetting has a significant effect on the overall mass transfer coefficient. Aqueous organic solutions, especially alkanolamine, can penetrate into the membrane pores over prolonged periods of operation time. The effect of partial wetting in the membrane pores on the absorption flux was simulated as shown in Fig. 11.

The $CO_2$ flux decreased with an increase in the percentage of membrane wetting. The absorption performance dropped roughly 56%, 72%, 85% and 90% at the 10%, 20%, 50% and 100% wetting, respectively. The membrane resistance in the wetted and partially wetted mode was calculated from Eqs. (9) and (10), respectively. The membrane mass transfer resistance in the liquid-filled membrane pores depends on the diffusivity of gas in the liquid-phase, while the membrane mass transfer resistance in the gas-filled membrane pores depends on the molecular and Knudsen diffusivity. Based on the diffusion coefficients in Table 1, the ratio of diffusivity between totally gas-filled and completely liquid-filled membrane pores is about 8000:1 at room temperature. This factor directly affects the membrane mass transfer resistance and absorption flux as well as the overall mass transfer coefficient. Similar results were reported in the literature [2,7,12,28]. However, membrane wettability also depends on several factors such as contact angle, surface tension, membrane pore size, and breakthrough pressure [1,29]. When completely liquid-filled membrane pores occurred in the GAM system, the membrane mass transfer resistance was 92% of the total mass transfer resistance. The liquid velocity had a minor effect on the $CO_2$ absorption flux when the membrane pores were totally liquid-filled. This is due to the fact that the membrane mass transfer resistance is the main mass transfer resistance in the case of totally liquid-filled membrane pores, as shown in Fig. 12. In traditional gas–liquid absorbers, as well as in GAM systems, the liquid-phase mass transfer coefficient increases with an increase the liquid velocity [3]. When liquid penetrates into the membrane pores, the membrane mass transfer resistance increases rapidly. The membrane mass transfer resistance increases with an increase in the percent of membrane wetting due to the penetration of absorbent in the membrane pores. As seen in Figs. 11 and 12, it can be concluded that membrane mass transfer resistance, in the case of partially liquid-filled membrane pores, has a significant effect on the absorption performance. In

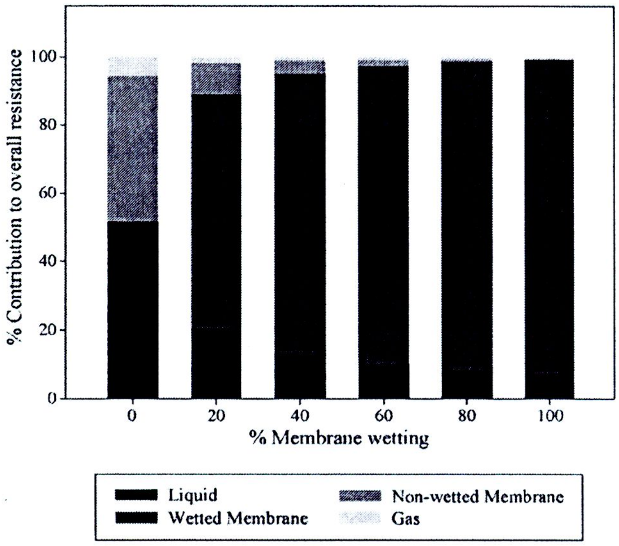

**Fig. 12.** Percentage of individual resistance to overall resistance ($\nu = 97.0\,m^3\,m^{-2}\,h^{-1}$, $\alpha = 0.30$).

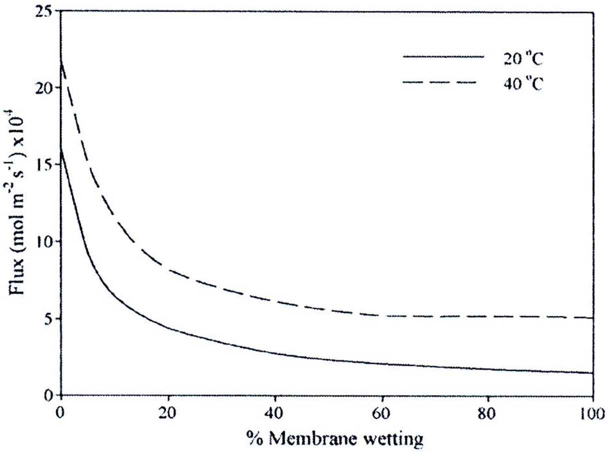

**Fig. 14.** Simulation of the effect of lean solution temperature on the absorption performance ($\nu = 97.0\,m^3\,m^{-2}\,h^{-1}$, $\alpha = 0.30$).

GAM systems, membrane wettability should be prevented to have the best performance. Li and Chen [29] suggested several methods to prevent membrane wetting problems in GAM systems including membrane surface modification, using a hydrophobic membrane, optimized operating conditions, and using suitable liquid surface tension solvents.

Fig. 13 shows the effect of membrane wetting on the overall gas-phase mass transfer coefficient ($K_G$). Results show that the $K_G$ decreased with an increase in the membrane wetting percentage. The membrane mass transfer resistance has a significant effect on the overall mass transfer resistance. The membrane resistance was transformed into the dominating resistance to mass transfer when the membrane pores were wetted with liquid solution. The absorption performance deteriorated with an increase in the membrane wetting. As seen in Fig. 13, the slope gradient decreases sharply when the membrane pores were partially filled by the liquid solution. The overall mass transfer coefficient decreased sharply until 40% membrane wetting is reached, as seen from the slope. When the membrane pores were partially liquid-filled, the overall mass transfer coefficient starts deteriorating. At 40% membrane wetting, the slope gradient is more constant in comparison with that of previous membrane wetting. The membrane wetting can be approximated by measuring absorption efficiency. When membrane wetting occurs in GAM systems, the absorption flux and overall mass transfer coefficient will drop in comparison with that of a fresh membrane (non-wetted mode of operation). The absorption flux and overall mass transfer coefficient dropped roughly 78% and 86%, respectively, from the non-wetted mode of operation by the time the membrane was 40% wet. Membrane cartridges should be replaced once they reach 40% membrane wetting in order to maintain the absorption performance. With this in mind, there is another way to maintain the performance of GAM systems. Wang et al. [2] increased the operating pressure on the gas side of the GAM system. By doing this, some liquids in the membrane pores were pushed back to the inside of the membrane and the $CO_2$ flux was restored to 90% of the non-wetted mode of operation.

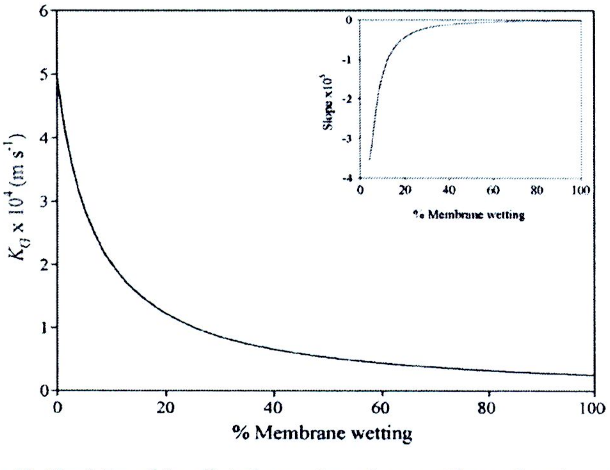

**Fig. 13.** Simulation of the effect of percent membrane wetting on the volumetric overall mass transfer coefficient ($\nu = 97.0\,m^3\,m^{-2}\,h^{-1}$, $\alpha = 0.30$, $Y = 0.173$).

### 5.4. *Effect of lean solution temperature on membrane wetting*

The effect of lean solution temperatures was simulated to investigate any change in absorption performance in the GAM system as seen in Fig. 14. The absorption performance dropped by roughly 90% and 76% from a non-wetted mode to a totally wetted mode at 20 and 40 °C lean solution temperature, respectively. An increasing solution temperature leads to a greater second-order reaction rate constant, which can increase the overall mass transfer coefficient. Although the overall mass transfer coefficient increases with an increased temperature, the absorption efficiency will deteriorate at too high a temperature. This is because the reaction between $CO_2$ and MEA solution is a reversible exothermic reaction. An increase in temperature can enhance the absorption performance in the GAM system, but the chance of membrane wetting also increases. Fig. 14 shows that the absorption performance dropped roughly 26% with a decrease of lean solution temperature in the non-wetted mode of operation. The chemical reaction rate constant and the overall mass transfer coefficient are affected by temperature.

At 40% partial membrane wetting the absorption performance dropped roughly 55% with a decrease in lean solution temperature from 40 to 20 °C. The non-wetted mode of operation had the lowest reduction of absorption flux when the lean solution temperature decreased from 40 to 20 °C. It can be concluded that an increase in lean solution temperature had an effect on membrane wetting and absorption performance in the GAM systems. The liquid entry pressure tends to decrease with an increase in temperature as reported by Garcia-Payo et al. [30]. This leads to an easier wetting of the membrane pores at high operation temperatures in GAM systems.

An increase in lean solution temperatures had a significant effect on the chemical and physical properties including the density, viscosity, solubility, diffusivity, and reaction rate constant, as well as membrane wetting in the GAM system.

## 6. Conclusion

A gas absorption membrane mathematical model was developed and validated with experimental results. PTFE hollow fiber membranes were used in the experiment, which absorbed $CO_2$ into MEA solutions. The membrane mass transfer resistance was determined using the Wilson plot method and a theoretical approach. The membrane resistance values from the two methods were used in the mathematical model, and the simulation results were computed. It was found that the membrane mass transfer resistance from the Wilson plot method could predict the $CO_2$ concentration profiles with a higher accuracy than the theoretical method. The predicted $CO_2$ concentration and $CO_2$ loading profiles agreed well with the experimental results. Partial membrane wetting was investigated to determine the effect of membrane mass transfer resistance on the absorption performance and the overall mass transfer coefficient. An increase in the percent wetting decreased the absorption flux and overall mass transfer coefficient. The maximum acceptable percent wetting of the membrane in GAM systems was found to be 40%. After 40% wetting, membrane cartridges should be changed to maintain the best conditions for operation. The operation temperature had a significant effect on membrane wetting in the GAM system. This factor enhances the chance for membrane wetting.

## Nomenclature

| | |
|---|---|
| $a$ | specific surface area ($m^2\,m^{-3}$) |
| $C$ | concentration ($kmol\,m^{-3}$) |
| $C_{pj}$ | heat capacity of solution $j$ ($kJ\,kmol^{-1}\,K^{-1}$) |
| $C_{PL}$ | heat capacity of solution ($kJ\,kmol^{-1}\,K^{-1}$) |
| $d_h$ | hydraulic diameter (m) |
| $d_i$ | inside diameter of membrane (m) |
| $d_{int}$ | interfacial diameter (m) |
| $d_{ln}$ | logarithmic mean diameter of dry membrane (m), $d_{ln} = \frac{d_o - d_{int}}{\ln(d_o/d_{int})}$ |
| $d'_{ln}$ | logarithmic mean diameter of wetted membrane (m), $d'_{ln} = \frac{d_{int} - d_i}{\ln(d_{int}/d_i)}$ |
| $d_o$ | outside diameter of membrane (m) |
| $d_{pore}$ | diameter of membrane pore (cm) |
| $D_i$ | diffusivity of species $i$ ($m^2\,s^{-1}$) |
| $D_{G,eff}$ | effective diffusion coefficient of gas in the gas-filled membrane pores ($m^2\,s^{-1}$) |
| $E$ | enhancement factor (dimensionless) |
| $E^*_\infty$ | asymptotic enhancement factor (dimensionless) |
| $G_B$ | inert gas flow rate ($kmol\,m^{-2}\,h^{-1}$) |
| $h$ | heat transfer coefficient ($kJ\,s^{-1}\,cm^{-2}\,K^{-1}$) |
| $H$ | Henry's constant (dimensionless or $kPa\,m^3\,kmol^{-1}$) |
| $Ha$ | Hatta number (dimensionless) |
| $\Delta H_R$ | heat of chemical reaction between $A$ and $R$ ($kJ\,kmol^{-1}$) |
| $k_{Gj}$ | gas-phase mass transfer coefficient for component $j$ ($m\,s^{-1}$) |
| $k^0_L$ | physical liquid-phase mass transfer coefficient ($m\,s^{-1}$) |
| $k_M$ | gas-filled membrane pores mass transfer coefficient ($m\,s^{-1}$) |
| $k'_M$ | liquid-filled membrane pores mass transfer coefficient ($m\,s^{-1}$) |
| $K_G$ | overall gas-phase mass transfer coefficient ($kmol\,m^{-2}\,kPa^{-1}\,h^{-1}$) |
| $L$ | membrane length (m) |
| $L_M$ | molar liquid flow rate ($kmol\,m^{-2}\,s^{-1}$) |
| $M_i$ | molecular weight of component $i$ |
| $P$ | total system pressure (kPa) |
| $q_i$ | heat transfer flux of component $i$ ($kJ\,m^{-2}\,s^{-1}$) |
| $R$ | excess Henry's coefficient ($kPa\,m^3\,kmol^{-1}$) |
| $Re$ | Reynolds number (dimensionless) |
| $Sc$ | Schmidt number (dimensionless) |
| $Sh$ | Sherwood number (dimensionless) |
| $T$ | temperature (K) |
| $v$ | liquid velocity ($m\,s^{-1}$) |
| $V$ | molar volume of solution ($cm^3\,mol^{-1}$) |
| $x$ | mole fraction |
| $y$ | $CO_2$ mole fraction in the bulk gas-phase |
| $y^*$ | $CO_2$ mole fraction in equilibrium |
| $Y$ | mole ratio |
| $Z$ | membrane length (m) |

*Greek letters*

| | |
|---|---|
| $\Omega$ | mass percent of amine |
| $\Omega_D$ | collision integral for molecular diffusion |
| $\Phi_j$ | volume faction of component $j$ |
| $\alpha$ | $CO_2$ loading ($mol\,mol^{-1}$) |
| $\delta$ | membrane thickness (m) |
| $\varepsilon$ | membrane porosity (dimensionless) |
| $\lambda$ | latent heat of vaporization ($kJ\,kmol^{-1}$) |
| $\eta$ | viscosity (mPa s) |
| $\rho$ | density ($g\,cm^{-3}$) |
| $\tau$ | membrane tortuosity (dimensionless) |

*Subscript*

| | |
|---|---|
| 0 | base for enthalpy |
| $A$ | component $A$, solute gas |
| $B$ | component $B$, inert gas |
| $e$ | equilibrium |
| $G$ | gas |
| $i$ | interface or component $i$ |
| $L$ | liquid |
| $R$ | non-volatile reactive component of solution |
| $S$ | volatile component of solution |

## Acknowledgements

The authors gratefully acknowledge financial support from the Thailand Research Fund (TRF) through the Royal Golden Jubilee Ph.D. Program, the TRF Senior Research Scholar Grant, and the International Test Centre for $CO_2$ Capture, University of Regina.

## References

[1] A. Gabelman, S. Hwang, Hollow fiber membrane contactors, J. Membr. Sci. 159 (1999) 61–106.
[2] R. Wang, H.Y. Zhang, P.H.M. Feron, D.T. Liang, Influence of membrane wetting on $CO_2$ capture in microporous hollow fiber membrane contactors, Sep. Purif. Technol. 46 (2005) 33–40.
[3] D. deMontigny, P. Tontiwachwuthikul, A. Chakma, Comparing the absorption performance of packed columns and membrane contactors, Ind. Eng. Chem. Res. 44 (2005) 5726–5732.
[4] S. Atchariyawut, R. Jiraratananon, R. Wang, Mass transfer study and modeling of gas–liquid membrane contacting process by multistage cascade model for $CO_2$ absorption, Sep. Purif. Technol. 63 (2008) 15–22.
[5] J.G. Lu, Y.F. Zheng, M.D. Cheng, Wetting mechanism in mass transfer process of hydrophobic membrane gas absorption, J. Membr. Sci. 308 (2008) 180–190.
[6] M. Mavroudi, S.P. Kaldis, G.P. Sakellaropoulos, A study of mass transfer resistance in membrane gas–liquid contacting process, J. Membr. Sci. 272 (2006) 103–115.
[7] S. Khaisri, D. deMontigny, P. Tontiwachwuthikul, R. Jiraratananon, Comparing membrane resistance and absorption performance of three different membranes in a gas absorption membrane contactor, Sep. Purif. Technol. 65 (2008) 290–297.

[8] E. Drioli, A. Criscuoli, E. Curcio, in: M. Wessling, K. Sirkar (Eds.), Membrane Contactors: Fundamentals, Applications and Potentialities. Membrane Science and Technology Series (vol. 11), Elsevier, Amsterdam, 2006.

[9] M.C. Yang, E.L. Cussler, Designing hollow-fiber contactors, AIChE J. 32 (1986) 1910–1916.

[10] H. Kreulen, C.A. Smolders, G.F. Versteeg, W.P.M. Van Swaaij, Determination of mass transfer rates in wetted and non-wetted microporous membranes, Chem. Eng. Sci. 48 (1993) 2093–2102.

[11] H.A. Rangwala, Absorption of carbon dioxide into aqueous solutions using hollow fiber membrane contactors, J. Membr. Sci. 112 (1996) 29–240.

[12] D. deMontigny, P. Tontiwachwuthikul, A. Chakma, Using polypropylene and polytetrafluoroethylene membranes in a membrane contactor for $CO_2$ absorption, J. Membr. Sci. 277 (2006) 99–107.

[13] J.D. Pandya, Adiabatic gas absorption and stripping with chemical reaction in packed towers, Chem. Eng. Commun. 19 (1983) 343–361.

[14] A. Aboudheir, P. Tontiwachwuthikul, R. Idem, Rigorous model for predicting the behavior of $CO_2$ absorption into AMP in packed-bed absorption columns, Ind. Eng. Chem. Res. 45 (2006) 2553–2557.

[15] A. Aboudheir, P. Tontiwachwuthikul, A. Chakma, R. Idem, Kinetics of the reactive absorption of carbon dioxide in high $CO_2$-loaded, concentrated aqueous monoethanolamine solutions, Chem, Eng. Sci. 58 (2003) 5195–5210.

[16] W.J. DeCoursey, Absorption with chemical reaction: development of a new relation for the Danckwerts model, Chem. Eng. Sci. 29 (1974) 1867–1872.

[17] J. Kiusalaas, Numerical Methods in Engineering with MATLAB, Cambridge University Press, New York, 2005.

[18] R.H. Weiland, J.C. Dingman, D.B. Cronin, G.J. Browning, Density and viscosity of some partially carbonated aqueous alkanolamine solutions and their blends, J. Chem. Eng. Data 43 (1998) 378–382.

[19] T.C. Tsai, J.J. Ko, H.M. Wang, C.Y. Lin, M.H. Li, Solubility of nitrous oxide in alkanolamine aqueous solutions, J. Chem. Eng. Data 45 (2000) 341–347.

[20] Y.W. Wang, S. Xu, F.D. Otto, A.E. Mather, Solubility of $N_2O$ in alkanolamines and in mixed solvents, Chem. Eng. J. 48 (1992) 31–40.

[21] G.F. Versteeg, W.P.M. Van Swaaij, Solubility and diffusivity of acid gases ($CO_2$, $N_2O$) in aqueous alkanolamine solutions, J. Chem. Eng. Data 33 (1988) 29–34.

[22] J.J. Ko, T.C. Tsai, C.Y. Lin, H.M. Wang, M.H. Li, Diffusivity of nitrous oxide in aqueous alkanolamine solutions, J. Chem. Eng. Data 46 (2001) 160–165.

[23] W. Hayduk, H. Laudie, Prediction of diffusion coefficients for nonelectrolytes in dilute aqueous solutions, AIChE J. 20 (1974) 611–615.

[24] R.C. Reid, J.M. Prausnitz, B.E. Poling, The Properties of Gases and Liquids, 4th, McGraw-Hill, Inc., New York, 1987.

[25] J.R. Welty, C.E. Wicks, R.E. Wilson, G. Rorrer, Fundamentals of Momentum, Heat, and Mass Transfer, John Wiley & Sons, Inc., New York, 2001.

[26] W. Horeitz, Association of official analytical chemists (AOAC) methods, 12th, George Banta, 1975.

[27] Z. Qi, E.L. Cussler, Microporous hollow fibers for gas absorption. I. Mass transfer in the liquid, J. Membr. Sci. 23 (1985) 321–332.

[28] S. Atchariyawut, C. Feng, R. Wang, R. Jiraratananon, D.T. Liang, Effect of membrane structure on mass-transfer in the membrane gas–liquid contacting process using microporous PVDF hollow fibers, J. Membr. Sci. 285 (2006) 272–281.

[29] J.L. Li, B.H. Chen, Review of $CO_2$ absorption using chemical solvents in hollow fiber membrane contactors, Sep. Purif. Technol. 41 (2005) 109–122.

[30] M.C. Garcia-Payo, M.A. Izquierdo-Gil, C. Fernandez-Pineda, Wettting study of hydrophobic membranes via liquid entry pressure measurements with aqueous alcohol solutions, J. Colloid Interface Sci. 230 (2000) 420–431.

Desalination 253 (2010) 30–37

Contents lists available at ScienceDirect

Desalination

journal homepage: www.elsevier.com/locate/desal

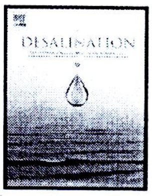

# Experimental study on micellar-enhanced ultrafiltration (MEUF) of aqueous solution and wastewater containing lead ion with mixed surfactants

Paiboon Yenphan, Ampai Chanachai, Ratana Jiraratananon *

*Department of Chemical Engineering, King Mongkut's University of Technology Thonburi, 126 Prachauthit Road, Tungkru, Bangkok 10140, Thailand*

ARTICLE INFO

*Article history:*
Received 17 August 2009
Received in revised form 25 November 2009
Accepted 27 November 2009
Available online 6 January 2010

*Keywords:*
Lead removal
Micellar-enhanced ultrafiltration
Polyoxyethylene nonylphenyl ether (NP12)
Resistance-in-series model
Sodium dodecyl sulfate (SDS)
Triton X-100 (TX-100)

ABSTRACT

We studied the performance of single and mixed surfactants for removal of $Pb^{2+}$ from aqueous solution and wastewater by MEUF. Anionic surfactant, SDS and 2 nonionic surfactants, TX-100 and NP12 were used. The experiments were carried out using a flat sheet module with polyethersulfone membrane (MWCO 10 kDa). Single surfactants, SDS gave high $Pb^{2+}$ rejections but low SDS rejections while TX-100 and NP12 showed opposite results. The use of mixed surfactants between SDS and nonionic surfactants can effectively enhance both $Pb^{2+}$ and surfactant rejections. The optimum amount of nonionic surfactants added was at mole fractions of 0.1 for both SDS/TX-100 and SDS/NP12 systems in which the highest $Pb^{2+}$ rejection can be achieved. At this mole fraction (1.37 mM) of TX-100 and NP12 with 12.3 mM of SDS, the $Pb^{2+}$ rejections were higher than 98.4%. High rejections of SDS (80%), TX-100 and NP12 (>99%) were also obtained. The MEUF showed promising results of real wastewater tested.

The analysis of transport resistances showed that polarization resistance was dominant and fouling was very low for both single and mixed surfactants. Fouling resistances of mixed surfactants were higher than that of pure SDS but lower than those of pure nonionic surfactants.

## 1. Introduction

Heavy metal ion contaminants in wastewaters have been a serious environmental problem and require proper treatments. Various treatment techniques have been employed to remove metal ions, such as chemical precipitation [1,2], ion exchange [3], coagulation–flocculation [4], flotation [5,6] and adsorption [7–9]. However, these methods may not be cost-effective and energy efficient. Attempts have been made in developing alternative methods which are more practical and efficient.

Micellar-enhanced ultrafiltration (MEUF) is a technique to separate metal ions [10–22], organic pollutants [21–23] or inorganic compounds [24,25] from aqueous streams. In MEUF process, the surfactant over its critical micelle concentration (CMC) is added to form micelles in the aqueous stream. Metal ions and organic compounds tend to be soluble in the micelles by electrostatic or Van der Waals force. Micelles containing solubilized metal ions or organic compounds with sizes bigger than the membrane pore size are rejected by the membrane during the ultrafiltration process.

In removal of metal ions by MEUF, the anionic surfactants such as sodium dodecyl sulfate (SDS) have been shown to be very effective [12–14,22] since it has opposite charge with metal ions. However, the concentrations of surfactants greater than their CMC must be used for effective separation. Since CMC of anionic surfactants are relatively high, large amount of surfactants must be used. This resulted in excessive concentration polarization, fouling and contamination of surfactants in the permeate. In order to decrease the amount of anionic surfactants used, the nonionic surfactants such as nonylphenol polyethoxylate (NPE) [15,17], monoalkylphenol polyethoxylate (OP-10) [16] and Triton X-100 (TX-100) [18,21] have been added into anionic surfactants [15–18,21] to reduce the repulsive force between anionic charges resulting in a decrease of anionic surfactant CMC.

$Pb^{2+}$ is one of the harmful metal ions [8,26,27] found in wastewaters from various industries such as metal plating and battery plants. It is a very toxic element which can damage the nervous system, kidneys and reproductive system [27]. MEUF was used to remove $Pb^{2+}$ and other metal ions using cetylpyridinium chloride (CPC) as surfactant [19]. Ethylenediaminetetraacetic acid (EDTA) with equal molar ratio to metal ions must be added to form $Pb\cdot EDTA^{2-}$ complex which had an affinity to CPC cationic surfactant. In order to obtain rejection of $Pb^{2+}$ over 90%, high concentration of CPC, i.e., 10 mM (11.3 CMC) must be used [19].

There has been no report on MEUF of $Pb^{2+}$ using mixed surfactants. The objective of this research was to apply MEUF for removal of $Pb^{2+}$ from aqueous solutions using mixed surfactants. SDS was selected as anionic surfactant since it has been reported to be very effective for removal of many heavy metals [12–18]. TX-100 which is widely used and polyoxyethylene nonylphenyl ether (NP12) which can form complex with some metal ions [16] were used as nonionic surfactants in order to study the effect of ethylene oxide (EO) groups.

---

* Corresponding author. Tel.: +66 24709222; fax: +66 24283534.
*E-mail address:* ratana.jir@kmutt.ac.th (R. Jiraratananon).

0011-9164/$ – see front matter © 2009 Elsevier B.V. All rights reserved.
doi:10.1016/j.desal.2009.11.040

The aqueous model solutions of $Pb^{2+}$ ions were used in the experiments. Moreover, the wastewater from a battery factory was also used in order to study a practical application of MEUF.

The focus of this work also includes the study of flux decline due to concentration polarization and fouling. Fouled membranes need to be frequently cleaned by chemicals resulting in high operating cost and shortening of the membrane life. A serious flux decline during MEUF of metal ions (Cd, Cu, Pb and Zn) using CPC surfactant and EDTA chelating agent was reported [19]. In MEUF of $Cu^{2+}$ ions using SDS/TX-100 with hydrophilic regenerated cellulose membrane (Millipore, YM10), membrane fouling was found to be totally reversible [28]. However, for polyethersulfone membrane, some irreversible fouling was observed in removal of alachlor using nonionic surfactants, ocytylphenol ethoxylates (Triton series) and alcohol ethoxylates [29]. In this work, the extent of flux decline due to concentration polarization and fouling was interpreted in terms of transport resistances using resistance-in-series model.

## 2. Analysis of transport resistances

In the resistance-in-series model, the total resistance is defined as in the following equations;

$$R_t = R_m + R_p + R_f \tag{1}$$

where

$R_t$ = total resistance ($m^{-1}$)
$R_m$ = membrane resistance ($m^{-1}$)
$R_p$ = polarization resistance ($m^{-1}$)
$R_f$ = fouling resistance ($m^{-1}$).

From the experimental data on solution flux ($J_v$), the total resistance can be calculated from;

$$R_t = \frac{\Delta P}{\mu_v J_v} \tag{2}$$

where

$\Delta P$ = applied pressure (Pa)
$\mu_v$ = permeate viscosity (Pa s).

The membrane resistance ($R_m$) is available from the pure water flux data, i.e.,

$$R_m = \frac{\Delta P}{\mu_w J_w} \tag{3}$$

where

$J_w$ = water flux ($m^3/m^2$ s)
$\mu_w$ = viscosity of pure water (Pa s).

The polarization resistance ($R_p$) is assumed to be reversible and can be removed by water cleaning. If $J'_w$ is the pure water flux after water cleaning, $R_m + R_f$ is thus calculated from

$$R_m + R_f = \frac{\Delta P}{\mu_w J'_w} \tag{4}$$

Therefore, by systematic experimental and cleaning procedure, all transport resistances can be calculated.

## 3. Materials and method

### 3.1. Materials and analysis

All reagents used were of analytical grade. Lead (II) chloride ($PbCl_2$, 98% purity) and SDS (96% purity) were obtained from Ajax Finechem. TX-100, 99% purity was supplied by Panreac. NP12 (Igepal CO-720) with 99% purity was supplied by Aldrich. The properties of surfactants are listed in Table 1. Deionized water was used throughout the experiments to prepare the aqueous solutions. A sample of wastewater from GS Battery with total solid and suspended solid of 4800 mg/l and 12 mg/l, respectively, and pH of 2.2 was also tested. A sample was filtered with 0.2 µm paper filter before use.

Concentration of $Pb^{2+}$ ions was measured by Atomic Absorption Spectrophotometer, AA (Hitachi, Model Z8200). SDS concentration was determined by Ion Chromatography, IC (Alltech, Model 650) using conductivity detector (Alltech). High-performance liquid chromatography, HPLC (Waters-Model 600E) with UV detector (Waters 2487 dual) was used to measure TX-100 and NP12 concentrations at 229 nm [30]. In order to determine the SDS concentration and nonionic surfactant concentration in permeate and retentate of wastewater, the samples were neutralized with $NH_4OH$ to prevent the damage of equipment. In addition, the viscosities of surfactant solutions were also measured by a viscometer (HAKKE VT 500).

### 3.2. Experimental

The experimental setup is shown in Fig. 1. Feed was recirculated by a peristaltic pump (Masterflex, model 7520-47). The membrane module was a radial flow across a flat circular membrane sheet. Polyethersulfone (PES) flat sheet membrane with molecular weight cut off (MWCO) 10 kDa obtained from Millipore Corporation was used. The effective membrane area was 19.64 $cm^2$. The water flux of new membranes was around 183 $l/m^2h$ at an applied pressure of 10 kPa and at a room temperature (25 °C).

In the preparation of feed solutions, lead chloride and surfactant(s) were mixed at the required concentrations. The mixture was then stirred at 230 rpm for 15 min to allow for the formation of micelles. Then, the solution was fed to the membrane module at a flow rate of 55 l/h, and at the applied pressure of 10 kPa. Both retentate and permeate were returned to a feed tank to maintain a constant concentration. The permeation fluxes ($J_v$) were measured every 10 min, and the permeate collected was quickly returned to the feed tank. It was found that the permeation fluxes were almost constant after 1 h of operation. Then, the retentate and permeate were collected to analyze for the concentrations. The temperature was kept constant at room temperature about 25 °C for all experiments. The experiments were carried out in duplicates. The reported values were the averages.

In order to find the transport resistances, the used membrane was washed continuously with deionized water at a flow rate of 70 l/h and an applied pressure of 10 kPa for 30 min. Then, the water flux of membrane after water washing was measured ($J'_w$). The membrane was then cleaned with 0.1 N NaOH until the water flux was close to

**Table 1**
Properties of surfactants [31–33].

| Name | Chemical formula | MW ($g\ mol^{-1}$) | CMC (mM) | Aggregation number | MW of micelle |
|---|---|---|---|---|---|
| SDS | $CH_3(CH_2)_{10}CH_2OSO_3^-Na^+$ | 288 | 8.2 | 80 | 23,040 |
| TX-100 | $(CH_3)_3CCH_2C(CH_3)_2(C_6H_4)[C_2H_4O]_{9.5}H$ | 625 | 0.24 | 140 | 87,500 |
| NP12 | $(C_9H_{19}(C_6H_4)O[C_2H_4O]_nH$, $n = 10.5–12$ | 749 | 0.082 | 54 | 40,446 |

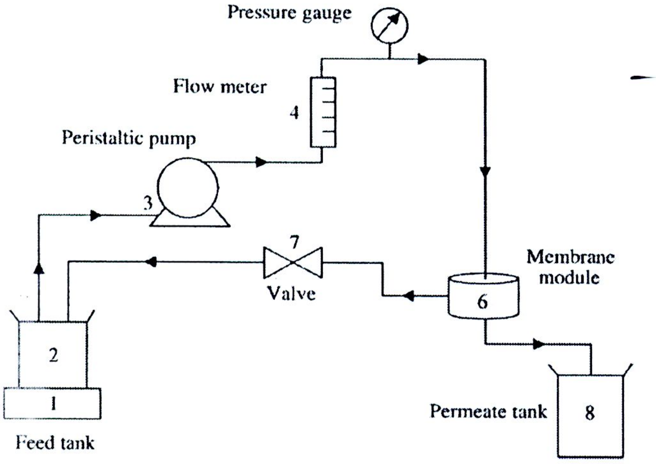

**Fig. 1.** A schematic of ultrafiltration experimental setup.

the original value (of the new membrane). From the data of $J_v$, $J_w$ and $J'_w$, all the transport resistances can be determined as outlined in Section 2. The condition for measuring water flux was the same as the UF condition of solution (55 l/h, 10 kPa).

In this work, the $Pb^{2+}$ concentration was kept constant at 0.1 mM (20 ppm), an approximate concentration in wastewater from a battery industry. In the study of removal of $Pb^{2+}$ using single surfactants, the concentrations of SDS, TX-100 and NP12 used were 0.5 CMC, 1 CMC and 1.5 CMC. In case of using mixed surfactants, SDS/TX-100 and SDS/NP12, SDS concentrations were fixed at 4.1 mM, 8.2 mM and 12.3 mM while mole fractions of TX-100 and NP12 were varied between 0.01 and 0.3. The corresponding concentrations of TX-100 and NP12 for each mole fraction are shown in Table 3.

The effectiveness of MEUF process was represented by percentage rejection of $Pb^{2+}$ ions and surfactants as follows.

$$\%R = \left(1 - \frac{C_P}{C_R}\right) \times 100\% \tag{5}$$

where $C_P$ and $C_R$ denote the concentrations of solutes in permeate and retentate, respectively.

## 4. Results and discussion

### *4.1. Effect of surfactant concentrations on flux and rejection for single surfactant systems*

The effects of surfactant concentrations on fluxes and rejections of $Pb^{2+}$ and surfactants are shown in Fig. 2 for SDS, TX-100 and NP12.

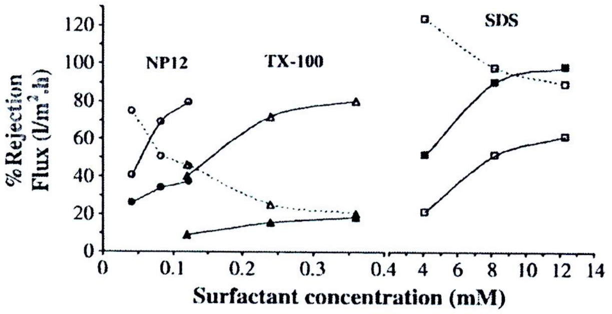

**Fig. 2.** Effect of surfactant concentration on flux and rejections of $Pb^{2+}$ ions and surfactants; SDS: —□— %R SDS, —■— %R $Pb^{2+}$, - -□- - flux; TX-100: —△— %R TX-100, —▲— %R $Pb^{2+}$, - -△- - flux; NP12: —○— %R NP12, —●— %R $Pb^{2+}$, - -○- - flux.

For all surfactants, an increase of surfactant concentration resulted in an increase of $Pb^{2+}$ and surfactant rejections. In order to explain this behavior, the distribution coefficient ($D$) and the equilibrium distribution constant ($K_s$) were calculated. Distribution coefficient is the ratio of $Pb^{2+}$ concentration in retentate and in permeate. An increase in the value of $D$ indicates that more and more surfactant molecules join the micellar phase, binding more and more metal ions [14].

The equilibrium distribution constant, $K_s$, which represents the relative affinity of $Pb^{2+}$ ions for the micelles was calculated by the following [14].

$$K_s = \frac{[Pb^{2+}]_m}{[Pb^{2+}]_w S_m}$$

where $[Pb^{2+}]_m$ and $[Pb^{2+}]_w$ are the concentration of $Pb^{2+}$ ions dissolved in the micelles and in the bulk water (free $Pb^{2+}$ ions), respectively. $S_m$ is the concentration of surfactants present in micelle form. The higher $K_s$ represents the higher affinity of $Pb^{2+}$ ions for the micelle. It is assumed that only free $Pb^{2+}$ ions and surfactants in monomer form pass the membrane and the concentration of $Pb^{2+}$ ions and surfactants in free form in retentate is the same as the concentration of $Pb^{2+}$ ions and surfactants (in monomer form) that pass the membrane or in the permeate, therefore [14],

$$C_m = C_R - C_P$$

where $C_m$ is the concentration of $Pb^{2+}$ ions dissolved in the micelles or the concentration surfactants present in micelle form (mM). For mixed surfactant systems, $S_m$ was calculated by combination of $S_m$ of SDS and of nonionic surfactant.

The calculated $S_m$, $D$ and $K_s$ values for single surfactant systems are shown in Table 2. At higher surfactant concentration, the number of active sites of surfactant to bind with $Pb^{2+}$ ions increased. Therefore, the binding between $Pb^{2+}$ ions and surfactant, represented by $D$ in Table 2, increased. In addition, higher amount of surfactant presented in micelle form (higher $S_m$) at higher surfactant concentration, in other words, lower surfactant in monomer form [34] also led to high rejection of surfactants. These resulted in higher rejection for $Pb^{2+}$. However, the equilibrium distribution constant, $K_s$, decreased as the surfactant concentration increased due to an increase of amount of surfactant in micelle form [14]. The increase in number of the micelles was also the reason for flux decline as surfactant concentration was increased.

At surfactant concentrations below the CMC (0.5 CMC), there were still some rejections of surfactants as well as the $Pb^{2+}$ ions. This was supposed to be due to accumulation of surfactant molecules on the membrane surface which enabled the surfactant concentration to exceed the CMC. Therefore, micelles can be formed in this region [12,18,28]. Furthermore, in case of SDS, the CMC of SDS may decrease when $Pb^{2+}$ counterions were presented in SDS solution because of the reduction of repulsive force between the micelle heads [35].

**Table 2**
$S_m$, $D$ and $K_s$ for single surfactant systems.

| Surfactant | Concentration (mM) | $S_m$ (mM) | $D$ | $K_s$ ($mM^{-1}$) |
|---|---|---|---|---|
| SDS | 4.1 | 0.80 | 2.24 | 1.55 |
| | 8.2 | 4.35 | 7.83 | 1.57 |
| | 12.3 | 8.83 | 14.06 | 1.48 |
| TX-100 | 0.12 | 0.05 | 1.10 | 2.21 |
| | 0.24 | 0.17 | 1.19 | 1.11 |
| | 0.36 | 0.27 | 1.23 | 0.85 |
| NP12 | 0.041 | 0.02 | 1.35 | 19.68 |
| | 0.082 | 0.06 | 1.51 | 9.09 |
| | 0.123 | 0.10 | 1.60 | 6.25 |

**Table 4**
Viscosity of surfactant/$Pb^{2+}$ mixtures.

| [SDS] (mM) | Mole fraction of nonionic surfactants | Viscosity ($10^{-3}$ Pa s) | |
|---|---|---|---|
| | | SDS/TX-100 | SDS/NP12 |
| 4.1 | 0.1 | 0.914 | 0.922 |
| | 0.2 | 1.193 | 1.235 |
| | 0.3 | 1.282 | 1.312 |
| 12.3 | 0.1 | 1.058 | 1.160 |
| | 0.2 | 1.258 | 1.290 |
| | 0.3 | 1.286 | 1.359 |

surfactant systems of SDS/TX-100 and SDS/Brij-35 for cadmium ions [18] and SDS/NPE for zinc ions [15].

### 4.3.4. Flux

The addition of both nonionic surfactants, TX-100 and NP12 resulted in a decrease of permeation flux at fixed SDS concentration as shown in Fig. 4. Since the CMC of SDS decreases with increasing nonionic surfactant concentration [17], therefore, the number of SDS micelles may increase, leading to higher concentration polarization near the membrane surface. In addition, the nonionic surfactant screened the charged groups between different micelles allowing closer micelle to micelle distances and a denser gel layer. Moreover, the viscosity of feed solution increased by the addition of nonionic surfactants [16,17] as shown in Table 4. All these were accounted for the reduction of flux.

### 4.4. Effect of SDS concentration on flux and rejection for mixed surfactants

Effects of SDS concentration on rejections and fluxes are presented in Figs. 5 and 6 for SDS/TX-100 mixed surfactant system. The results for SDS/NP12 mixed surfactant system also showed similar trends. It can be clearly seen from Fig. 5 that the SDS concentration had much effect on SDS rejection. It was probably because the number of micelles increased with SDS concentrations. High number of micelles at high SDS concentration also resulted in low permeation flux (Fig. 6).

The effect of SDS concentration on rejection of TX-100 (and NP12 also) was small, especially when mole fraction of nonionic surfactants was equal to 0.1 or higher as shown in Fig. 5. At these mole fractions, nonionic surfactant concentrations were higher than their CMC, therefore most of the nonionic surfactants were presented in the micelle form, resulting in very high rejections (>97%).

For pure SDS surfactant used, the SDS concentration had much effect on $Pb^{2+}$ ion rejection. The effect of SDS concentration was reduced for mixed surfactant systems (Fig. 6). It was possible that the formation of micelles was easier when nonionic surfactants were added into anionic surfactant, even at low SDS concentration.

When SDS concentration was increased, the amount of SDS forming the micelles and the number of active sites of surfactant were increased, leading to an increase of *D* (Table 3) and $Pb^{2+}$ rejection consequently. From the above results, SDS concentration of only 4.1 mM with 0.1 mole fraction (0.46 mM) of nonionic surfactants showed excellent MEUF performances, i.e., high rejection of $Pb^{2+}$ ions and nonionic surfactants as well as high flux. However, if the high SDS rejections are required, high SDS concentration must be used.

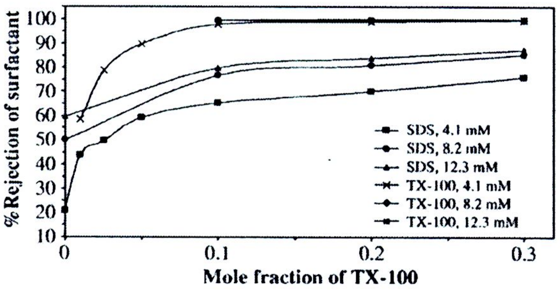

**Fig. 5.** Effect of mole fraction of TX-100 on rejection of surfactants for SDS/TX-100 systems with different SDS concentrations.

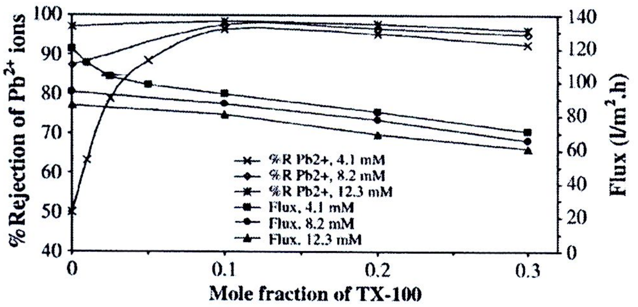

**Fig. 6.** Effect of mole fraction of TX-100 on permeation flux and rejection of $Pb^{2+}$ ions for SDS/TX-100 systems with different SDS concentrations.

### 4.5. Effect of type of nonionic surfactant on flux and rejection for mixed surfactants

SDS/NP12 system gave higher rejection of $Pb^{2+}$ ions and SDS than SDS/TX-100 system as seen in Figs. 3 and 4 which may be attributed to higher number of hydrophilic EO groups of NP12 which led to higher *D* and $K_s$ (Table 3). The permeation flux of SDS/NP12 was slightly higher than that of SDS/TX-100 system, probably due to higher number of EO groups of NP12. Moreover, NP12 had a less bulky alkyl side chain and could more effectively insert itself into micelle to screen the charged groups in the polar outer layer. The micelle could therefore have been smaller and thus had lower concentration polarization. These also caused a low fouling resistance (see Section 4.8).

### 4.6. MEUF of wastewater

The amount of nonionic surfactant should be optimized to get high number of micelles as well as high micelle charge density which would give highest $Pb^{2+}$ ion rejection. The optimum amount of nonionic surfactant was shown at a mole fraction of 0.1 for both SDS/TX-100 and SDS/NP12 systems. The highest $Pb^{2+}$ ion rejection was achieved at 12.3 mM with the mole fraction of nonionic surfactants of 0.1. High rejections of SDS, TX-100 and NP12 were also obtained. Therefore, these conditions were used to test the MEUF of wastewater from a battery factory. Furthermore, the SDS concentration of 4.1 mM was also used, since it gave excellent MEUF results with low amount of surfactant used. The results are shown in Fig. 7 compared with MEUF of aqueous model solution (Section 4.3–4.5). It can be seen that rejections of surfactants and $Pb2^{+}$ ions of wastewater were a little bit lower than the model solutions. Therefore, the results showed promising application of MEUF for removal of $Pb^{2+}$ ions from real wastewater. However, flux of wastewater was much lower than that of model solutions which may be due to the contaminants in wastewater.

### 4.7. Transport resistances for single surfactant systems

The resistance-in-series model was used to determine the significance of fouling in MEUF. The resistances to permeation were divided into membrane resistance ($R_m$), polarization resistance, $R_p$, (reversible) and fouling resistance ($R_f$, irreversible).

It can be seen from Fig. 8 that $R_p$ was the dominant resistance to permeation flux in MEUF of $Pb^{2+}$ ions with TX-100 and NP12. For SDS,

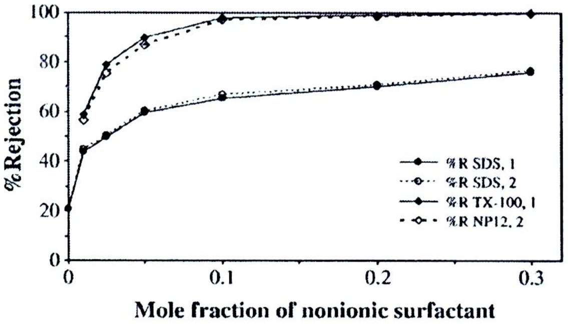

Fig. 3. Effect of mole fraction of nonionic surfactants on rejections of surfactants; [SDS] = 4.1 mM, 1 = SDS/TX-100 and 2 = SDS/NP12.

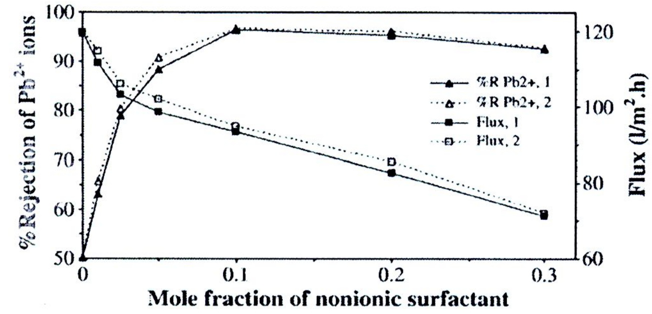

Fig. 4. Effect of mole fraction of nonionic surfactants on permeation flux and rejection of $Pb^{2+}$ ions; [SDS] = 4.1 mM, 1 = SDS/TX-100 and 2 = SDS/NP12.

### *4.2. Effect of type of surfactants on flux and rejection for single surfactants*

The rejection of $Pb^{2+}$ ions when using anionic surfactant SDS was relatively high compared to nonionic surfactants (see Fig. 2). Since SDS micelles have negative charges, therefore, cationic $Pb^{2+}$ can solubilize in SDS micelles by ionic interaction. By using nonionic surfactants, the $Pb^{2+}$ ions rejections were low, about 9%–18% for TX-100 and 30%–37% for NP12. The complex formation between the $Pb^{2+}$ ions and EO groups of TX-100 and NP12 is believed to be the reason for rejections. Since the number of EO groups of NP12 was higher than that of TX-100, the binding between $Pb^{2+}$ ions and NP12 was higher which can be seen from higher values of both $D$ and $K_s$ for NP12 than TX-100 (Table 2). Therefore, the $Pb^{2+}$ rejection using NP12 was higher. A previous work reported that $Ni^{2+}$ rejection was higher than 40% by using OP-10 (or NP10, nonionic surfactant) [16] but rejection of $Cu^{2+}$ ion using TX-100 was extremely low [28].

SDS gave high $Pb^{2+}$ rejection (90% at the CMC), however, SDS rejection was below 50%. This resulted in contamination of SDS in the permeate (3–5 mM) which means that it must be separated from the wastewater. In addition, large amount of the surfactant must be used to compensate the loss in the permeate during ultrafiltration. The reasons can be the following. The formation of SDS micelles may be difficult due to the repulsive force between negative charges of micelle heads. Therefore, there may be a large number of free SDS molecules, resulting in low SDS rejection. In case of TX-100 and NP12 which are nonionic surfactants, the micelles can be formed easier since there is no repulsive force between the micelle heads. Thus, the rejections of both TX-100 and NP12 were high. The rejection of TX-100 was slightly higher than NP12 due to higher micelle molecular weight.

From Fig. 2, it can be also seen that the permeation fluxes were in the following order, SDS > NP12 > TX-100, which corresponded to their micelle molecular weights, i.e., 23,040 Da, 40,446 Da and 87,500 Da, respectively (Table 1).

### *4.3. Effect of mole fraction of nonionic surfactants on flux and rejection for mixed surfactants*

#### *4.3.1. SDS rejection*

The rejections of SDS for both SDS/TX-100 and SDS/NP12 mixed surfactant systems were much higher than that of SDS single system (Fig. 3). In addition, the SDS rejection increased with the mole fraction of nonionic surfactants. The addition of nonionic surfactants reduced the repulsive force of negative charges between micelle heads, therefore, the CMC of SDS decreased with increasing nonionic surfactant concentration [17]. Accordingly, more SDS became available in the micelle form [18] or there was low SDS in monomer form. In other words, the number of micelles was increased, resulting in an increase of SDS rejection at higher mole fraction of nonionic surfactants.

#### *4.3.2. Nonionic surfactant rejections*

From Fig. 3, when mole fractions of nonionic surfactants were increased, the rejections of TX-100 and NP12 also increased due to higher number of micelles as described. The similar results were reported for SDS/TX-100 and SDS/Brij-35 in MEUF of cadmium ions [18].

#### *4.3.3. $Pb^{2+}$ ion rejection*

The rejections of $Pb^{2+}$ ions were significantly increased by the addition of nonionic surfactant and then they slightly decreased for further addition (Fig. 4). As described earlier, the number of micelles increased with increasing nonionic surfactant concentration which enhanced the surfactant rejection and rejection of $Pb^{2+}$ ions solubilized in the micelles of surfactants. However, when the mole fraction of nonionic surfactant in the micelles was further increased, the micelle charge density decreased and the counter ion binding capacity reduced [18] which resulted in decreases of $D$ and $K_s$ for both SDS/TX-100 and SDS/NP12 (Table 3). This had negative effect on rejection of $Pb^{2+}$ ion. These trends agreed well with the mixed

**Table 3**
$S_m$, $D$ and $K_s$ for mixed surfactant systems.

| [SDS] (mM) | Mole fraction of nonionic surfactants | [Nonionic surfactants] (mM) | $S_m$ (mM) | | $D$ | | $K_s$ ($mM^{-1}$) | |
|---|---|---|---|---|---|---|---|---|
| | | | SDS/TX-100 | SDS/NP12 | SDS/TX-100 | SDS/NP12 | SDS/TX-100 | SDS/NP12 |
| 4.1 | 0.1 | 0.46 | 3.28 | 3.14 | 27.92 | 29.98 | 8.21 | 9.23 |
| | 0.2 | 1.03 | 3.88 | 3.90 | 21.28 | 25.58 | 5.22 | 6.30 |
| | 0.3 | 1.76 | 5.23 | 5.11 | 13.53 | 13.92 | 2.39 | 2.53 |
| 8.2 | 0.1 | 0.91 | 9.60 | 7.76 | 40.22 | 49.73 | 4.08 | 6.28 |
| | 0.2 | 2.05 | 11.13 | 10.04 | 30.13 | 32.94 | 2.62 | 3.18 |
| | 0.3 | 3.51 | 12.95 | 11.58 | 20.02 | 20.74 | 1.47 | 1.71 |
| 12.3 | 0.1 | 1.37 | 12.33 | 12.11 | 64.38 | 75.67 | 5.14 | 6.16 |
| | 0.2 | 3.08 | 14.50 | 14.59 | 42.58 | 50.20 | 2.87 | 3.37 |
| | 0.3 | 5.27 | 17.62 | 17.74 | 26.15 | 26.99 | 1.43 | 1.47 |

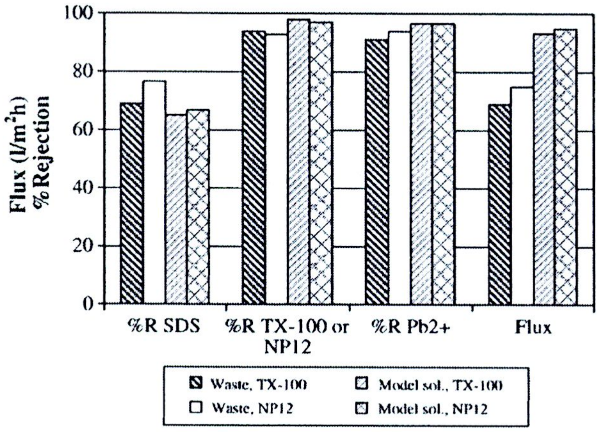

Fig. 7. Flux and %Rejection in MEUF of wastewater with SDS/TX-100 and SDS/NP12 compared to model solutions.

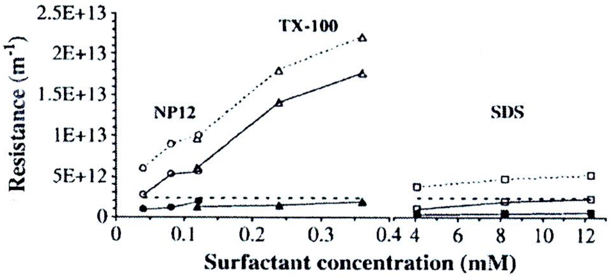

Fig. 8. Resistances in MEUF of $Pb^{2+}$ ions with SDS, TX-100 and NP12 surfactants; SDS: --□-- $R_t$, —□— $R_p$, —■— $R_f$; TX-100: --△-- $R_t$, —△— $R_p$, —▲— $R_f$; NP12: --○-- Rt, —○— Rp, —●— $R_f$; ------ $R_m$.

the system was controlled by the membrane resistance. Fouling resistances were low for all systems. Since the heads of all micelles were hydrophilic, though there was no charge for nonionic surfactants, the interaction between hydrophilic micelles and hydrophobic membrane was weak, resulting in low fouling.

Polarization resistance and fouling resistance increased with surfactant concentration (Fig. 8). Since the number of micelles increased with surfactant concentration, the accumulation of micelles on the membrane surface was, thus, accounted for the increase of polarization resistance. Furthermore, the probability of the accumulated micelles to foul the membrane surface also increased.

From Fig. 8, it can be also seen that SDS system had the lowest $R_p$ though its concentration was highest. It was probably because SDS has the lowest molecular weight of micelle (see Table 1), resulting in the lowest accumulation of SDS micelle on the membrane surface. $R_p$ of NP12 was lower than that of TX-100 due to lower micelle molecular weight of NP12.

SDS surfactant also gave the lowest $R_f$ due to its highest hydrophilicity of negative charges of micelles. TX-100 had higher $R_f$ than NP12 because TX-100 had lower number of EO groups which are hydrophilic.

### 4.8. *Transport resistances for mixed surfactants*

Fig. 9 shows resistances in MEUF of $Pb^{2+}$ with SDS/TX-100 and SDS/NP12 mixed surfactants for fixed SDS concentration of 4.1 mM. The resistances for fixed SDS concentration of 8.2 mM and 12.3 mM also showed similar trend. The resistance to permeation in MEUF with mixed surfactants was dominated by polarization resistance as in the case of single surfactants. MEUF with mixed surfactants also gave very low fouling resistance. An addition of nonionic surfactant caused a slight increase of fouling resistance compared to SDS pure surfactant (see Fig. 10). In the concentration range studied, $R_f$ of mixed surfactants with both nonionic surfactants were only about 0.9–1.8 times of that of pure SDS surfactant. However, $R_f$ of mixed surfactants was lower than that of both pure nonionic surfactants (Figs. 9 and 8), though the concentration of nonionic surfactants used in mixed surfactants (0.46 mM– 5.23 mM) was much higher than in pure surfactants (0.12 mM–0.36 mM for TX-100 and 0.041 mM–0.123 mM for NP12).

As the mole fraction of nonionic surfactants increased, the polarization resistance rapidly increased (Fig. 11). The number of micelles increased with the concentration of nonionic surfactant, leading to higher accumulation of micelles on the membrane surface, therefore, polarization resistance increased. This also increased the probability of fouling as seen in Fig. 10. The above reasons can be used

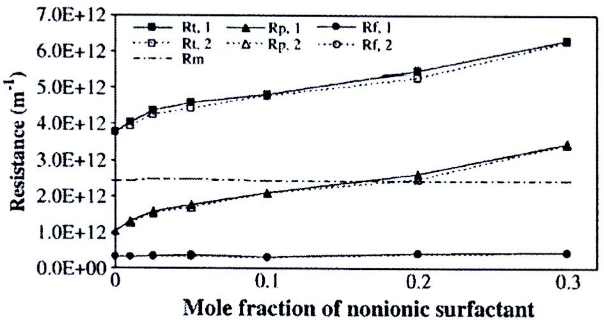

Fig. 9. Resistances in MEUF of $Pb^{2+}$ ions with mixed surfactants at fixed [SDS] = 4.1 mM; 1 = SDS/TX-100 and 2 = SDS/NP12.

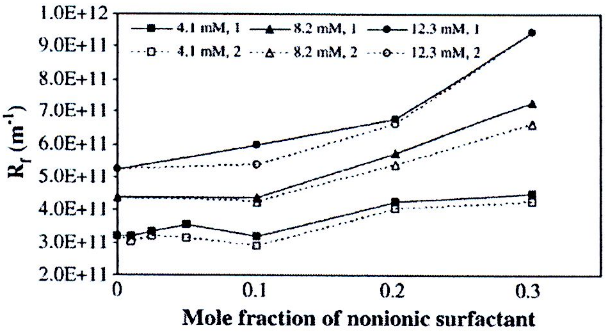

Fig. 10. Fouling resistance in MEUF of $Pb^{2+}$ ions with mixed surfactants for different SDS concentrations; 1 = SDS/TX-100 and 2 = SDS/NP12.

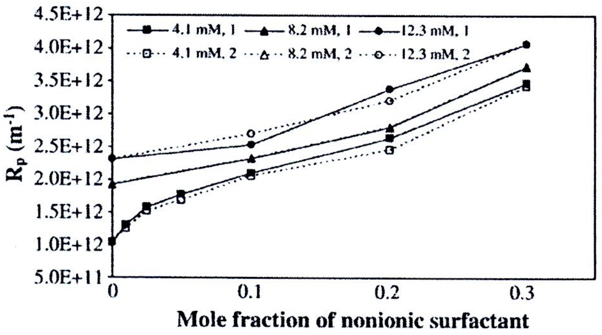

Fig. 11. Polarization resistance in MEUF of $Pb^{2+}$ ions with mixed surfactants for different SDS concentrations; 1 = SDS/TX-100 and 2 = SDS/NP12.

to explain the increase of both $R_p$ and $R_f$ with increasing SDS concentration.

At the same SDS mole fraction in which the concentrations of TX-100 and NP12 were equal, $R_p$ of SDS/TX-100 and SDS/NP12 systems were very close. It was likely that micelle sizes of SDS/TX-100 and SDS/NP12 were not significantly different. However, lower $R_f$ was obtained from SDS/NP12 system because NP12 had higher number of EO groups.

In MEUF of $Pb^{2+}$ ions with single surfactant, the percentage of each resistance to total resistance was $R_m$ 13.4%–64.0%, $R_f = 8.3\%–19.1\%$, and $R_p = 27.5\%–80.3\%$. For mixed surfactant systems, it was found that $R_m = 32.5\%–50.7\%$, $R_f = 6.1\%–12.7\%$ and $R_p = 43.5\%–54.8\%$ of total resistance. These results agreed well with the report of Doulia and Xiarchos [29] for PES membrane and Triton series surfactant. However, no irreversible fouling was reported for regenerated cellulose membrane and SDS/TX-100 surfactant [28]. The difference may be due to higher hydrophobicity of PES membrane used in this study.

In other UF processes, it was reported that $R_f$ was about 10.8%–35% in UF of passion fruit juice with PS membrane [36]. For UF of bovine serum albumin (BSA) protein with cellulose acetate/silica blend membrane, $R_f$ was about 25%–39% of total resistance [37]. Therefore, it seemed that fouling in MEUF was less significant in comparison with other UF processes, such as fruit juice and protein.

## 5. Conclusions

For single surfactants, rejections of $Pb^{2+}$ ions and surfactants increased with surfactant concentrations while the permeation fluxes decreased. SDS gave high $Pb^{2+}$ ion rejection but low SDS rejection. On the contrary, TX-100 and NP12 gave low $Pb^{2+}$ ion rejection and high SDS rejection.

The use of mixed surfactants between anionic (SDS) and nonionic (TX-100 and NP12) surfactants can effectively enhance the $Pb^{2+}$ ion and surfactant rejections. The $Pb^{2+}$ ion rejection of over 92% can be achieved for all concentrations of SDS studied. The optimum amount of nonionic surfactants added was at their mole fractions of 0.1 for both SDS/TX-100 and SDS/NP12 systems in which the highest $Pb^{2+}$ ion rejection can be achieved. At this mole fraction (1.37 mM) of TX-100 and NP12 with 12.3 mM of SDS, the $Pb^{2+}$ ion rejections were 98.4% and 98.7%, respectively. High rejections of SDS (80%), TX-100 and NP12 (>99%) were also obtained.

Polarization resistance was the dominant resistance in MEUF of $Pb^{2+}$. Fouling appeared to be very low for MEUF using both single surfactants and mixed surfactants. Fouling of mixed surfactants was higher than that of pure SDS but lower than pure nonionic surfactants, TX-100 and NP12. Thus, the application of MEUF may be practical if membrane lifetime is concerned since there is no need of frequent chemical cleaning of membranes.

For mixed surfactants, as the mole fraction of nonionic surfactants increased, flux and $Pb^{2+}$ ion rejection decreased while rejections of SDS and TX-100 or NP12 increased. Moreover, $R_f$ increased with mole fraction of nonionic surfactant. Since the reduction of $Pb^{2+}$ ion rejection with increasing nonionic mole fraction was not significant, therefore, mixing of SDS with low concentration of nonionic surfactant seemed to be better.

Flux and rejections of $Pb^{2+}$ ions and SDS of SDS/NP12 system were slightly higher than those of SDS/TX-100 system and $R_f$ was lower, while NP12 or TX-100 rejection was almost the same. Therefore, addition of NP12 nonionic surfactant with higher numbers of EO groups showed a little better performance than TX-100.

## Acknowledgements

The authors gratefully acknowledge the financial support from the Thailand Research Fund (TRF) and from the Commission on Higher Education.

## References

[1] M.M. Matlock, B.S. Howerton, D.A. Atwood, Chemical precipitation of heavy metals from acid mine drainage, Water Research 36 (2002) 4757–4764.
[2] T.A. Kravchenko, L.L. Polyanskiy, V.A. Krysanov, E.S. Zelensky, A.I. Kalinitchev, W.H. Hoell, Chemical precipitation of copper from copper–zinc solutions onto selective sorbents, Hydrometallurgy 95 (2009) 141–144.
[3] M.M. Matlock, K.R. Henke, D.A. Atwood, Effectiveness of commercial reagents for heavy metal removal from water with new insights for future chelate designs, Journal of Hazardous Materials 92 (2002) 129–142.
[4] E. Assaad, A. Azzouz, D. Nistor, A.V. Ursu, T. Sajin, D.N. Miron, F. Monette, P. Niquette, R. Hausler, Metal removal through synergic coagulation–flocculation using an optimized chitosan-montmorillonite system, Applied Clay Science 37 (2007) 258–274.
[5] X.Z. Yuan, Y.T. Meng, G.M. Zeng, Y.Y. Fang, J.G. Shi, Evaluation of tea-derived biosurfactant on removing heavy metal ions from dilute wastewater by ion flotation, Colloids and Surfaces A: Physicochemical and Engineering Aspects 317 (2008) 256–261.
[6] M. Ulewicz, W. Walkowiak, R.A. Bartsch, Ion flotation of zinc(II) and cadmium(II) with proton-ionizable lariat ethers—effect of cavity size, Separation and Purification Technology 48 (2006) 264–269.
[7] S.H. Jang, Y.G. Jeong, B.G. Min, W.S. Lyoo, S.C. Lee, Preparation and lead ion removal property of hydroxyapatite/polyacrylamide composite hydrogels, Journal of Hazardous Materials 159 (2008) 294–299.
[8] T. Gan, K. Wu, Sorption of Pb (II) using hydrogen peroxide functionalized activated carbon, Colloids and Surfaces A: Physicochemical and Engineering Aspects 330 (2008) 91–95.
[9] L.V.A. Gurgel, R.P. de Freitas, L.F. Gil, Adsorption of Cu(II), Cd(II), and Pb(II) from aqueous single metal solutions by sugarcane bagasse and mercerized sugarcane bagasse chemically modified with succinic anhydride, Carbohydrate Polymers 74 (2008) 922–929.
[10] S. Akita, L. Yang, H. Takeuchi, Micellar-enhanced ultrafiltration of gold(III) with nonionic surfactant, Journal of Membrane Science 133 (1997) 189–194.
[11] S. Akita, L.P. Castillo, S. Nii, K. Takahashi, H. Takeuchi, Separation of Co(II)/Ni(II) via micellar-enhanced ultrafiltration using organophosphorus acid extractant solubilized by nonionic surfactant, Journal of Membrane Science 162 (1999) 111–117.
[12] R.-S. Juang, Y.-Y. Xu, C.-L. Chen, Separation and removal of metal ions from dilute solutions using micellar-enhanced ultrafiltration, Journal of Membrane Science 218 (2003) 257–267.
[13] C.-K. Liu, C.-W. Li, Combined electrolysis and micellar enhanced ultrafiltration (MEUF) process for metal removal, Separation and Purification Technology 43 (2005) 25–31.
[14] V.D. Karate, K.V. Marathe, Simultaneous removal of nickel and cobalt from aqueous stream by cross flow micellar enhanced ultrafiltration, Journal of Hazardous Materials 157 (2008) 464–471.
[15] B.R. Fillipi, L.W. Brant, J.F. Scamehorn, S.D. Christian, Use of micellar-enhanced ultrafiltration at low surfactant concentration and with anionic–nonionic surfactant mixtures, Journal of Colloid and Interface Science 213 (1999) 68–80.
[16] L. Yurlova, A. Kryvoruchko, B. Kornilovich, Removal of Ni(II) ions from wastewater by micellar-enhanced ultrafiltration, Desalination 144 (2002) 255–260.
[17] M. Aoudia, N. Allal, A. Djennet, L. Toumi, Dynamic micellar-enhanced ultrafiltration: use of anionic (SDS)–nonionic (NPE) system to remove $Cr^{3+}$ at low surfactant concentration, Journal of Membrane Science 217 (2003) 181–192.
[18] Y.-Y. Fang, G.-M. Zeng, J.-H. Huang, J.-X. Liu, X.-M. Xu, K. Xu, Y.-H. Qu, Micellar-enhanced ultrafiltration of cadmium ions with anionic–nonionic surfactants, Journal of Membrane Science 320 (2008) 514–519.
[19] J. Jung, J.-S. Yang, S.-H. Kim, J.-W. Yang, Feasibility of micellar-enhanced ultrafiltration (MEUF) for the heavy metal removal in soil washing effluent, Desalination 222 (2008) 202–211.
[20] K. Baek, J.-W. Yang, Competitive bind of anionic metals with cetylpyridinium chloride micelle in micellar-enhanced ultrafiltration, Desalination 167 (2004) 101–110.
[21] C.C. Tung, Y.M. Yang, C.H. Chang, J.R. Maa, Removal of copper ions and dissolved phenol from water using micellar-enhanced ultrafiltration with mixed surfactants, Waste Management 22 (2002) 695–701.
[22] A. Witek, A. Koltuniewicz, B. Kurczewski, M. Radziejowska, M. Hatalski, Simultaneous removal of phenols and $Cr^{3+}$ using micellar-enhanced ultrafiltration process, Desalination 191 (2006) 111–116.
[23] M.K. Purkait, S. DasGupta, S. De, Separation of aromatic alcohols using micellar-enhanced ultrafiltration and recovery of surfactant, Journal of Membrane Science 250 (2005) 47–59.
[24] K. Baek, J.-W. Yang, Effect of valences on removal of anionic pollutants using micellar-enhanced ultrafiltration, Desalination 167 (2004) 119–125.
[25] J. Yoon, Y. Yoon, G. Amy, J. Cho, D. Foss, T.-H. Kim, Use of surfactant modified ultrafiltration for perchlorate ($ClO_4^-$) removal, Water Research 37 (2003) 2001–2012.
[26] E.W. Shin, H.S. Choi, T.-D. Nguyen-Phan, J.S. Chung, E.J. Kim, Interaction of $Pb^{2+}$ ions with surfactant-containing mesoporous silicates, Journal of Industrial and Engineering Chemistry 14 (2008) 510–514.
[27] M.H. Entezari, T. Soltani, Simultaneous removal of copper and lead ions from a binary solution by sono-sorption process, Journal of Hazardous Materials 160 (2008) 88–93.
[28] C.-W. Li, C.-K. Liu, W.-S. Yen, Micellar-enhanced ultrafiltration (MEUF) with mixed surfactants for removing Cu(II) ions, Chemosphere 63 (2006) 353–358.
[29] D. Doulia, I. Xiarchos, Ultrafiltration of micellar solutions of nonionic surfactants with or without alachlor pesticide, Journal of Membrane Science 296 (2007) 58–64.
[30] T.M. Schmitt, Analysis of surfactant, Revised and Expanded, 2nd edition, Marcel Dekker Inc, New York, 2001, p. 256.

[31] S.-H. Chang, K.-S. Wang, P.-I. Hu, I.-C. Lui, Rapid recovery of dilute copper from a simulated Cu–SDS solution with low-cost steel wool cathode reactor, Journal of Hazardous Materials 163 (2009) 544–549.

[32] S. Dai, K.C. Tam, Isothermal titration calorimetric studies of alkyl phenol ethoxylate surfactants in aqueous solutions, Colloids and Surfaces A: Physicochemical and Engineering Aspects 229 (2003) 157–168.

[33] S.K. Ghosh, P.K. Khatua, S.Ch. Bhattacharya, Characterization of micelles of polyoxyethylene nonylphenol (Igepal) and its complexation with 3, 7-diamino-2, 8-dimethyl-5-phenylphenazinium chloride, Journal of Colloid and Interface Science 275 (2004) 623–631.

[34] S.R. Jadhav, N. Verma, A. Sharma, P.K. Bhattacharya, Flux and retention analysis during micellar enhanced ultrafiltration for the removal of phenol and aniline, Separation and Purification Technology 24 (2001) 541–557.

[35] N. Kamenka, R. Zana, Interaction of magnesium and cadmium dodecyl sulfates with poly(ethylene oxide) and poly(vinylpyrrolidone): conductance, self-diffusion and fluorescence probing investigations, Journal of Colloid and Interface Science 188 (1997) 130–138.

[36] R. Jiraratananon, A. Chanachai, A study of fouling in the ultrafiltration of passion fruit juice, Journal of Membrane Science 111 (1996) 39–48.

[37] G. Arthanareeswaran, T.K. Sriyamuna Devi, M. Raajenthiren, Effect of silica particles on cellulose acetate blend ultrafiltration membranes: part I, Separation and Purification Technology 64 (2008) 38–47.

Desalination 253 (2010) 38–45

Contents lists available at ScienceDirect

Desalination

journal homepage: www.elsevier.com/locate/desal

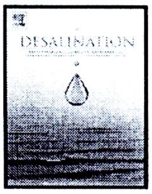

# Effect of operating conditions and solution chemistry on model parameters in crossflow reverse osmosis of natural organic matter

Supatpong Mattaraj [a,b,*], Wongphaka Phimpha [a], Pakasit Hongthong [a], Ratana Jiraratananon [c]

[a] *Environmental Engineering Program, Department of Chemical Engineering, Faculty of Engineering, Ubon Ratchathani University, Ubonratchathani 34190, Thailand*
[b] *National Center of Excellence for Environmental and Hazardous Waste Management, Ubon Ratchathani University, Ubonratchathani 34190, Thailand*
[c] *Department of Chemical Engineering, Faculty of Engineering, King Mongkut's University of Technology Thonburi, Bangkok 10140, Thailand*

ARTICLE INFO

*Article history:*
Received 18 August 2009
Received in revised form 19 November 2009
Accepted 27 November 2009
Available online 3 Janaury 2010

*Keywords:*
Cake resistance
Flux decline
Natural organic matter
Reverse osmosis

## ABSTRACT

This paper describes the effect of operating conditions and solution chemistry on model parameters in crossflow reverse osmosis of natural organic matter. Mathematical fouling model based on the combined osmotic pressure and cake filtration model was used to evaluate model parameters (i.e. steady-state flux, $J^*$ and specific cake resistance, $\alpha_{cake}$). In addition, the empirical equation for steady-state flux ($J^* = 9.12 \times 10^{-8} \Delta P^{1.04} v^{0.223} R^{-1.18} I^{-0.590}$) was successfully determined to characterize reverse osmosis operation. Steady-state flux increased with increased operating pressure, indicating a pressure-dependent steady-state flux under laminar flow condition. The specific cake resistance ($\alpha_{cake} = 7.943 \times 10^{12} \Delta P^{-2.03} v^{-0.739} R^{6.29} I^{1.37}$) was inversely related to increased operating pressure and crossflow velocity, while the specific cake resistance increased linearly with recovery effects and ionic strength. Recovery effects with high ionic strength resulted in the highest flux decline, corresponding to high specific cake resistance (i.e. lowering cake porosity) due to combined salt concentration polarization and NOM cake compaction near the membrane surface.

## 1. Introduction

Reverse osmosis (RO) is the well-known membrane separation process which can be applied for seawater and brackish water desalination, softening, disinfection by-product control, and removal of organics and specific inorganic contaminants such as arsenic, barium, nitrite, nitrate, and other inorganic contaminants [1,2]. The application of membranes has been increasingly used for water treatment in order to control a precursor of the formation of disinfection by-products such as natural organic matter (NOM) during chlorination operation in conventional water treatment [3]. However, fouling of membranes caused by NOM and inorganic salts on the membrane surface can be a major cause of a significant loss of water productivity [4–6].

Membrane fouling can be dependent on membrane characteristics (i.e. pore size, charge, and roughness) [7,8], solution compositions (i.e. humic acid concentration, pH, ionic strength, and calcium concentration) [9,10], and hydrodynamic conditions (i.e. flux, pressure, and crossflow velocity) [10,11]. Fouling can also lead to decreased solution flux due to adsorption/deposition of solute on the membrane surface and in the membrane pores, and cake formation at the membrane surface. Tang et al. [10] indicated that flux reduction during RO of humic acid increased with increasing initial flux (i.e. increased operating pressure), while the tight RO showed less flux decline than the more permeable membranes. Higher operating pressure in NF of humic acids increased flux decline, while higher crossflow velocity increased solution flux due to increased back-transport of solute to the bulk solution, thus decreasing solute accumulation at the membrane surface [12]. Zhu and Elimelech [13] studied the fouling mechanisms during RO of silica colloids. They found that higher permeate flux caused by increasing transmembrane pressure resulted in a greater rate of particle deposition onto membrane surface, and thus an increased rate of membrane fouling. However, previous work showed different results indicating that the specific flux normalized to the initial value was found to be inversely related to the initial permeate rate [14]. The specific resistance of particle deposits on membranes decreased as the initial permeation rate increased, suggesting that cake morphology was an important parameter in determining permeate flux [14]. Kilduff et al. [15] indicated that the rate of flux decline increased with increasing recovery because of the increase of solute concentration on the membrane surface caused by enhancing the convective transport of mass to the membrane surface. Previous studies indicated that the operating conditions could influence membrane performance with different membrane uses and solutions [10], but there is a lack of characterization of model parameters and development of the empirical relationship among membrane operating conditions and solution chemistry.

The objective of this study was to investigate the effects of operating conditions on model parameters (i.e. steady-state flux, $J^*$

---

* Corresponding author. Environmental Engineering Program, Department of Chemical Engineering, Faculty of Engineering, Ubon Ratchathani University, Ubonratchathani 34190, Thailand. Tel.: +66 45 353 344; fax: +66 45 353 333.
*E-mail addresses:* mattas@ubu.ac.th, supatpong.m@hotmail.com (S. Mattaraj).

0011-9164/$ – see front matter © 2009 Elsevier B.V. All rights reserved.
doi:10.1016/j.desal.2009.11.039

and specific cake resistance, $\alpha_{cake}$) with different ionic strengths during reverse osmosis of natural organic matter and to develop an empirical relationship among membrane operating conditions and solution chemistry. The empirical equations for $J^*$ and $\alpha_{cake}$ were developed with dependent variables for operating pressure ($\Delta P$), crossflow velocity ($v$), recovery ($R$), and ionic strength ($I$). Experimental results exhibited flux decline and rejection with different operating conditions and ionic strengths. The model parameters were determined using the combined osmotic pressure and cake filtration model, while a resistance-in-series model was used to characterize fouling resistances of tight RO system operation. The experimental results of this work could provide an insight evidence for changes in the model parameters as a function of system operating conditions and solution chemistry during crossflow RO.

## 2. Theory

### 2.1. Resistance-in-series model

Resistance-in-series model has been widely applied to describe the permeation flux of the membrane processes. This model incorporates membrane hydraulic resistance ($R_m$) and hydraulic resistances of fouling layer ($R_f$) on membrane surface. The membrane hydraulic resistance can be determined from the pure water flux without materials deposited on the membrane surface or within the membrane pore by using Darcy's law as shown in Eq. (1).

$$J_o = \frac{1}{A_m}\frac{dV}{dt} = \frac{\Delta P}{\mu R_m} \tag{1}$$

where $J_o$ is the clean water flux (LMH), $t$ is the filtration time (min), $V$ is the permeate volume (L), $\Delta P$ is the transmembrane pressure (kPa), $A_m$ is the membrane area (m$^2$), $\mu$ is the dynamic viscosity (kg m$^{-1}$s$^{-1}$). Eq. (2) accounts for total hydraulic resistance ($R_{Total}$) due to the combination between membrane hydraulic resistance ($R_m$) and the hydraulic resistances of fouling layer ($R_f$) caused by a combination of salt concentration polarization and/or cake formation, and resistant fouling as follows:

$$J_v = \frac{\Delta P - \sigma\Delta\pi}{\mu(R_m + R_f)} = \frac{\Delta P - \sigma\Delta\pi}{\mu(R_m + R_{c1} + R_{c2} + R_{c3} + R_{non-rec})} \tag{2}$$

where $J_v$ is the solution flux (LMH), $\sigma$ is the osmotic reflection coefficient (−), $\pi$ is the osmotic pressure (kPa), $R_{c1}$ is the fouling resistance caused by salt concentration polarization and/or cake formation, which can be recovered by hydrodynamic cleaning (m$^{-1}$), $R_{c2}$ is the recoverable fouling resistance caused by salt layer using acidic cleaning (m$^{-1}$), $R_{c3}$ is the reversibly adsorbed NOM layer resistance recoverable using alkaline cleaning (m$^{-1}$), and $R_{non\text{-}rec}$ is the "non-recoverable" resistance ($R_{non\text{-}rec}$) that remains after hydrodynamic and chemical cleaning (m$^{-1}$).

### 2.2. Combined osmotic pressure and cake filtration model

The combined osmotic pressure and cake filtration model was previously described by Mattaraj et al. [16]. The model has been previously used to characterize the nanofiltration performance of a solution containing both salt and NOM. The change in solution flux with time is related to the change in osmotic pressure as a result of salt concentration polarization, and the change in the hydraulic resistance of the NOM cake accumulated on the membrane surface as shown below:

$$\frac{dJ_v}{dt} = -\frac{\sigma_s \alpha_s R_{mem,s}\beta_s}{\mu(R_{m,s} + R_{non\text{-}rec} + R_c)}\left(\frac{dC_{reten,s}}{dt}\right) - \frac{J_v}{(R_{m,s} + R_{non\text{-}rec} + R_c)}\left(\frac{dR_c}{dt}\right) \tag{3}$$

where the subscript s refers to salt species (i.e. NaCl). The first term in the right-handed side describes the osmotic pressure model based on increased salt concentration, while the second term illustrates the additional resistance due to cake formation of NOM accumulation on the membrane surface. In the cake filtration with constant specific cake resistance ($\alpha_{cake}$), the change in cake resistance with time is related to the rate of change in cake mass, $m_{cake}$ (kg), which equals to the net rate of mass transport towards the membrane surface; i.e., the convective flux, $J_v$, minus the steady-state flux, $J^*$ (LMH), associated with back-transport resulting from crossflow velocity. Therefore,

$$\frac{dR_c}{dt} = \alpha_{cake}\frac{dm_{cake}}{A_m dt} = \alpha_{cake}C_{reten,NOM}(t)(J_v - J^*) \tag{4}$$

where $\alpha_{cake}$ is the specific cake resistance (m kg$^{-1}$), $C_{reten,NOM}$ is the NOM concentration in the retentate (kg m$^{-3}$). Eqs. (3) and (4) can be determined using the fitting model parameters (i.e. steady-state flux, $J^*$ and specific cake resistance, $\alpha_{cake}$ ) in a fourth-order Runge-Kutta routine in order to minimize the sum squared errors between the experimental data and estimated data from the combined mathematical fouling model. The fitted model parameters were determined based on 95% confidence interval for non-linear regression described by Draper and Smith [17]. In this work, the combined osmotic pressure and cake filtration model (Eq. (3)) was used to determine model parameters with different operating conditions and ionic strengths.

## 3. Experimental

### 3.1. Natural organic matter (NOM)

Natural organic matter (NOM) was obtained from the surface water reservoir at Ubon Ratchathani's University (UBU), Thailand. A polyamide thin-film composite (TFC) reverse osmosis (RO) membrane (model: AG4040F-spiral wound crossflow, GE osmonics, USA) was used to isolate NOM components and subsequently applied the isolated NOM for the crossflow reverse osmosis experiments. The isolation procedure was previously described by Kilduff et al. [18]. The characteristics of natural water were previously described by Jarusutthirak et al. [19]. The isolated NOM and salt were diluted and mixed with deionized water to obtain the required concentrations for both NOM and ionic strengths.

### 3.2. Crossflow filtration experiments

A bench-scale crossflow test cell with a recycle loop was used for crossflow filtration experiments. A thin-film polyamide reverse osmosis (Model AG 2540F1328 spiral wound crossflow), obtained from GE Osmonics, Inc. USA, was used to investigate membrane performance during filtration experiments. According to manufacturer's information, averaged salt (NaCl) rejection (based on a 2000 mg L$^{-1}$ NaCl solution, pH 7.5, 15% recovery, and 25 °C) is about 99.5% at 1551 kPa. Typical operating pressure is approximately 1379 kPa. The operating pH is in the range of 4–11, while the cleaning pH is in the range of 2–12. The maximum operating temperature is about 45 °C. Membrane sheets were initially cleaned and pre-compacted with deionized water. Clean water flux was determined with a function of operating pressure. After membrane compaction, averaged RO membrane permeability was approximately $1.231\times10^{-8} \pm 0.053\times10^{-8}$ m s$^{-1}$ kPa$^{-1}$(0.0443 LMH kPa$^{-1}$, number of samples are 17 samples within 95% confidence interval). The membrane hydraulic resistance ($R_m$) for RO was about $9.39\times10^{13}$ m$^{-1}$. All filtration experiments were conducted at room temperature at about 26 °C. Membrane sheets were stored in 1% $Na_2S_2O_5$ and kept in a refrigerator at about 4 °C to minimize bacterial activity.

For filtration experiments, NaCl solution contained salt concentration (NaCl) with ionic strengths ($I$) of 0.01 M and 0.05 M, while feed NOM concentration was maintained at 10 mg $L^{-1}$ with solution pH of 7. System operation was adjusted to achieve an initial solution flux of 30 LMH, while membrane operating pressure was kept constant during filtration experiments. The operating conditions tested included operating pressures ($\Delta P$) in the range of 551.4 to 965 kPa, crossflow velocity ($v$) in the range of 0.1 to 0.4 m $s^{-1}$, and recovery ($R = Q_{perm}/Q_{feed}$) in the range of 75 to 95%.

### 3.3. Analytical methods

Salt concentrations were determined using a conductivity meter (model: inoLab cond Level 2, Germany). Solution pH was measured with pH meter (model: inoLab pH level 1, Wissenschaftlich-Technische Werkstatten, GMBH, Germany). Ionic strength of samples was calculated using a correlation between conductivity and ionic strength; for NaCl standards, I.S.[mol $L^{-1}$] $= 0.5\Sigma C_i Z_i^2 = 9.5\times10^{-6}\times(\mu S\ cm^{-1})$ at 25 °C ($R^2 = 0.999$). NOM concentrations were measured as dissolved organic matter (DOC) using total organic carbon (TOC) analyzer (Shimadzu Corporation, TOC-VCPH model, Japan). Standard solutions were prepared using potassium hydrogen phthalate in deionized water. UV absorbance was measured using a UV-visible spectrophotometer (Shimadzu Corporation, model UV mini 1240, Japan). The weight-averaged molecular weights of NOM were determined using high pressure size exclusion chromatography (HPSEC) (Shimadzu Corporation, model CTO-10Avp, Japan). The procedure was employed as described by Chin et al. [20]. Poly(styrene sulfonate) standards (MW 4300, 6800, 17,000, and 32,000 Da) were used as standard solutions. Low molecular weight standard included benzoic acid ($Na^+$ form) (MW 122 g/mol), which was detected at wavelength of 254 nm, for standard solution with correlation: $\log MW = -0.3702\times t + 7.1471$, $R^2 = 0.987$. NOM mass balance was determined using a series of ultrafiltration membranes including 1, 3, 5, 10, 30, and 100 kDa molecular weight cutoff (MWCO).

### 3.4. Membrane cleaning

Cleaning procedure included hydrodynamic cleaning followed by chemical cleaning incorporating acidic and alkaline cleaning. First, for hydrodynamic cleaning, deionized water was recirculated in the recycle loop for 30 min at high crossflow velocity of 0.2 to 0.4 m $s^{-1}$. Deionized water was subsequently used to determine permeate flow as a function of operating pressures. For chemical cleaning, acidic solutions (using citric acid) with pH 4 and followed with alkaline solutions (using sodium hydroxide) with pH of 10 were used to remove inorganic salt and adsorbed NOM with 30-min each for recirculation in the system. Deionized water was further used to measure water flux with different operating pressures. After each cleaning, the water flux as a function of operating pressures was used to determine the recoverable fouling resistances ($R_{c1}$, $R_{c2}$, and $R_{c3}$) and the non-recoverable resistance ($R_{non\text{-}rec}$).

## 4. Results and discussion

### 4.1. NOM molecular weight

Fig. 1 shows the NOM molecular size distribution. The response of $UV_{254\ nm}$ was presented in wide range of high molecular weight (10,000–100,000 Da) and low molecular weight (less than 5000 Da). The weight-averaged NOM molecular weight ($M_w$) was approximately 4144 Da, while the number-averaged NOM molecular weight ($M_n$) was about 244 Da. The polydispersity of NOM solution (the ratio of the weight- ($M_w$) to number-averaged ($M_n$) molecular weights) was approximately 16.98, indicating wide molecular size distribution. NOM was further fractionated using several molecular weights of ultrafiltration (UF). It was found that organic carbons of NOM were approximately 18.6%, 11.1%, 17.9%, 11.5% and 40.9% for less than 1 K, 1–5 K, 5–30 K, 30–100 K, and greater than 100 K UF, respectively. The organic carbon fractions of greater than 5 K were relatively high, more than 70%, indicating higher molecular weight fractions than relatively low molecular weight fractions.

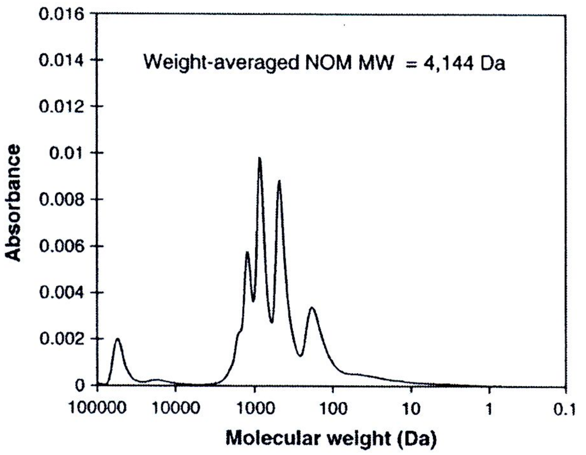

Fig. 1. NOM molecular size distribution.

### 4.2. Effect of operating pressure on normalized flux and rejection

Fig. 2 presents the effect of operating pressure on normalized flux, while the reverse osmosis performance is tabulated in Table 1. Dot points were the experimental data, while the solid lines were the values obtained from the combined osmotic pressure and cake filtration model (Eq. (3)). Experimental results revealed that increased operating pressures resulted in increased initial solution flux (graph not shown) and significantly increased steady-state solution flux at the end of filtration (as determined within 95% confidence interval shown in Table 1), indicating a pressure-dependent solution flux. Solutions having low operating pressure showed greater flux decline than those having high operating pressure, especially at low ionic strength. At high ionic strength of 0.05 M, the normalized fluxes were slightly increased with operating pressures ranging from 551.4 kPa to 965 kPa, while normalized fluxes of low and high ionic strengths ranged from 0.369 to 0.499 and 0.175 to 0.209, respectively. Fig. 3 illustrates the best fit values of the steady-state flux with a function of operating pressures. The model correlates linearly in the log–log plot with the slopes of 1.134 (1.07,1.205) and 0.96 (0.937,0.987) for low and high ionic strength,

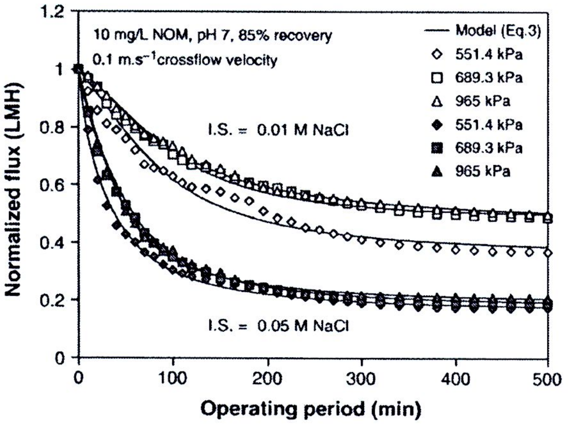

Fig. 2. Effect of operating pressure on normalized flux.

**Table 1**
Effect of operating pressure on reverse osmosis performance.

| Parameters | I.S. = 0.01 M NaCl<br>Operating pressure (kPa) | | | I.S. = 0.05 M NaCl<br>Operating pressure (kPa) | | |
|---|---|---|---|---|---|---|
| | 551.4 | 689.3 | 965 | 551.4 | 689.3 | 965 |
| $J_v/J_{vo}$ (−) | 0.369 | 0.489 | 0.499 | 0.175 | 0.190 | 0.209 |
| $J^*$ (m s$^{-1}$) × 10$^6$ | 2.82 (2.68–2.96) | 3.922 (3.84–4.0) | 5.371 (5.32–5.421) | 1.292 (1.226–1.358) | 1.536 (1.506–1.565) | 2.2 (2.125–2.275) |
| $C_{reten,s}$ (M) | 0.0569 | 0.0617 | 0.0626 | 0.1179 | 0.1349 | 0.1782 |
| $C_{perm,s}$ (M) | 0.0033 | 0.0035 | 0.0034 | 0.0341 | 0.0261 | 0.0333 |
| $R_{feed,s}$ (%) | 68.7 | 63.7 | 68.2 | 36.8 | 41.0 | 40.8 |
| $R_{reten,s}$ (%) | 94.2 | 94.3 | 94.6 | 71.1 | 80.7 | 81.3 |
| $R_{reten,NOM}$ (%) | 97.0 | 97.1 | 97.0 | 95.1 | 95.9 | 96.4 |
| $R_{m,s}$ (m$^{-1}$) × 10$^{-14}$ | 2.029 | 2.159 | 1.535 | 2.050 | 1.564 | 1.659 |
| $R_{non\text{-}rec}$ (m$^{-1}$) × 10$^{-14}$ | 0.0491 | 0.0462 | 0.037 | 0.0494 | 0.0639 | 0.0559 |
| $\alpha_{cake}$ (m kg$^{-1}$) × 10$^{-17}$ | 3.163 (2.664–3.66) | 2.418 (2.151–2.685) | 0.826 (0.778–0.874) | 18.572 (17.268–19.876) | 10.828 (10.565–11.09) | 7.31 (6.723–7.898) |

The membrane hydraulic resistance ($R_m$) for RO was about $9.39\times10^{13}$ m$^{-1}$. The $C_{reten,s}$ and $C_{perm,s}$ are the salt concentration in the retentate and permeate. The $R_{feed,s}$, $R_{reten,s}$ and $R_{reten,NOM}$ are the rejections in the feed and retentate for salt and in the retentate for NOM, respectively. The values in parenthesis indicate the 95% confidence interval for the model parameters.

respectively. The values in the parenthesis indicate the 95% confidence interval for the fitted parameters. Experimental data and calculated results were shown to be in good agreement with high correlation $R^2$ of greater than 0.98. For both low and high ionic strengths, the averaged salt rejections in the retentate ($R_{reten,s}$) increased from 94.2% to 94.6% and 71.1% to 81.3% with increased operating pressures. The results corresponded to an increased salt concentration in the retentate with operating pressure, while the ratio between the salt concentration in the retentate ($C_{reten,s}$) and in the feed ($C_{feed,s}$) decreased with ionic strength as a continuous removal of salt concentration in the permeate ($C_{perm,s}$) (values shown in Table 1). The reduction in salt rejection at high ionic strength was caused by reduced charge repulsion between negatively charged membrane and positively charged sodium, enhancing decreased double layer thickness at the membrane surface, thus lowering salt rejection [16]. Solution flux in the presence of salt could enhance a reduction in flux decline. This indicated a decreased in membrane permeability, thus increased membrane hydraulic resistance [6]. The membrane hydraulic resistance with the presence of salt can be determined based on the change in solution flux due to increased salt concentration as described by Mattaraj et al. [16]. Salt effects could cause membrane pore structure due to decreased electrostatic repulsion (or charge neutralization at the membrane surface), causing a change in membrane porosity [21]. The membrane hydraulic resistances in the presence of salt ($R_{m,s}$) were in the range of $1.535\times10^{14}$ to $2.159\times10^{14}$ m$^{-1}$, higher than membrane hydraulic resistances of $9.39\times10^{13}$ m$^{-1}$ (increased by 1.63 to 2.3 times). Based on the combined osmotic pressure and cake filtration model (Eq. (3)), the specific cake resistance ($\alpha_{cake}$) decreased with increased operating pressures, while the specific cake resistance increased with increased ionic strengths. Chellam and Wiesner [14] indicated that the specific cake resistance of particle deposits on crossflow membrane decreased as the initial permeate rate increased. Increased ionic strengths resulted in an increase of specific cake resistance during nanofiltration of NOM [6,16]. At low operating pressures of 551.4 kPa, the specific cake resistances of low and high ionic strengths were about $3.163\times10^{17}$ m kg$^{-1}$ and $1.857\times10^{18}$ m kg$^{-1}$, respectively. This indicated that solution flux decreased as a result of the combined salt and NOM accumulation at the membrane surface. The averaged NOM rejections were relatively high in the trend of increased operating pressures about 97% to 97.1% and 95.1% to 96.4% for low and high ionic strength, respectively. The results suggested that RO could possibly remove most organic carbon fractions in NOM components (i.e. large NOM molecular weight), while some organic carbon fractions (i.e. small NOM molecular weights) could pass through the membrane surface depending on solution chemistry (i.e. high ionic strength). Increased ionic strength decreased NOM rejection, possibly due to more compacted NOM configuration (possibly becoming more a rigid, coiled, and spherical) on nanofiltration membrane [6]. The effect of a thin foulant deposit layer may cause significant flux decline through enhanced salt concentration polarization, thus enhancing salt passage through the membrane surface [22]. After hydrodynamic and chemical cleaning, the non-recoverable resistances ($R_{non\text{-}rec}$) were relatively low in the range of $3.7\times10^{12}$ m$^{-1}$ to $4.91\times10^{12}$ m$^{-1}$ and $4.94\times10^{12}$ m$^{-1}$ to $6.39\times10^{12}$ m$^{-1}$ for low and high ionic strength, respectively.

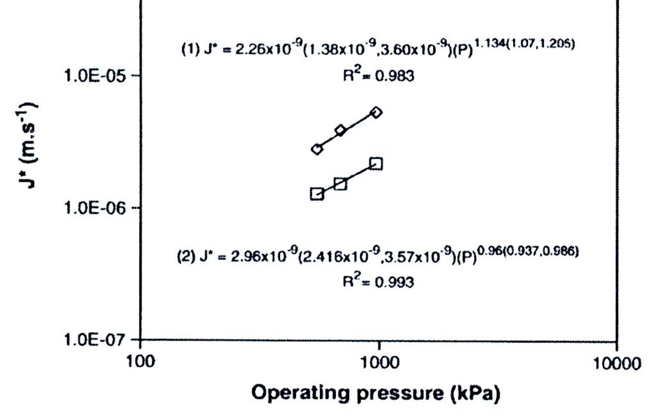

**Fig. 3.** Best fit values of steady-state flux with a function of operating pressure. The values in parenthesis indicate the 95% confidence interval for the fitted parameters.

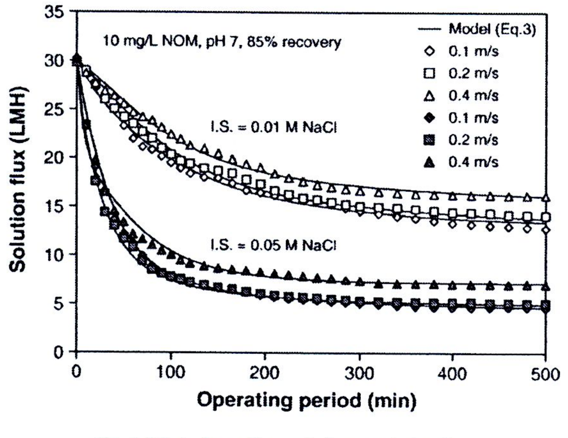

**Fig. 4.** Effect of crossflow velocity on solution flux.

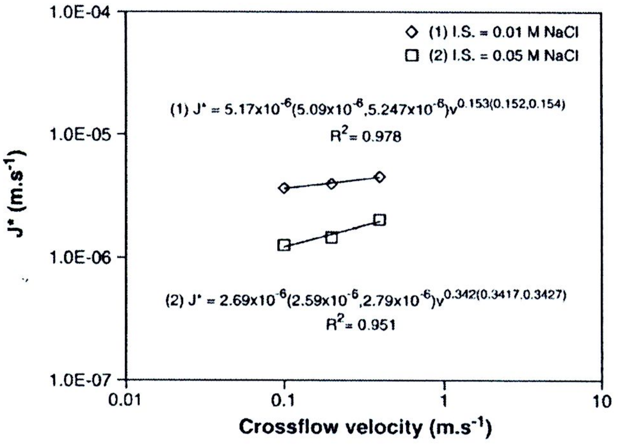

Fig. 5. Best fit values of steady-state flux with a function of crossflow velocity. The values in parenthesis indicate the 95% confidence interval for the fitted parameters.

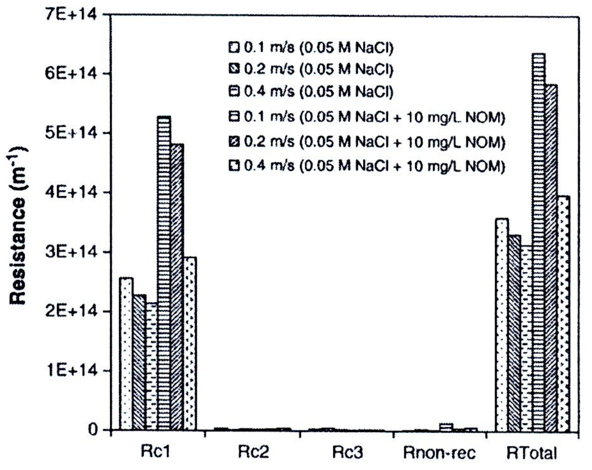

Fig. 6. Resistance parameters due to crossflow velocity effects ($R_m = 0.939 \times 10^{13}\ \mathrm{m}^{-1}$).

### *4.3. Effect of crossflow velocity on normalized flux and rejection*

Fig. 4 exhibits the effect of crossflow velocity on solution flux. The reverse osmosis performance with crossflow velocity effects is shown in Table 1. Increased crossflow velocity showed no significant effect at the initial rate of solution flux, while it enhanced significant effect in flux decline for longer period of filtration. The initial rates of solution flux decline were caused primarily by salt concentration polarization and membrane permeability reduction (i.e. increased membrane hydraulic resistances, $R_{m,s}$). The permeate flux decline of initial stage of colloid crossflow filtration was independent of shear rate [23]. Increased crossflow velocity ranging from 0.1 to 0.4 m s$^{-1}$ increased steady-state solution flux from $3.663 \times 10^{-6}$ m s$^{-1}$ to $4.531 \times 10^{-6}$ m s$^{-1}$ and from $1.264 \times 10^{-6}$ m s$^{-1}$ to $2.031 \times 10^{-6}$ m s$^{-1}$ for low and high ionic strength, respectively. The results corresponded to decrease in flux decline with increased crossflow velocity, thus decreased solute accumulation swept away from the membrane surface at high crossflow velocity. Fig. 5 shows the best fit values of the steady-state flux with a function of crossflow velocity. The log–log plot between the steady-state flux and crossflow velocity exhibits high correlation with a slope of 0.153 (0.152,0.154) and 0.342 (0.3417,0.3427) for low and high ionic strength, respectively. The results suggested system operation in the range of laminar flow condition, previously described by Cheryan [24]. Based on the combined osmotic pressure and cake filtration model, the specific cake resistances ($\alpha_{cake}$) at low ionic strength of 0.01 M NaCl decreased from $2.484 \times 10^{17}$ m kg$^{-1}$ to $0.414 \times 10^{17}$ m kg$^{-1}$ with increasing crossflow velocity. Similar trend was found for solutions having high ionic strength, indicating greater specific cake resistances than those having low ionic strength. Increased salt concentration could reduce charge repulsion at the membrane surface, thus increased $R_{m,s}$ and lowered salt rejection ($R_{reten,s}$) (data shown in Table 2). Salt concentration could present in the cake layer possibly reduced charge repulsion between ionized functional groups on single NOM molecule and between NOM molecules. The results in more compact configuration and NOM cake, suggesting in lower cake porosity. The specific cake resistances described by the Carman–Kozeny equation can be written in terms of cake porosity ($\varepsilon_{cake}$) (−), density ($\rho$) (kg m$^{-3}$), and particle diameter ($d_p$) (m) [25].

$$\alpha_{cake} = \left( \frac{180(1-\epsilon_{cake})^2}{\rho d_p^2 \epsilon_{cake}^3} \right) \tag{5}$$

The above equation indicates that the specific cake resistance is inversely related to $\varepsilon_{cake}^3$ and is linearly corresponded to $(1-\varepsilon_{cake})^2$. Therefore, the equation predicts that decreases in cake porosity result in an increase in the specific cake resistance due to increased NOM cake compaction with the presence of high salt concentration.

A resistance-in-series model was used to determine fouling resistances after hydrodynamic and chemical cleaning. Fig. 6 presents the resistance parameters due to crossflow velocity effects. In the absence of NOM (solution flux not shown), the increased recoverable fouling resistances ($R_{c1}$) were caused by increased salt concentration polarization, while the combined effects of salt concentration and compacted NOM cake enhanced relatively high in recoverable fouling resistances. It was observed that the recoverable fouling resistance ($R_{c1}$) decreased from $5.27 \times 10^{14}$ m$^{-1}$ to $2.92 \times 10^{14}$ m$^{-1}$ with increased crossflow velocity. The parameter showed greater values than other

**Table 2**
Effect of crossflow velocity on reverse osmosis performance.

| Parameters | I.S. = 0.01 M NaCl<br>Crossflow (m s$^{-1}$) | | | I.S. = 0.05 M NaCl<br>Crossflow (m s$^{-1}$) | | |
|---|---|---|---|---|---|---|
| | 0.1 | 0.2 | 0.4 | 0.1 | 0.2 | 0.4 |
| $J_v/J_{vo}$ (−) | 0.429 | 0.473 | 0.540 | 0.152 | 0.171 | 0.234 |
| $J^*$ (m s$^{-1}$) × 10$^6$ | 3.663 (3.615–3.712) | 3.964 (3.906–4.023) | 4.531 (4.465–4.596) | 1.264 (1.211–1.317) | 1.46 (1.431–1.49) | 2.031 (1.945–2.118) |
| $C_{reten,s}$ (M) | 0.0561 | 0.0572 | 0.0597 | 0.1316 | 0.1376 | 0.1325 |
| $C_{perm,s}$ (M) | 0.0036 | 0.0038 | 0.0035 | 0.0309 | 0.0291 | 0.0360 |
| $R_{feed,s}$ (%) | 67.9 | 64.0 | 64.2 | 39.7 | 42.7 | 36.1 |
| $R_{reten,s}$ (%) | 93.6 | 93.4 | 94.1 | 76.5 | 78.9 | 72.8 |
| $R_{reten,NOM}$ (%) | 95.2 | 95.3 | 96.2 | 94.5 | 95.4 | 95.2 |
| $R_{m,s}$ (m$^{-1}$) × 10$^{-14}$ | 2.081 | 1.109 | 1.069 | 1.321 | 1.093 | 1.339 |
| $R_{non\text{-}rec}$ (m$^{-1}$) × 10$^{-14}$ | 0.0375 | 0.0501 | 0.011 | 0.1312 | 0.0462 | 0.0529 |
| $\alpha_{cake}$ (m kg$^{-1}$) × 10$^{-17}$ | 2.484 (2.335–2633) | 0.681 (0.574–0789) | 0.414 (0.345–0.483) | 17.545 (17.065–18.02) | 14.33 (13.49–15.174) | 13.94 (12.69–15.18) |

The membrane hydraulic resistance ($R_m$) for RO was about $9.39 \times 10^{13}$ m$^{-1}$. Initial solution flux is about 30 LMH. The values in parenthesis indicate the 95% confidence interval for the model parameters.

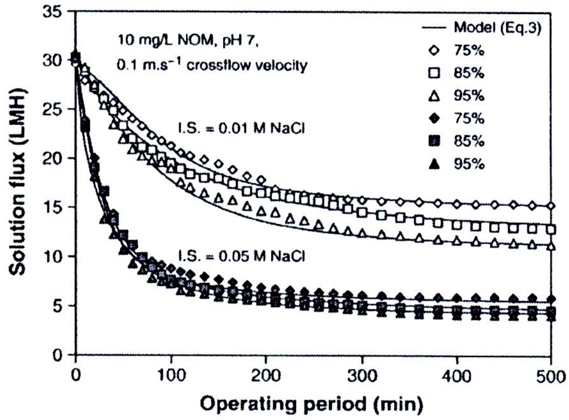

Fig. 7. Effect of recovery on solution flux.

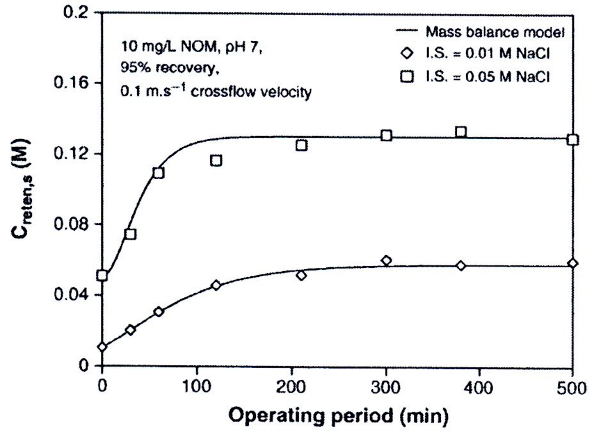

Fig. 8. Effect of ionic strength on salt concentration in the retentate ($C_{reten,s}$).

resistance parameters ($R_{c2}$, $R_{c3}$, and $R_{non\text{-}rec}$) ranging relatively low from $1.1\times10^{12}$ to $5.44\times10^{12}$ m$^{-1}$. System cleaning (i.e. hydrodynamic and chemical cleaning) could effectively remove salt concentration and adsorbed NOM components from the membrane surface and/or pores, suggesting less fouling resistances from the membrane surface due to large NOM molecular weight fractions removed with relatively high NOM rejection.

### 4.4. Effect of recovery on normalized flux and rejection

Fig. 7 illustrates the effect of recovery on solution flux. The reverse osmosis performance is tabulated in Table 3. Increased recovery from 75% to 95% resulted in greater flux decline, possibly caused by increased solute accumulation at the membrane surface. Solution flux decline was more pronounced at the highest recovery of 95%. Solutions having high ionic strength of 0.05 M NaCl showed greater flux decline than those having low ionic strength of 0.01 M NaCl. With increasing recovery from 75% to 95%, normalized flux decreased from 0.519 to 0.369 and 0.195 to 0.136 for low and high ionic strength, respectively. The rate of flux decline increased with increasing recovery because of the increase of solute concentration on the membrane surface caused by enhancing the convective transport of mass to the membrane surface [15]. The salt rejections in the retentate ($R_{reten,s}$) decreased with increasing recovery as a result of increased salt concentration at the membrane surface. Averaged salt rejections decreased from 93.4%–94.6% to 72.6%–81.2% with increased ionic strengths, while averaged NOM rejections were relatively high ranging from 94.4% to 95.9% (possibly due to large molecular weight fractions). Fig. 8 shows the effect of ionic strength on salt concentration in the retentate ($C_{reten,s}$). Dot points represent the experimental results during filtration experiments, while solid lines demonstrate the mathematical model from mass balance equation, previously studied by Mattaraj et al. [16]. From this figure, solutions having high ionic strength of 0.05 M NaCl showed greater values than those having low ionic strength of 0.01 M NaCl. The steady-state salt concentrations for high ionic strength exhibited greater values (about 2.2 times) than those for low ionic strength. Recovery effects can enhance NOM concentration on the membrane surface, suggesting increased specific cake resistances. Increased recovery from 75% to 95% increased specific cake resistances from $1.02\times10^{17}$ m kg$^{-1}$ to $4.405\times10^{17}$ m kg$^{-1}$ and $7.222\times10^{17}$ m kg$^{-1}$ to $3.242\times10^{18}$ m kg$^{-1}$ for low and high ionic strengths, respectively. The specific cake resistance was the highest values at high ionic strength of 0.05 M NaCl at high recovery of 95%. The results suggested the combined effects of salt concentration and NOM accumulation by adopting more compacted NOM molecules at the membrane surface. Fig. 9 presents the best fit values of specific cake resistance ($\alpha_{cake}$) with a function of recovery. The correlation was found to be in good agreement with relatively high correlation ($R^2$>0.99). The slopes of the graph were ranged from 6.207(5.728,6.812) to 6.367(6.118,6.577) with 95% confidence interval. After system cleaning, the non-recoverable resistances ($R_{non\text{-}rec}$) showed relatively high at high ionic strength of 0.05 M NaCl, when compared the values with low ionic strength. This suggested that NOM cake accumulation could result in a highly compacted fouling layer at the membrane surface.

### 4.5. Relationship among operating conditions and ionic strengths on model parameters

Membrane system operation and solution chemistry could significantly affect reverse osmosis performance and model parameters (i.e.

**Table 3**
Effect of recovery on reverse osmosis performance.

| Parameters | I.S. = 0.01 M NaCl<br>Recovery (%) | | | I.S. = 0.05 M NaCl<br>Recovery (%) | | |
|---|---|---|---|---|---|---|
| | 75 | 85 | 95 | 75 | 85 | 95 |
| $J_v/J_{vo}$ (−) | 0.519 | 0.429 | 0.369 | 0.195 | 0.152 | 0.136 |
| $J^*$ (m s$^{-1}$) × $10^6$ | 4.289 (4.181–4.396) | 3.663 (3.615–3.712) | 3.188 (3.144–3.233) | 1.542 (1.502–1.583) | 1.264 (1.211–1.317) | 1.194 (1.136–1.252) |
| $C_{reten,s}$ (M) | 0.0569 | 0.0561 | 0.0575 | 0.1302 | 0.1316 | 0.129 |
| $C_{perm,s}$ (M) | 0.0031 | 0.0036 | 0.0038 | 0.0245 | 0.0309 | 0.0354 |
| $R_{feed,s}$ (%) | 70.3 | 67.9 | 64.1 | 49.3 | 39.7 | 30.4 |
| $R_{reten,s}$ (%) | 94.6 | 93.6 | 93.4 | 81.2 | 76.5 | 72.6 |
| $R_{reten,NOM}$ (%) | 95.9 | 95.2 | 95.0 | 95.7 | 94.5 | 194.4 |
| $R_{m,s}$ (m$^{-1}$) × $10^{-14}$ | 1.179 | 2.081 | 0.9834 | 1.025 | 1.321 | 1.457 |
| $R_{non\text{-}rec}$ (m$^{-1}$) × $10^{-14}$ | 0.0033 | 0.0375 | 0.0396 | 0.9046 | 0.1312 | 0.9090 |
| $\alpha_{cake}$ (m kg$^{-1}$) × $10^{-17}$ | 1.0201 (0.84–1.20) | 2.484 (2.335–2.633) | 4.405 (4.175–4.635) | 7.222 (6.81–7.633) | 17.545 (17.065–18.02) | 32.415 (28.75–36.08) |

The membrane hydraulic resistance ($R_m$) for RO was about $9.39\times10^{13}$ m$^{-1}$. Initial solution flux is about 30 LMH. The values in parenthesis indicate the 95% confidence interval for the model parameters.

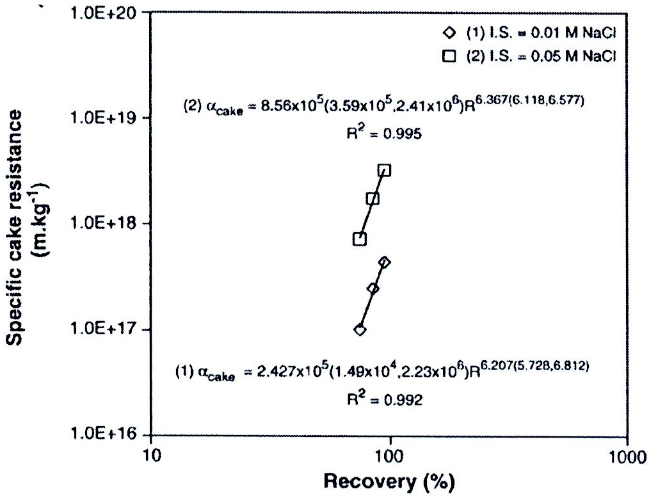

**Fig. 9.** Best fit values of specific cake resistance ($\alpha_{cake}$) with a function of recovery. The values in parenthesis indicate the 95% confidence interval for the fitted parameters.

steady-state flux, $J^*$ and specific cake resistance, $\alpha_{cake}$), which were evaluated based on the combined osmotic pressure and cake filtration model (Eq. (3)). The steady-state fluxes and specific cake resistances were previously characterized to depend on membrane operating pressure ($\Delta P$), crossflow velocity ($v$), recovery ($R$), and feed ionic strength ($I$), while solution pH of 7 and NOM concentration of 10 mg L$^{-1}$ were maintained constant for all filtration experiments. The fouling in membrane pores caused by NOM molecular size was assumed to be less significant effect due to tight RO membrane with relatively high NOM rejection and low non-recoverable fouling ($R_{\text{non-rec}}$). The model parameters can be determined using an empirical relationship with a function of operating conditions and ionic strength ($J^* = a\Delta P^b v^c R^d I^e$, where $a$, $b$, $c$, $d$, and $e$ are the empirical constants). This empirical relationship can be rearranged in the log-log scale as follows:

$$\log J^* = \log a + b\log\Delta P + c\log v + d\log R + e\log I. \quad (6)$$

A multiple linear regression using $\log J^*$ (m s$^{-1}$) as the dependent variable and $\log\Delta P$ (kPa), $\log v$ (m s$^{-1}$), $\log R$ (−) and $\log I$ (M) as the dependent variables produces an intercept [equal to $\log a$] and slopes equal to $b$, $c$, $d$, and $e$. Based on the statistical analysis on experimental data, the empirical equation can be written as follow:

$$J^* = 9.12\times10^{-8}\Delta P^{1.04}v^{0.223}R^{-1.18}I^{-0.590}(R^2 = 0.989). \quad (7)$$

The slopes for operating pressure, crossflow velocity, recovery, and ionic strength are 1.04, 0.223, −1.18, and −0.590, respectively. The correlation coefficient is relatively high with $R^2$ of 0.989. The 95% confidence interval for $a$, $b$, $c$, $d$, and $e$ ranged from ($7.762\times10^{-8}$, $1.072\times10^{-7}$), (1.01,1.08), (0.219,0.229), (−1.16,−1.21), and (−0.58,−0.601), respectively. The negative values indicate a decreased steady-state flux with recovery ($d = -1.18$) and ionic strength ($e = -0.590$), while the positive values suggest an increased in steady-state flux with operating pressure ($b = 1.04$) and crossflow velocity ($c = 0.223$). The empirical constants ($b$) and ($c$) indicate a pressure-dependent steady-state flux and system operation under laminar flow condition, respectively. Recovery effect and ionic strength showed the worst flux decline, indicating negative values for empirical constants. Increased high ionic strength resulted in a reduction of electrostatic charge repulsion (reducing charge interaction between a negatively charged NOM macromolecule and positively charged salt, thus causing a densely packed cake layer, NOM accumulation and increasing permeate flow resistance) [26].

Specific cake resistance, $\alpha_{cake}$, (m kg$^{-1}$) obtained from Eq. (3) can be developed with a function of operating condition and ionic strength ($\alpha_{cake} = f\Delta P^g v^h R^i I^j$, where $f$, $g$, $h$, $i$, and $j$ are the empirical constants). The statistical analysis with multiple linear regressions can be successfully used to evaluate empirical constants in the log–log scale relationship. The empirical equation of specific cake resistance can be written as follows:

$$\alpha_{cake} = 7.943\times10^{12}\Delta P^{-2.03}v^{-0.739}R^{6.29}I^{1.37}(R^2 = 0.94). \quad (8)$$

The 95% confidence interval for $f$ is in the range of $1.995\times10^{12}$ and $1.585\times10^{13}$. The slopes for $g$, $h$, $i$, and $j$ are −2.03(−1.98,−2.07), −0.739(−0.706,−0.779), 6.29(6.15,6.47), and 1.37(1.34,1.41), respectively. The values in parenthesis were determined within 95% confidence interval. The correlation coefficient is relatively high with $R^2$ of 0.94. The results showed negative values for operating pressures ($g = -2.03$) and crossflow velocity ($h = -0.739$), indicating decreased specific cake resistances. Similar observation was observed by Chellam and Wiesner [14]. They indicated that the specific resistance of particle deposits on membranes decreased as the initial permeation rate increased [14]. The increase in $\alpha_{cake}$ can be observed with positive values of recovery ($i = 6.29$) and ionic strength ($j = 1.37$). The results corresponded to the highest specific cake resistance with solutions having high ionic strength at recovery of 95%. Both empirical equations with combined operating conditions and feed solution chemistry can be successfully determined to interpret reverse osmosis performance.

## 5. Conclusions

The performance of crossflow reverse osmosis process of NOM with different solution chemistry was analyzed using resistance-in-series model, the combined osmotic and cake filtration model, and the empirical model. The empirical equations for steady-state flux ($J^*$) and specific cake resistances ($\alpha_{cake}$) were successfully developed with combined dependent variables of operating pressure ($\Delta P$), crossflow velocity ($v$), recovery ($R$). Steady-state flux increased with increased operating pressure and crossflow velocity, while the flux decreased with increased recovery effects and ionic strength. The experimental results indicated a pressure-dependent steady-state flux under laminar flow condition. Flux decline at the initial stage of filtration was due to salt concentration polarization affecting membrane permeability reduction. The specific cake resistance was inversely related to increased operating pressure and crossflow velocity ($\alpha_{cake} = 7.943\times10^{12}\Delta P^{-2.03}v^{-0.739}R^{6.29}I^{1.37}$), while the specific cake resistance increased linearly with recovery effects and ionic strength. Recovery with high ionic strength resulted in the significant flux decline, thus increased specific cake resistance (i.e. lowering cake porosity) due to combined salt concentration polarization and NOM cake compaction near the membrane surface.

*Nomenclature*

| | |
|---|---|
| $a$ to $j$ | empirical constants |
| $A_m$ | membrane area (m$^2$) |
| $C_{feed,s}$ | salt concentration in the feed (mol L$^{-1}$) |
| $C_{perm,s}$ | salt concentration in the permeate (mol L$^{-1}$) |
| $C_{reten,NOM}$ | NOM concentration in the retentate (kg m$^{-3}$) |
| $C_{reten,s}$ | salt concentration in the retentate (mol L$^{-1}$) |
| $d_p$ | particle diameter (m) |
| $I$ | ionic strength (M) |
| $J_o$ | clean water flux (L m$^{-2}$h$^{-1}$, LMH) |
| $J_v$ | solution flux (L m$^{-2}$h$^{-1}$, LMH) |
| $J^*$ | steady-state flux associated with back-transport resulting from crossflow (LMH) |
| $m_{cake}$ | cake mass (kg) |
| $M_n$ | number-averaged NOM molecular weight (Da) |
| $M_w$ | weight-averaged NOM molecular weight (Da) |

| | |
|---|---|
| $\Delta P$ | transmembrane pressure (kPa) |
| $Q_{feed}$ | flow in the feed (mL min$^{-1}$) |
| $Q_{perm}$ | flow in the permeate (mL min$^{-1}$) |
| $R$ | recovery (−) |
| $R_c$ | cake resistance (m$^{-1}$) |
| $R_{c1}$ | fouling resistance by concentration polarization and/or cake formation (m$^{-1}$) |
| $R_{c2}$ | recoverable resistant fouling caused by salt layer (m$^{-1}$) |
| $R_{c3}$ | reversibly adsorbed NOM layer resistance (m$^{-1}$) |
| $R_f$ | hydraulic resistance of fouling layer (m$^{-1}$) |
| $R_{feed,s}$ | salt rejection in the feed (−) |
| $R_m$ | membrane hydraulic resistance (m$^{-1}$) |
| $R_{m,s}$ | membrane resistance in the presence of salt (m$^{-1}$) |
| $R_{non\text{-}rec}$ | non-recoverable resistance (m$^{-1}$) |
| $R_{reten,s}$ | rejection in the retentate for salt (−) |
| $R_{reten,NOM}$ | rejection in the retentate for NOM (−) |
| $R_{Total}$ | total hydraulic resistance (m$^{-1}$) |
| $t$ | operating time (min) |
| $v$ | crossflow velocity (m s$^{-1}$) |
| $V$ | permeate volume (L) |

*Greek letters*

| | |
|---|---|
| $\alpha_s$ | correlation between osmotic pressure and salt concentration (kPa L mol$^{-1}$) |
| $\alpha_{cake}$ | specific cake resistance (m kg$^{-1}$) |
| $\beta_s$ | salt concentration polarization (−) |
| $\varepsilon_{cake}$ | cake porosity (−) |
| $\rho$ | density (kg m$^{-3}$) |
| $\mu$ | dynamic viscosity (kg m$^{-1}$s$^{-1}$) |
| $\pi$ | osmotic pressure (kPa) |
| $\sigma$ | osmotic reflection coefficient (−) |

## Acknowledgements

The authors would like to thank the Thailand Research Fund (TRF) for TRF senior research scholar grant (No. RTA5080014) and the Commission on Higher Education, Thailand, for financial support. We also would like to thank the Department of Chemical Engineering, Faculty of Engineering, Ubon Rachathani University, and the National Center of Excellence for Environmental and Hazardous Waste Management, Ubon Ratchathani University, Ubonratchathani, Thailand, for all experimental equipments applied in this research.

## References

[1] F. Wang, V.V. Tarabara, Coupled effects of colloidal deposition and salt concentration polarization on reverse osmosis membrane performance, J. Membr. Sci. 293 (2007) 111–123.

[2] R. Molinari, P. Argurio, L. Romeo, Studies on interactions between membranes (RO and NF) and pollutants (SiO$_2$, NO$_3^-$, Mn$^{++}$, and humic acid) in water, Desalination 138 (2001) 271–281.

[3] A.I. Schafer, A.G. Fane, T.D. Waite, Fouling effects on rejection in the membrane filtration of natural waters, Desalination 131 (2000) 215–224.

[4] W. Yuan, A.L. Zydney, Effects of solution environment on humic acid fouling during microfiltration, Desalination 122 (1999) 63–76.

[5] J. Cho, G. Amy, J. Pellegrino, Membrane filtration of natural organic matter: initial comparison of rejection and flux decline characteristics with ultrafiltration and nanofiltration membranes, Water Res. 33 (1999) 2517–2526.

[6] J.E. Kilduff, S. Mattaraj, G. Belfort, Flux decline during nanofiltration of naturally-occurring dissolved organic matter: effects of osmotic pressure, membrane permeability, and cake formation, J. Membr. Sci. 239 (1) (2004) 39–53.

[7] M. Elimelech, X. Zhu, A.E. Childress, S. Hong, Role of membrane surface morphology in colloidal fouling of cellulose acetate and composite aromatic polyamide reverse osmosis membranes, J. Membr. Sci. 127 (1997) 101–109.

[8] A.R. Costa, M.N. de Pinho, Effect of membrane pore size and solution chemistry on the ultrafiltration of humic substances solutions, J. Membr. Sci. 255 (2005) 49–56.

[9] A.I. Schafer, A. Pihlajamaki, A.G. Fane, T.D. Waite, M. Nystrom, Natural organic matter removal by nanofiltration: effects of solution chemistry on retention of low molar mass acids versus bulk organic matter, J. Membr. Sci. 242 (2004) 73–85.

[10] C.Y. Tang, Y.-N. Kwon, J.O. Leckie, Fouling of reverse osmosis and nanofiltration membranes by humic acid—effects of solution composition and hydrodynamic conditions, J. Membr. Sci. 290 (2007) 86–94.

[11] L. Paugam, S. Taha, G. Dorange, P. Jaouen, F. Quemeneur, Mechanism of nitrate ions transfer in nanofiltration depending on pressure, pH, concentration, and medium composition, J. Membr. Sci. 231 (2004) 37–46.

[12] Z. Wang, Y. Zhao, J. Wang, S. Wang, Studies on nanofiltration membrane fouling in the treatment of water solutions containing humic acids, Desalination 178 (2005) 171–178.

[13] X. Zhu, M. Elimelech, Colloidal fouling of reverse osmosis membranes: measurements and fouling mechanisms, Environ. Sci. Technol. 31 (1997) 3654–3662.

[14] S. Chellam, M.R. Wiesner, Particle back-transport and permeate flux behavior in crossflow membrane filters, Environ. Sci. Technol. 31 (1997) 819–824.

[15] J.E. Kilduff, S. Mattaraj, M. Zhou, G. Belfort, Kinetics of membrane flux decline: the role of natural colloids and mitigation via membrane surface modification, J. Nanopart. Res. 7 (2005) 525–544.

[16] S. Mattaraj, C. Jarausutthirak, R. Jiraratananon, A combined osmotic pressure and cake filtration model for crossflow nanofiltration of natural organic matter, J. Membr. Sci. 322 (2008) 475–483.

[17] N.R. Draper, H. Smith, Applied Regression Analysis, 3rd editionWiley Interscience0-471-17082-8, 1998.

[18] J.E. Kilduff, S. Mattaraj, A. Wigton, M. Kitis, T. Karanfil, Effects of reverse osmosis isolation on reactivity of naturally occurring dissolved organic matter in physicochemical processes, Water Res. 38 (4) (2004) 1026–1036.

[19] C. Jarusutthirak, S. Mattaraj, R. Jiraratananon, Factors affecting nanofiltration performances in natural organic matter rejection and flux decline, Sep. Purif. Technol. 58 (2007) 68–75.

[20] Y.-P. Chin, G. Aiken, E. O'Loughlin, Molecular weight, polydispersity, and spectroscopic properties of aquatic humic substances, Environ. Sci. Technol. 28 (1994) (1994) 1853–1858.

[21] M.R. Teixeira, M.J. Rosa, M. Nystrom, The role of membrane charge on nanofiltration performance, J. Membr. Sci. 265 (2005) 160–166.

[22] E.M.V. Hoek, M. Elimelech, Cake-enhanced concentration polarization: a new fouling mechanism for salt-rejecting membranes, Environ. Sci. Technol. 37 (2003) 5581–5588.

[23] S. Hong, R.S. Faibish, M. Elimelech, Kinetics of permeate flux decline in crossflow membrane filtration of colloidal suspensions, J. Colloid Interface Sci. 196 (1997) 267–277.

[24] M. Cheryan, Ultrafiltration and Microfiltration Handbook, Technomic Publishing Co., Inc., Lancaster, PA, 1998.

[25] M.R. Wiesner, P. Aptel, Mass transport and permeate flux and fouling in pressure-driven processes, in: J. Mallevialle, P.E. Odendaal, M.R. Wiesner (Eds.), Water Treatment Membrane Processes, McGraw-Hill, New York, 2009, ISBN 0-07-0019-7-00151996.

[26] A. Braghetta, F.A. DiGiano, W.P. Ball, NOM accumulation at NF membrane surface: impact of chemistry and shear, J. Environ. Eng. ASCE 124 (11) (1998) 1087–1098.

Separation and Purification Technology 72 (2010) 186–193

Contents lists available at ScienceDirect

Separation and Purification Technology

journal homepage: www.elsevier.com/locate/seppur

# Ozonation of dye wastewater by membrane contactor using PVDF and PTFE membranes

Sahawet Bamperng[a], Tarakorn Suwannachart[a], Supakorn Atchariyawut[b], Ratana Jiraratananon[a,*]

[a] *Department of Chemical Engineering, King Mongkut's University of Technology Thonburi, Bangkok 10140, Thailand*
[b] *WorleyParsons (Thailand) Limited, Sriracha, Chonburi 20110, Thailand*

ARTICLE INFO

*Article history:*
Received 2 November 2009
Received in revised form 2 February 2010
Accepted 3 February 2010

*Keywords:*
Decolorization
Dyes
Membrane contactor
Ozonation
PTFE membrane
PVDF membrane

ABSTRACT

This work aimed to study the decolorization of dye wastewater by ozonation membrane contacting process. Three different dyes, i.e., Direct red 23, Acid blue 113 and Reactive red 120 were selected to be used in this work. The effects of operating parameters which were gas and liquid velocity, liquid phase temperature, dye auxiliary reagents were investigated along with the mass transfer study. Membranes used in this work were PVDF and PTFE hollow fiber membranes. The ozone mass transfer performance and long term performance in ozonation by these two different types of membrane were studied. In addition, decolorization performance and kinetic study of ozonation in the batch system with various operating parameters and dye types were investigated.

From the results, the ozone mass transfer increased with increasing liquid velocity, liquid phase temperature, and with the presence of $Na_2CO_3$. On the contrary, the ozone flux was not influenced by gas velocity. PVDF membrane provided higher ozone flux than PTFE, but PTFE membrane gave more stable and higher flux than PVDF for a long operation period. The ozone flux of different types of dye was in the following order: Direct red 23 > Reactive red 120 > Acid blue 113. Conversely, the decolorization performance of Acid blue 113 was higher than those of Direct red 23 and Reactive red 120. Kinetic analysis showed that decolorization of dyes followed the first order kinetics and the rate constants were in the following order: Acid blue 113 > Reactive red 120 > Direct red 23.

## 1. Introduction

Textile industry generates large amount of wastewater which varies greatly in quantity and compositions. Treatment of textile wastewater by chemical coagulation and biological methods can usually reduce biological oxygen demand (BOD) and chemical oxygen demand (COD) satisfactorily, except for the removal of dye color. A direct solution to this problem is treatment by chemical oxidation. Bouwers [1] reported the comparison between different oxidants such as $Cl_2$, $H_2O_2$, $KMnO_4$ and $O_3$. It was found that ozone generally produced non-toxic breakdown products which were finally converted to $CO_2$ and $H_2O$ if the conditions were drastic enough. Excess ozone decomposes after a few minutes to oxygen without harmful residue, as opposed other inorganic oxidants.

Ozone is a powerful oxidant for water and wastewater treatment. Depending on the pH of the liquid phase, ozone may react with a great number of organic compounds by direct oxidation as molecular ozone or by indirect reaction through formation of secondary oxidants like hydroxyl radical [2]. Conventional ozone contacting methods include bubble column, impellers, and others. The conventional reactors to perform ozonation mentioned above are easy to set up and operate as reported in the literature [3–5]. However, there are the problems that hinder the use of those techniques such as, flooding, uploading, and foaming. Further study is needed to enhance the mass transfer rate and to avoid those problems. Due to the low solubility of ozone in water a high contact area would increase the ozone transfer from the gas to liquid phase. A recent study of Chu et al. [6] on the application of microbubble technology in ozonation process reported that a specific surface area, mass transfer, and oxidation of ozone were enhanced. However, they concluded that the total energy cost should be further analysed.

As far as the specific surface area for mass transfer is concerned, the application of a bubbleless membrane contactor system for ozonation is the potential approach, especially when the hollow fibers are used. A gas–liquid membrane contactor is a membrane process in which the hydrophobic porous membrane acts as a barrier separating gas phase and liquid phase. The mass transfer in a membrane contactor for absorption gas into the liquid phase consists of a transport of the interested gas from the bulk of gas phase to the interface between gas phase and a membrane, transport of gas through the membrane pores, and the dissolution of a gas

---

* Corresponding author. Tel.: +66 0 2470 9222; fax: +66 0 2428 3534.
*E-mail address:* ratana.jir@kmutt.ac.th (R. Jiraratananon).

1383-5866/$ – see front matter © 2010 Elsevier B.V. All rights reserved.
doi:10.1016/j.seppur.2010.02.006

**Nomenclature**

| | |
|---|---|
| $a$ | parameter in Eq. (3) |
| $C$ | concentration of dye at any reaction times, mol m$^{-3}$ |
| $C_0$ | initial dye concentration, mol m$^{-3}$ |
| $D$ | diffusion coefficient of ozone in the liquid phase, m$^2$ s$^{-1}$ |
| $D_A$ | continuum gas diffusion coefficient, m$^2$ s$^{-1}$ |
| $D_K$ | Knudsen diffusion coefficient, m$^2$ s$^{-1}$ |
| $D_{g,eff}$ | effective diffusion coefficient of gas in the pores, m$^2$ s$^{-1}$ |
| $d_i$ | inside diameter of membrane, m |
| $d_{ln}$ | logarithmic mean diameter of membrane, m |
| $d_o$ | outside diameter of membrane, m |
| E | enhancement factor |
| $H$ | Henry's constant |
| $K_{ol}$ | overall mass transfer coefficient, m s$^{-1}$ |
| $k$ | pseudo-first-order rate constant, min$^{-1}$ |
| $k_l$ | individual mass transfer coefficient of liquid phase, m s$^{-1}$ |
| $k_m$ | individual mass transfer coefficient of membrane, m s$^{-1}$ |
| $k_g$ | individual mass transfer coefficient of gas phase, m s$^{-1}$ |
| $L$ | effective length of the membrane module, m |
| $l_m$ | thickness of the hollow fiber, m |
| $R$ | gas constant, 8.314 Pa m$^3$ mol$^{-1}$ K$^{-1}$ |
| $Re$ | Reynolds number |
| $r_p$ | membrane pore size, m |
| $Sc$ | Schmidt number |
| $Sh$ | Sherwood number |
| $T$ | temperature, K |
| $t$ | time, min |
| $V$ | velocity, m s$^{-1}$ |
| *Greek letters* | |
| $\alpha$ | parameter in Eq. (3) |
| $\beta$ | parameter in Eq. (3) |
| $\varepsilon_m$ | membrane porosity |
| $\sigma_{AB}$ | characteristic length, Å |
| $\tau_m$ | membrane tortuosity |
| $\Omega_D$ | collision integral |

component into a liquid (with or without the reaction). The mass transfer in the hollow fiber membrane contacting process is shown in Fig. 1. Membrane contactors have been widely studied for the process such as liquid–liquid extraction, gas–liquid absorption, for example, the absorption of $CO_2$ [7,8].

Most studies on the application of membrane contactors for ozonation involve liquid feeds which were solutions of NOM (natural organic matter) [9,10] and humic substance [11]. We recently published our work [12] on ozonation membrane contacting system for dye wastewater treatment using PVDF (polyvinylidene fluoride) hollow fiber membrane (UMP-153, Pall Corperation). In that study the ozone mass transfer, the effects of HRT (hydraulic retention time) on color removal were investigated.

The polymer membranes which have been used as contactors are usually made from PP (polypropylene), PVDF (polyvinylidene fluoride), and PTFE (polytetrafluoroethylene). In general, the hydrophobicity is in the order of PTFE > PVDF > PP [13]. For ozonation by membrane contactors it is important that the membranes are resistant to ozone which is a strong oxidant. Mori et al. [14] reported that the ozone resistance was in the following order; PTFE > PVDF > PE (Polyethylene). However, in previous research [9–12] only PVDF membranes were selected for the study and there has been no investigation on the comparison of the long-term performance of PVDF and PTFE membranes for ozonation of dye wastewater. Accordingly, the main objective of this work was to study the performance of both PVDF and PTFE membranes for decolorization of dye wastewater by ozonation. Three types of azo dye, i.e., Reactive red 120, Direct red 23, and Acid blue 113 were selected for the study. The effects of auxiliary reagents (NaCl, $Na_2SO_4$) were also investigated. In addition, this study also included the reaction kinetics of these dyes with ozone.

## 2. Basic principle of mass transfer in gas–liquid membrane contactor

The mass transfer mechanism in the gas–liquid membrane contacting process can be described by using the resistance-in-series model. Fig. 1 demonstrates the mass transport of gas in dry operating mode of membrane contactors, i.e., diffusion from the bulk gas through the membrane pores and dissolution in the liquid absorbent. The resistance-in-series model can be expressed as Eq. (1).

$$\frac{1}{K_{ol}} = \frac{1}{Ek_l} + \frac{d_o}{Hk_m d_{ln}} + \frac{d_o}{Hk_g d_i} \tag{1}$$

where $K_{ol}$ is the overall mass transfer coefficient based liquid phase (m/s), $E$ is the enhancement factor which is included to account for the effect of the reaction. $k_l$, $k_m$, $k_g$ are the individual mass transfer coefficients of the liquid phase, membrane and gas phase, respectively. $d_i$, $d_o$, $d_{ln}$ are the inner, outer and logarithmic mean diameters of the fibers, respectively. $H$ represents Henry's constant. For the dissolution of ozone in water at 295 K, the Henry's constant is 3.823 $(mg/l)_g/(mg/l)_l$ [12].

In the operation of a membrane contactor, either the gas phase or liquid phase can be fed through the shell side or tube side of the hollow fiber membrane module. In our work liquid was fed through the tube while gas was fed into the shell side. The well-known Graetz-Lévêque mass transfer correlation was widely used to predict the tube side mass-transfer coefficient [7,15];

$$Sh = \frac{k_l d_i}{D} = 1.62\left(\frac{d_i^2 V}{LD}\right)^{1/3} \tag{2}$$

where $Sh$ is Sherwood number, $D$ is the diffusion coefficient, $L$ is the tube length and $V$ is the fluid velocity.

Many correlations have been proposed to determine the shell side mass transfer coefficient [15–17]. However, each of them is applicable to a certain limited range of operation. In general, it can be expressed in the following form:

$$Sh = aRe^{\alpha}Sc^{\beta} \tag{3}$$

where $Re$ and $Sc$ are Reynolds and Schmidt numbers, respectively. The membrane mass transfer coefficient can be calculated independently using the pore structure properties [18]:

$$k_m = \frac{D_{g,eff}\varepsilon_m}{\tau_m l_m} \tag{4}$$

where $\varepsilon_m$ is the membrane porosity, $l_m$ is the membrane thickness, and $\tau_m$ is tortuosity which can be calculated from the following empirical correlation [19].

$$\tau_m = \frac{(2-\varepsilon_m)^2}{\varepsilon_m} \tag{5}$$

Eq. (5) is recommended and has been successfully employed for polymer membrane manufactured by phase inversion method. In Eq. (4), $D_{g,eff}$ is the diffusion coefficient of gas in the membrane

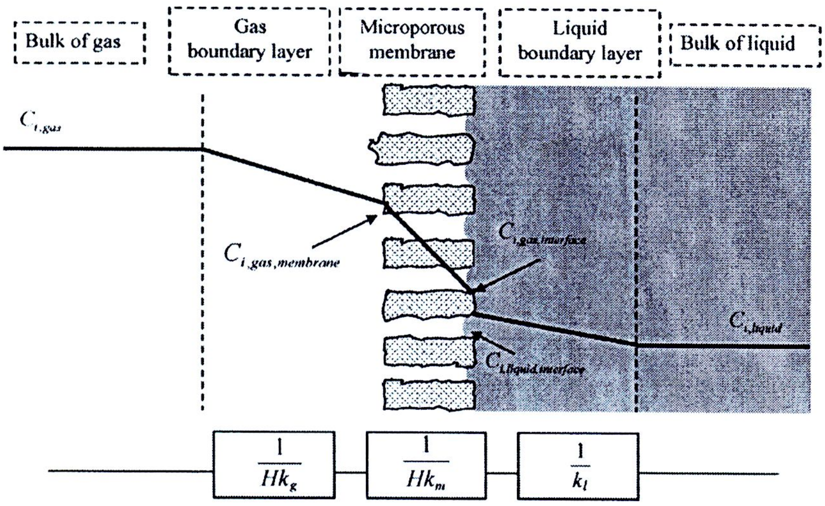

**Fig. 1.** Mass transfer regions and resistance-in-series in non-wetted membrane contactor.

pores governed by both the continuum and Knudsen diffusion coefficients, and is expressed by [20]:

$$\frac{1}{D_{\mathrm{g,eff}}} = \frac{1}{D_{\mathrm{A}}} + \frac{1}{D_{\mathrm{K}}} \tag{6}$$

where $D_{\mathrm{A}}$ is the continuum gas diffusion coefficient, while $D_{\mathrm{K}}$ is the Knudsen diffusion coefficient which can be expressed as:

$$D_{\mathrm{A}} = \frac{0.00266T^{3/2}}{PM_{\mathrm{AB}}^{1/2}\sigma_{\mathrm{AB}}^{2}\Omega_{\mathrm{D}}} \tag{7}$$

$$D_{\mathrm{K}} = \frac{2r_{\mathrm{p}}}{3}\sqrt{\frac{8RT}{\pi M_{\mathrm{A}}}} \tag{8}$$

In Eqs. (7) and (8), $T$ is the absolute temperature (K), $P$ is the pressure (bar), $M_{\mathrm{AB}} = 2\left[1/M_{\mathrm{A}} + 1/M_{\mathrm{B}}\right]^{-1}$, $M_{\mathrm{A}}$ and $M_{\mathrm{B}}$ are molecular weights of gas A and B, $\sigma_{\mathrm{AB}}$ is the characteristic length (Å), $\Omega_{\mathrm{D}}$ is the collision integral, $r_{\mathrm{p}}$ is the membrane pore radius, $R$ is the gas constant. Therefore, each mass transfer coefficient in Eq. (1) can be evaluated as outlined above provided that the physical properties of the membrane and those of ozone gas and dye solution are available. $K_{\mathrm{ol}}$ is then obtained. Alternatively, $K_{\mathrm{ol}}$ may be calculated from the experimental data [8] which also requires the value of Henry's constant of the ozone–dye system.

## 3. Experimental

The hollow fiber polyvinylidenefluoride (PVDF) membrane supplied by Memcor Australia (South Windsor, New South Wales, Australia) and polytetrafluoroethylene (PTFE) membrane provided by Markel Corporation (PA, USA) was used in the experiments. The specifications of the membranes are listed in Table 1. The azo reactive dye C.I. Reactive Red 120 was kindly provided by DyStar Textilfarben GmbH & Co. and Dystar Thai Ltd. Molecular formula of RR 120 and its molecular weight are $C_{44}H_{24}Cl_2N_{14}O_{20}S_6H_6$ and 1337.34 g/mol, respectively. The Acid blue 113 ($C_{32}H_{21}N_5Na_2O_6S_2$, 681 g/mol) and Direct red 23 ($C_{35}H_{25}N_7Na_2O_{10}S_2$, 814 g/mol) were supplied by Modern Dyestuff & Pigment. A reagent grade NaCl and $Na_2CO_3$ used as additives in dye solution were bought from Merck Ltd. Pure oxygen (99.8%) was used to produce ozone in all experiments.

**Table 1**
Specifications of the hollow fiber membrane module used.

| Membranes | Polyvinylidene fluoride | Polytetrafluoroethylene |
|---|---|---|
| Fiber o.d. (mm) | 1.00 | 1.97 |
| Fiber i.d. (mm) | 0.65 | 1.60 |
| Module i.d. (mm) | 10 | 10 |
| Membrane pore size (urn) | 0.2 | 0.3 |
| Membrane porosity | 0.75 | 0.4 |
| Number of fibers | 70 | 25 |
| Effective module length (mm) | 320 | 320 |
| Effective contact area ($m^2$) | 0.0377 | 0.0327 |

The mass transfer study and effect of dyeing auxiliary reagents on color removal were carried out. The experimental setup is schematically shown in Fig. 2. The ozone was produced with ozone generator (Model: VGsa 010, Siamese twins Ltd., Thailand) by pure oxygen. The ozone concentration in the gas phase was measured by the ozone analyser, QuantOzon'2, Erwin sander Ltd. with 1.5% measurement uncertainty. For all runs, the ozone concentration in the feed stream was kept at 40 mg/l and it was fed to the top of the membrane module which was oriented vertically (through the shell side of the membrane module). The pure water or dye solution was pumped by peristaltic pump (L/S® Easy-load® II, Masterflex) from the feed tank to the bottom of the module, through the lumen side of the hollow fibers. The flow of both liquid and gas stream was once through. The outlet liquid was sampled for the analysis (after a steady state was reached) and it was then collected for further disposal. For studying of the dye removal efficiency and kinetic part, the experimental equipments were setup the same as the above part, besides, the dyeing solution volume was kept at 500 ml and

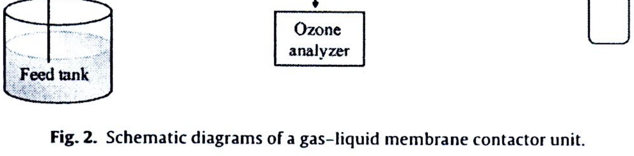

**Fig. 2.** Schematic diagrams of a gas–liquid membrane contactor unit.

**Table 2**
The mass transfer coefficient of liquid phase ($k_l$) for physical absorption.

| Liquid velocity (m/s) | $Re_L$ | $k_l$ (m/s) |
|---|---|---|
| 0.46 | 354 | $3.42 \times 10^{-5}$ |
| 0.62 | 483 | $3.79 \times 10^{-5}$ |
| 0.76 | 588 | $4.05 \times 10^{-5}$ |
| 0.89 | 687 | $4.26 \times 10^{-5}$ |

it was re-circulated through the membrane, then back to the feed tank until the required ozonation time was reached.

Ozone concentration in the water was measured by colorization method by indigo reagent [21]. The ozone fluxes for pure water were determined by mass balance in the liquid phase, whereas ozone fluxes for dye solution were calculated by the mass balance in the gas phase. For all experiments, the synthetic dye wastewater was used. The colors of the dye solution were measured with U 3000 spectrophotometer, Hitachi at 535 nm wavelength.

## 4. Results and discussion

### 4.1. Effects of operating conditions on ozone mass transfer performance

The effects of various operating parameters, i.e., liquid and gas phase velocity, operating temperature, and dyeing auxiliary reagent on the ozone mass transfer performance were investigated with the intention of gaining a better understanding in choosing the appropriate conditions for dyeing wastewater treatment.

#### 4.1.1. Liquid phase velocity and types of dye

Before the experiments on ozonation of dye solution were carried out, the experiments on physical absorption (using pure water and ozone) were performed in order to compare the results with chemical absorption and to estimate $k_l$ (the liquid side mass transfer coefficient). The result in Table 2 showed that the increase of liquid velocity resulted in the increase of $k_l$, according to Eq. (2). The low values of $k_l$ in comparison with the membrane mass transfer coefficients (see also Table 3) implied that the main mass transfer resistance was in the liquid phase as reported in previous literature in membrane gas absorption processes [8,12,13].

The effects of liquid phase velocity and types of dye on the ozone mass transfer performance are presented in Fig. 3. Three different dye solutions, i.e., Direct red 23, Acid blue 113 and Reactive red 120 as well as pure water were selected to be used as liquid phase. It was found that the ozone flux was in the sequence of Direct red 23 > Reactive red 120 > Acid blue 113 > water. In case of water used as liquid phase (physical absorption), the ozone flux depends on its solubility in water or there is no chemical reaction between water and ozone gas, therefore, the ozone flux was lowest. The ozone flux of Direct red 23 dye solution was higher than those of Reactive red 120 and Acid blue 113. The pH of Direct red 23 dye solution (pH = 6.83) was higher than Reactive red 120 (pH = 6.74) and Acid blue 113 (pH = 6.14).

At higher pH, the indirect reaction pathway involves radicals as follows:

$$O_3 + OH^- \rightarrow O_2^{-\bullet} + HO_2^{\bullet} \qquad (9)$$

The first step is the decay of ozone, accelerated by initialtors, e.g., $OH^-$, to form secondary oxidants such as hydroxyl radical ($OH^\bullet$). They react nonselectively and immediately ($k = 10^8–10^{10}\,M^{-1}\,s^{-1}$) with solute. On the contrary, at low pH, there is direct oxidation reaction rate constant, typically being in the range of $k = 1.0–10^3\,M^{-1}\,s^{-1}$.

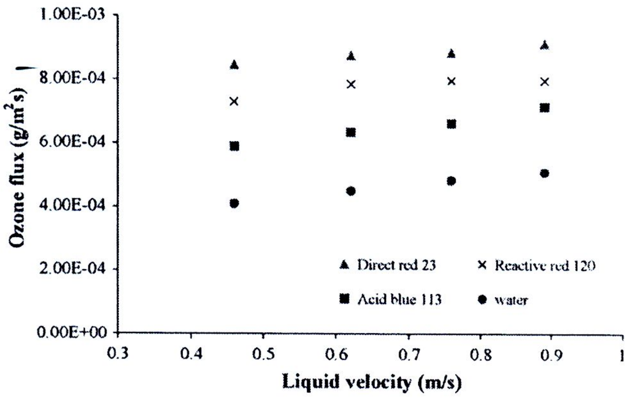

**Fig. 3.** Effect of liquid velocity on ozone flux. (Membrane: PVDF, Dye concentration: 100 mg/l, Operating temperature: 28 °C, Gas phase velocity: 0.12 m/s).

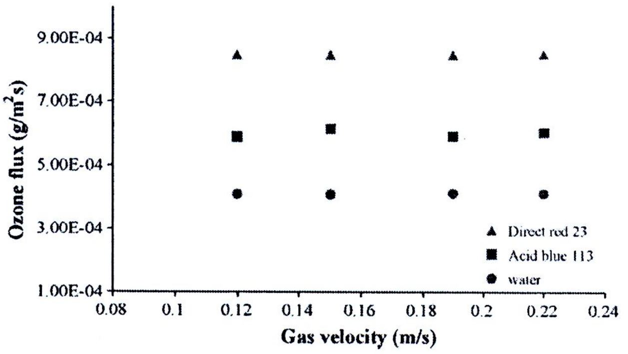

**Fig. 4.** Effect of gas velocity on ozone flux. (Membrane: PVDF, Dye concentration: 100 mg/l, Operating temperature: 28 °C, Liquid phase velocity: 0.46 m/s).

At higher pH, Direct red 23 (pH = 6.83) and Reactive red (pH = 6.74), there is more $OH^-$ which induces ozone decay to $OH^\bullet$ [23] resulting in higher concentration gradient between gas and liquid phases. So, more ozone can be dissolved into the liquid phase and thus increases the mass transfer flux of ozone. The difference in rate constant of direct and indirect reaction cited above confirms that, at higher pH, more ozone can be quickly consumed by indirect reaction

It can also be found that the ozone mass transfer flux increased with increasing liquid phase velocity for both physical and chemical absorption since the mass transfer coefficient was increased resulted in the mass transfer driving force. The similar trends of the results regarding effect of liquid phase velocity on the gas flux for both physical and chemical reaction systems were reported in the literature [8].

#### 4.1.2. Gas phase velocity

The effect of gas phase velocity on the ozone mass transfer performance was studied. The experimental results are shown in Fig. 4. The gas phase velocity was varied from 0.12–0.22 m/s and the ozone

**Table 3**
Comparison of membrane mass transfer coefficients at 28 °C between PVDF and PTFE.

| Membrane type | $\varepsilon_m$ | $\tau_m$ | $r_p$ (μm) | $l_m$ (m) | $D_A$ (m²/s) | $D_K$ (m²/s) | $D_{g,eff}$ (m²/s) | $k_m$ (m/s) |
|---|---|---|---|---|---|---|---|---|
| PVDF | 0.75 | 2.08 | 0.10 | $1.75 \times 10^{-4}$ | $2.08 \times 10^{-5}$ | $2.43 \times 10^{-5}$ | $1.12 \times 10^{-5}$ | $2.31 \times 10^{-2}$ |
| PTFE | 0.40 | 6.40 | 0.15 | $1.86 \times 10^{-4}$ | $2.08 \times 10^{-5}$ | $3.64 \times 10^{-5}$ | $1.32 \times 10^{-5}$ | $0.44 \times 10^{-2}$ |

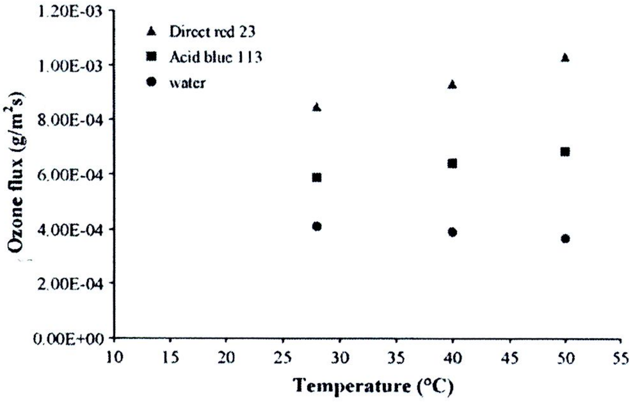

**Fig. 5.** Effect of liquid phase temperature on ozone flux. (Membrane: PVDF, Dye concentration: 100 mg/l, Liquid phase velocity: 0.46 m/s, Gas phase velocity: 0.12 m/s).

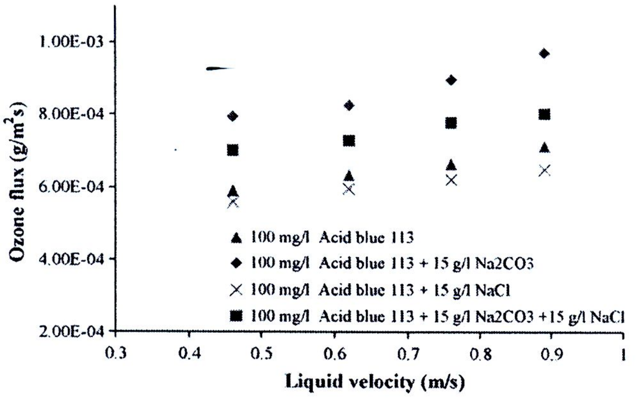

**Fig. 6.** Effect of dye auxiliary reagents on ozone flux. (Membrane: PVDF, Operating temperature: 28 °C, Gas phase velocity: 0.12 m/s).

concentration was set as 40 mg/l. It can be found that for both water and dye solution used as liquid phase the ozone flux was constant with increasing gas phase velocity. This can be explained that the mass transfer resistance was mainly controlled by the liquid phase as previously discussed, therefore, the change of gas phase velocity did not influence the ozone mass transfer performance [12].

### 4.1.3. Operating temperature

Fig. 5 depicts the effect of operating temperature on the ozone mass transfer flux for water, Direct red 23 and Acid blue 113 used as liquid phase. The experiments were carried out by varying the operating temperatures in the range of 28–50 °C. The results showed two different trends. For dye solution used as liquid phase, the ozone flux increased with increasing operating temperature. This is due to the increase of chemical reaction rate between ozone and dye in which the chemical reaction rate constant of ozone is temperature-dependent [23]. Conversely, in case of using water as liquid phase, the ozone flux was decreased as the operating temperature was increased owing to the decrease of gas solubility in the water. The ozone solubility in the water can be estimated by Henry's constants for the temperature range of 273–333 K [24]:

$$\log\left(\frac{H_{O_3}}{\text{kPam}^3\text{mol}^{-1}}\right) = 5.12 - \frac{1230}{T(K)} \tag{10}$$

The ozonation of dyeing solution process will take an advantage of higher ozone flux since the dye wastewater has normally high temperature.

### 4.1.4. Dye auxiliary reagents

Normally, NaCl and $Na_2CO_3$ are utilized as dye auxiliary reagents. Fig. 6 shows the effect of dye additives on the ozone flux. It can be found that the ozone flux increased when the $Na_2CO_3$ was presented in dye solution. The pH of dye solution (Acid blue 113) increased from 6.14 to 10.1 when $Na_2CO_3$ was added. The decomposition of ozone molecule to $OH^\bullet$ radical at high pH enhanced the oxidation ability resulted in increasing the mass transfer in the liquid phase (ozone concentration difference between gas and liquid phase increased). The similar trends of the results were reported in the literature [12]. When NaCl was added into the dye solution, the ozone fluxes were found to decrease due to the decrease of gas solubility in the salts solution (salting out effect) [25].

## 4.2. Effects of types of membrane on ozone mass transfer performance

In the gas–liquid membrane contacting process, the membrane wetting which leads to the separation performance deterioration has been considered as a challenging problem. The approach promoting the membrane contactor to be industrially competitive with the conventional processes is that the system performance has to be maintained during the prolonged period of operation (preventing the membrane wetting). Membrane wetting depends on a number of parameters. One of crucial parameters is the type of membrane used. In this work, the two different types of membranes, i.e., PVDF and PTFE which have different degrees of hydrophobicity [13] and characteristics were selected to be used as membrane contactor in order to compare their ozone mass transfer performance for dye decolorizaiton.

The effect of different membrane types on the ozone mass transfer performance for both using water and dye solution as liquid phases is presented in Fig. 7. It can be seen that, for both conditions, the ozone mass transfer flux of PVDF membrane was higher than that of PTFE membrane. This can be quantitatively explained that the membrane porosity of PVDF membrane (0.75) was higher than that of PTFE membrane (0.40). In addition, the result can be confirmed by the values of membrane mass transfer coefficient ($k_m$) in Table 3. The membrane mass transfer coefficient for ozone gas of PVDF membrane ($2.31 \times 10^{-2}$ m/s) was higher than that of PTFE ($0.44 \times 10^{-2}$ m/s) by approximately 5 times. The high values of $k_m$, compared to $k_l$ (Table 2) confirmed that the main mass transfer resistance was in the liquid phase as mentioned earlier.

The comparison of ozone mass transfer flux in the long-term test of PVDF and PTFE membranes by using Direct Red 23 solution as the liquid phase was carried out. The experimental results are shown in Fig. 8. The ozone flux was constant through 16 h of testing when PTFE membrane was used. For using PVDF membrane

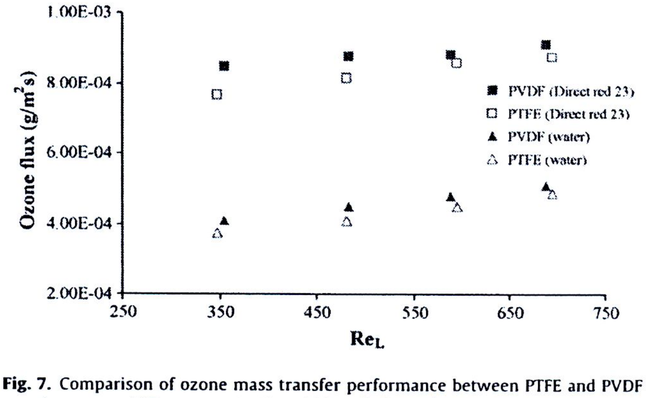

**Fig. 7.** Comparison of ozone mass transfer performance between PTFE and PVDF membranes used (Dye concentration: 100 mg/l, Operating temperature: 28 °C, Gas phase velocity: 0.12 m/s).

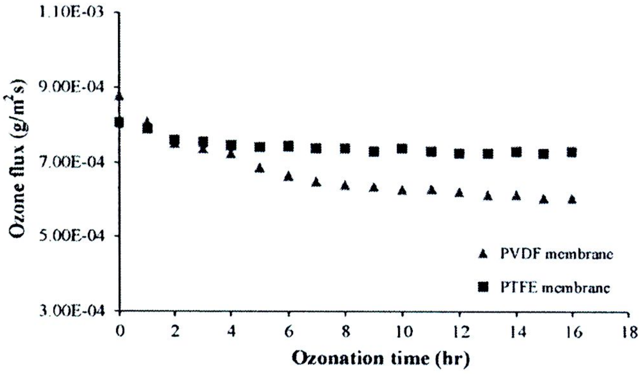

Fig. 8. Long term performance of PTFE and PVDF membranes with 100 mg/l Direct Red dye solution (Operating temperature: 28 °C, $Re_L$: 483 Gas phase velocity: 0.12 m/s).

as a membrane contactor, the ozone flux reduced approximately 30% of the initial flux during the testing period. The decrease in the ozone flux for PVDF membrane was likely due to the increase of the total mass transfer resistance. Since the operating conditions were the same for both membranes, obviously, the membrane contributed to the increase of overall mass transfer resistance as a result of the membrane wetting and possibly due to the change of membrane morphology because of the ozone oxidation. We examined the surface structure of PVDF membrane before and after long-term operation. The SEM images showed obvious change of membrane structure. Previous studies [13,14] indicated that PTFE membrane was more hydrophobic than PVDF membrane and was more resistant to ozone attack. Therefore, it can be concluded that PTFE membrane was more suitable to be used as membrane contactor for ozonation since it gives high and stable flux throughout the long operation period.

### 4.3. Effects of operating conditions and dye auxiliary reagent on dye removal efficiency

In this part, the experimental equipment was set up as in Fig. 2, but the volume of dye solution in the feed tank was kept constant at 500 ml and the outlet solution was re-circulated to the feed tank.

#### 4.3.1. Effects of dye solution type and dye solution velocity

Fig. 9 illustrates the decolorization of Acid blue 113 and Direct red 23 at the different liquid velocity flow rate against ozonation time. The decolorization performance of Acid blue 113 was higher than that of Direct red 23. After 60 min of ozonation time, the color of Acid blue 113, and Direct red 23 decreased around 97% and 72% of the initial dye concentration. The reason is that for Acid blue 113 solution in which the pH (6.14) was lower than that of Direct red 23 pH (6.83), therefore, most ozone was presented as molecules. Ozone molecule is selective and attacks preferentially the unsaturated bonds of chromophores. For this reason, color removal by action of the ozone is fast [22].

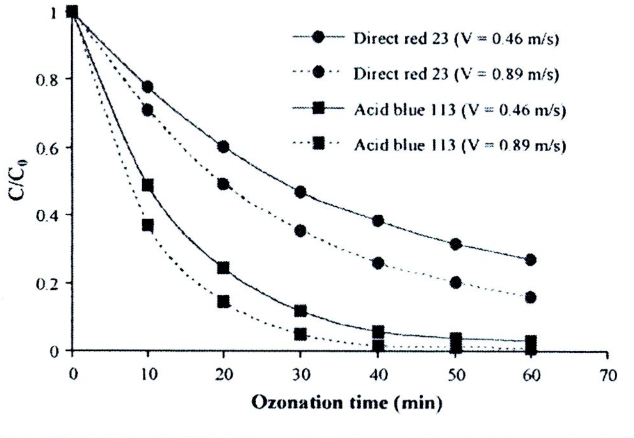

Fig. 9. Effect of liquid phase velocity and dye type on decolorization efficiency. (Membrane: PVDF, Initial dye concentration: 300 mg/l, Gas phase velocity: 0.12 m/s).

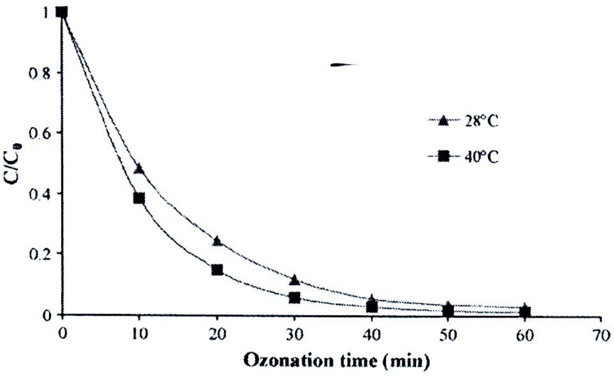

Fig. 10. Effect of operating temperature on the Acid blue 113 removal efficiency (Membrane: PVDF, Initial dye concentration: 300 mg/l, Liquid phase velocity: 0.46 m/s, Gas phase velocity: 0.12 m/s).

It is also found that the decolorization performance was increased with increasing liquid velocity. The increase of liquid velocity resulted in increase of mass transfer coefficient of the system. The decolorization performances was increased from 97 to 99% and 73 to 84% for Acid blue 113 and Direct red 23, respectively, when the liquid velocity was increased from 0.46 m/s to 0.89 m/s.

#### 4.3.2. Effect of liquid phase temperature

The effect of liquid phase temperature on the decolorization performance of the ozonation was carried out and is presented in Fig. 10. When the temperature was increased from 28 °C to 40 °C, the decolorization performance of Acid blue 113 at 60 min ozonation time was increased from 97% to 99%. The results can also be explained that the increase of temperature led to enhancing the chemical reaction rate constant between ozone and dye molecule (see also Section 4.1.3).

#### 4.3.3. Effect of dye auxiliary reagent

NaCl and $Na_2CO_3$ are widely utilized as the dye auxiliary reagents. The effect of dye auxiliary reagent on decolorization performance is shown in Fig. 11. At 60 min ozonation time, decol-

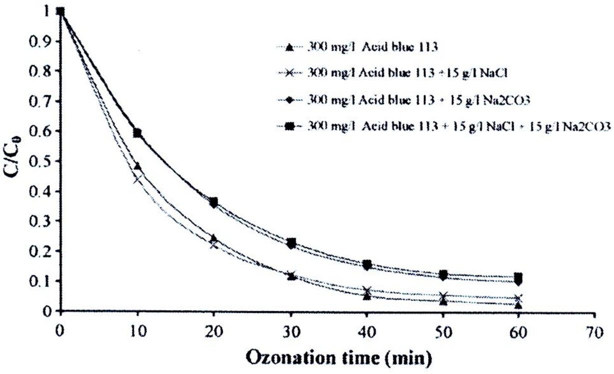

Fig. 11. Effect of dyeing auxiliary reagents on the Acid blue 113 removal efficiency. (Membrane: PVDF, Liquid phase velocity: 0.46 m/s, Gas phase velocity: 0.12 m/s, Operating temperature: 28 °C).

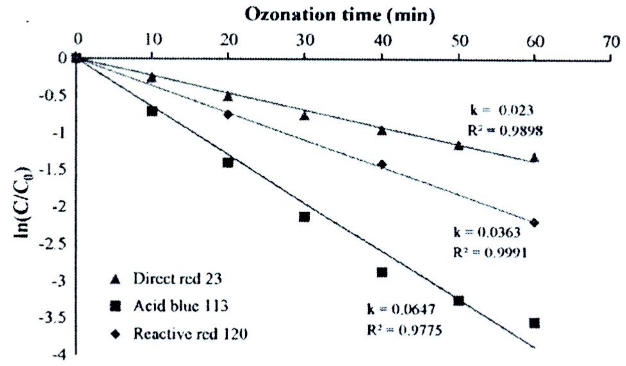

Fig. 12. Kinetics of ozonation for dye decolorization of Direct red 23, Acid blue 113 and Reactive red 120. (Membrane: PVDF, Initial dye concentration: 300 mg/l, Liquid phase velocity: 0.46 m/s, Gas phase velocity: 0.12 m/s, Operating temperature: 28 °C).

orization of Acid blue 113 decreased from 97% to 87% when the $Na_2CO_3$ was added into dye solution. This can be explained that the pH of dye solution was increased when $Na_2CO_3$ was added into dye solution (see Section 4.1.4) leading to decomposition of ozone molecules to $OH^\bullet$ radical. As previously mentioned, the ozone molecule has more double bond selectivity than $OH^\bullet$ radical. Therefore, the decolorization performance of dye solution was reduced when $Na_2CO_3$ was presented in dye solution. The decolorization performance of dye solution with presence of NaCl decreased from 97 to 93% due to the decrease of gas solubility in the salt solution (see also Section 4.1.4).

### *4.4. Ozonation reaction kinetic for dye solution*

The ozonation kinetic of dye solution plays an important role in evaluating the efficiency and feasibility of decolorization process. In the present study, the pseudo-first order behavior with respect to the dye concentration was observed in all experimental runs. The kinetics of dye ozonation were assessed by plotting $\ln(C/C_0)$ values versus reaction time as the following equation [4,26,27]:

$$\ln\left(\frac{C}{C_0}\right) = -kt \tag{11}$$

where $C$ and $C_0$ are dye concentrations at any reaction time ($t$) during ozonation and the initial dye concentration, respectively. The $k$ is pseudo-first-order rate constant ($\text{min}^{-1}$).

The kinetic study experiments were carried out for three different types of dye solutions at 300 mg/l dye concentration. The liquid temperature was kept at 28 °C. The ozone gas concentration of 40 mg/l was applied.

Fig. 12 shows that the curves were well fitted to the pseudo-first-order kinetics, and the square of the relative correlative coefficients ($R^2$) of the experimental results were higher than 0.97 for all dye solutions. The slopes of the curves correspond to pseudo-first-order rate constants and were 0.023 $\text{min}^{-1}$, 0.036 $\text{min}^{-1}$, and 0.065 $\text{min}^{-1}$ of Direct red 23, Reactive red 120, and Acid blue 113, respectively. Therefore, the decolorization rate of Acid blue 113 was highest. Since pH of Acid blue 113 dye solution was lowest, hence, most ozone was presented as molecules. As previously mentioned, ozone molecule is more selective in attacking the unsaturated bond of chromophores. The similar result was reported in the literatures [28,29].

## 5. Conclusions

The potential of gas–liquid membrane contactor for dye decolorization by ozone was investigated by means of experimental study in combination with mass transfer analysis. It was found that the ozone flux was in the order of Direct red 23 > Reactive red 120 > Acid blue 113 > water. The ozone flux did not change with gas phase velocity for both water and dye solution used as liquid phase. As the liquid phase temperature was increased, the ozone flux was also increased. Conversely, for water used as liquid phase, the ozone flux decreased with liquid phase temperature. When the $Na_2CO_3$ was added into dye solution as the auxiliary reagent, the ozone flux was enhanced due to the increase of solution pH. The PTFE membrane exhibited the better long-term performance than PVDF membrane in ozonation process since ozone flux was kept almost unchanged over 16 h of operation. The decolorizaton performance of the process was increased with liquid phase velocity and temperature. The decolorization performance was in the sequence of Acid blue 113 > Reactive red 120 > Direct red 23. The values of kinetic rate constants confirmed the decolorization performance of ozone.

## Acknowledgements

The authors gratefully acknowledge the financial support from the Thailand Research Fund (TRF) and from the Commission on Higher Education, Thailand through the TRF senior research scholar grant. We also would like to thank the Markel Corporation for the PTFE membranes provided for this work.

## References

[1] A.R. Bouwers, Chemical Oxidation of Aromatic Compounds Comparison of H2O2, KMnO4, and Ozone for Toxicity, Vanderbilt University, USA, 1990.
[2] S. Baig, P.A. Liechit, Ozone treatment for biological COD removal, Water Sci. Technol. 43 (2) (2001) 197–204.
[3] I. Arslan, I.A. Balcioglu, Effect of common reactive due auxiliaries on the ozonation of dyehouse effluents containing vinylsulphone and aminochlorotriazene dyes, Desalination 130 (2000) 61–71.
[4] A.H. Konsawa, Decolorizaton of wastewater containing direct dye by ozonation in a batch bubble column reactor, Desalination 158 (2003) 233–240.
[5] H. Selcuk, Decolorization and detoxication of textile wastewater by ozonation and coagulation processes, Dyes Pigments 64 (2005) 217–222.
[6] L.B. Chu, X.H. Xing, A.F. Yu, Y.N. Zhou, X.L. Sun, B. Jurcik, Enhanced ozonation of simulated dyestuff wastewater by microbubble, Chemosphere 68 (2007) 1854–1860.
[7] A. Gabelman, S.T. Hwang, Hollow fiber membrane contactors, J. Membr. Sci. 304 (1999) 61–106.
[8] S. Atchariyawut, R. Jirattananon, R. Wang, Separation of $CO_2$ from $CH_4$ by using gas–liquid membrane contacting process, J. Membr. Sci. 304 (2007) 163–172.
[9] J. Phattaranawik, T. Leiknes, W. Pronk, Mass transfer studies in flat-sheet membrane contactor with ozonation, J. Membr. Sci. 247 (2005) 153–167.
[10] T. Leiknes, J. Phattaranawik, M. Boller, U.V. Gunten, W. Pronk, Chem. Eng. J. 111 (2005) 53–61.
[11] R.H.S. Sausen, S.W. de Rijk, A. Zwijneuburg, M.H.V. Mulder, M. Wessling, Hollow fiber membrane contactors-A means to study the reaction kinetics of humic substance ozonation, J. Membr. Sci. 257 (2005) 48–59.
[12] S. Atchariyawut, J. Phattaranawik, T. Leiknes, R. Jiraratananon, Application of ozonation membrane contacting system for dye wastewater treatment, Sep. Purif. Technol. 66 (2009) 153–158.
[13] S. Khaisri, D. deMontigny, P. Tontiwachwuthikul, R. Jiraratananon, Comparing membrane resistance and absorption performance of three different membranes in a gas absorption membrane contactor, Sep. Purif. Technol. 65 (2009) 290–297.
[14] Y. Mori, T. Oota, M. Hashino, M. Takamura, Y. Fujii, Ozone-microfiltration system, Desalination 117 (1998) 211–218.
[15] M.C. Yang, E.L. Cussler, Designing hollow-fiber contactors, AIChE. J. 32 (11) (1986) 1910–1916.
[16] R. Prasad, K.K. Sirkar, Dispersion-free solvent extraction with microporous hollow-fiber modules, AIChE. J. 34 (1988) 177–188.
[17] S.R. Wickramasinghe, M.J. Semmens, E.L. Cussler, Mass transfer in various hollow fiber geometries, J. Membr. Sci. 69 (1992) 235–250.
[18] M. Mavroudi, S.P. Kaldis, G.P. Sakellaropoulos, A study of mass transfer resistance in membrane gas-liquid contacting processes, J. Membr. Sci. 272 (2006) 103–115.
[19] S.B. Iversen, V.K. Bhatia, K. Dam-Johansen, G. Jonsson, Characterization of microporous membranes for use in membrane contactors, J. Membr. Sci. 130 (1997) 205–217.
[20] H. Kreulen, C.A. Smolders, G.F. Versteeg, W.P.M. Van Swaaij, Determination of mass transfer reates in wetted and non-wetted microporous membranes, Chem. Eng. Sci. 48 (1993) 2093–2102.

[21] D. Eaton, L.S. Clesceri, A.E. Greenberg, Standard methods for the examination of water and wastewater, 21st ed., American public health association (APAH), 2005.

[22] W. Chu, C.W. Ma, Quantitative prediction of direct and indirect dye ozonation kinetics, Water Res. 34 (12) (2000) 3153–3160.

[23] C. Gottschalk, J.A. Libra, A. Saupe, Ozonation of water and waste water, in: A practical guide to understanding ozone and its application, Wiley-vch Verlag GmbH, Weinheim, 2000.

[24] E. Rischbieter, H. Stein, A. Schumpe, Ozone solubilities in water and aqueous salt solutions, J. Chem. Eng. Data 45 (2000) 338–340.

[25] S. Weisenberger, A. Schumpe, Estimation of gas solubilities in salt solution at temperatures from 273 K to 363 K, AIChE. J. 42 (1) (1996) 298–300.

[26] S. Song, H. Ying, Z. He, J. Chen, Mechanism of decolorization and degradation of CI Direct Red 23 by ozonation combined with sonolysis, Chemosphere 66 (2007) 1782–1788.

[27] H.Y. Shu, C.R. Hunag, Degradation of commercial azo dye in water using ozonation and UV enhanced ozonation process, Chemosphere 31 (1995) 3813–3825.

[28] M. Muthukumar, N. Selvakumar, Studies on the effect of inorganic salts on decolouration of acid dye effluents by ozonation, Dyes Pigments 62 (2004) 221–228.

[29] L.A. Lopez, J.S. Pic, H. Debellefontaine, Ozonation of azo dye in semi-batch reactor: a determination of the molecular and radical contributions, Chemosphere 66 (2007) 2120–2126.

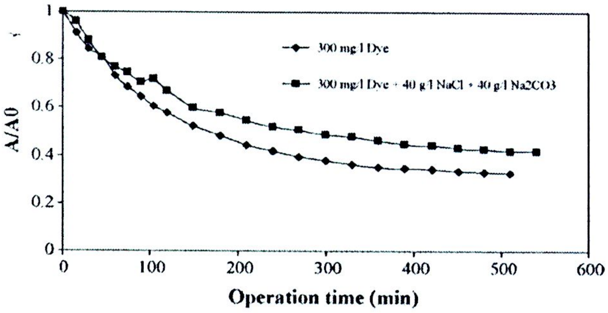

**Fig. 12.** Effects of ozonation time and dye auxiliary reagents on decolorization (gas flow rate: 350 ml/min; operating temperature: 25 °C; HRT system: 4 h; HRT membrane: 0.1 min).

## 4. Conclusions

Mass transfer of ozone in membrane contactor was studied by changing the gas and liquid flow rate. It was found that the ozone flux increased with liquid velocity for water and 300 mg/l dye solution used as liquid phase. On the other hand, the ozone flux did not change with increasing the gas flow rate. Therefore, it was clear that the main mass transfer resistance was in the liquid phase for both cases. $Na_2CO_3$ and NaCl were utilized as the auxiliary reagents for dyeing process and their effects on the ozonation process in the effluents were studied. When the $Na_2CO_3$ was present in the dye solution, the ozone flux increased since the ozone molecules was decomposed to $OH^\bullet$ radical resulted in increase mass transfer coefficient in the liquid. The ozone flux decreased with adding NaCl due to the salting out effect. The reagents inhibited the decolorization performance of the ozone due to lesser double bond selectivity of $OH^\bullet$ radical. After 30 min ozonation time, the COD of the dye solution was reduced around 32% which was an advantage of using ozone in dye effluent.

The reactor tank was added in order to separate the effect of HRT system and membrane and to achieve the continuous mode of operation. The decolorization performance was developed with increasing the HRT in the system and decreasing the HRT in the membrane. The increase of HRT system was an increase of the contact time between ozone and dye solution. The decreasing in HRT membrane was equal to the increase of liquid velocity which resulted in the increase of mass transfer coefficient in the liquid phase. The dye removal efficiency decreased around 10% when the auxiliary reagents were added in the dye solution. The continuous ozonation membrane contacting system showed that the dye color was removed roughly 68% in the 4 h HRT system and 0.1 min HRT membrane.

## Acknowledgements

The authors gratefully acknowledge the financial support from the Thailand Research Fund (TRF) and from the Commission on Higher Education, Thailand through the TRF senior research scholar grant. We also would like to thank the Department of Hydraulic and Environmental Engineering, NTNU Norwegian University of Science and Technology for the experimental facilities provided for this work.

## References

[1] F.P. van der Zee, S. Villaverde, Combined anaerobic–aerobic treatment of azo dyes—a short review of bioreactor studies, Water Res. 39 (2005) 1425–1440.
[2] H.M. Freeman (Ed.), Standard Handbook of Hazardous Waste Treatment and Disposal, Mcgraw-Hill, 1989.
[3] A. Gutowska, J. Kaluzna-Czaplinska, W.K. Jozwiak, Degradation mechanism of Reactive Orange 113 dye by $H_2O_2/Fe^{2+}$ and ozone in aqueous solution, Dyes Pigments 74 (2007) 41–46.
[4] A.R. Bowers, Chemical Oxidation of Aromatic Compounds: Comparison of $H_2O_2$, $KMnO_4$ and Ozone for Toxicity, Vanderbilt University, USA, 1990.
[5] A.H. Konsowa, Decolorization of wastewater containing direct dye by ozonation in a batch bubble column reactor, Desalination 158 (2003) 233–240.
[6] B. Langkaus, D.A. Reckhow, D.R. Brink (Eds.), Ozone in Water Treatment: Application and Engineering, Lewis, Michigan, 1991.
[7] U.V. Gunter, Review: ozoneation of drinking water. Part I. Oxidation kinetics and product formation, Water Res. 37 (2003) 1443–1467.
[8] I. Arslar, I.A. Balcioglu, Effect of common reactive dye auxiliaries on the ozonation of dyehouse effluents containing vinylsulphone and aminochlorotriazine dyes, Desalination 130 (2000) 61–71.
[9] H. Selcuk, Decolorization and detoxification of textile wastewater by ozonation and coagulation processes, Dyes Pigments 64 (2005) 217–222.
[10] A. Gabelman, S.T. Hwang, Hollow fiber membrane contactors, J. Membr. Sci. 159 (1999) 61–106.
[11] S. Atchariyawut, R. Jiraratananon, R. Wang, Separation of $CO_2$ from $CH_4$ by using gas–liquid membrane contacting process, J. Membr. Sci. 304 (2007) 163–172.
[12] R.H.S. Jansen, J.W. de Rijk, A. Zwijnenburg, M.H.V. Mulder, M. Wessling, Hollow fiber membrane contactors—a means to study the reaction kinetics of humic substance ozonation, J. Membr. Sci. 257 (2005) 48–59.
[13] T. Leiknes, J. Phattaranawik, M. Boller, U. Von Gunten, W. Pronk, Ozone transfer and design concepts for NOM decolourization in tubular membrane contactor, Chem. Eng. J. 111 (2005) 53–61.
[14] J. Phattaranawik, T. Leiknes, W. Pronk, Mass transfer studies in flat-sheet membrane contactor with ozonation, J. Membr. Sci. 247 (2005) 153–167.
[15] P. Janknecht, P.A. Wilderer, C. Picard, A. Larbot, Ozone-water contacting by ceramic membranes, Sep. Purif. Technol. 25 (2001) 341–346.
[16] S. Masuda, M. Sato, T. Seki, High-efficiency ozonizer using traveling wave pulse voltage, IEEE Trans. Ind. Appl. IA-22 (1986) 886–891.
[17] D. Eaton, L.S. Clesceri, A.E. Greenberg, Standard Methods for the Examination of Water and Wastewater, 21st ed., American Public Health Association (APAH), 2005.
[18] R. Wang, H.Y. Zhang, P.H.M. Feron, D.T. Liang, Influence of membrane wetting on $CO_2$ capture in microporous hollow fiber membrane contactors, Sep. Purif. Technol. 46 (2005) 33–40.
[19] S. Weisenberger, A. Schumpe, Estimation of gas solubilities in salt solution at temperatures from 273 K to 363 K, AIChE J. 42 (1) (1996) 298–300.
[20] F. Zhang, A. Yediler, X. Liang, Decomposition pathways and reaction intermediate formation of the purified, hydrolyzed azo reactive dye C.I. Reactive Red 120 during ozonation, Chemosphere 67 (2007) 712–717.

© IWA Publishing 2010 **Water Science & Technology: Water Supply—WSTWS | 10.2 | 2010**

# Nanofiltration performance of lead solutions: effects of solution pH and ionic strength

Wuthikorn Saikaew, Supatpong Mattaraj and Ratana Jiraratananon

## ABSTRACT

Nanofiltration performance (i.e. rejection and flux decline) of lead solutions was investigated using a dead-end test cell at room temperature. An aromatic polyamide NF-90 membrane was chosen to determine the impacts of solution chemistry. The experimental results revealed that solution flux decline was dependent on solution pH, ionic strength, and type of lead solutions. Solution flux conducted with different types of lead solutions (i.e. $PbCl_2$ and $Pb(NO_3)_2$) decreased with increased solution pH. Solutions having high pH exhibited greater flux decline than those having low solution pH, while lead ion rejections were relatively high. Increased ionic strengths resulted in a greater flux decline, while lead ion rejections decreased with decreasing solution pH and increasing ionic strengths. Such results were related to low solution pH, suggesting an increase in fixed charge of proton ($H^+$), decreasing electrical double layer thickness within membrane, thus allowing increased lead concentration passing through the membrane surface. Solution flux and rejection decreased further at higher ionic strengths, which caused a reduced negatively charged membrane, and thus decreased rejections. It was also found that lead ion for $PbCl_2$ solution exhibited higher rejections than that of $Pb(NO_3)_2$ solution.

**Key words** | flux decline, lead solution, nanofiltration, solution chemistry

**Wuthikorn Saikaew**
Environmental Engineering Program, Department of Chemical Engineering,
Ubon Ratchathani University,
Ubonratchathani 34190,
Thailand

**Supatpong Mattaraj** (corresponding author)
Department of Chemical Engineering, Faculty of Engineering,
Ubon Ratchathani University,
Ubonratchathani 34190,
Thailand
E-mail: *mattas@ubu.ac.th*;
*supatpong.m@hotmail.com*

**Supatpong Mattaraj**
National Center of Excellence for Environmental and Hazardous Waste Management,
Ubon Ratchathani University,
Ubonratchathani 34190,
Thailand

**Ratana Jiraratananon**
Department of Chemical Engineering,
King Mongkut's University of Technology Thonburi,
Bangkok 10140,
Thailand

## INTRODUCTION

Membrane technologies have been widely used in the field of water treatment due to stringent water quality regulations (Hong & Elimelech 1997). They are efficient technologies to remove feed source water in terms of natural organic matter (NOM) (Cho *et al.* 1999; Kilduff *et al.* 2004; Mattaraj *et al.* 2008), inorganic scalants (Lisdonk *et al.* 2000; Lin *et al.* 2006; Jarusutthirak *et al.* 2007), salt solution (Anne *et al.* 2001; Labbez *et al.* 2003; Childress & Elimelech 2007) and heavy metals (Mehiguene *et al.* 1999; Molinari *et al.* 2001; Ipek 2005; Ku *et al.* 2005; Turek *et al.* 2007). Nanofiltration (NF), one of membrane technologies, is a relatively new membrane process, which is considered to be intermediate between ultrafiltration (UF) and reverse osmosis (RO) in terms of operating conditions. NF membrane processes operate at pressures between 50 and 150 psi much lower than RO (200 to 1,000 psi), but higher than UF (10 to 70 psi). At the present time, NF is increasingly applied in the field of water treatment. For example, ground waters containing high color due to dissolved organic matter (DOM), partially decomposed from plant materials, high hardness from the composition of calcium ($Ca^{2+}$) and magnesium ($Mg^{2+}$), and high iron ($Fe^{2+}$) and manganese ($Mn^{2+}$) concentration. NF can provide high water quality and large amount of water production in the short period of operation. It can give water quality within drinking water standards. However, membrane fouling caused by organic and inorganic substances can be a major factor limiting more widespread use of membrane technologies, reducing long-term filtration performance (i.e. water production), and increasing costs for membrane operation through

doi: 10.2166/ws.2010.062

higher labor, frequent chemical cleaning, and membrane replacement.

Inorganic fouling (i.e. negative and positive ions) can be a significant factor that enhances permeate flux decline during filtration. This may cause an increased concentration polarization that exceeds solubility limit, resulting precipitative fouling of scale-forming species (i.e. $Ca^{2+}$, $Mg^{2+}$, $CO_3^{2-}$, $SO_4^{2-}$, and $PO_4^{3-}$). This has been recently investigated by Jarusutthirak *et al.* (2007). Molinari *et al.* (2001) investigated the interactions between membranes (RO and NF) and inorganic pollutants (i.e. $SiO_2$, $NO_3^-$, $Mn^{2+}$, and humic acid). They showed that increased flux decline was caused by the interactions between the membranes and other ions. Other factors, which can increase flux decline, are solution pH, ionic strength, concentration, operating conditions, and solution compositions. In addition, inorganic fouling caused by the presence of metal ion in the aquatic environment has also been a subject of importance because of its toxicity for human health and environment, while the applications of nanofiltration for removing metal ions are recently limited in terms of solution chemistry affecting NF performance during filtration period. However, previous study mentioned the efficient use of membrane separation processes for the control of lead and copper corrosion (Taylor & Jacobs 1996), and the feasible recovery of valuable metals (Ku *et al.* 2005). The metallic ions can also produce stable complexes with organic compounds, which can be more resistant to metal oxidation in natural water. Lead ($Pb^{2+}$), known to occur widely as a result of lead plumbing materials and the action of corrosive water, is one of interested inorganic materials used in this study due to relatively low maximum contaminant levels in primary standards (affecting directly to human health) for water quality regulations (Cotruvo & Vogt 1990), while there is a lack of nanofiltration performance of lead solution using various solution pHs and ionic strengths. Therefore, the objective of this paper was to investigate the effects of solution chemistry on nanofiltration performance of different types of lead solutions. The effects of solution chemistry (i.e. solution pH and ionic strength) were determined to evaluate nanofiltration performance of lead solutions. The results of this study could be used to provide system performance of membrane filtration throughout the long operating period.

## MATERIALS AND METHODS

### Nanofiltration membrane characteristics

An aromatic polyamide thin-film composite NF-90 membrane, produced by Dow-FilmTec., was chosen to determine the effect of solution chemistry on nanofiltration performance of different types of lead solutions. The molecular weight cut-off (MWCO) of the NF-90 membrane was about 90 Da, indicating a tight NF membrane (Tahaikt *et al.* 2007). According to the manufacturer's information, the maximum operating pressure is 4,137.6 kPa, maximum feed flow rate is $3.6\,m^3\,hr^{-1}$, maximum operating temperature is 45°C and the operating pH ranges from 1 to 12. Free chlorine tolerance is less than 0.1 ppm. NF-90 is generally a tight NF membrane with a very high surface roughness (Bellona & Drewes 2005).

In operation, membrane flat sheets were stored in 1% sodium meta-bisulfite ($Na_2S_2O_5$) and kept in refrigerator at 4°C to prevent microbial activity. The water flux characteristics were determined for 30-min operation with clean water for membrane compaction. The membrane permeability was determined from the clean water flux data at different operating pressures.

### Analytical method

Lead concentration was measured by using atomic absorption (AA) spectrometry (AAnalyst 200 Version 2, Perkin Elmer Corp.). Measurements of solution pH, conductivity and temperature were made using pH meter (Inolab pH level 1, Weilheim, Germany), and conductivity meter connected with temperature (Inolab cond. level 2, Weilheim, Germany), respectively. Ionic strengths of samples were calculated using a correlation between conductivity and ionic strength of NaCl standards, $I.S.[M] = 0.5\Sigma C_i Z_i^2$ ($C_i$ is the ion concentration and $Z_i$ is the number of ions).

### Flux decline experiments

The experiments were carried out with three liters of solution containing lead solutions ($PbCl_2$ and $Pb(NO_3)_2$) at fixed concentration about $20\,mg\,L^{-1}$, while solution pH from 4 to 6 and ionic strengths (0.01, 0.05 M as NaCl) were varied in this study. As shown in Figure 1, the experiments were tested by using a 400-ml dead end membrane filtration

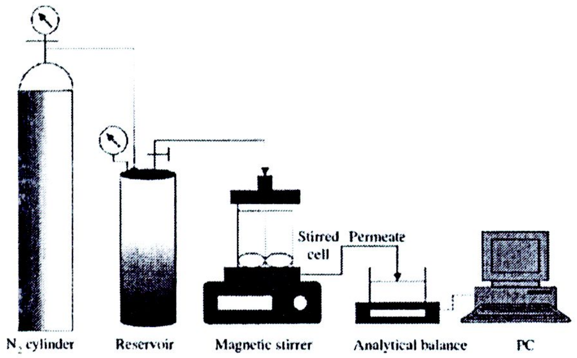

**Figure 1** | Schematic diagram of the experimental setup.

apparatus (Amicon 8400, USA) with magnetic stirrer (LABINCO, LD-12), while the magnetic spin bar fitted into the cell provided the agitation. While the dead end filtration system may not be practical compared with the crossflow one, it has been widely used in the laboratory study in order to simulate the situation of severe flux decline and fouling. The stirring speed was about 300 rpm. A membrane sheet was fitted to the cell with the membrane active area of 41.38 $cm^2$. The operating pressure was employed via high-pressure regulator of nitrogen cylinder. The permeate volume was determined during filtration by using the electrical balances (Mettler Toledo Monobloc PB-3002-S, USA). After filtration was terminated, two steps of cleaning, i.e. hydrodynamic cleaning followed by chemical cleaning, were performed. For hydrodynamic cleaning, the membrane sheet was cleaned with deionized (DI) water, then followed with chemical cleaning, acidic solution (using citric acid) with pH of 4 for 30-min each. After each cleaning, water fluxes at different operating pressures were measured to determine water flux recovery. For the next run of the experiment, new membrane sheet was used in order to avoid non-recoverable resistance from the previous filtration experiment. New membrane sheet was initially used to characterize clean water flux for membrane compaction, and subsequently used to determine water flux after hydrodynamic and chemical cleaning.

### Analysis of results

The parameters taken into account were:

The volumetric flux $J_v$ ($L m^{-2} h^{-1}$ or LMH) was determined by measuring the volume of permeate collected in a given time interval divided with membrane area by the relation:

$$J_v = L_p(\Delta P - \sigma\Delta\pi) = \frac{Q_p}{A} \tag{1}$$

where $L_p$ is the membrane permeability (LMH $kPa^{-1}$); $\Delta P$ is the transmembrane pressure (kPa); $\sigma$ is the osmotic reflection coefficient (−); $\pi$ is the osmotic pressure (kPa); $Q_p$ and $A$ represent flow rate of permeate ($L h^{-1}$) and the membrane area ($m^2$), respectively.

The observed rejection was calculated by the following relation:

$$\%R = \left(1 - \frac{C_p}{C_i}\right) \times 100 \tag{2}$$

where $C_p$ and $C_i$ are the solution concentrations in the permeate ($mg L^{-1}$), and in the initial feed solution ($mg L^{-1}$), respectively.

## RESULTS AND DISCUSSION

### Water flux characteristics

Before the experiments, the membrane permeability was measured after membrane compaction by measuring water flux as a function of operating pressure using DI water. The effect of osmotic pressure in Equation (1) was neglected for DI water. Clean water flux increased linearly with increased operating pressure with the correlation coefficient of 0.999. The slope represents the membrane permeability ($L_p$) of 0.0714 LMH $kPa^{-1}$. The measured membrane permeability was considered as reference to evaluate cleaning procedure and water flux recovery after system cleaning.

After filtration experiments, the membrane sheets were cleaned with DI water and followed with citric acid in order to investigate water flux recovery. As shown in Figure 2, the clean water flux after system cleaning of $PbCl_2$ and $Pb(NO_3)_2$ solutions at pH 6 was similar to clean water flux after membrane compaction, while water flux observed after hydrodynamic cleaning was lower when compared with clean water flux after membrane compaction. This suggested the inorganic lead resulted in an increase in flow resistance during filtration experiments. Increased flux caused by chemical cleaning was possibly due to

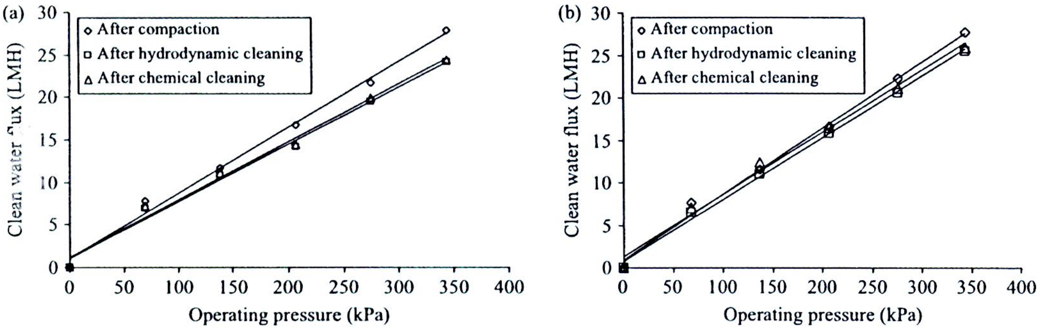

**Figure 2** | Clean water flux after system cleaning; (a) $PbCl_2$ and (b) $Pb(NO_3)_2$.

protons from acid, which could efficiently dissolve inorganic lead from the membrane surface, thus enhancing flux recovery. This suggested that an increase in water flux recovery was found for the membrane sheets cleaned by deionized (clean) water and chemical cleaning agent. The comparisons of clean water fluxes were similarly found with two types of lead solutions. This indicated that ionic lead ($PbCl_2$ and $Pb(NO_3)_2$ solutions) showed less non-recoverable resistance after system cleaning, indicating high water flux recovery.

## Effects of solution pH on flux and rejection

The effect of solution pH on flux decline of $PbCl_2$ and $Pb(NO_3)_2$ solutions were carried out at pH 4, 5 and 6 with constant ionic strength 0.01 M as NaCl at 413.6 kPa operating pressure. Feed concentration was kept at 20 mg $L^{-1}$. Figure 3 shows the effect of solution pH on relative flux. It was evident that the extent of flux decline increased with increasing solution pH for both $PbCl_2$ and $Pb(NO_3)_2$ solutions. For higher pH, relative fluxes of $Pb(NO_3)_2$ solution ($J_v/J_{v0} = 0.88$ at pH 6) showed higher flux decline than those of low solution pH ($J_v/J_{v0} = 0.90$ at pH 4). At low pH, it suggested an increased fixed charge of $H^+$, which decreased electrical double layer thickness within membrane or both, thus decreased concentration at the membrane surface. At high pH of 6, the membrane surface and pores became more negatively charged, while the anions from lead dissociation was presented in the feed solution. As a result, the pore size of the membrane was reduced because of the electrostatic repulsion between neighboring negatively charged groups, thus adopting an extended conformation (Schaep & Vandecasteele 2001; Teixeira *et al.* 2005). In addition, the osmotic pressure near the membrane surface increased due to high salt rejection, resulting in a decrease of the net driving pressure, thus affecting flux reduction. These mechanisms resulted in a decrease of permeate flux and an increase in salt rejection with increased solution pH.

Figure 4 shows the effect of solution pH on lead ion rejection. It was observed that lead ion rejection was relatively constant throughout filtration period. This indi-

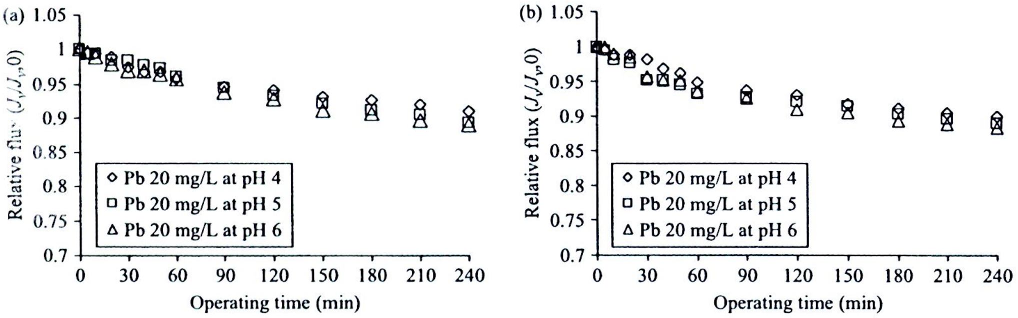

**Figure 3** | Effect of solution pH on relative flux; (a) $PbCl_2$ and (b) $Pb(NO_3)_2$.

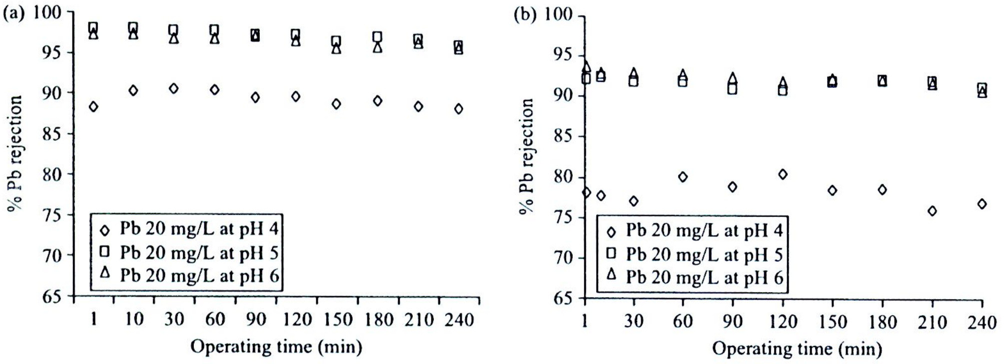

**Figure 4** | Effect of solution pH on lead ion rejection; (a) $PbCl_2$ and (b) $Pb(NO_3)_2$.

cated that high diffusive transport became more important than convective transport for the tight NF membrane at constant operating pressure (413.7 kPa). With increasing pressure, convective transport becomes more important and retention, therefore, increases (Mehiguene *et al.* 1999). However, concentration polarization can also increase with increasing pressure, which results in a decrease in retention. The counteracting contributions of increased convective transport and increased concentration polarization result in a constant retention value in the pressure range of 5–15 atm (Mehiguene *et al.* 1999). Lead ion rejection was found to decrease with decreasing solution pH. At higher solution pH, membrane surface became more negatively charged, thus attracting more lead ions. Consequently, for $PbCl_2$, at solution pH of 5–6, higher ion rejections were achieved (about 96–98%), while solution with low pH exhibited lower rejections about 88–91%. For $Pb(NO_3)_2$ solution, the ion rejection percentages of high solution pH (5–6) and low solution pH of 4 were 91–94% and 76–81%, respectively. At low pH, the lead ion rejections of $Pb(NO_3)_2$ solution were lower than that of $PbCl_2$ solution, possibly due to $H^+$ ion reducing negative charge at the membrane, reducing double layer thickness at the membrane, thus increased membrane pores. This allowed negatively charged anion ion passing through the membrane, thus increasing lead ion concentration in the permeate in order to maintain electroneutrality condition. This result showed higher lead ion concentration for $Pb(NO_3)_2$ solution than that for $PbCl_2$ solution. Kilduff *et al.* (2004) concluded that the effective membrane permeability increased when a pH was increased, but the flux decreased as a result of increased osmotic pressure effects resulting from increased solute rejection. Such behavior was in contrast to looser membranes having low salt rejection, for which flux increased with pH as a result of the increased membrane permeability.

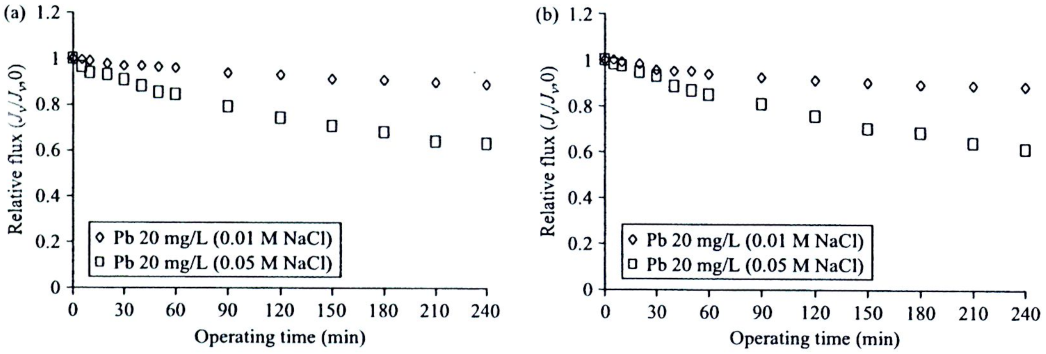

**Figure 5** | Effect of ionic strength on relative flux; (a) $PbCl_2$ and (b) $Pb(NO_3)_2$.

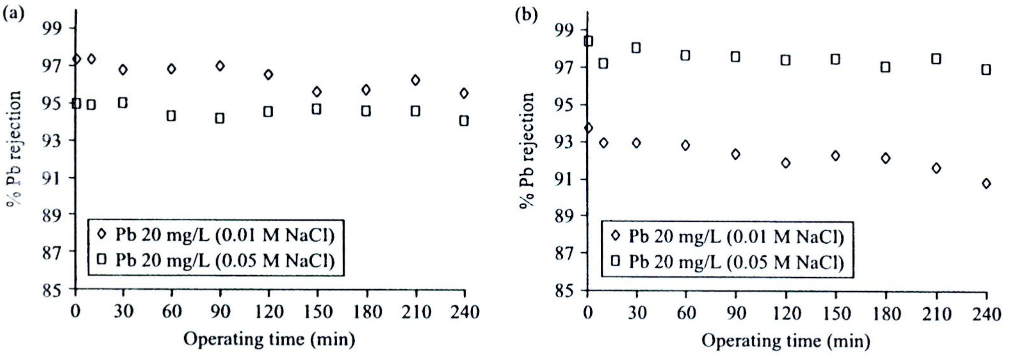

**Figure 6** | Effect of ionic strength on lead ion rejection; (a) $PbCl_2$ and (b) $Pb(NO_3)_2$.

## Effects of ionic strength on flux and rejection

Figure 5 presents the effect of ionic strength on relative flux. The filtration experiments were carried out at pH 6 with different ionic strengths of 0.01 and 0.05 M as NaCl. The solution pH of 6 was selected in order to avoid lead precipitation at high pH and high hydrogen ion concentration at low pH, which could affect membrane performance. It was observed that the extent of solution flux decline increased with increasing ionic strengths. This was possibly due to reduced electrostatic repulsion at the membrane surface, indicating high flux decline. Many studies indicated that increases in ion concentration could reduce the permeability of charged membranes (Eriksson 1988; Van Reenan & Sanderson 1992; Yaroshchuk & Staude 1992; Mattaraj *et al.* 2008), thus reducing permeate flux. The results showed similar trend for both $PbCl_2$ and $Pb(NO_3)_2$ solutions with increasing ionic strengths, thus suggesting an increase in flux decline.

Figure 6 exhibits the effect of ionic strength on lead ion rejection. It was found that at ionic strength 0.05 M lead ion rejections were lower than those of at 0.01 M. Increased salt concentration can provide positively charged $Na^+$ ion at the membrane surface, thus decreased electrostatic charge repulsion. The phenomena can enhance a reduction in double layer thickness on the membrane surface, thus affecting a reduction in membrane permeability caused by increased salt concentration on the membrane surface. This can allow lead ion passage through the membrane, suggesting a decrease in ion rejection.

## Effect of co-ion on solution flux decline

The effect of the co-ion of lead solution on flux decline was carried out with two types of $Pb^{2+}$ ($PbCl_2$ and $Pb(NO_3)_2$ solutions) at the concentration of $20\,mg\,L^{-1}$. The experiments were performed at pH 4, 5 and 6 with constant ionic strength of 0.01 M NaCl and 413.7 kPa operating pressure

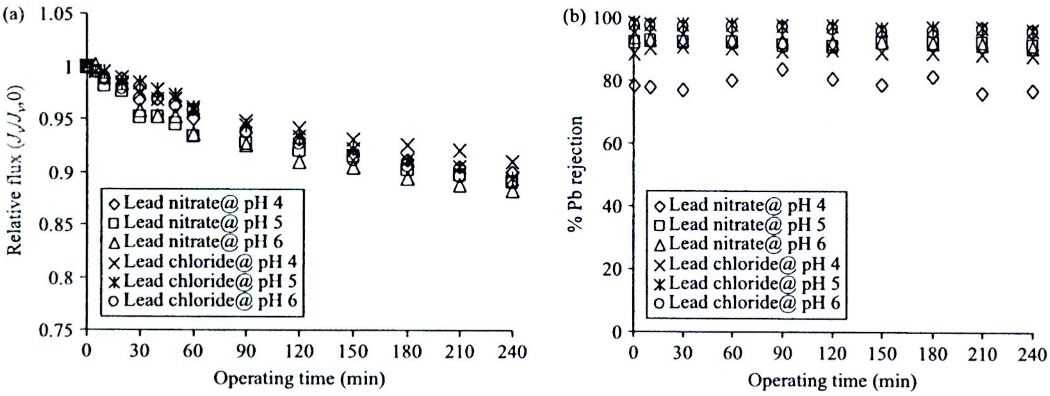

**Figure 7** | Comparisons of co-ion on nanofiltration performance of lead solution; (a) relative flux and (b) rejection.

during filtration. Figure 7 shows the comparisons of co-ion on nanofiltration performance of lead solution. It was observed that $Pb(NO_3)_2$ solution showed higher flux decline than $PbCl_2$ solution, while $PbCl_2$ solution presented higher rejections than $Pb(NO_3)_2$ solution. Since the NF membrane is more negatively charged, the monovalent anion of $Cl^-$ ion is more excluded than $NO_3^-$ ion resulting in greater rejection. The lead ion rejections for $PbCl_2$ solution showed higher than those of $Pb(NO_3)_2$ solution. It was possibly caused by higher charge repulsion of negatively charged $Cl^-$ ion, when compared with negatively charged $NO_3^-$ ion, thus increased lead concentration for $PbCl_2$ solution in order to satisfy an electroneutrality condition. The lead ions were retained on the membrane surface which resulted in high lead rejection.

In addition, Mehiguence *et al.* (1999) concluded that the retention of metallic cations was enhanced when the charge valency of associated co-ion increased. These observations were explained by Donnan exclusion phenomena (Donnan 1995), and were described by thermodynamic equilibrium. Consequently, as the membrane is negatively charged, co-ions are excluded and cations were also rejected in order to ensure electroneutrality at both side of the membrane. This was an important feature in nanofiltration (Mehiguene *et al.* 1999). Moreover, the difference effects in hydration energy of co-ions ($Cl^-$ and $NO_3^-$) could be also explained for this experiment. Chloride ion has larger hydration energy than nitrate ion, thus resulting in greater rejection (Mehiguene *et al.* 1999). Similar results were observed by Choi *et al.* (2001). The rejection ratio between chloride and nitrate ion was determined about 1.08 for RO membrane (Amiri & Samiei 2007), while the rejection ratio was about 1.14 for NF-90 membrane (Tahaikt *et al.* 2007) and 1.45 for the loose NF Nanomax 50 (MWCO about 300) (Frares *et al.* 2005).

## CONCLUSIONS

Lead ion rejection and flux decline from aqueous solution by nanofiltration membrane were strongly influenced by solution pH and ionic strengths. Flux decline of filtration experiments conducted for both $PbCl_2$ and $Pb(NO_3)_2$ solutions increased with increased solution pH. Solutions having high solution pH showed greater flux decline than those having low solution pH, while lead rejections exhibited higher rejection. Increased ionic strengths resulted in a greater increase in flux decline. Lead ion rejection was found to be decreased with decreasing solution pH and increasing ionic strengths. The experimental results of the study can be applied to improve system performance by adjusting system feed solution (i.e. avoiding low solution pH and high ionic strength) in order to control high rejection efficiency and high water production throughout the long operating period.

## ACKNOWLEDGEMENTS

This work was granted by the Office of the Higher Education Commission, which was supported by Strategic Scholarship Fellowships Frontier Research (CHE-Ph.D. THA-NEU). The authors also gratefully acknowledge support from the Thailand Research Fund (TRF) for TRF senior research scholar grant (No. RTA5080014) and the Commission on Higher Education, Thailand. The authors would like to thank the Department of Chemical Engineering, Faculty of Engineering, Ubon Rachathani University, and the National Center of Excellence for Environmental and Hazardous Waste Management, Ubon Ratchathani University, Ubonratchathani, Thailand, for all experimental equipments applied in this research.

## REFERENCES

Amiri, M. C. & Samiei, M. 2007 Enhancing permeate flux in a RO plant by controlling membrane fouling. *Desalination* **207**, 361–369.

Anne, C. O., Trebouet, D., Jaouen, P. & Quemeneur, F. 2001 Nanofiltration of seawater: fractionation of mono-and multi-valent cations. *Desalination* **140**, 67–77.

Bellona, C. & Drewes, J. E. 2005 The role of membrane surface charge and solute physico-chemical properties in the rejection of organic acids by NF membranes. *J. Membr. Sci.* **249**, 227–234.

Childress, A. E. & Elimelech, M. 2007 Effect of solution chemistry on the surface charge of polymeric reverse osmosis and nanofiltration membrane. *J. Membr. Sci* **119**, 253–268.

Cho, J., Amy, G. & Pellegrino, J. 1999 Membrane filtration of natural organic matter: initial comparison of rejection and flux decline characteristics with ultrafiltration and nanofiltration membranes. *Water Res.* **33**(11), 2517–2526.

Choi, S., Yun, Z., Hong, S. & Ahn, K. 2001 The effect of co-existing ions and surface characteristics of nanomembranes on the removal of nitrate and fluoride. *Desalination* **133**, 53–64.

Cotruvo, J. A. & Vogt, C. D. 1990 Rationale for water quality standards and goals. *Water Quality and Treatment*, 4th edition. McGraw-Hill, Inc, New York, USA.

Donnan, F. G. 1995 Theory of membrane equilibria and membrane potentials in the presence of non dialysing electrolytes. A contribution to physical-chemical physiology. *J. Membr. Sci.* **100**, 45–55.

Eriksson, P. 1988 Water and salt transport through two types of polyamide composite membrane. *J. Membr. Sci.* **36**, 297–313.

Frares, N. B., Taha, S. & Dorange, G. 2005 Influence of the operating conditions on the elimination of zinc ions by nanofiltration. *Desalination* **185**, 245–253.

Hong, S. & Elimelech, M. 1997 Chemical and physical aspects of natural organic matter (NOM) fouling of nanofiltration membranes. *J. Membr. Sci.* **132**, 159–181.

Ipek, U. 2005 Removal of Ni(II) and Zn(II) from an aqueous solution by reverse osmosis. *Desalination* **174**, 161–169.

Jarusutthirak, C., Mattaraj, S. & Jiraratananon, R. 2007 Influence of inorganic scalants and natural organic matter on nanofiltration membrane fouling. *J. Membr. Sci.* **287**, 138–145.

Kilduff, J. E., Mattaraj, S. & Belfort, G. 2004 Flux decline during nanofiltration of naturally-occurring dissolved organic matter: effects of osmotic pressure, membrane permeability, and cake formation. *J. Membr. Sci.* **239**(1), 39–53.

Ku, Y., Chen, S.-W. & Wang, W.-Y. 2005 Effect of solution composition on the removal of copper ions by nanofiltration. *Sep. Purif. Technol.* **43**, 135–142.

Labbez, C., Fievet, P., Szymczyk, A., Vidonne, A., Foissy, A. & Pagetti, J. 2003 Retention of mineral salts by a polyamide nanofiltration membrane. *Sep. Purif. Technol.* **30**, 47–55.

Lin, C. J., Shirazi, S., Rao, P. & Agarwal, S. 2006 Effects of operational parameters on cake formation of $CaSO_4$ in nanofiltration. *Water Res.* **40**, 806–816.

Lisdonk, C. A. C., van Paassen, J. A. M. & Schippers, J. C. 2000 Monitoring scaling in nanofiltration and reverse osmosis membrane systems. *Desalination* **132**, 101–108.

Mattaraj, S., Jarusutthirak, C. & Jiraratananon, R. 2008 A combined osmotic pressure and cake filtration model for crossflow nanofiltration of natural organic matter. *J. Membr. Sci.* **322**, 475–483.

Mehiguene, K., Garba, Y., Taha, S., Gondrexon, N. & Dorange, G. 1999 Influence of operating conditions on the retention of copper and cadmium in aqueous solutions by nanofiltration: experimental results and modelling. *Sep. Purif. Technol.* **15**, 181–187.

Molinari, R., Argurio, P. & Romeo, L. 2001 Studies on interactions between membranes (RO and NF) and pollutants ($SiO_2$, $NO_3^-$, $Mn^{++}$, and humic acid) in water. *Desalination* **138**, 271–281.

Schaep, J. & Vandecasteele, C. 2001 Evaluating the charge of nanofiltration membranes. *J. Membr. Sci.* **188**, 129–136.

Tahaikt, M., El Habbani, R., Ait Haddou, A., Achary, I., Amor, Z., Taky, M., Alami, A., Boughriba, A., Hafsi, M. & Elmidaoui, A. 2007 Fluoride removal from groundwater by nanofiltration. *Desalination* **212**, 46–53.

Taylor, J. S. & Jacobs, Ed. P. 1996 Reverse osmosis and nanofiltration. In: Mallevialle, J., Odendaal, P. E. & Weisner, M. R. (eds) *Water Treatment Membrane Processes*. McGraw-Hill, New York, USA.

Teixeira, M. R., Rosa, M. J. & Nystrom, M. 2005 The role of membrane charge on nanofiltration performance. *J. Membr. Sci.* **265**, 160–166.

Turek, M., Dydo, P., Trojanowska, J. & Campen, A. 2007 Adsorption/co-precipitation reverse osmosis system for boron removal. *Desalination* **205**, 192–199.

Van Reenan, A. J. & Sanderson, R. D. 1992 Dynamically formed hydrous zirconium (IV) oxide-polyelectrolyte membranes. VII. Poly (acrylic acid-co-vinyl acetate) and poly (acrylic acid-co-vinyl alcohol) membranes: the effect of feed salt concentration on membrane properties. *Desalination* **85**, 247–262.

Yaroshchuk, E. & Staude, A. 1992 Charged membranes for low pressure reverse osmosis properties and applications. *Desalination* **86**, 115–134.

Separation and Purification Technology 72 (2010) 217–224

Contents lists available at ScienceDirect

Separation and Purification Technology

journal homepage: www.elsevier.com/locate/seppur

# Coating of hydrophobic hollow fiber PVDF membrane with chitosan for protection against wetting and flavor loss in osmotic distillation process

Ampai Chanachai, Kittikun Meksup, Ratana Jiraratananon*

*Department of Chemical Engineering, King Mongkut's University of Technology Thonburi, Bangkok 10140, Thailand*

ARTICLE INFO

*Article history:*
Received 4 December 2009
Received in revised form 9 February 2010
Accepted 11 February 2010

*Keywords:*
Chitosan
Flavor loss
Membrane coating
Osmotic distillation
Wetting

ABSTRACT

This research studied the coating of hydrophobic membrane PVDF with chitosan, a highly hydrophilic polymer, for protection against wetting by oils from fruit juice and for reduction of flavor losses in osmotic distillation process (OD). FTIR and SEM results indicated that chitosan was well coated on PVDF membrane surface. The protection against wetting of the membranes was tested by OD of oil solution (limonene 2%, v/v) for 5 h. The results indicated that the coated membrane was able to protect the membrane against wetting-out and could maintain stable flux. An uncoated membrane was obviously wetted which was supported by the existence of $CaCl_2$ in the retentate solution and the decrease of the permeate flux.

Coating of membrane with chitosan resulted in membrane with higher water flux. For the membrane coated with chitosan crosslinked by formaldehyde, water flux decreased with increasing formaldehyde concentration. In OD of flavors (ethyl acetate and ethyl hexanoate)–limonene–water mixtures, when limonene concentration was increased, water flux decreased significantly while flavor fluxes and flavor losses increased. Coated membranes not only gave higher water flux but they also gave lower flavor flux. The results suggested that the coated membrane was appropriate for feed containing high limonene oil.

## 1. Introduction

At present, there are several methods to concentrate fruit juices such as evaporation concentration, freeze concentration and reverse osmosis. However, these methods suffer disadvantages such as, loss of flavor compounds of the final product due to relatively high temperature, high investment cost, and the limit of final concentration that can be obtained. An alternative process which operates at room temperature and atmospheric pressure has been studied and it is called osmotic distillation (OD). OD process is a membrane contactor in which hydrophobic porous membrane separates two aqueous streams, the feed and stripping streams, having the vapor difference as a driving force. Only water vapor is allowed to transfer through the membrane pores provided that wetting does not exist. Wetting can be protected, in general, if the pressure difference across the feed and stripping streams is lower than the wetting pressure.

OD has received increasing interest in concentration of fruit juices because of no or less degradation of heat-sensitive components such as flavors, and higher final concentration that can be obtained (up to 75%TS) [1,2]. However, OD still has some important disadvantages in concentration of fruit juices that are low flux and the possibility of membrane wetting by oil in fruit juices especially, for oily feeds. These lead to the decrease of flux and the loss of separation property of membrane [2–6], and loss of flavors [7] occurred by through membrane pores, even though OD can be operated at room temperature.

Membrane wetting can occur by the adsorption and accumulation of amphiphilic proteins, lipids or fat on the membrane surface [3]. The affinity between these molecules and membrane reduce surface tension of liquid at the membrane surface which in turn, reduce wetting pressure. If wetting pressure is lower than operating pressure gradient, liquid can enter the membrane pores. Membrane wetting increases mass transfer resistance of membrane because the diffusivity in the liquid phase is lower than vapor phase. If membrane is completely wetted-out, water molecules would not diffuse in vapor form any longer and both feed and stripping solutions will mix, resulting in zero flux.

Typically, limonene oil is the major oil found in fruit juice. Fruit juices contain oil in various concentration levels, depending on the variety and methods of juice extraction [3]. Due to high hydrophobicity of limonene oil, it has high affinity with hydrophobic membrane and can cause membrane wetting, even in low concentration [2]. To protect the membrane against wetting by oil (limonene) in osmotic distillation, the hydrophobic membrane was coated with hydrophilic polymers such polyvinyl alcohol (PVA) [2], alginate [3], alginic acid-silica [4], and alginate-carrageenan [5,6]. Mansouri and Fane [2] coated PVDF membrane surface with PVA by

---

* Corresponding author. Tel.: +66 24709221; fax: +66 24283534.
*E-mail address:* ratana.jir@kmutt.ac.th (R. Jiraratananon).

1383-5866/$ – see front matter © 2010 Elsevier B.V. All rights reserved.
doi:10.1016/j.seppur.2010.02.014

dip-coating method. The crosslinking agents, glutaraldehyde and maleic acid, were used for crosslinking of PVA. The results indicated that the coated membranes well protect~~ed~~ the membranes against wetting from oil. Coated membranes used to concentrate the solution of 1 wt% oil for 1 h were not wetted out during flux measurement and no visual damage nor coating detachment was observed. In contrast, membranes without the PVA coating were wetted out very rapidly by the 0.2 wt% oil as a feed.

PTFE membrane surface was coated with alginate and alginic acid-silica hydrogel in osmotic distillation [3,4]. Coating solution was precipitated onto the membrane surface. The coating layer decreased the overall OD mass transfer coefficient by less than 5% [3] and by 10% [4]. OD flux measurements using coated membranes with 0.2, 0.4 and 0.8 wt.% limonene oil–water mixtures over a period of 300 min indicated that coating was successful in protecting the membrane against wetting. An uncoated membrane was immediately wetted by a 0.2 wt% oil OD feed. In a separate trial, a coated membrane retained its integrity after contacting with 1.2 wt% oil for 72 h.

In OD of fruit juices, though the flavor losses were lower than other conventional processes, however, the losses may be as high as 70% depending on flavor types. Ali et al. [7] studied the flavor loss of PP membrane in osmotic distillation of sucrose solution. The studied flavors were hexyl acetate, ethyl butyrate, benzaldehyde, and hexanol. The results indicated that the loss of flavor in osmotic distillation of hexyl acetate, ethyl butyrate, benzaldehyde and hexanol were in interval of 37–77, 43–77, 36–52, and 25–38% respectively. Compared with vacuum evaporation process, the loss of these flavors were higher than 99%. OD, therefore, induced lower flavor losses. Moreover, the loss of these flavors decreased with decreasing velocity and temperature of sucrose solution.

Barbe et al. [8] investigated the retention of volatile organic flavor/flagrance components such as ethanol, 3-methylbutanal, ethyl acetate (EA), alpha-pinene, beta-myrcene, ethyl hexanoate (EH), and limonene in concentration of liquid foods by osmotic distillation. It was found that the ratio of flavor flux to water flux ($J_V/J_W$) of real grape juice and orange juice was much higher than that of the model solutions. For example, for ethyl acetate (using polypropylene membrane, Celgard 2500), $J_V/J_W$ of model solution, grape juice and orange juice were $1 \times 10^{-4}$, $25 \times 10^{-4}$, and $50 \times 10^{-4}$, respectively. Thus, ethyl acetate losses of grape juice and orange juice were 25–50 times of model solution. However, the reason for high flavor loss of real juice was not clear yet. Though, limonene was added into the model solution, however, in very low concentration (1 ppm) which was lower than concentrations of limonene oil in orange juice 22–400 ppm [9,10]. The concentrations of limonene in the juices tested in that research was not reported.

Due to high hydrophobicity of oil molecules, the accumulation of oil molecules on the membrane surface may impede the transport of water molecules to the membrane surface but enhance the transport of flavors to membrane surface, leading to higher flavor loss. Many researches studied the coating of hydrophobic membrane reported a successful protection of membrane against wetting in OD [2–6]. However, there has been no report on the capability of the coated layer on the reduction of flavor loss. It was expected that hydrophilic polymers coated on the membrane surface may help reduce flavor loss because flavor components have lower hydrophilicity and larger molecule sizes than water which may reduce their diffusion through hydrophilic coated layer. Therefore, this research purposed to study the protection of membrane against wetting by coating of membrane surface with hydrophilic polymer. The membrane selected for the study was the hydrophobic PVDF hollow fiber membrane. The hydrophilic polymer selected was chitosan (CS). It was successfully used to modify PVDF membrane in our previous study [11]. This research also included the effect of limonene oil on water and flavor fluxes, and the study of flavor loss.

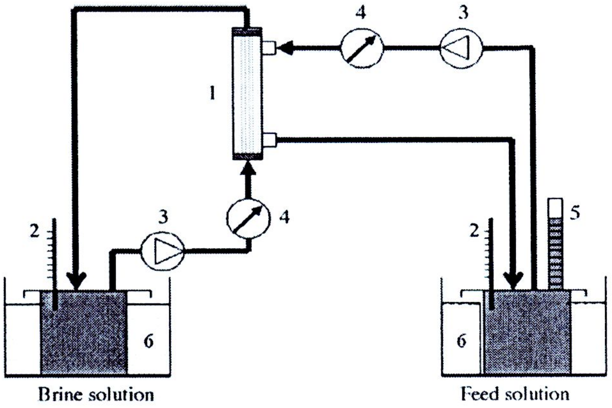

**Fig. 1.** Experimental setup of OD. (1) Hollow fiber module, (2) thermometer, (3) peristaltic pump, (4) flow meter, (5) pipette and (6) water bath.

## 2. Experimental

### 2.1. Materials

Chitosan (CS) was procured from NNC production Co. Ltd., Thailand (molecular weight 50,000 Da and 85% deacetylation). Acetic acid was purchased from LAB-SCAN. Calcium chloride dihydrate was purchased from VolChem. Limonene and formaldehyde (FM) were supplied by Sigma–Aldrich. Sodium hydroxide was obtained from CARLO ERBA. The aroma used in this work were ethyl acetate (EA) and ethyl hexanoate (EH). They represent the major aroma present in orange juices. The properties of flavor used are summarized in Table 1 [12–15]. Ethyl acetate was purchased from BDH chemical Co. Ethyl hexanoate and ethanol was purchased from Merck. All reagents used were analytical grade.

### 2.2. Analysis of flavors

The concentrations of ethyl acetate and ethyl hexanoate were analyzed by gas chromatograph (GC-14B) in which J&W DB-Wax Column was used. Injector and detector (FID) temperatures were 230 and 250 °C, respectively. After the sample was injected, the oven temperature was held at 40 °C for 4 min then it was increased to 65 °C at a rate of 15 °C/min and was held at 65 °C for 8 min.

### 2.3. Membrane

Polyvinylidene fluoride (PVDF) hollow fiber membranes used in this research was provided by Memcor (South Windsor, New South Wales, Australia). The fibers had an inner diameter and an outer diameter of 800 and 1300 μm, respectively and the pore size was 0.2 μm as provided by the manufacturer. The fibers were potted in the glass module with length and inner diameter of 250 and 8 mm respectively. Each module contained 15 fibers with the effective length of 225 mm. The membrane surface area was 0.01378 $m^2$ per module.

### 2.4. OD experimental setup

Fig. 1 depicted the experimental setup. The feed solution was pumped by peristaltic pump (Masterflex easy load II model 7518-00) from feed tank to shell side of membrane while the brine solution ($CaCl_2$, 45 wt%) was supplied to tube side of membranes. Circulation of both feed and brine was counter-current with vertical

**Table 1**
Properties of flavors [12–15].

| Compound | MW | Boiling point (°C) | $P_{sat}$ at 25°C (mmHg) | $\gamma^\infty$ in water at 25 °C (SD) | Relative volatility,[a] $\alpha_{i/w}$ | Hydrophobic constant, log *P* |
|---|---|---|---|---|---|---|
| Ethyl acetate | 81.1 | 71.1 | 87.32 | 70 (4) | 259 | 0.73 |
| Ethyl hexanoate | 144.2 | 168 | 1.18 | 32,700 (920) | 1638 | 2.80 |
| Limonene | 136.3 | 176 | 0.66 | 370,000 (37,000) | 10,365 | 4.57 |

[a] Calculated from $\alpha_{i/w} = \gamma_i^\infty P_i^{sat}/P_w^{sat}$ [12]; $\gamma_i^\infty$ is activity coefficient of *i* for dilute aqueous solution and $P^{sat}$ is saturation vapor pressure.

direction. The volumetric flow rates of the feed and the brine were controlled by flow meters at 455 and 452.4 ml/min, respectively which corresponded to velocities of 0.25 and 1 m/s, respectively. The water baths (YCW-010 series, KK) with the temperature control were used to control the feed and brine temperatures. The temperature of both water baths was set at 25 °C. During OD operation, the water flux was obtained by measuring the reduction of feed volume in the pipette connected to the feed tank.

### 2.5. Coating of membrane with chitosan with and without crosslinking

Chitosan was dissolved in 2 wt% acetic acid aqueous solutions with various concentrations of 0.1, 0.5, 1 and 2% (w/v). The solutions were then stirred for 20 min. After chitosan completely dissolved, the solution was filtered with vacuum filtration (filter paper no. 1). In case of crosslinking study, the chitosan concentration was fixed at 2% (w/v) and the concentration of formaldehyde was varied to be 0.2, 0.3, 0.4 and 0.8% (w/v) of chitosan solution. Then, the chitosan-formaldehyde solution was stirred until the solution became homogeneous.

Dip-coating method was used to coat outer surface of PVDF hollow fiber membrane in this work. Each hollow fiber was dipped in the coating solution for 5 min, then it was hung to dry at room temperature for 1 h. Later, the coated fibers were dried in the oven at 45, 50, 55 °C for 1 h at each temperature and then at 60 °C for 2 h [16] to vaporize all solvent from the coated layer. After drying, coated membranes were soaked in 4% (w/v) of sodium hydroxide in 50% (v/v) of ethanol solution for 1 h to neutralize chitosan film from water dissoluble form into water indissoluble form. Afterwards, the coated fibers were rinsed several times with deionised (DI) water and were left to dry at room temperature. The dried fibers were then potted into the glass fiber module.

### 2.6. Examination of membrane properties

#### 2.6.1. Morphology of the coated layer on the membrane surface

The effect of chitosan concentration on morphology of chitosan coated layer was examined by scanning electron microscopy (SEM, LEO model 1455VP). The cross-section of membranes was prepared by fracturing the membrane sample in liquid nitrogen. All samples were dried in vacuum for 12 h at room temperature and were gold-coated. The scanning was performed at an accelerating voltage of 10 kV.

#### 2.6.2. Examination of chemical structure of coated layer on membrane surface

The presence of uncrosslinked and crosslinked chitosan layers on membrane surface were examined by Fourier Transform Infrared (FTIR) Spectroscopy instrument. Thermo-Nicolet Magna 550 FTIR was used with 50° angle of incidence. Each spectrum was collected by cumulating 32 scans at a resolution of 4 cm$^{-1}$.

#### 2.6.3. Water flux measurement

The experimental setup depicted in Fig. 1 was used for determining water flux of uncoated and coated membranes. Feed tank was filled with DI water. The volume of the feed can be seen from level indicated on the pipette. Level of the feed was normally recorded every 5 min and the change in water feed volume was calculated as water flux of membrane. The coated membranes were triplicatedly prepared for water flux measurement and the average values of water flux were reported.

#### 2.6.4. Examination of membrane wetting and membrane stability

The test of membrane wetting was carried out by OD of 2% (v/v) limonene feed. The wetting of membrane was investigated by checking the presence of $CaCl_2$ salt in the retentate after 5 h of OD operation. The retentate solution was titrated with 0.0124 M silver nitrate ($AgNO_3$). Potassium chromate ($K_2CrO_4$) solution was used as indicator. If the membrane was wetted, the white precipitate of AgCl was observed. If the membrane was not wetted, the red precipitate of $Ag_2CrO_4$ can be observed. In case of white sediment was observed, the titration was continued until red precipitate was seen, then, the amount of $CaCl_2$ in retentate can be calculated.

In testing of the long-term performance against wetting of the coated membranes, membranes coated with chitosan 2% (w/v) without crosslinking and uncoated membranes were immersed in 4% (v/v) limonene solution for 48 h. Then the membranes were washed with DI water and water flux was again measured.

#### 2.6.5. Flavor loss study

The uncoated and coated membranes were used to test the flavor loss in OD. The coated membranes used in this test were coated with 2% (w/v) CS without and with crosslinking with formaldehyde 0.2% (w/v). Ethyl acetate and ethyl hexanoate were used to represent the flavors. The feed solution was the mixture of ethyl acetate, ethyl hexanoate, limonene and water. The concentrations of ethyl acetate and ethyl hexanoate were fixed at 500 mg/l. The limonene concentrations were varied 0–500 mg/l in order to study the effect of limonene oil on water and flavor fluxes and flavor losses. Samples were collected from retentate solution before and after OD processing for 7 h to analyze concentration of flavors by gas chromatograph. Then, water and flavor fluxes and flavor losses were calculated by Eqs. (1)–(4).

### 2.7. Calculation

The total flux (*J*, kg/m$^2$ h) and flavor flux ($J_v$, kg/m$^2$ h) were calculated by the following.

$$J = \frac{(V_0 - V_f)\rho}{1000At} \tag{1}$$

$$J_v = \frac{V_0 C_{i0} - V_f C_{if}}{1 \times 10^6 At} \tag{2}$$

$$J_w = J - \sum J_v \tag{3}$$

where $J$, $J_v$, $J_w$ are the total flux, flavor flux and water flux, respectively (kg/m$^2$ h), $V_0$ and $V_f$ the initial and final volumes of feed solution (l), $C_{i0}$ and $C_{if}$ the initial and final concentrations of flavor in feed (mg/l), $A$ the membrane area (m$^2$), $t$ operating time (h), and $\rho$ is the water density (1 g/l).

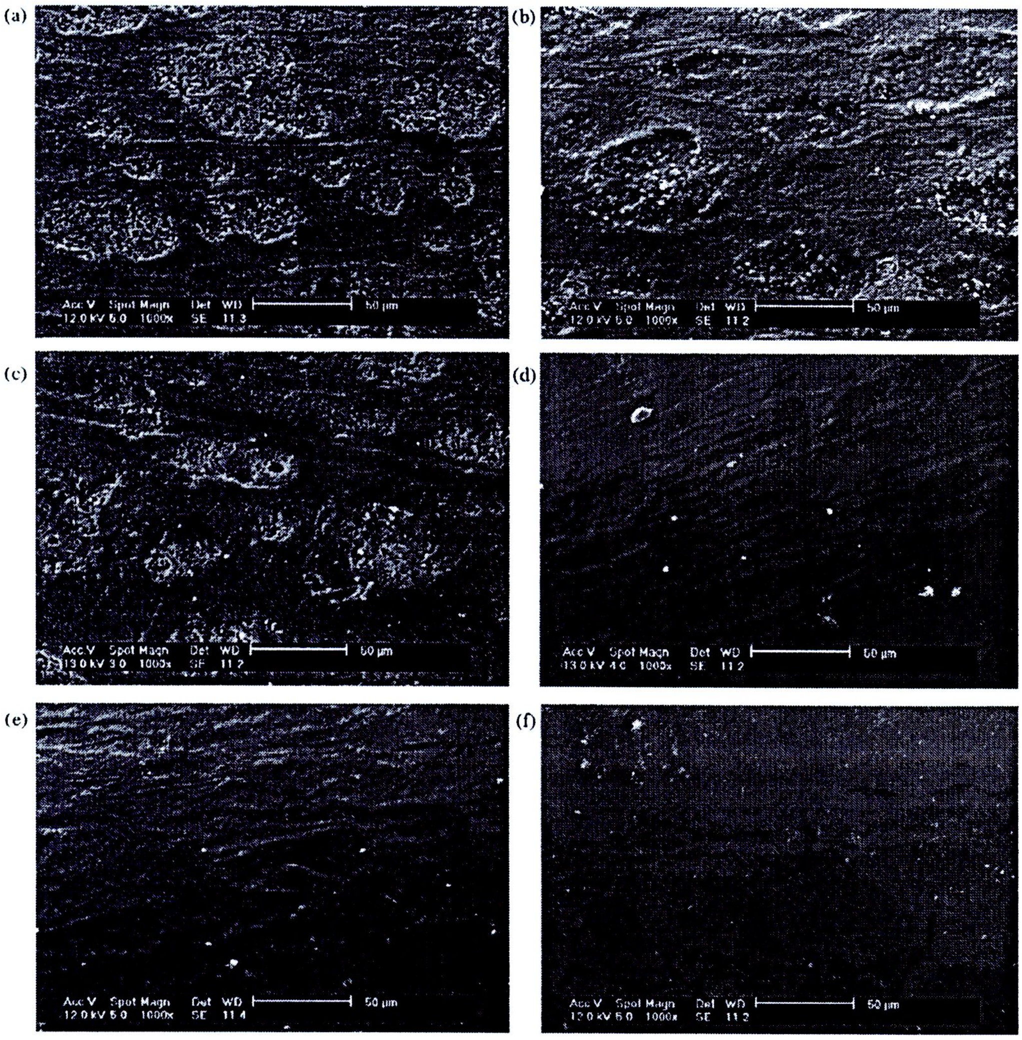

**Fig. 2.** SEM images of surface of PVDF membranes: (a) uncoated membrane; coated membrane with chitosan without crosslinking (b) 0.1% (w/v) CS, (c) 0.5% (w/v) CS chitosan, (d) 2.0% (w/v) CS, (e) 2.0% (w/v) CS after OD of limonene–water mixture and (f) coated membrane with chitosan 2.0% (w/v) crosslinked with 0.2% formaldehyde after OD of limonene–water mixture.

%Flavor loss was calculated by the following equation:

$$\%\text{Flavor loss} = \frac{V_0 C_{i0} - V_f C_{if}}{V_0 C_{i0}} \times 100 \qquad (4)$$

## 3. Results and discussion

### 3.1. Membrane morphology

The morphology of chitosan layer coated on the external surface of the hollow fibers was examined by SEM and is shown in Fig. 2. The pores of an uncoated membrane can be clearly seen and they were not uniformly distributed on membrane surface (Fig. 2a). For the membrane coated with chitosan 0.1% (w/v), chitosan layer covered some area of membrane surface as seen in Fig. 2b. At 0.5% (w/v) of chitosan concentration, chitosan layer covered all of membrane pores (Fig. 2c). At higher concentration (2.0%, w/v chitosan), coating was more uniform than that at low chitosan concentration (Fig. 2d). The SEM images of external surfaces of the membranes coated with chitosan at various concentrations indicated that chitosan was well coated on membrane surface.

Fig. 2e and f shows the SEM images of membrane coated with chitosan 2.0% (w/v) without and with crosslinking with 0.2% formaldehyde, respectively, after OD of limonene–water mixture. It can be seen that the chitosan coated layer was still stable and covered the whole membrane surface. The damage or rupture of the coated layer could not be observed, indicating the stability of coated layer on the base membrane.

### 3.2. Chemical structure of coated layer on the membrane surface

The chemical structures of the uncoated and coated membranes with and without crosslinking were characterized by FTIR and the results are presented in Fig. 3. For the FTIR spectra of chitosan, the bands at 1657 and 1592 cm$^{-1}$ were characteristics of >C=O stretching of N-acetyl group and –N–H deformation of amino group, respectively. Also the bands at 896 and 1152 cm$^{-1}$ characterized –N–H wagging and –C–O–C stretching of ether linkage, respectively [17]. The broad and strong band ranging from 3200 to 3600 cm$^{-1}$ indicated the presence of –OH stretching of hydroxyl group and –$NH_2$ stretching of amino group in chitosan.

For the uncoated PVDF membrane, the peaks of –$CF_2$ and C=C stretching were shown at 1180 and 1475 cm$^{-1}$, respectively [18]. The absorption peaks at 795 and 854 cm$^{-1}$ were the typical characteristic of PVDF.

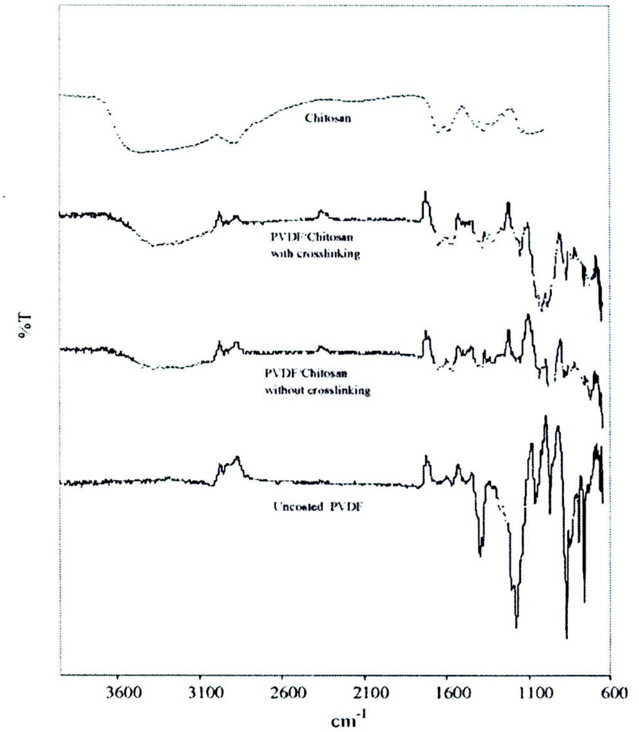

Fig. 3. FTIR sprectra of uncoated and coated membrane with chitosan with and wtihout crosslinked with formaldehyde.

Comparing between uncoated and coated PVDF membrane, it was found that the absorption peaks assigned to $-CF_2$ and C=C stretching at 1180 and 1475 $cm^{-1}$ almost disappeared for coated membrane. The absorption peaks at 795 and 854 $cm^{-1}$ which were the typical characteristic of PVDF also disappeared. These indicated that chitosan coated layer were coated and covered the entire membrane surface. In addition, the absorption peaks characteristic of chitosan, appeared on the adsorption peak of coated membrane such as the broad and strong band of –OH and $-NH_2$ ranging from 3200 to 3600 $cm^{-1}$. The >C=O stretching was shifted from 1657 to 1652 $cm^{-1}$. The –C–O–C stretching of ether linkage appeared at 1152 $cm^{-1}$ and the –N–H deformation of amino group was shifted from 1592 to 1576 $cm^{-1}$. The results confirmed that, there was chitosan coated on the PVDF membrane surface.

For the membrane coated with crosslinking with formaldehyde, the absorption peaks of ether group were stronger at 1051 $cm^{-1}$, suggesting the formation of a new chain ether linkage in chitosan after crosslinked reaction [19]. The adsorption peak at 1152 $cm^{-1}$, characteristic of C–N stretching, became stronger by the presence of secondary amine formed by crosslinking reaction between amino group in chitosan and aldehyde group of formaldehyde.

### 3.3. *Effect of membrane coating and crosslinking of chitosan on water flux*

The results of the average water flux within 1 h for uncoated membrane and coated membrane (without crosslinking) at various concentrations are shown in Fig. 4. It was found that no $CaCl_2$ was found in feed solution after operation, for all membranes. This indicated that the membranes were not wetted. It can also be found from Fig. 4 that coating of PVDF membrane with chitosan resulted in higher water flux. Coating of membrane with hydrophilic polymer can increase the hydrophilicity of the membrane surface or the repulsive force between hydrophobic membrane and water molecules decrease [20]. Moreover, diffusion of water molecules through hydrophilic chitosan layer was enhanced, resulted in higher water flux. Higher chitosan concentration resulted in higher hydrophilicity, water flux was, then, increased. For the membrane coated with chitosan 0.1% (w/v), the water flux was slightly higher than that of uncoated membrane because at this chitosan concentration, chitosan layer did not cover all membrane surface as shown in Fig. 2. At high chitosan concentration, 2% (w/v), water flux tended to decrease due to thicker chitosan layer on membrane surface that increased the membrane resistance to flow.

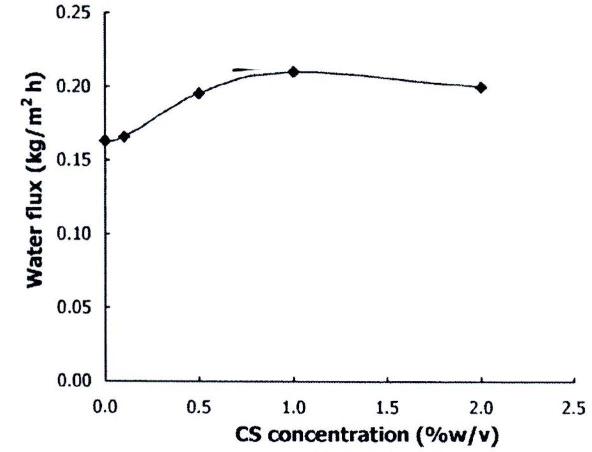

**Fig. 4.** Average water flux within 1 h of uncoated membrane and coated membranes coated with various chitosan concentrations without crosslinking.

The average water flux within 1 h for membrane coated with chitosan crosslinked with formaldehyde is shown in Fig. 5. It was found that membranes coated with chitosan crosslinked with formaldehyde had lower water flux than an uncrosslinked one and water flux of the membranes decreased with an increasing of formaldehyde concentration. For coated membrane crosslinked with formaldehyde 0.4% (w/v), water flux was rather closed to that of uncoated membrane (see Fig. 4). Since crosslinking of chitosan with formaldehyde occurred at hydrophilic groups (–OH) of chitosan, therefore, chitosan became more hydrophobic. This interfered the interaction between chitosan and water [21] and

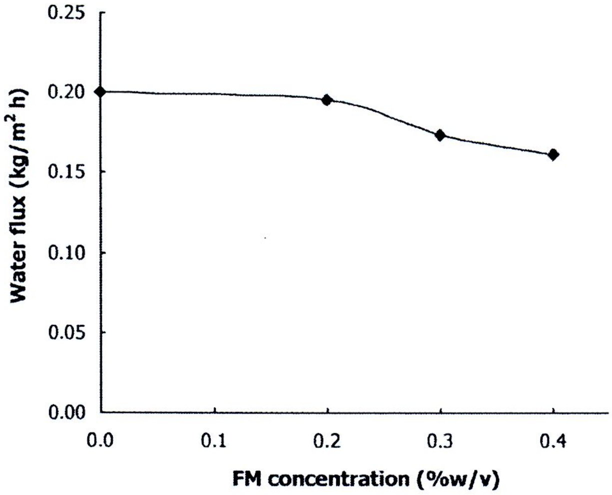

**Fig. 5.** Average water flux within 1 h for coated membranes with chitosan 2% (w/v) and crosslinked with various formaldehyde (FM) concentrations.

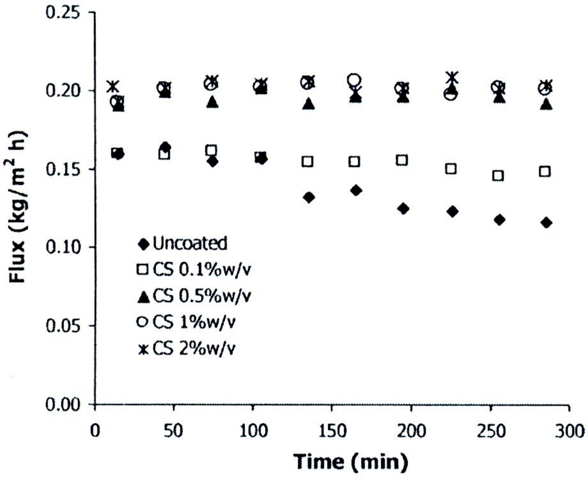

**Fig. 6.** Flux versus time of membranes coated with various chitosan concentrations without crosslinking for limonene solution feed.

reduced swelling property of chitosan, resulting in lower water flux.

Previous work [3] reported that the coated layer of alginate on PTFE membrane decreased the overall OD mass transfer coefficient by less than 5%. In that work, the alginate coated layer was crosslinked with 1-ethyl-3(3dimethylaminopropyl) carbodiimide. However, it was found from this research that if the concentrations of chitosan and crosslinking agent was not too high, in other words, be at the optimum, the water flux of coated membrane can be higher than that of uncoated membrane.

### 3.4. *Effect of membrane coating on the protection of wetting and membrane stability*

The test of membrane wetting was conducted by using 2% (v/v) limonene solution as feed. Water flux of an uncoated membrane continuously dropped after 100 min of operation (Fig. 6) and 18.86 mg/l of $CaCl_2$ was found in retentate solution, after 5 h of operation. This implied significant wetting of an uncoated membrane. In contrast, water fluxes of all coated membranes were quite constant and no $CaCl_2$ was detected in retentate solution. Therefore, the coated membranes can protect membrane wetting by limonene oil. It can be explained that hydrophilic chitosan polymer allows water diffusion, but, inhibits a transport of limonene oil. These results agreed well with the report of Mansouri and Fane [2] and Xu et al. [3] in which PVDF membrane was coated with PVA and PTFE membrane was coated with alginate.

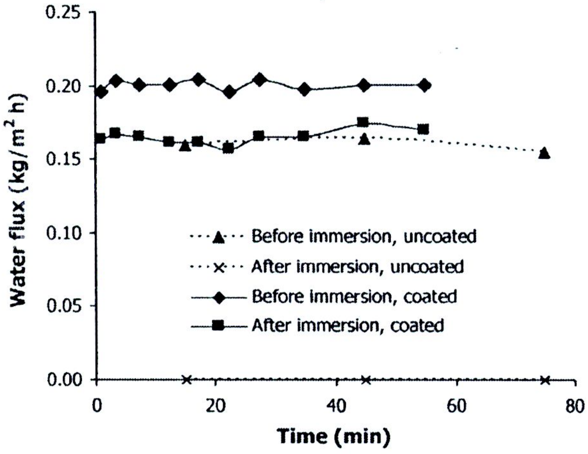

**Fig. 7.** Water flux versus time of uncoated membrane and membrane coated with uncrosslinked chitosan 2% (w/v) before and after immersion of membrane in 4% (v/v) limonene solution for 48 h.

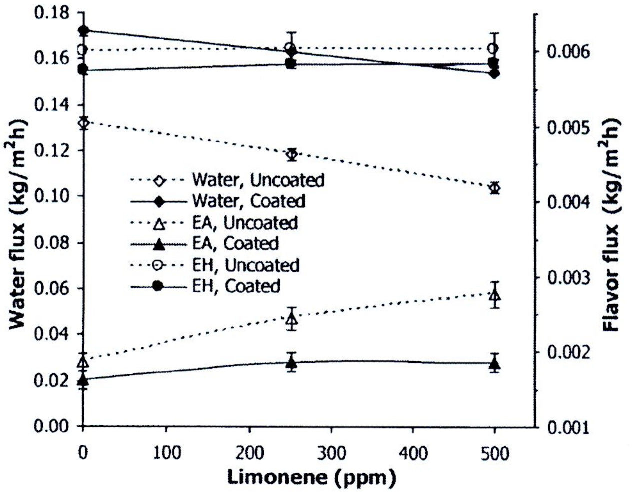

**Fig. 8.** Effect of limonene concentration on water and flavor fluxes in OD of flavor/limonene aqueous solutions with an uncoated membrane and uncrosslinked coated membrane with CS 2% (w/v).

In the long-term test of wetting resistance of the coated membrane, membranes coated with chitosan 2% (w/v) and uncoated membranes were immersed in 4% (v/v) limonene solution for 48 h, then, the membranes were washed with DI water and water flux was again measured. The water flux results indicated that a coated membrane retained its integrity of wetting protection, even though water flux decreased from 0.200 to 0.165 kg/h m² as shown in Fig. 7 and no $CaCl_2$ was found in retentate solution. A decrease of water flux may be attributed to adsorption of some limonene oil on the membrane surface which could not be washed out by water. While the water flux of an uncoated membrane dropped to zero and the membrane completely lost its hydrophobicity. 482 mg/l of $CaCl_2$ was detected in the retentate solution within the first 15 min of operation.

### 3.5. *Flavor loss*

#### 3.5.1. *Effect of limonene oil on water and flavor fluxes*

In this study, the aqueous feed solutions were the mixtures of ethyl acetate, ethyl hexanoate and limonene oil at various concentrations. The concentrations of each flavor were fixed at 500 mg/l. The membrane used was an uncoated PVDF membrane. It can be seen from Fig. 8 that an increase of limonene concentration in feed solution resulted in a decrease of water flux but an increase of flavor fluxes. The reason was the deposition and accumulation limonene molecules on membrane surface due to hydrophobic property of both limonene and membrane. Thus, water and flavor molecules must diffuse from bulk solution through limonene layer to membrane surface. The diffusivity of water decreased due to the repulsion between polar water molecule and hydrophobic limonene, resulted in a reduction of water flux. On the contrary, flavor fluxes were enhanced because of the hydrophobicity of flavor and limonene molecules.

It can be also seen that flux of ethyl hexanoate was higher than ethyl acetate. The molecular size of ethyl hexanoate is larger than ethyl acetate, however, its relative volatility and hydrophobicity was much higher (Table 1). These are the reason for higher flux and higher loss of ethyl hexanoate.

**Table 2**
Comparison of water and flavor flux and percentage of flavor loss of both ethyl acetate and ethyl hexanoate in OD for 7 h.

| Membrane | Flux (g/m² h) | | | %Flavor loss | |
|---|---|---|---|---|---|
| | $J_W$ | $J_{EA}$ | $J_{EH}$ | EA | EH |
| Uncoated | 131.70 ± 0.12 | 1.86 ± 0.10 | 5.98 ± 0.02 | 29.72 ± 1.65 | 95.09 ± 0.12 |
| Coated without crosslinking | 171.97 ± 0.11 | 1.62 ± 0.11 | 5.76 ± 0.005 | 26.06 ± 1.88 | 91.57 ± 0.05 |
| Coated with crosslinking | 163.66 ± 0.13 | 1.36 ± 0.09 | 5.72 ± 0.03 | 21.84 ± 0.53 | 91.05 ± 0.32 |

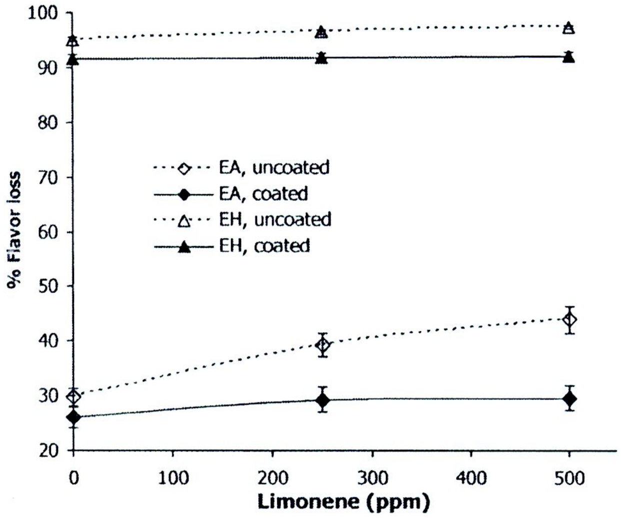

Fig. 9. Effect of limonene concentration on %flavor loss in OD of flavor/limonene aqueous solutions with an uncoated membrane and uncrosslinked coated membrane with CS 2% (w/v).

### 3.5.2. *Effect of coated layer on water and flavor fluxes*

Comparison of water and flavor fluxes in OD of flavor/limonene aqueous solutions between uncoated and coated membrane are shown in Fig. 8. The results showed that water flux of coated membrane were higher than that of uncoated membrane as described in Section 3.3. It can be also seen that coated membrane gave lower flavor fluxes than those uncoated membrane. Since flavors were more hydrophobic and had higher molecular size than water molecules, therefore, it was more difficult for flavors to solubilize and diffuse through hydrophilic chitosan layer, leading to lower flavor flux of coated membrane.

The relations between limonene concentration versus water and flavor fluxes of coated membrane were similar to uncoated membrane. However, a decrease in water flux with increasing limonene concentration was lower in case of coated membrane which is the advantage. On the contrary, the increase of flavor flux with limonene concentration should be low. The results in Fig. 8 exhibit that the increase of flavor flux was not significant for coated membranes. It can be explained that the deposition of hydrophobic limonene on hydrophilic chitosan coated layer was low due to their opposite properties, resulted in a reduction of effect of limonene concentration on water and flavor fluxes. Since flavor fluxes of coated membrane were lower than those of uncoated membrane, thus, the %flavor losses of coated membrane were also lower. In addition, an increase of %flavor losses with limonene concentration was small for coated membrane (Fig. 9). The results suggested that the coated membrane was more appropriate for feed containing high limonene oil.

### 3.5.3. *Effect of crosslinking of coated layer on water and flavor fluxes*

Table 2 shows the OD results of ethyl acetate-ethyl hexanoate-water mixture (no limonene) for uncoated and coated membrane with and without crosslinking. As mentioned in Section 3.3 that crosslinked coated membrane had lower water flux than that of an uncrosslinked one. Flavor fluxes of crosslinked coated membrane were lower than those of uncoated and uncrosslinked coated membranes due to a tighter structure of the crosslinked layer, resulted in its lowest %flavor loss.

## 4. Conclusion

The membrane coated with chitosan provided better protection against membrane wetting and also increased water flux of PVDF membrane. The crosslinking of chitosan with formaldehyde reduced water flux due to the decrease in swelling property of chitosan. The coated membrane had better resistance to flavor loss than an uncoated membrane. The coated membrane crosslinked with formaldehyde slightly improved flavor retention compared with the coated membrane without crosslinking. The results suggested that the coated membrane was more appropriate for feed containing high limonene oil. The results of these work presented the promising alternative for concentration of fruit juice by OD process.

## Acknowledgements

The authors gratefully acknowledge the financial support from the Thailand Research Fund (TRF) and the Commission on Higher Education, Thailand. Memcor (South Windsor, New South Wales, Australia) is also thanked for their kind supports of membrane.

## References

[1] V.A. Bui, M.H. Nguyen, J. Muller, A laboratory study on glucose concentration by osmotic distillation in hollow fibre module, J. Food Eng. 63 (2004) 237–245.
[2] J. Mansouri, A.G. Fane, Osmotic distillation of oily feeds, J. Membr. Sci. 153 (1999) 103–120.
[3] J.B. Xu, S. Lange, J.P. Bartley, R.A. Johnson, Alginate-coated microporous PTFE membranes for use in the osmotic distillation of oily feeds, J. Membr. Sci. 240 (2004) 81–89.
[4] J.B. Xu, D.A. Spittler, J.P. Bartley, R.A. Johnson, Alginic acid-silica hydrogel coatings for the protection of osmotic distillation membranes against wet-out by surface-active agents, J. Membr. Sci. 260 (2005) 19–25.
[5] J.B. Xu, J.P. Bartley, R.A. Johnson, Preparation and characterization of alginate-carrageenan hydrogel films crosslinked using a water-soluble carbodiimide (WSC), J. Membr. Sci. 218 (2003) 131–146.
[6] J.B. Xu, J.P. Bartley, R.A. Johnson, Application of sodium alginate-carrageenan coatings to PTFE membranes for protection against wet-out by surface-active agents, Sep. Sci. Technol. 40 (2005) 1067–1081.
[7] F. Ali, M. Dornier, A. Duquenoy, M. Reynes, Evaluating transfers of aroma compounds during the concentration of sucrose solutions by osmotic distillation in a batch-type pilot plant, J. Food Eng. 60 (2003) 1–8.
[8] A.M. Barbe, J.P. Bartley, A.L. Jacobs, R.A. Johnson, Retention of volatile organic flavour/fragrance components in the concentration of liquid foods by osmotic distillation, J. Membr. Sci. 145 (1998) 67–75.
[9] S. Selli, T. Cabaroglu, A. Canbas, Volatile flavour components of orange juice obtained from the cv. Kozan of Turkey, J. Food Comp. Anal. 17 (2004) 789–796.
[10] P.E. Shaw, M. Lebrun, M. Dornier, M.N. Ducamp, M. Courel, M. Reynes, Evaluation of concentrated orange and passion fruit juices prepared by osmotic evaporation, Lebensm.-Wiss. u.-Technol. 34 (2001) 60–65.
[11] S. Boributh, A. Chanachai, R. Jiraratananon, Modification of PVDF membrane by chitosan solution for reducing protein fouling, J. Membr. Sci. 342 (2009) 97–104.
[12] J.A. Ragazzo-Sanchez, P. Chalier, D. Chevalier, C. Ghommidh, Electronic nose discrimination of aroma compounds in alcoholised solutions, Sens. Actuators B 114 (2006) 665–673.

[13] I. Fichan, C. Larroche, J.B. Gros, Water solubility, vapor pressure, and activity coefficients of terpenes and terpenoids, J. Chem. Eng. Data 44 (1999) 56–62.

[14] M.F. Sancho, M.A. Rao, D.L. Downing, Infinite dilution activity coefficients of apple juice aroma compounds, J. Food Eng. 34 (1997) 145–158.

[15] G. Savary, E. Guichard, J.-L. Doublier, N. Cayot, Mixture of aroma compounds: determination of partition coefficients in complex semi-solid matrices, Food Res. Int. 39 (2006) 372–379.

[16] H.A. Tsai, W.H. Chen, C.Y. Kuo, K.R. Lee, J.Y. Lai, Study on the pervaporation performance and long-term stability of aqueous iso-propanol solution through chitosan/polyacrylonitrile hollow fiber membrane, J. Membr. Sci. 309 (2008) 146–155.

[17] D.A. Musale, A. Kumar, G. Pleizier, Formation and characterization of poly(acrylonitrile)/chitosan composite ultrafiltration membranes, J. Membr. Sci. 154 (1999) 163–173.

[18] S. Rajendran, M. Sivakumar, R. Subadevi, M. Nirmala, Characterization of PVA-PVDF based solid polymer blend electrolytes, Physica B 348 (2004) 73–78.

[19] A. Singh, S.S. Narvi, P.K. Dutta, N.D. Pandey, External stimuli response on a novel chitosan hydrogel crosslinked with formaldehyde, Bull. Mater. Sci. 29 (2006) 233–238.

[20] J.M. Dickson, R.F. Childs, B.E. McCarry, D.R. Gagnon, Development of a coating technique for the internal structure of polypropylene microfiltration membranes, J. Membr. Sci. 148 (1998) 25–36.

[21] M.M. Beppu, R.S. Vieira, C.G. Aimoli, C.C. Santana, Crosslinking of chitosan membranes using glutaraldehyde: effect on ion permeability and water adsorption, J. Membr. Sci. 301 (2007) 126–130.